Award Number: W81XWH-15-1-0272

TITLE: Low-Cost, High-Throughput 3-D Pulmonary Imager Using Hyperpolarized Contrast Agents and Low-Field MRI

PRINCIPAL INVESTIGATOR: Boyd M. Goodson, Ph.D.

CONTRACTING ORGANIZATION: Southern Illinois University, Carbondale, IL 62901

REPORT DATE: JULY 2020

TYPE OF REPORT: Annual

PREPARED FOR: U.S. Army Medical Research and Materiel Command
Fort Detrick, Maryland, 21702-5012

DISTRIBUTION STATEMENT: Approved for Public Release;
Distribution Unlimited

The views, opinions and/or findings contained in this report are those of the author(s) and should not be construed as an official Department of the Army position, policy or decision unless so designated by other documentation

REPORT DOCUMENTATION PAGE

Form Approved
OMB No. 0704-0188

Public reporting burden for this collection of information is estimated to average 1 hour per response, including the time for reviewing instructions, searching existing data sources, gathering and maintaining the data needed, and completing and reviewing this collection of information. Send comments regarding this burden estimate or any other aspect of this collection of information, including suggestions for reducing this burden to Department of Defense, Washington Headquarters Services, Directorate for Information Operations and Reports (0704-0188), 1215 Jefferson Davis Highway, Suite 1204, Arlington, VA 22202-4302. Respondents should be aware that notwithstanding any other provision of law, no person shall be subject to any penalty for failing to comply with a collection of information if it does not display a currently valid OMB control number. **PLEASE DO NOT RETURN YOUR FORM TO THE ABOVE ADDRESS.**

1. REPORT DATE	**2. REPORT TYPE**	**3. DATES COVERED**
JULY 2020	ANNUAL	30SEPT2019 - 29SEPT2020

4. TITLE AND SUBTITLE
Low-Cost, High-Throughput 3-D Pulmonary Imager
Using Hyperpolarized Contrast Agents and Low-Field MRI

5a. CONTRACT NUMBER
W81XWH-15-1-0272

5b. GRANT NUMBER

5c. PROGRAM ELEMENT NUMBER

6. AUTHOR(S)
Boyd M. Goodson, Ph.D.

E-Mail: bgoodson@chem.siu.edu

5d. PROJECT NUMBER

5e. TASK NUMBER

5f. WORK UNIT NUMBER

7. PERFORMING ORGANIZATION NAME(S) AND ADDRESS(ES)

Southern Illinois University
900 SOUTH NORMAL
WOODY HALL C 206
CARBONDALE IL 62901

8. PERFORMING ORGANIZATION REPORT NUMBER

9. SPONSORING / MONITORING AGENCY NAME(S) AND ADDRESS(ES)

U.S. Army Medical Research and Materiel Command
Fort Detrick, Maryland 21702-5012

10. SPONSOR/MONITOR'S ACRONYM(S)

11. SPONSOR/MONITOR'S REPORT NUMBER(S)

12. DISTRIBUTION / AVAILABILITY STATEMENT

Approved for Public Release; Distribution Unlimited

13. SUPPLEMENTARY NOTES

14. ABSTRACT

This report covers the second period of the no-cost extension period. Overall, this is the fifth year of the project performance. During the indicated period of performance, we have focused our activities on two specific aims. With regards to Aim #1 (^{129}Xe polarizer development), we have been on testing the final ^{129}Xe automated hyperpolarizer, publishing the results and also developing the quality assurance experiments for future *in vivo* validation studies. With respect to Aim 3, the custom imaging equipment has been delivered by the vendor. However, due to COVID-19, we could not complete the installation process (the site was under the governor's lock-down order). The remaining efforts (in the next year) will primarily focus on the installation of the 0.35 T MRI scanner and completion of the second polarizer. With respect to the delivery and installation of the 0.35 T MRI scanner, we have been engaged with the vendor to ensure that the delivered MRI scanner will be customized to our needs to meet the specifications for scan speed and resolution. As with previous years, we also note that we are submitting a duplicating report for two partnering PI awards of the same project: W81XWH-15-1-0271 and W81XWH-15-1-0272.

15. SUBJECT TERMS
low-field MRI; pulmonary imaging, high-throughput; low cost

16. SECURITY CLASSIFICATION OF:			**17. LIMITATION OF ABSTRACT**	**18. NUMBER OF PAGES**	**19a. NAME OF RESPONSIBLE PERSON**
a. REPORT	**b. ABSTRACT**	**c. THIS PAGE**			USAMRMC
Unclassified	Unclassified	Unclassified	Unclassified	113	**19b. TELEPHONE NUMBER** *(include area code)* f

Table of Contents

Page

1. INTRODUCTION 4

2. KEYWORDS 4

3. ACCOMPLISHMENTS 5
TASK 1.6 FINAL TESTING OF THE ^{129}XE HYPERPOLARIZER 5
TASK 1.8 REPLICA POLARIZER CONSTRUCTION AND TESTING 6
TASK 3.1. DESIGN LOW-FIELD MRI SYSTEM WITH COMMERCIAL VENDORS 7
TASK 3.2. LOW-FIELD MRI SYSTEM CONSTRUCTION BY VENDORS 8
TASK 3.4. RF COILS (^{129}XE AND ^{1}H) CONSTRUCTION FOR PULMONARY IMAGING 8
TASK 3.5. PULSE-SEQUENCE DEVELOPMENT AND INSTALLATION 8
WHAT OPPORTUNITIES FOR TRAINING AND PROFESSIONAL DEVELOPMENT HAS THE PROJECT PROVIDED? 8
HOW WERE THE RESULTS DISSEMINATED TO COMMUNITIES OF INTEREST? 8

4. IMPACT 8
WHAT WAS THE IMPACT ON THE DEVELOPMENT OF THE PRINCIPAL DISCIPLINE(S) OF THE PROJECT? 8
WHAT WAS THE IMPACT ON OTHER DISCIPLINES? 8
WHAT WAS THE IMPACT ON TECHNOLOGY TRANSFER? 8
WHAT WAS THE IMPACT ON SOCIETY BEYOND SCIENCE AND TECHNOLOGY? 8

5. CHANGES / PROBLEMS 8

6. PRODUCTS 9
ORAL PRESENTATIONS 9
CONFERENCE ABSTRACTS 9
PEER-REVIEWED MANUSCRIPTS, DISSERTATION & BOOK CHAPTERS 9
INVENTIONS, PATENT APPLICATIONS AND LICENSES: 10
FUNDING APPLIED FOR BASED ON WORK SUPPORTED BY THIS AWARD 10

7. PARTICIPANTS & OTHER COLLABORATING ORGANIZATIONS 13
INDIVIDUALS WORKED ON THE PROJECT 13
HAS THERE BEEN A CHANGE IN THE ACTIVE OTHER SUPPORT OF THE PD/PI(S) OR SENIOR/KEY PERSONNEL SINCE THE LAST REPORTING PERIOD? 15

8. SPECIAL REPORTING REQUIREMENTS 16
COLLABORATIVE AWARD 16

9. APPENDICES 17
APPENDIX 1: ORIGINAL STATEMENT OF WORK, YEARS 1-3 17
APPENDIX 2: ABSTRACTS PRESENTED AND MANUSCRIPTS PUBLISHED AND ACCEPTED 20

1. Introduction

We are developing clinical scale production of two gaseous hyperpolarized contrast agents and hyperpolarized MRI allowing for ultrafast (potentially sub-second) and high-throughput molecular imaging of lung function. The key additional focus of this project is on significantly lower cost of our imaging technology of low-field MRI compared to conventional high-field MRI (1.5 T and beyond) due to much higher patient throughput/much faster exams and the use of low field = low cost MRI. We focus our research effort on the high-risk critical challenges that must be solved to enable clinical implementation of hyperpolarized gases for pulmonary imaging.

Specifically, the research efforts during Year 5 have focused on three specific aims as described in the Statement of Work (Appendix 1):

Aim 1: Develop and construct a fully automated high-pressure low-cost stand-alone ^{129}Xe hyperpolarizer

During Year 3 the original laser of the ^{129}Xe hyperpolarizer failed (due to a design flaw), and it was replaced by a different laser (from the same vendor) during Year 4 of the project performance. During Year 4, this laser has failed too (for unknown reasons), which we have reported in the previous report. The laser was fixed during Year 5 (shortly before the COVID-19 outbreak in MI), and it is now in our possession. The efforts during Year 5 focused on development of advanced quality assurance protocols for our automated hyperpolarizer (generation-3 device), publishing previous results and development of protocols for ejection of hyperpolarized ^{129}Xe gas in the Tedlar bag (for temporary storage (and transport) between production and administration). Since the new generation-3 device was waiting for the repairs (laser as discussed above), we have employed our previously developed device (generation-2) as a test bed for development of the quality assurance practices – we note that we use nearly the same design of the core component (glass optical cell) on both devices. So, most of what we learned so far is nearly directly translatable to the generation-3 device. In June 2020, we started phased re-opening after COVID-19. During the final year of the project, we will transfer all the gained knowledge and implement it on the generation-3 device. Since the laser has been fixed by the vendor, we expect the device to be operational for integration with the low-field MRI scanner.

Aim 2: Develop a large-scale hyperpolarization method for HP propane

The activities during Year 5 of the project primarily focused on publishing the results obtained during the previous years of performance.

Aim 3: Develop and construct a 0.35 T MRI scanner

As descried in the previous reports, we have placed the order for a custom 0.35 T clinical MRI scanner from Time-Medical, which will provide FDA-approved proton imaging capability and clinical research ^{129}Xe imaging capabilities. This report describes our activities during Year 5 and the estimated time line for device installation at Wayne State University, which has been altered by COVID-19.

2. Keywords

Low-field MRI, lung imaging, molecular imaging, functional imaging; propane; xenon-129; NMR; MRI; hyperpolarization.

3. ACCOMPLISHMENTS

Please refer to Appendix 1 for the statement of work of the entire project. The following sections describe the specific areas/tasks of the project conducted during Year 5 of this project.

Aim 1.

Task 1.6 Final Testing of the ^{129}Xe Hyperpolarizer

During this period of performance, we have repaired the laser of the hyperpolarizer device. It was installed back in our device shortly before the COVID-19 outbreak.

Because the xenon-129 hyperpolarizer (generation-3) device was mostly unavailable during this period of performance, our team has employed a previously developed device to develop good manufacturing procedures for routine production of HP ^{129}Xe contrast agent. To this end, we have performed a pilot multi-site study (reference #1 under section 6. Products/peer-reviewed papers). We were able to show that a single reload of the optical pumping cell with Rb metal can be employed for production of several hundred batches of HP ^{129}Xe gas. This study is first in kind for clinical-scale ^{129}Xe hyperpolarizers (of any sort). The results of the study are briefly summarized in the technical Figure 1 below. We have also translated this protocol for quality assurance to the generation-3 device from the perspective of programming the quality assurance study into our hardware. Once we are operational (from COVID-19), we will employ our best practices on the new device.

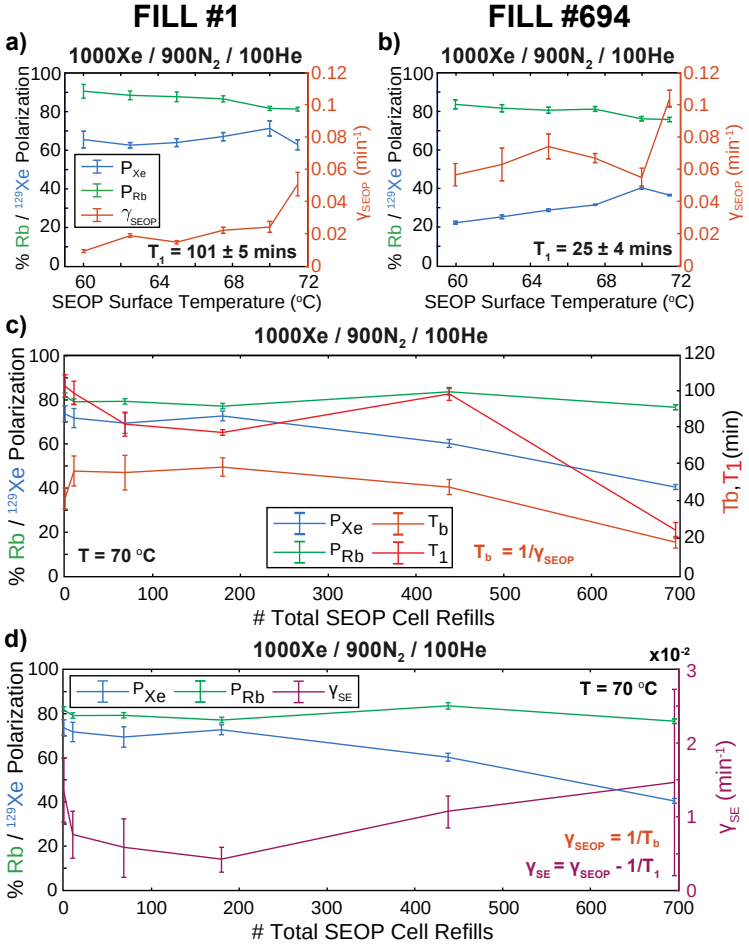


Figure 1. (a) Steady-state values of maximum ^{129}Xe nuclear polarization ($\%P_{Xe}$), optical pumping rate (γ_{SEOP}), and Rb electron polarization ($\%P_{Rb}$) measurements as a function of SEOP cell surface temperature following fill #1 (the initial 1000 Torr Xe / 900 Torr N_2 / 100 Torr ^{4}He gas mixture fill at the commencement of the QA study). (b) Steady-state $\%P_{Xe}$, γ_{SEOP}, and $\%P_{Rb}$ measurements as a function of SEOP cell surface temperature following fill #694 (the final 1000 Torr Xe / 900 Torr N_2 / 100 Torr ^{4}He gas mixture fill at the conclusion of the QA study); note the shorter ^{129}Xe T_1 value. (c) Steady-state $\%P_{Xe,}$, $\%P_{Rb}$, and T_b measurements after polarization build-up at a SEOP cell surface temperature of 70 °C, as well as post-build-up T_1 relaxation measurements, as a function of the number of total gas mixture refills. (d) Rb-^{129}Xe spin-exchange rate, γ_{SE}, as a function of the number of the number of total gas mixture refills compared to associated steady-state $\%P_{Xe}$ and T_b measurements. The solid lines are added to guide the eye. Note that data in display b) was taken after the last point (694th total fill) in displays c) and d).

During Year 5, we have also published the initial performance tests of the new Xenon-129 hyperpolarizer device showing that this new device offers the additional benefits of significantly enhanced production speed (versus the previous-generation device) by approximately 4-6-fold due to novel design of the metal jacket that surrounds the optical pumping glass cell (reference #2 under 6. Products/peer-reviewed papers). The overall design and the key results are summarized in the technical Figure 2 below.

Moreover, during Year 5 we have published the studies on the use of He buffering gas in our hyperpolarizer device (which was reported previously). This work has been published in reference #3 under section 6. Products/peer-reviewed papers.

Furthermore, during Year 5 we have published the studies on the theoretical simulations of the SEOP process in our hyperpolarizer design. The key motivation for this work to gain theoretical insights with the overarching aim to improve the performance of our hyperpolarizers. This work has been published in reference #9 under section 6. Products/peer-reviewed papers.

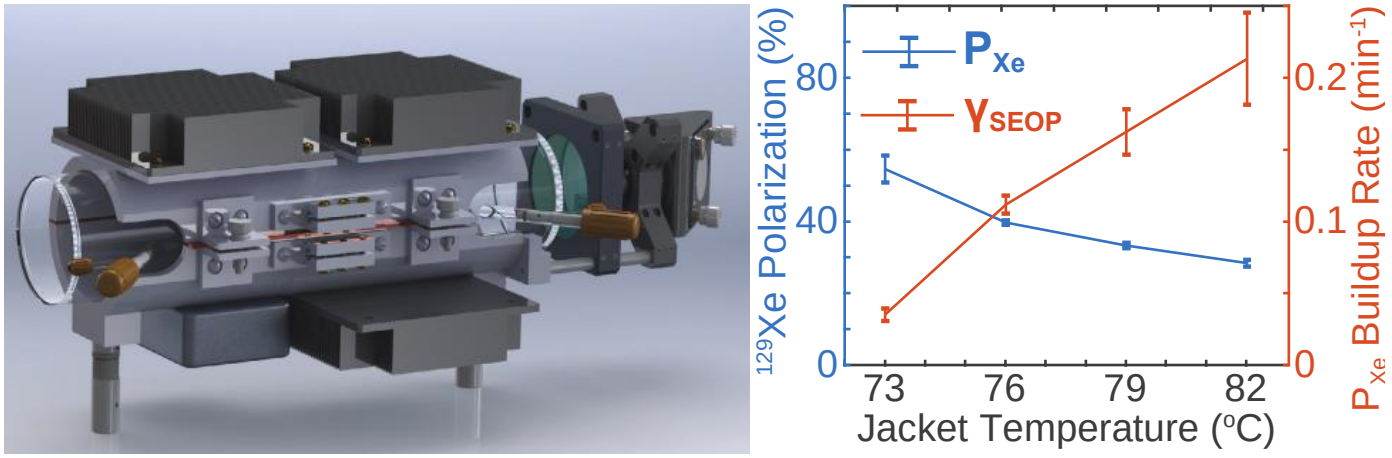


Figure 2. (left) 3D CAD rendering of the metal jacket covering the optical pumping cell. (right) performance mapping (as a function of temperature) of the hyperpolarizer performance: ^{129}Xe polarization (P_{Xe}) and the polarization build-up rate γ_{SEOP}.

The other remaining activities during Year 6 will focus on the hyperpolarizer device integration with the MRI scanner. To this end, we have designed the space for the robust operation of the hyperpolarizer device (see below).

Task 1.8 Replica Polarizer Construction and Testing

Construction of the second polarizer (at the partnering site) is ongoing. Most components have been procured, and many of the components directly dedicated to optical pumping have been assembled, tested, and used separately to generate hyperpolarized xenon (both ^{129}Xe and ^{131}Xe). Final design features are informed by changes made in light of tests performed at WSU. However, completion of the apparatus was delayed because of our institution's response to COVID-19; we now expect to complete the assembly of the device in the next year (given that the no-cost extension was granted by DoD).

Aim 2. As briefly mentioned in the Introduction, the activities during Year 5 of the project primarily focused on publishing the results obtained during the previous years of performance.

Moreover, while working on routine assessment of polarization levels obtained with parahydrogen induced polarization reactions at 1.4 T, we accidently discovered that stimulated emission of the NMR signal occurs (in a manner similar to that of lasers and masers, but at arbitrary frequency range spanning from tens of kHz to tens of MHz). While this effect was detrimental for our quality assurance studies, we hope to employ this effect in the future as an additional means to boost the detection sensitivity of parahydrogen hyperpolarized compounds including hyperpolarized propane gas, which we are developing under this award. This work has been published in reference #6 under section 6. Products/peer-reviewed papers.

Aim 3. Develop and construct a 0.05 T MRI scanner

Task 3.1. Design low-field MRI system with commercial vendors

We have described our plan for acquisition of a 0.35 T MRI system from Time Medical previously. As a part of the PI's transition to Wayne State University (WSU), WSU has made the commitment for space and infrastructure (up to $1.1M) of the 0.35 T MRI system to support this funded project. No space option was found at VUMC (previous institution).

The order to Time-Medical was placed during Year 4 of the project for the MRI scanner and its delivery. The space renovation to suit the needs of the proposed research has been completed during Year 5 of the project. The completion of the space renovation was in line with our expected date by the end of February 2020 (descried in the previous report). The MRI equipment was delivered in Dec. 2019 and placed in a temporary storage facility. The magnet was loaded in the custom MRI suite. See Figure 3 for representative photos of the area (as under construction in Dec. 2019). This space is now completed and operational. The installation of the MRI scanner console was scheduled for March 2020. Unfortunately, we had to cancel the site visit by the vendor (based in Hong Kong) in the last moment due to COVID-19 concerns. As a result of COVID-19 direct impact on our project, we have asked for an additional no-cost extension to complete the scanner installation and the integration of the hyperpolarization equipment in the overall suite (approximately 850 sq. ft of dedicated space).

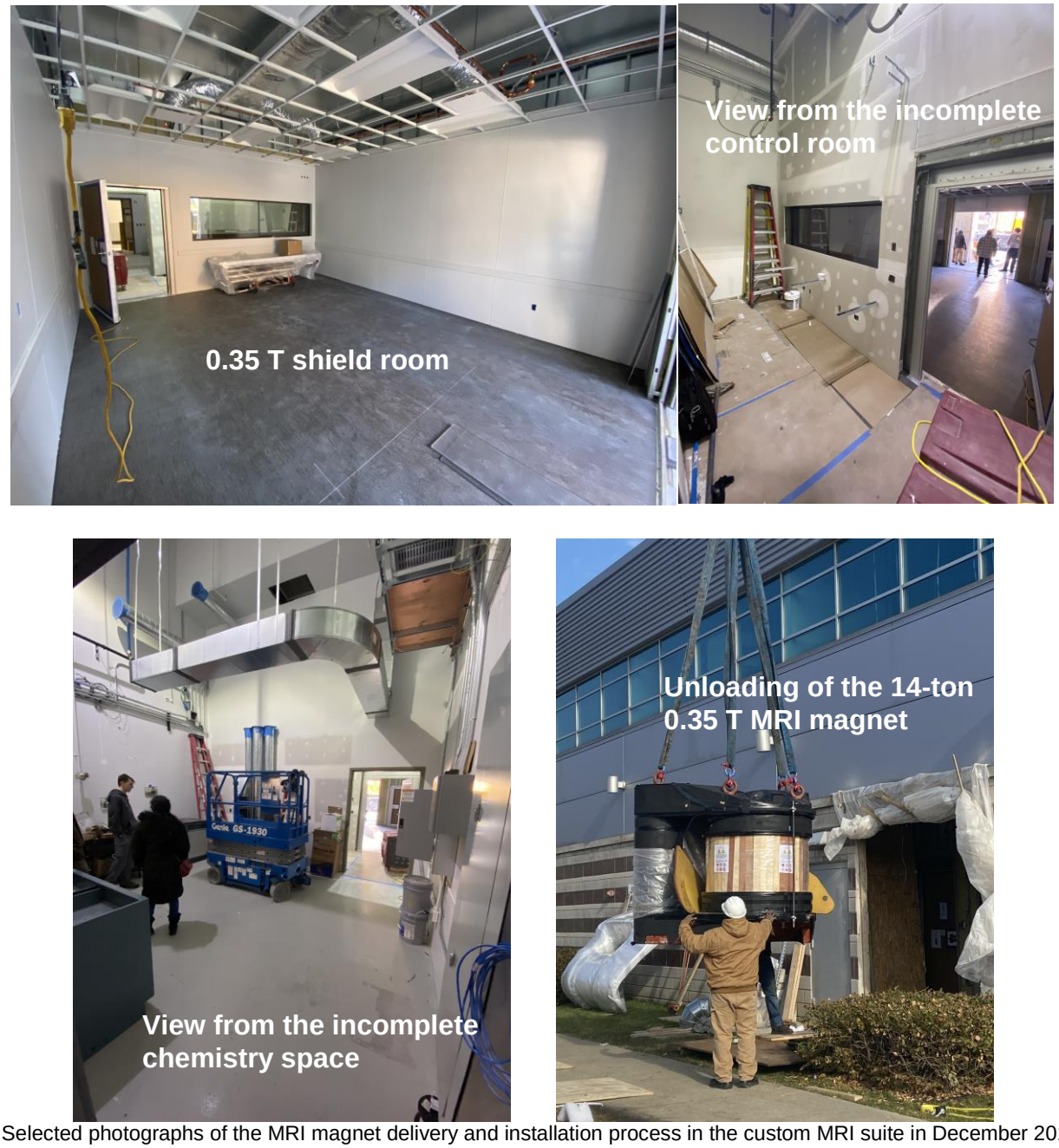


Figure 3. Selected photographs of the MRI magnet delivery and installation process in the custom MRI suite in December 2019.

The MRI suite has consisting of four major areas:

(1) chemistry space for production of parahydrogen and hyperpolarized ^{129}Xe. The ^{129}Xe hyperpolarizer developed under this project will be installed in this facility. This space will also be equipped with a dual channel ^{129}Xe/^{1}H benchtop NMR spectrometer for quality assurance of hyperpolarized ^{129}Xe gas and proton-hyperpolarized hydrocarbons;
(2) control room equipped with computer stations for MRI image acquisition and image processing;
(3) shield room that contains the 0.35 T MRI magnet equipped with patient bed. This area will also contain the clinical-scale propane hyperpolarizer.
(4) equipment room, which will house the remaining equipment including the MRI scanner console.

The MRI scanner vendor (Time-Medical) plans to complete the installation of the MRI system in Year 6; the scanner is FDA-approved in the USA. This scanner will have a significant benefit in terms of the potential clinical translation of propane MRI scans as the hardware is already FDA approved. Once the HP agent is approved, the entire scan can be easily translated to clinical setting. During Year 5, we worked with the vendor on the logistics of the ^{129}Xe hardware/software frame, and also worked extensively on the siting preparation (of note our first siting option on campus did not meet our collective requirements to bring together MRI and novel chemistries of HP contrast agent production, but luckily this problem was remedied with the second siting option). We also performed the magnet installation in the dedicated MRI suite.

We expect the vendor to complete the installation and training by the end of the funding period 06/06/2021.

Task 3.2. Low-field MRI system construction by Vendors

This task has been completed. The system was shipped by the vendor during Year 5.

Task 3.4. RF coils (^{129}Xe and ^{1}H) construction for pulmonary imaging

The ^{1}H RF coils have been shipped. The ^{129}Xe chest coil is being developed by the vendor. It will be delivered during Year 6 of the project.

Task 3.5. Pulse-sequence development and installation

Two sequences have been discussed with the vendor: gradient echo imaging and eco-planar imaging (2D and 3D). The vendor is aware of the requirement that the HP gas scan is to be completed on a single breath hold of a large animal or a human. We expect the vendor to integrate the required sequences during the installation.

What opportunities for training and professional development has the project provided?

Several trainees from Wayne State University (WSU) and from the partnering site Southern Illinois University Carbondale (SIUC) attended the 61th Experimental Nuclear Magnetic Resonance conference.

How were the results disseminated to communities of interest?

Via oral and poster presentations (see below).

4. IMPACT

What was the impact on the development of the principal discipline(s) of the project?

Nothing to Report.

What was the impact on other disciplines?

Nothing to Report.

What was the impact on technology transfer?

Nothing to Report.

What was the impact on society beyond science and technology?

Nothing to Report.

5. CHANGES / PROBLEMS

Because of the impact of COVID-19 on the MRI scanner installation, we have requested (and kindly have been granted) the no-cost extension by the CDMRP.

6. PRODUCTS

Oral Presentations

1) Goodson BM. MEOP and SEOP: A Tutorial. International Society for Magnetic Resonance in Medicine 27th Meeting; May 16; Montreal, QC, Canada 2019 (not reported previously).
2) Goodson BM. Hyperpolarization of ^{131}Xe via Spin-Exchange Optical Pumping: Targets for Neutron Optics Searches for Time-Reversal Invariance Violation." Contributed talk at the NOPTREX Virtual Meeting (hosted by Indiana University), May 12-13, 2020.
3) Goodson BM. Hyperpolarizing nuclear spins of atoms and molecules with light and parahydrogen. Invited virtual talk for the Warren Lab Alumni Seminar Series (hosted by Duke University), June 1, 2020.
4) Goodson BM. Hyperpolarizing Nuclear Spins with SABRE--Potential Application for Neutron Optics TRIV searches with ^{117}Sn." Boyd M. Goodson. Invited talk for the "Mini-NOPTREX" extended collaboration seminar series (hosted by Indiana University), June 7, 2020.

Conference Abstracts

5) Ariyasingha NM, Chekmenev EY. SLIC-based Sensing And Polarization Transfer In Parahydrogen Induced Polarization. 61th Experimental NMR Conference; March 8-13; Baltimore, MD, USA 2020.
6) Birchall J, Nikolaou P, Irwin R, Coffey AM, Pokochueva E, Kidd BE, Murphy M, Molway M, Bales L, Ranta K, Barlow MJ, Kovtunov KV, Koptyug IV, Goodson BM, Chekmenev EY. Advances in High-Density Batch-Mode ^{129}Xe Hyperpolarization Using Spin-Exchange Optical Pumping. 61th Experimental NMR Conference; March 8-13; Baltimore, MD, USA2020.
7) Basler D, Albin K, Bales L, Gafar AT, Lu H, Snow WM, Babcock E, Chekmenev EY, Barlow MJ, Goodson BM. NMR of ^{131}Xe Spin Exchange Optical Pumping in Aluminosilicate (GE180) Cells: Targets for Neutron Optics Searches for Time-Reversal Invariance Violation. 61th Experimental NMR Conference; March 8-13; Baltimore, MD, USA 2020.
8) Porter J, Basler D, Plummer JW, Russell G, Kidd BE, Chekmenev EY, Barlow MJ, Goodson BM. Optically Detected ^{85}Rb / ^{133}Cs Electron Spin Resonance (ODESR) in “Hybrid” Spin-Exchange Optical Pumping Cells with Xenon Density Variance. 61th Experimental NMR Conference; March 8-13; Baltimore, MD, USA 2020.

Peer-Reviewed Manuscripts, Dissertation & Book Chapters

1) Birchall JR, Irwin RK, Nikolaou P, Pokochueva EV, Kovtunov KV, Koptyug IV, Barlow MJ, Goodson BM, Chekmenev EY. Pilot multi-site quality assurance study of batch-mode clinical-scale automated xenon-129 hyperpolarizers. Journal of Magnetic Resonance. 2020;316:106755. doi: https://doi.org/10.1016/j.jmr.2020.106755.
2) Birchall JR, Nikolaou P, Coffey AM, Kidd BE, Irwin RK, Murphy M, Molway M, Bales LB, Goodson BM, Barlow MJ, Chekmenev EY. Batch-Mode Clinical-Scale Optical Hyperpolarization of Xenon-129 Using an Aluminum Jacket with Rapid Temperature Ramping. Analytical Chemistry. 2020;92(6):4309-16.
3) Birchall JR, Nikolaou P, Irwin RK, Barlow MJ, Ranta K, Coffey AM, Goodson BM, Pokochueva EV, Kovtunov KV, Koptyug Igor V, Chekmenev EY. Helium-Rich Mixtures for Improved Batch-Mode Clinical-Scale Spin-Exchange Optical Pumping of Xenon-129. Journal of Magnetic Resonance. 2020;315:106739. doi: https://doi.org/10.1016/j.jmr.2020.106739.
4) Chekmenev EY. Parahydrogen-Induced Magnetization of Jovian Planets? ACS Earth and Space Chemistry. 2020;4(4):495–8. doi: 10.1021/acsearthspacechem.9b00326.
5) Colell J, Logan AWJ, Zhou Z, Lindale JR, Laasner R, Shchepin R, Chekmenev E, Blum V, Warren WS, Malcolmson SJ, Theis T. Rational ligand choice extends the SABRE substrate scope. Chemical Communications. 2020:DOI 10.1039/D0CC01330G. doi: 10.1039/D0CC01330G.
6) Joalland B, Ariyasingha NM, Lehmkuhl S, Theis T, Appelt S, Chekmenev EY. Parahydrogen-Induced Radio Amplification by Stimulated Emission of Radiation. Angewandte Chemie International Edition. 2020;132(22):8732-8. doi: 10.1002/anie.201916597.
7) Kovtunov KV, Koptyug IV, Fekete M, Duckett SB, Theis T, Joalland B, Chekmenev EY. Parahydrogen-induced Hyperpolarization of Gases. Angewandte Chemie International Edition. 2020:DOI 10.1002/anie.201915306. doi: 10.1002/anie.201915306.
8) Schaper DC, Auton C, Barrón-Palos L, Borrego M, Chavez A, Cole L, Crawford CB, Curole J, Dhahri H, Dickerson KA, Doskow J, Fox W, Gervais MH, Goodson BM, Knickerbocker K, Jiang C, King PM, Lu H,

Mocko M, Olivera-Velarde D, Otero Munoz JG, Penttilä SI, Pérez-Martín A, Short B, Snow WM, Steffen K, Vanderwerp J, Visser G. A modular apparatus for use in high-precision measurements of parity violation in polarized eV neutron transmission. Nuclear Instruments and Methods in Physics Research Section A: Accelerators, Spectrometers, Detectors and Associated Equipment. 2020;969:163961. doi: https://doi.org/10.1016/j.nima.2020.163961.

9) Skinner JG, Ranta K, Whiting N, Coffey AM, Nikolaou P, Rosen MS, Chekmenev EY, Morris PG, Barlow MJ, Goodson BM. High Xe Density, High Photon Flux, Stopped-Flow Spin-Exchange Optical Pumping: Simulations versus Experiments. Journal of Magnetic Resonance. 2020;312:106686. doi: https://doi.org/10.1016/j.jmr.2020.106686.

Inventions, patent applications and licenses:

Nothing to Report.

Funding applied for based on work supported by this award

1. Title “Novel Theragnostic Hypoxia Imaging of Breast Cancer”
   DOD BC200264 (PI=Chekmenev, co-investigator=Goodson)
   Performance period: 10/01/2020-09/30/2023
   Supporting agency: Department of Defense
   Level of funding: $500,000 (total direct costs);
   Time Commitment: Principal Investigator (2.35 calendar months)
   To address the limitations of PET imaging with ^{18}F-FMISO and other ^{18}F labeled nitroimidazoles, we propose a new hypoxia imaging approach of breast cancer using hyperpolarized (HP) MR Spectroscopic Imaging (HP-MRSI) with non-radioactive nitrogen-15 (^{15}N)-labeled nitroimidazoles as a novel class of contrast agents.
   Aim 1: Develop a bio-injectable solution of hyperpolarized $^{15}N_3$-metronidazole contrast agent by performing SABRE-SHEATH hyperpolarization, fast purification, and agent reconstitution into aqueous media. The metrics of success will be 12% ^{15}N polarization at 100 mM concentration prior to *in vivo* injection.
   Aim 2: Validate the feasibility of hypoxia sensing using hyperpolarized $^{15}N_3$-metronidazole enzymatic assays *in vitro*.
   Aim 3: Validate the feasibility of *in vivo* hypoxia sensing using hyperpolarized $^{15}N_3$-metronidazole in an animal (mouse) model of breast cancer. We will perform tail-vein injection of hyperpolarized $^{15}N_3$-metronidazole in tumor-bearing mice and will correlate the detected metabolic signatures in hypoxic and non-hypoxic tumors—the hypoxic status of the tumor will be independently verified by the *ex vivo* staining of excised and sliced breast tumors using pimonidazole.
   Overlap: the potential overlap of Aims 1 and 2 (with this proposal) will be resolved if both applications are funded.

2. Title “Clinical-scale SABRE Polarizer”
   (PI=Chekmenev, co-investigator=Goodson)
   Time Commitment: PI of subcontract (27.5% effort; 3.3 calendar months)
   Supporting agency: NIH / NIGMS
   1R01GM139819-01
   Program Official (PO) Contact Name: Krepkiy, Dmitriy
   Program Contact Phone: not available
   Program Contact Email:
   Performance period: 09/01/2020 to 08/31/2023
   Level of funding: $ 1,152,364 (total costs including direct costs)
   This proposal focuses on technology research and development of instrumentation for production of hyperpolarized contrast agents using the Signal Amplification by Reversible Exchange (SABRE) technique. Our overall goal is to develop a low-cost and high-throughput production device capable of clinical-scale production of a wide range of pure contrast agents for future clinical trials and ultimately, to enable molecular imaging without ionizing radiation. The proposed device will be constructed and optimized for production of a wide range of ^{13}C and ^{15}N hyperpolarized contrast agents.
   We propose the following specific aims to develop and construct an automated SABRE-SHEATH hyperpolarizer for fast and inexpensive production of ^{13}C and ^{15}N HP contrast agents:

Aim 1. SABRE-SHEATH hyperpolarizer development and construction for preclinical use. We will design high-parahydrogen-pressure / high-flow reactors with variable temperature, advanced magnetic field control, and in-situ quality assurance. The hyperpolarizer will operate as an automated stand-alone device. Metrics of success will include production of pure (from SABRE catalyst) HP solutions (~3 mL or less) of HP contrast agent in 1 minute. We will optimize the hyperpolarization process via systematic variation of key hyperpolarization process parameters, including temperature, parahydrogen pressure and flow rate, and catalyst-to-substrate ratio with the goal of maximizing the payload of achieved hyperpolarization for production of six HP contrast agents to demonstrate broad applicability of the device: metronidazole-$^{15}N_3$ (an FDA-approved antibiotic, potential hypoxia sensor with ^{15}N T_1 ~ 10 min), nicotinamide-1-^{15}N (vitamin B_3), imidazole-$^{15}N_2$ (pH sensor), acetate-1-^{13}C (brain and liver metabolism), pyruvate-$^{13}C_2$ (elevated glycolysis), and nimorazole-$^{15}N_3$ (radio-sensitizer). The second set of metrics of success will be production of six HP contrast agents at concentration of 0.1 moles/liter and polarization of 15% (^{13}C) and 30% (^{15}N).
Aim 2. Scaling the hyperpolarizer output to enable production of 1 g of HP contrast agent in 1 minute: We will scale the reaction chamber for parahydrogen exchange with biomolecules to enable clinical-scale production of HP contrast agents. The device will be tested for excipients. The goal is to ensure that the developed device will be able to enter clinical trials after the required regulatory clearance. The metrics of success will be production of 1 g of HP contrast agent to polarization level of 15% (^{13}C) and 30% (^{15}N).
Impact: In accordance with PAR-17-045 Focused Technology Research and Development R01 (*No Biological Aims*), the current stage of SABRE technology development does not include immediate short-term application to challenging biomedical research questions because an immature technology's effectiveness in that context can distort development of the technology. In this early stage of SABRE technology development, insistence on biomedical applications can indeed be counterproductive. Therefore, in this program, application to specific biomedical questions in the timeframe of the proposed project is considered beyond the scope of the program, and is thus not included in our 3-Year project. Development and construction of our device will enable new molecular imaging modalities for a wide range of diseases and disorders in the future.
Overlap: none —this is a technology/device-development proposal.

3. Title “Molecular MRI of Brain Metabolism enabled by Long-Lived Spin States”
   PI: Thomas Theis, NC State (Chekmenev & Goodson: co-investigators, PIs of sub-awards)
   Time Commitment: co-investigator (8.3% effort; 1.0 calendar months)
   Supporting agency: NIH
   Program Official Contact Name: not available yet
   Program Official Contact Phone: not available yet
   Program Official Contact Email: not available yet
   Performance period: 06/01/2020-5/31/2022
   In this proposal, we bring together a team of engineers, chemists and physicists that will work in close collaboration with leading neuroimaging experts to develop a new technology to monitor brain metabolism in real time. The proposed technique promises non-invasive, real-time, 3D imaging of metabolic transformations of vitamins, drugs and metabolites at low concentrations. Our interdisciplinary team believes that we can revolutionize the imaging of brain function and brain energy homeostasis with our technique, because it promises real-time mapping of metabolic pathways in health and disease at the molecular level. To deliver on this promise we will develop “Cost-Efficient Hyperpolarized MRI with Long-Lived Spin States”, which will enhance MRI signals of metabolites and drugs by up to 7 orders of magnitude. In addition, the Long-Lived Spin States preserve the signal enhancements for up to hours, such that metabolic turnover can be tracked on biological timescales, yet with sub-second time resolution. Specifically, we envision injection of an innocuous, hyperpolarized marker that will be imaged by low-cost, low-field MRI scanners with exquisite sensitivity. Given that both our hyperpolarization approach and the imager are also low in cost, our technology emerges as simple, fast, and safe—and could be deployed in any research center, hospital, or point-of-care center for safe scanning of broad patient populations.
   Our approach is radically different from current modalities because it is fast, simple, and enables long-term tracking of biochemical transformations. In addition, current hyperpolarized MRI uses expensive superconducting MRIs, whereas our approach works in inexpensive low-field scanners without loss in sensitivity. Accordingly, if successful, the proposed technology is likely to generate an exceptionally

high impact because it can be deployed broadly and give unprecedented insight into brain metabolism at the “speed of thought”.
Specific Aims:
Aim 1. Technology Development for Molecular MRI of Brain Metabolism, which entails: Hyperpolarization of Long-Lived Spin States in 13C2-Pyruvate, Ethyl-13C2-pyruvate, 13C2-Vitamin C, ^{15}N-Vitamin B3, 15N3-Metronidazole (well-tolerated antibiotic and potential hypoxia probe) and 13C2-Acetate; Preparation of injectable, innocuous, aqueous solutions of listed hyperpolarized markers; Characterization of Long-Lived Hyperpolarization in “hidden” quantum spin states; and design of RF hardware and sequences for hyperpolarized spectroscopy and imaging in phantoms.
Aim 2. First proof-of-concept of Molecular MRI of Brain Metabolism in heathy rats, which entails: MR-spectroscopy (MRS) of metabolic turnover of listed compounds in the whole brain; spectroscopic monitoring of changes in metabolic turnover upon induced hypoxia; and MR-spectroscopic Imaging (MRSI) of metabolic turnover of listed compounds.
Overlap: some overlap with respect to 15N3-metronidazole hyperpolarization. If both projects are funded, the potential overlap will be resolved.

7. PARTICIPANTS & OTHER COLLABORATING ORGANIZATIONS

Individuals worked on the project

The following personnel worked on the project

Name:	Eduard Chekmenev
Project Role:	Initiating PI (Wayne State University)
Researcher Identifier (ORCID ID):	orcid.org/0000-0002-8745-8801
Nearest person month worked:	3
Contribution to Project:	Dr. Chekmenev was responsible for the overall progress of the project, performing some experiments with hyperpolarized propane and hyperpolarized xenon-129, developing RF coils, analyzing some of the data for the above-mentioned experiments, preparing the manuscripts.
Funding Support:	DOD W81XWH-12-1-0159/BC112431; NIH 1R21CA220137; NSF CHE-1904780.

Name:	Nuwandi M. Ariyasingha
Project Role:	PhD student
Researcher Identifier (ORCID ID):	
Nearest person month worked:	3
Contribution to Project:	Nuwandi M. Ariyasingha worked on many of the experiments concerning hyperpolarized clinical-scale propane hyperpolarization. She also analyzed the data, prepared figures, and manuscripts.
Funding Support:	DOD W81XWH-12-1-0159/BC112431, NSF CHE-1904780.

Name:	Jonathan R. Birchall https://orcid.org/0000-0003-3920-4038
Project Role:	PhD
Researcher Identifier (ORCID ID):	
Nearest person month worked:	6
Contribution to Project:	Dr. Jonathan R. Birchall worked on many of the experiments concerning hyperpolarized clinical-scale Xenon hyperpolarization. He also analyzed the data, prepared figures, and manuscripts.
Funding Support:	DOD W81XWH-12-1-0159/BC112431, NSF CHE-1904780.

Name:	Baptiste Joalland
Project Role:	PhD
Researcher Identifier (ORCID ID):	http://orcid.org/0000-0003-4116-6122
Nearest person month worked:	6
Contribution to Project:	Dr. Baptiste Joalland worked on PHIP hyperpolarization aspect of this project. He also analyzed the data, prepared figures, and manuscripts.
Funding Support:	DOD W81XWH-12-1-0159/BC112431, NSF CHE-1904780.

Name:	Boyd M. Goodson
Project Role:	Partnering PI (SIUC)
Researcher Identifier (ORCID ID):	orcid.org/0000-0001-6079-5077
Nearest person month worked:	1
Contribution to Project:	Prof. Goodson was responsible for the overall progress of the project at the partnering site, performing some experiments with hyperpolarized xenon-129, xenon-131, and ODESR polarization measurements, analyzing some of the data for the above-mentioned experiments, preparing manuscripts and presentations.
Funding Support:	SIUC DOD PRMRP W81XWH-15-1-0272 NSF-CHE-1905341 NSF DMR-1757954

Name:	Abdulbasit Tobi (“Tobi”) Gafar
Project Role:	MS chemistry graduate student
Researcher Identifier (ORCID ID):	
Nearest person month worked:	2
Contribution to Project:	Participated in xenon-129 and xenon-131 spin-exchange optical pumping experiments, as well as ODESR experiments. Processed and analyzed data, wrote up contents for presentations and manuscripts.
Funding Support:	SIUC / NMR Facility

Name:	Dustin Basler
Project Role:	Undergraduate student researcher
Researcher Identifier (ORCID ID):	Now leads xenon-129 and xenon-131 spin-exchange optical pumping experiments; participates in some optically detected ESR polarization measurements. Processes and analyzes data. Prepared conference presentations.
Nearest person month worked:	2
Contribution to Project:	
Funding Support:	DOD PRMRP W81XWH-15-1-0272 Research Corporation Cottrell SEED Award

Name:	Justin Porter
Project Role:	postgraduate student researcher
Researcher Identifier (ORCID ID):	
Nearest person month worked:	2
Contribution to Project:	Performed xenon-129 spin-exchange optical pumping experiments, led use of optically detected ESR efforts to characterize spin polarization during optical pumping. Analyzed data, prepared conference presentations (deferred medical school; will start at UIUC in fall).

Funding Support:	DOD PRMRP W81XWH-15-1-0272 Research Corporation Cottrell SEED Award

Name:	Kierstyn Albin
Project Role:	Undergraduate student researcher
Researcher Identifier (ORCID ID):	
Nearest person month worked:	1
Contribution to Project:	Assisted with some xenon-129 spin-exchange optical pumping experiments and laser characterization experiments, analyzed data.
Funding Support:	DOD PRMRP W81XWH-15-1-0272 NSF DMR-1757954 Research Corporation Cottrell SEED Award

Name:	Md Shahabuddin (“Alam”) Alam
Project Role:	PhD chemistry graduate student
Researcher Identifier (ORCID ID):	
Nearest person month worked:	2
Contribution to Project:	Participated in xenon-129 and xenon-131 spin-exchange optical pumping experiments, as well as ODESR experiments. Processed and analyzed data.
Funding Support:	SIUC / NMR Facility

Has there been a change in the active other support of the PD/PI(s) or senior/key personnel since the last reporting period?

Yes, a new DOD grant was awarded. Provided below, please see the detailed information. This newly funded project involves the direct utilization of the DOD-sponsored technologies developed under this award.

Title “Low-Cost, High-Throughput 3D Pulmonary Imaging Using Hyperpolarized Propane Gas”
(Eduard Y Chekmenev, Wayne State University, lead PI)
Time Commitment: PI (35% effort; 4.2 calendar months)
Initiating PI award: W81XWH2010576 (Wayne State University)
Level of funding: $ 1,732,500 (total award including IDC)
Partnering PI award: W81XWH2010578 (Southern Illinois University Carbondale)
Level of funding: $ 553,125 (total award including IDC)
Supporting agency: DOD PRMRP
Program Contact Name: Dr. Sandy Snyder
Program Contact Phone:
Program Contact Email:
Performance period: 07/15/2020 to 07/14/2023

We have worked to develop an alternative to hyperpolarized noble gases for MRI imaging applications. We recently demonstrated that hydrogen nuclei of gaseous propane can be hyperpolarized using parahydrogen induced polarization (PHIP) to a sufficiently high level suitable for 2D and 3D MRI. Our early efforts with HP propane at high magnetic field revealed a very short relaxation constant for the exponential decay of the propane gas hyperpolarized state of ~1 s. Importantly, our research recently demonstrated the existence of longer-lived spin states in hyperpolarized propane gas in lower magnetic fields (0.35 T and below). These spin states allow significantly extending the lifetime of hyperpolarized propane (e.g. increasing the decay constant of up to >13 s) making it suitably long-lived for administration as an inhalable contrast agent. Moreover, our research clearly demonstrates that the low-field MRI detection of hyperpolarized contrast agents in general offers the same or even better detection sensitivity as that of high-field MRI scanners. These two developments--long-lived proton-hyperpolarized propane gas and low-field MRI on conventional FDA-approved MRI scanners—should enable

the clinical use of HP propane gas, which can be mass-produced at significantly higher production rates (one dose every 2-5 seconds) at a fraction of the cost of hyperpolarized ^{129}Xe.

In 2014, Chekmenev and Goodson received this partnering PI CDMRP award. This award enabled the development of our human-scale hyperpolarizer device (successfully completed). Here (under new award), we propose taking the next significant step to develop and test a hyperpolarized propane production technology device under the following **Specific Aims:**

Aim 1. Develop a clinical low-cost and high-throughput biomedical device for production of hyperpolarized propane contrast agent: the future propane hyperpolarizer will be developed to enable its Good Manufacturing Practices (GMP), mass-production, and robust use;

Aim 2. Develop a safe method for HP propane gas administration and utilization, and test the purity and safety of the HP contrast agent produced by our device;

Aim 3. Assess the feasibility of MRI using HP propane gas for *in vivo* functional imaging of normal lungs and in a bleomycin-induced lung-injury model in sheep. We will compare the effectiveness of hyperpolarized propane MRI to that using a more established contrast agent (hyperpolarized ^{129}Xe gas—created using a polarizer we developed in our previous DOD-funded work), and also to the standards of care: computed tomography and spirometry. Furthermore, we will also investigate the effectiveness of hyperpolarized propane gas MRI to monitor the progression of bleomycin-induced lung injury in the sheep animal model.

Overlap: none

Personnel exchanges with collaborators:

We have been in regular tele-contact between the initiating and the partnering site as evident from the Products' section: multiple collaborative papers have been presented at scientific meetings and published in peer-reviewed scientific journals. We have also been engaged with the vendor of the MRI equipment. The WSU team hosted three site visits by the vendor of the MRI equipment.

Moreover, we have been collaborating with scientists engaged in this project for Aim 1 and Aim 3.

Organization Name: University of Nottingham

Location of Organization: Nottingham, UK

Partner's contribution to the project:

In-kind support: Our collaborators provided their insights in the design and installation of the 0.35 T MRI scanner, and their input in the improvement of the ^{129}Xe hyperpolarizer.

Collaboration: We have enjoyed regular (weekly to bi-weekly) teleconferences with the Nottingham team (lead PI: Michael J. Barlow). Moreover, we hosted a six-week long exchange visit with PhD student Robert Irwin, who visited Wayne State University site in the fall of 2019; two additional trainees from Nottingham, James Ball and Eleanor Sparling, performed capstone experiments for their MSC degrees at the partnering site (SIUC) for over 2 months. We also made plans and have six additional MsC students from the University of Nottingham arriving to our respective performance sites for a duration of 12 weeks. Unfortunately, the global COVID-19 outbreak changed all our plans – the MsC students were forced to return back to the University of Nottingham, but we were still able to arrange 'virtual' projects and all six students were able to complete their MsC degrees.

Organization Name: International Tomography Center (ITC)

Location of Organization: Novosibirsk, Russia

Partner's contribution to the project:

In-kind support: Our collaborators provided their insights in the improvement of the 129Xe hyperpolarizer.

Collaboration: We have enjoyed regular (weekly to bi-weekly) teleconferences with the ITC (lead PIs: Dr. Kirill Kovtunov and Dr. Igor Koptyug). Moreover, we hosted a four-week long exchange visit with PhD student Ekaterina Pokochueva, who visited Wayne State University site in the fall of 2019. One additional visit was scheduled by Dr. Kirill Kovtunov for the spring 2020. Unfortunately, he died from COVID-19 before he could visit our performance site.

8. SPECIAL REPORTING REQUIREMENTS

Collaborative Award

This is a collaborative award with two partnering PIs.

9. APPENDICES

Appendix 1: Original Statement of work, Years 1-3

STATEMENT OF WORK – 10/10/2014
PROPOSED START DATE September 1, 2015

Site 1:	Vanderbilt University **Now at Wayne State University**		Site 2:	Southern Illinois University
	1161 21st Ave South MCN AA-1105 Nashville, TN 37232-2310			900 SOUTH NORMAL AVENUE CARBONDALE, IL 62901
	PI: Chekmenev			Partnering PI: Goodson

Specific Aim 1	Timeline	Site 1 (Vanderbilt)	Site 2 (SIU)
Develop and construct a fully automated high-pressure low-cost stand-alone ^{129}Xe hyperpolarizer	Months		
1.1. Design	1-5	80%	20%
1.2. Prototyping	6-10	75%	25%
1.3. Prototype construction and testing	11-15	90%	10%
Milestone Achieved	Prototype ^{129}Xe polarizer constructed		
1.4. Final Design	16-20	80%	20%
1.5. Final Construction	21-24	90%	10%
1.6. Final Testing	25-30	75%	25%
1.7. Polarizer Integration with MRI scanner	31-34	90%	10%
Milestone Achieved	Final ^{129}Xe polarizer constructed		
1.8. Replica Polarizer Construction and Testing	31-36	50%	50%
Milestone Achieved	Replica ^{129}Xe polarizer constructed		

Specific Aim 2	**Timeline**	**Site 1 (Vanderbilt)**	**Site 2 (SIU)**
Develop a large-scale hyperpolarization method for HP propane			
2.1. Chemistry of Large Scale PHIP of propane	1-6	75%	25%
Milestone Achieved:	Clinical Scale Production of HP Propane is developed		
2.2. Initial Polarizer Design	7-12	100%	0%
2.3. Polarizer Prototyping	13-18	100%	0%
Milestone Achieved:	Prototype Polarizer Constructed		
2.4. Prototype Optimization	19-24	100%	0%
2.5. Final Polarizer Construction	25-30	100%	0%
2.6. Final Polarizer Testing and Integration with low-field MRI system	31-36	75%	25%
Milestone(s) Achieved:	Final Propane Polarizer Constructed		
Specific Aim 3	**Timeline**	**Site 1 (Vanderbilt)**	**Site 2 (SIU)**
Develop and construct a 0.05 T MRI scanner	Months		
3.1. Design low-field MRI system with commercial vendors	1-6	50%	50%
3.2. Low-field MRI system construction by Vendors	7-12	50%	50%
3.3. Low-field MRI system installation and fine-tuning at site 1 (Vanderbilt)	13-18	100%	0%

Milestone Achieved:	Clinical low-field MRI system for high-throughout pulmonary imaging is installed		
3.4. RF coils (^{129}Xe and ^{1}H) construction for pulmonary imaging	19-24	100%	0%
3.5. Pulse-sequence development and installation	25-30	50%	50%
Milestone Achieved:	Low-field MRI system is ready for use with contrast agents		
3.6. MRI system integration with Propane Hyperpolarizer	31-36	100%	0%
3.7. MRI system integration with Propane Hyperpolarizer	31-34	90%	10%
3.8. Demonstration of high-speed MRI and high-speed contrast agent production/ imaging scan	35-36	90%	10%
Milestones Achieved:	Functional high-speed MRI of hyperpolarized propane and ^{129}Xe; System ready for clinical trial.		

Appendix 2: Abstracts Presented and Manuscripts Published and Accepted

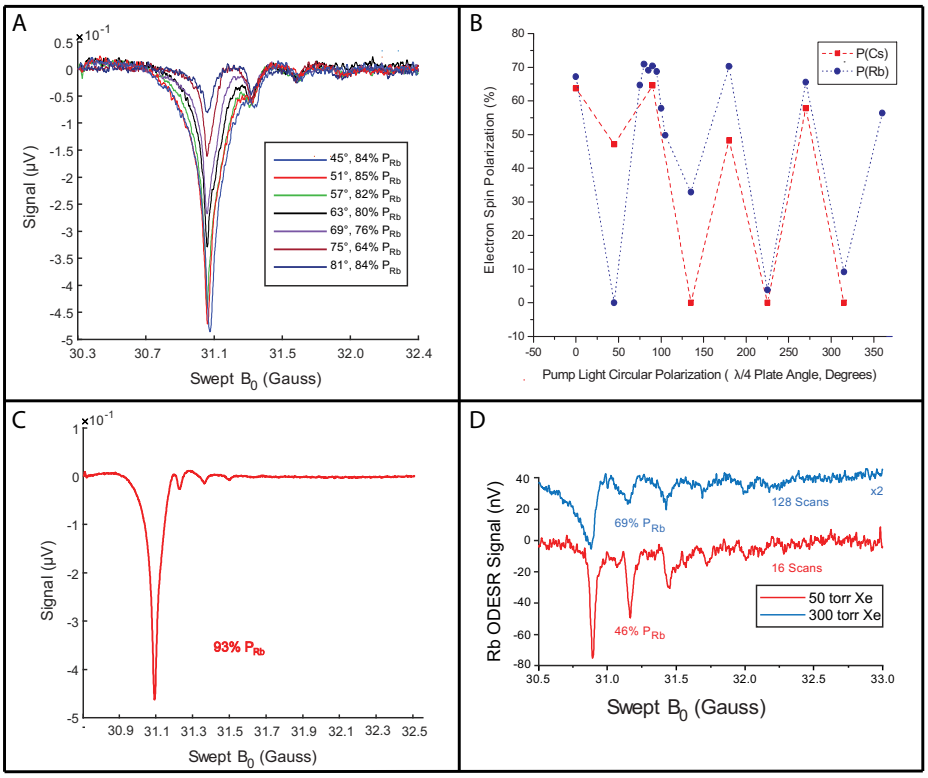
8 abstracts and 9 published peer-reviewed publications are reported. PDF files of 5 abstracts and 9 publications are provided below in the Appendix 2.

Optically Detected ^{85}Rb / ^{133}Cs Electron Spin Resonance (ODESR) in "Hybrid" Spin-Exchange Optical Pumping Cells with Xenon Density Variance

Justin Porter[1], Dustin Basler[1], Joseph W. Plummer[2], Graeme Russell[2], Bryce E. Kidd[1], Eduard Y. Chekmenev[3], Michael J. Barlow[2], and Boyd M. Goodson[1]

[1]Department of Chemistry & Biochemistry, Southern Illinois University, Carbondale, IL, United States; [2]School of Medicine, University of Nottingham, Queens Medical Centre, Nottingham, UK; [33]Wayne State University & Karmanos Cancer Institute (KCI), Detroit, MI, United States

One application of optically detected electron spin resonance (ODESR) is the direct measurement of the electron spin polarization (P_{AM}) of an alkali metal vapor during spin-exchange optical pumping (SEOP).[1-6] However, while the approach works well for ^{3}He SEOP, it can be challenging for xenon hyperpolarization (^{129}Xe or ^{131}Xe). High Xe densities (specifically, collisions with Xe) and high resonant laser fluxes[4] both can give rise to short ESR lifetimes, which in turn can drastically broaden the ESR lines. Thus, the high-[Xe], high-[hν] conditions commonly encountered during Xe SEOP—particularly when performing clinical-scale stopped-flow[7-8] SEOP[9] generally make it difficult to measure P_{AM} via ODESR.



Here, we report on our ongoing efforts to utilize and improve ODESR under the demanding conditions of clinical-scale stopped-flow Xe SEOP—particularly in the context of Rb/Cs "hybrid" cells. In our recent work,[9,10] ODESR signals were successfully detected from ^{85}Rb and ^{133}Cs within clinical-scale SEOP cells using an ODESR system comprised of a SEOP setup (using a high-power "pump" laser tuned to the Rb or Cs D1 line and a 3D-printed clinical-scale oven and 500 cc cell[8]), a waveform generator (WFG) that ramps the main magnetic field, a second WFG (with output broadcast through an RF coil), a "probe" diode laser (arranged perpendicular to the axis of the cell and pump laser beam, tuned to the D1 line of Rb or Cs), and a photodiode whose output is connect to an RF lockin amplifier that records the ODESR signals. The setup permits experiments to be performed where one metal vapor is optically pumped, but the other metal is optically probed, giving four modes of operation: $Cs_{(pump)}$-$Cs_{(probe)}$; $Cs_{(pump)}$-$Rb_{(probe)}$; $Rb_{(pump)}$-$Cs_{(probe)}$; and $Rb_{(pump)}$-$Rb_{(probe)}$. This capability allows metal-metal spin-exchange to be studied, and allows ESR spectra to be obtained from one metal (in the absence of pump resonant photons) while illuminating the other. At low pressure (e.g. 300 torr N_2), hyperfine ODESR lines from both metals can be well resolved (e.g. **Fig. 1A**), facilitating calculation of P_{AM}. The Rb/Cs metal vapors undergo efficient spin exchange to yield comparably high P_{AM} values (**Fig. 1B**). The system is sufficiently stable for long-time averaging with ~1 nV baselines (**Fig. 1C**). Moreover, given the absence of a low-noise linear amplifier, the ODESR signal is detected using the output from the waveform generator itself. One previous trick to measuring P_{AM} when polarization is high and/or the lines are broadened is to saturate the ESR lines with RF power, and then extrapolate P_{AM} to the limit of no RF. Here, we are able to instead systematically vary the pump light CP (**Fig. 1A**) in order to enable extrapolation of P_{AM} values of ODESR spectra to those of what would be obtained with perfect CP light. This helps enable measurement of P_{AM} in the presence of Xe (e.g. **Fig. 1D**); more generally, these efforts should allow measurement of various parameters of SEOP (e.g. Xe/Rb and Xe/Cs spin-destruction rates)—giving insight into the relative utility of Cs vs. Rb vs. hybrids for SEOP hyperpolarization of xenon. Finally, ODESR should allow comparison with / validation of bulk P_{AM} estimates made using an indirect Beer's law / magnetic-field-cycling approach[7,8]; we are also working to see if it is possible to infer PXe from ODESR line shifts using our setup.[11]

Acknowledgements: We thank several members of the SEOP community over the years for their help and advice, including Geoff Schrank, Brian Saam, Thad Walker, Tom Gentile, and Earl Babcock, as well as former SIUC students Nick Whiting and Kaili Ranta. This work was funded in part by DoD (W81XWH-12-1-0159/BC112431, W81XWH-15-1-0271, & W81XWH-15-1-0272) as well as a SEED Award from the Research Corporation for Science Advancement. ***References:*** [1]Young et al., *APL*, **70**, 3081, 1997; [2]Levron et al., *APL* **73**, 2666, 1998; [3]Appelt et al., *APL* **75**, 427, 1999; [4]Appelt et al., *PRA* **59**, 2078, 1999; [5]Chann et al., *PRA* **66**, 032703, 2002; [6]Baranga et al., *PRA* **58**, 1412, 1998; [7]Nikolaou, et al., *PNAS*, **110**, 14150, 2013; [8]Nikolaou, et al., *JACS*, **136**, 1636, 2014; [9]Kidd et al., ENC 2018; [10]Porter, et al. ENC 2019; [11]Ma et al. *PRL* 2011.

Advances in High-Density Batch-Mode ^{129}Xe Hyperpolarization Using Spin-Exchange Optical Pumping

Jonathan Birchall,[1] Peter Nikolaou,[2] Robert Irwin,[3] Aaron Coffey,[4] Ekaterina Pokochueva,[5,6] Bryce Kidd,[7] Megan Murphy,[7] Michael Molway,[7] Liana Bales,[7] Kaili Ranta,[7] Michael Barlow,[3] Kirill Kovtunov,[5,6] Igor Koptyug,[5,6] Boyd Goodson,[7] Eduard Chekmenev[1,8]

[1]Department of Chemistry, Ibio, Karmanos Cancer Institute, Wayne State University, Detroit, MI 48202, USA
[2]XeUS Technologies LTD, Nicosia, Cyprus
[3]Sir Peter Mansfield Imaging Centre, University of Nottingham, Nottingham, NG7 2RD, United Kingdom
[4]Department of Radiology, Vanderbilt University Institute of Imaging Science (VUIIS), Nashville, TN, 37232, United States
[5]Novosibirsk State University, [6]International Tomography Center SB RAS, Institutskaya 3A, Novosibirsk 630090, Russia
[7]Department of Chemistry and Biochemistry, Southern Illinois University, Carbondale, Illinois 62901, USA
[8]Russian Academy of Sciences, Moscow, 119991, Russia

Hyperpolarized (HP) noble gases such as ^{3}He, ^{83}Kr and ^{129}Xe have seen use in a multitude of NMR and Magnetic Resonance Imaging (MRI) applications, including spectroscopic biosensing of porous media, theranostic imaging of the lungs and brain, and characterization of metabolic pathways. Hyperpolarization can be used to increase the net nuclear spin polarization (P) of such nuclear spin systems far beyond thermal equilibrium levels, overcoming their low natural abundance and achievable signal-to-noise ratios (SNR). Here, we employed the Spin-Exchange Optical Pumping (SEOP) hyperpolarization technique (1,2)—a two-stage process whereby circularly polarized laser photons first transfer spin angular momentum to rubidium electrons (optical pumping), followed by transfer of this electron spin angular momentum to ^{129}Xe nuclei via a Fermi contact interaction (spin exchange). A nitrogen buffer gas is used to quench radiative, randomly polarized emission (fluorescence) from excited Rb electrons via binary gas-phase collisions, thus reducing spin-relaxation effects (3). Batch-mode ^{129}Xe SEOP has been shown to achieve near-unity ^{129}Xe polarization (P_{Xe}) in moderately high Xe densities, though these levels have been reported at low polarization build-up rates (4,5). Here, we report on two significant developments aiming to translate high P_{Xe} levels and fast build-up rates (γ_{SEOP}) at high Xe densities and partial pressures on a clinical production scale.

The first development is the inclusion of ^{4}He in tertiary gas mixtures, which has been shown to increase achievable P_{Xe} values by factors of 1.14 and 1.39 at 2000 and 2660 Torr total SEOP cell pressures, respectively, for gas mixtures comprising 50% Xe, 45% ^{4}He and 5% N_2 when compared to 50% Xe, 50% N_2 gas mixtures at identical total SEOP cell pressures (**Figure 1a,b**). Record-high P_{Xe} levels have been achieved using this approach: 85.1 ± 2.7% at 1000 Torr Xe partial pressure and 73.9 ± 1.9% at 1330 Torr Xe partial pressure. Additionally, the ^{4}He-rich mixtures demonstrate an overall increase in SEOP thermal stability and improved management during the SEOP process. Moreover, the reduction in density of the overall gas mixture when employing ^{4}He may be desirable for HP ^{129}Xe inhalation by human subjects—especially in populations with heavily impaired lung function (6).

The second development is the use of a novel aluminum jacket design facilitating rapid temperature ramping of SEOP cells. This design is capable of heating SEOP cells from ambient temperature (typically 25 °C) to 70 °C (temperature of the SEOP process) in 4 minutes, and perform cooling of the SEOP gas mixture back to ambient temperature for release from the hyperpolarizer (with negligible quantity of Rb metal leaving the cell) in a further 4 minutes—substantially faster (by a factor of six) than previous second generation hyperpolarizer designs relying on air heat exchange (4,5). This design also incorporates a built-in RF coil with maximized EMF screening to outside noise sources, resulting in improved NMR signal-to-noise ratio (SNR) of in-situ HP ^{129}Xe polarimetry (7). P_{Xe} measurements exceeding 40% were observed at build-up rates γ_{SEOP} > 0.1 min^{-1} in 50% Xe, 45% ^{4}He and 5% N_2 gas mixtures (2000 Torr total SEOP cell pressure) using this design (**Figure 1c**). Moreover, our "third-generation" results clearly indicate the feasibility of ultra-fast SEOP build-up rates with γ_{SEOP} > 0.2 min^{-1}, and demonstrate improvements in P_{Xe} when utilizing ^{4}He-rich gas mixtures relative to Xe/N_2 binary gas mixtures and significantly greater stability to temperature fluctuation.

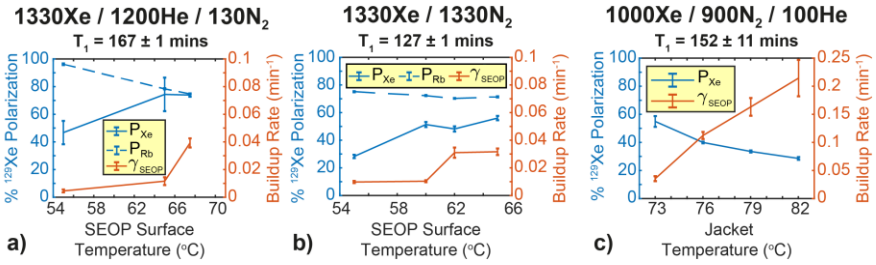


Figure 1. Steady-state P_{Xe}, γ_{SEOP} and rubidium polarization (P_{Rb}) measurements following high T_1 SEOP in 50% Xe partial pressure, (**a**) 2660 Torr He-rich gas mixture, **(b)** 2660 Torr binary (no ^{4}He) gas mixture and **(c)** 2000 Torr N_2-rich gas mixture as functions of oven/jacket temperature.

These significant decreases in temperature cycling time, improved temperature stability and improved P_{Xe} values, as well as the feasibility of ultra-fast polarization build-up rates will likely be highly beneficial for increasing HP ^{129}Xe production rates and improving quality assurance processes of batch-mode ^{129}Xe hyperpolarizers, which will be welcome in the clinical setting.

ACKNOWLEDGMENTS: DOD CDMRP under BRP W81XWH-12-1-0159/BC112431, W81XWH-15-1-0271, and W81XWH-15-1-0272. REFERENCES: (**1**) Walker, T. G., Happer, W., *Rev. Mod. Phys.* **1997,** *69* (2), 629-642. **(2)** Walker, T. G., *J. Phys. Conf. Ser.* **2011,** *294*, 012001. **(3)** Driehuys, B., et al., *Appl. Phys. Lett.* **1996,** *69* (12), 1668-1670. **(4)** Nikolaou, P., et al., *Proc. Natl. Acad. Sci. U. S. A.* **2013,** *110* (35), 14150-14155. **(5)** Nikolaou, P., et al., *J. Am. Chem. Soc.* **2014,** *136* (4), 1636–1642. **(6,7)** Birchall, J.R., et al., *Anal. Chem*. **2020**, 10.1021/acs.analchem.05051x and 10.1021/acs.analchem.05197c under review.

SLIC-based Sensing And Polarization Transfer In Parahydrogen Induced Polarization

Nuwandi M. Ariyasingha[1] and Eduard Y. Chekmenev[1,2]

[1]Department of Chemistry, Ibio, Karmanos Cancer Institute, Wayne State University, Detroit, MI 48202, USA
[2]Russian Academy of Sciences, Leninskiy Prospekt 14, Moscow 119991, Russia

SLIC. Spin-Lock Induced Crossing (SLIC) of the nuclear singlet and triplet states was first introduced by Rosen and co-workers in 2013 [1], which enabled the study of triplet-singlet polarization transfer. In this work, we show an advancement of the use of the application of SLIC for both Signal Amplification By Reversible Exchange (SABRE) and Parahydrogen Induced Polarization (PHIP) experiments [2].

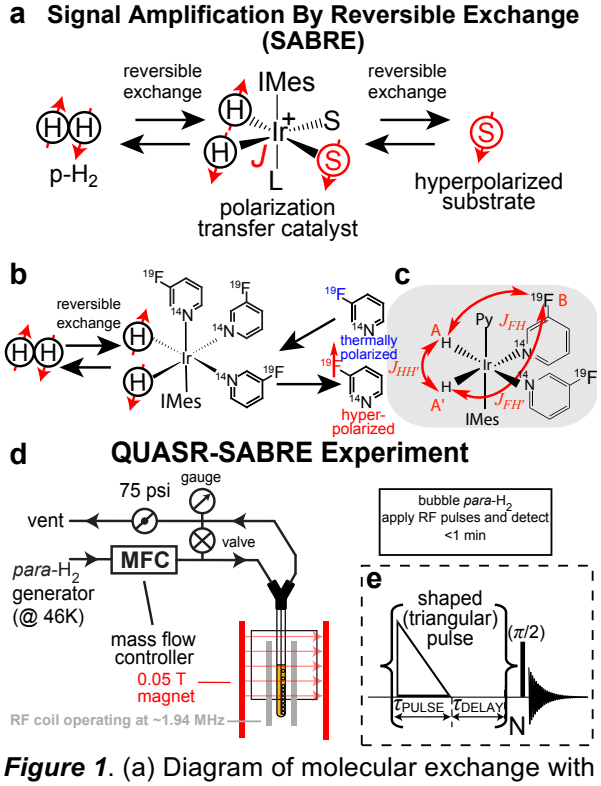


Figure 1. (a) Diagram of molecular exchange with p-H_2 in SABRE hyperpolarization. (b) schematic of SABRE chemical exchange with the substrate molecule, (c) spin system formed by the catalyst and the substrate. (d) Schematics of the experimental set up at 0.0475 T magnetic field for (QUASi Resonance) QUASR-SABRE.

SABRE. Polarization transfer from hyperpolarized (HP) hydrides to heteronuclear atoms such as ^{15}N and ^{19}F using SABRE and QUASi Resonance (QUASR) SABRE processes at 0.0487 T has been studied for different types of molecules [3,4]. Since ^{19}F spins have the second highest detection sensitivity with a gyromagentic ratio of 0.93 relative to a proton and it is nearly 100% naturally abundant isotope, the study of hyperpolarization of ^{19}F spins using SABRE is important. Figure 1 illustrates the reaction mechanisms for chemical exchange of parahydrogen (p-H_2), the spin systems created on the Ir-IMes catalyst with the substrate of interest and schematic diagram of the experimental setup used for QUASR-SABRE study. This work is an example of the capability of QUASR SABRE method to hyperpolarize ^{19}F nuclear spins although they are very weakly coupled. Polarization transfer from p-H_2-derived hydrides to ^{19}F was created via weak five-bond J coupling in 3-^{19}F-pyridine and 3-^{19}F-^{15}N-pyridine molecules by using a QUASR radio frequency pulse. Another study was performed for SLIC detection of radio frequency (rf) - based polarization transfer of ^{15}N polarization in three types of molecules: acetonitrile, six-membered pyridine and five-membered metronidazole antibiotic. A shaped SLIC-based rf pulse sequence was employed for QUASR-SABRE experiment with rf pulses applied to ^{15}N spins. This approach produces ^{15}N magnetization via polarization transfer from by parahydrogen-derived HP hydrides. The net results is the creation of ^{19}F magnetization or ^{15}N magnetization aligned along z-axis. Although the observed polarization levels were low here (0.1% for ^{19}F nucleus and ~2% for ^{15}N nucleus), potential improvements (due to better spectral selectivity of the applied RF pulses and longer ^{15}N T_1 values) of QUASR-SABRE approach could be studied to achieve higher levels of polarizations—ongoing work in progress in our laboratory on clinical 0.35 T MRI scanner.

PHIP. SLIC rf pulse has also been employed at 0.0475 T magnetic field in the study of relaxation dynamics of the long-lived spin states (LLSS) of parahydrogen-induced polarized propane and propane-d_6 compounds via heterogeneous pairwise parahydrogen addition to propylene. Transformation of LLSS of HP propane into observable magnetization was accomplished by rectangular SLIC pulses (Figure 2). T_{LLSS} of HP propane is about three times longer than the corresponding T_1 value at clinically relevant conditions of 1 atm (~3 s vs. ~1 s). Propylene deuteration results in shorter T_{LLSS} values. Additionally, presence of a buffering gas in the substrate mixture does not have a significant change on the T_1 and T_{LLSS} values of HP propane. Finally, we demonstrate the feasibility of T_{LLSS} relaxation measurements using SLIC sensing via a "partial" SLIC experiments (corresponding to ultra-short SLIC RF pulses), and demonstrate the utility of this approach in the relaxation studies of liquefied HP propane and others.

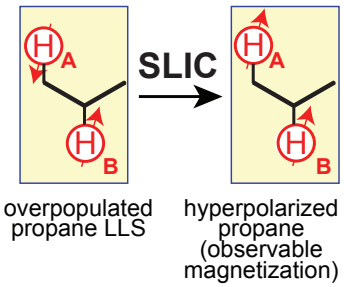


Figure 2. Schematic diagram of singlet-to-triplet transformation of the propane HP proton spins at 0.0475 T.

REFEERNCES: (1) DeVience, S.J.; Walsworth, R.L.; Rosen, M.S. *Phys. Rev. Lett.* **2013,** *111*, 173002. (2) Ariyasingha, N.M., Salnikov, O.G. *et al, JPCC* **2019**, *123*, 11734. (3) Theis, T.; Ariyasingha, N.M.; *et al, JPCL* **2018**, 9, 6136. (4) Ariyasingha, N. M., Lindale, J. R. *et al, JPCL* **2019**, *10*, 4229−4236.

ACKNOWLEDGEMENTS: NSF CHE-1836308, CHE 1416432, NIH 1R21EB020323, and 1R21CA220137, DOD CDMRP W81XWH-15-1-0271 and W81XWH-15-1-0272.

MEOP and SEOP: A Tutorial

Boyd Goodson, Department of Chemistry and Biochemistry, Southern Illinois University, Carbondale, IL 62901, USA

Abstract

Once limited to the realm of fundamental physics experiments, hyperpolarized (HP) noble gases have been exploited to enhance magnetic resonance signals for a wide range of applications, including biomedical and clinical imaging. The purpose of this tutorial is to introduce the principles and practice of the primary methods of preparing hyperpolarized noble gases: spin-exchange optical pumping (SEOP) and metastability-exchange optical pumping (MEOP). Alternative approaches (e.g. dynamic nuclear polarization, DNP), will also be discussed.

Spin-exchange optical pumping (SEOP) is a two-step process by which angular momentum from circularly polarized laser light is first transferred to the electronic spins of an alkali metal vapor, and then subsequently to the nuclear spins of the noble gas during gas-phase collisions. Over time, high bulk non-equilibrium spin polarization can accumulate in the nuclear spins of the noble gas, corresponding to an orders-of-magnitude increase in magnetic resonance sensitivity for MR spectroscopy and imaging. MEOP is a similar process, but one where no alkali metal vapor is present. Instead, electric discharge is used to create metastable helium-3 atoms, which can be optically polarized with a laser; over time, metastability exchange collisions then give rise to bulk hyperpolarized helium-3.

This tutorial lecture will focus on a number of key aspects governing the preparation and use of hyperpolarized noble gases for NMR and MRI, with a focus on biomedical applications. Following a brief introduction to the history of SEOP and MEOP and their early application to nuclear magnetic resonance nearly three decades ago, topics will include: fundamental principles of SEOP and MEOP; experimental aspects, methods, and instrumentation governing HP gas preparation; and "care and feeding" of HP gases to avoid premature loss of the hard-won but ultimately transient HP state. Particular attention will also be given to specific subjects of interest from my group's laboratory as well as those of collaborators, including: stopped-flow SEOP; SEOP at the "extremes" of high xenon density and resonant photon flux; "traditional" (low-pressure/re-compression) MEOP; high-field MEOP; technological developments in high-power frequency-narrowed lasers; and the development of clinical-scale "hyperpolarizers" capable of delivering near-unity nuclear spin polarization for human use. Time permitting, highlights from recent biomedical / clinical MRI demonstrations of HP noble gases will be reviewed.

Reference

"The Physics of Hyperpolarized Gas MRI." B.M. Goodson, K. Ranta, J. Skinner, A.M. Coffey, P. Nikolaou, M. Gemeinhardt, D. Anthony, S. Stephenson, S. Hardy, J. Owers-Bradley, M.J. Barlow, E.Y. Chekmenev, invited chapter for: Hyperpolarized and Inert Gas MRI From Technology to Application in Research and Medicine; M. Albert, F. Hane (Eds.), Academic Press / Elsevier (London); ISBN: 978-0-12-803675-4; pp 23-40 (2017).

NMR of ^{131}Xe Spin Exchange Optical Pumping in Aluminosilicate (GE180) Cells: Targets for Neutron Optics Searches for Time-Reversal Invariance Violation

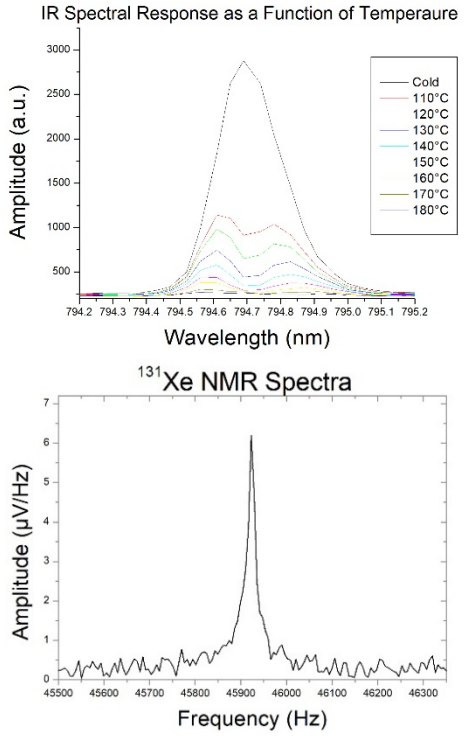
Dustin Basler[1], Kierstyn Albin[1], Liana Bales[1], Abdulbasit Tobi Gafar[1], Hao Lu[2], W. Michael Snow[2], Earl Babcock[3], Eduard Y. Chekmenev[4], Michael J. Barlow[5], and Boyd M. Goodson[1]

[1]Department of Chemistry & Biochemistry, Southern Illinois University, Carbondale, IL; [2]Department of Physics, Indiana University, Bloomington, IN, USA; [3]Forschungszentrum Jülich, Jülich Centre for Neutron Science (JCNS), Germany; [2]School of Medicine, University of Nottingham, Queens Medical Centre, Nottingham, UK; [3]Wayne State University & Karmanos Cancer Institute (KCI), Detroit, MI, United States



Fig. 1. Handblown GE180 cells.

The search for new physics beyond the Standard Model of particles and interactions aims to explain unanswered questions varying from the presence of dark matter and energy, to the large relative abundance of matter versus antimatter in the universe. It has been argued that detection and quantification of any new sources of time-reversal invariance violation (TRIV) may be the best places to look for new physical interactions that may help explain these observations.[1,2] Towards this end, the NOPTREX collaboration[3] is working to develop sensitive 'null-tests' for TRIV in the transmission of polarized neutrons passing through polarized targets of heavy nuclei that have neutron resonances that exhibit large parity-odd asymmetries. Of the identified isotopes, ^{131}Xe is promising because it is stable, has non-zero spin, has significant natural abundance (21.2%) and exhibits a p-wave resonance (and large parity-odd asymmetry) at 3.2 eV (4.3%).[4] Moreover, at least in principle, it can be hyperpolarized[5] via spin-exchange optical pumping (SEOP).[6] However, the need for the nuclei to be spin-polarized in bulk, at relatively high densities (and for long periods of time) presents a significant challenge. Indeed, the strong nuclear electric quadrupole moment of ^{131}Xe (I=3/2) gives rise to much faster T_1 relaxation; the binary collision pathway[7] is 3.95x10^{-2} amg^{-1}·s-1 (giving a T_1 of only ~25 s at ~1 atm of Xe); furthermore, Xe-^{131}Xe van der Waals complexes and wall collisions add on to give even shorter relaxation times.[5]



Figs. 2 & 3. Top: IR spectra at various GE-180 cell temperatures with the magnetic field on using a QPC U500 laser. **Bottom**. Aurora NMR spectrum (single scan) using a GE180 cell containing 150/150 torr ~84% 131Xe/N2 at ~46 kHz at a cell temperature of 140°C.

To mitigate this problem, we have been working to improve the polarization achievable by using high-power lasers, and adapting our previous improvements in clinical-scale production of ^{129}Xe via stopped-flow SEOP.[8] We have recently reported ^{131}Xe polarization values in excess of 3% in ^{131}Xe densities of 0.31 amagat in a 2" x 2" cylindrical Pyrex cell.[9,10] While these results represent a order-of-magnitude improvement over past attempts at bulk ^{131}Xe polarization, this cell is too small to be a useful target in planned neutron experiments; moreover, the borosilicate material is not appropriate (boron slows neutrons). Thus, we are now working to extend these results to larger cells made of aluminosilicate glass (GE180). Three custom GE180 aluminosilicate cells were created by glass-blowers at Jülich (**Fig. 1**); they are welded to commercial Pyrex stopcock assemblies that will be removed prior to neutron experiments (while maintaining their contents, including 150-300 Torr ^{131}Xe (84% enriched) and Rb films). SEOP is performed with a 180 W spectrally narrowed QPC Ultra500 laser and monitored via transmission near-IR spectroscopy (**Fig. 2**) and in situ low-field NMR (**Fig. 3**) performed with Magritek (Aurora and Kea) spectrometers, calibrated with thermally polarized water signals (taken at the same frequency despite the ~12-fold difference in ^{1}H/^{131}Xe gyromagnetic ratio)—allowing P_{Xe} to be estimated (**Fig. 4**). Current efforts concern more precise calculation of P_{Xe} and optimizing P_{Xe} as a function of cell temperature and laser offset (to combat the high laser absorption at Rb densities sufficient to allow spin-exchange to compete effectively with ^{131}Xe relaxation, prior to performing initial neutron beam experiments.

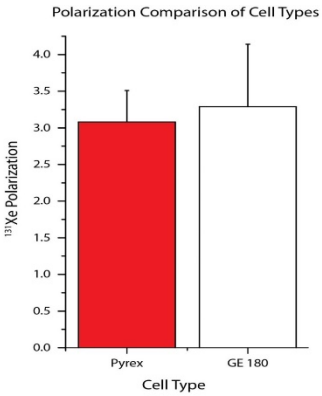


Fig. 4. ^{131}Xe Polarization comparison of 300/300 torr ~84% enriched ^{131}Xe/N_2 pyrex to 150/150 torr GE-180 cell.

Acknowledgements: This work was funded in part by DoD (W81XWH-12-1-0159/BC112431, W81XWH-15-1-0271, & W81XWH-15-1-0272) as well as a SEED Award from the Research Corporation for Science Advancement. ***References:***
[1]Bowman & Gudkov, *PRC*, **90**, 065503, 2014; [2]Fadeev & Flambaum, PRC 100, 015504, 2019; [3]Schaper et al. arXiv:2001.03432v1, 2020; [4]Mitchell et al., Phys. Reps., 354, 157. 2001; [5]Stupic, et al., *JMR*, 208, **58**, 2011; [6]Walker & Happer *Rev. Mod. Phys.* **69**, 629, 1997; [7]Brinkmann, et al., *Helv. Phys. Acta*, **35**, 431, 1962; [8]Nikolaou et al., *PNAS,* **110**, 14150, 2013; [9]Molway et al. ENC 2018; [10]Bales et al. ENC 2019

Journal of Magnetic Resonance 316 (2020) 106755

Contents lists available at ScienceDirect

Journal of Magnetic Resonance

journal homepage: www.elsevier.com/locate/jmr

Pilot multi-site quality assurance study of batch-mode clinical-scale automated xenon-129 hyperpolarizers

Jonathan R. Birchall [a,*], Robert K. Irwin [b], Panayiotis Nikolaou [c], Ekaterina V. Pokochueva [d,e], Kirill V. Kovtunov [d,e], Igor V. Koptyug [d,e], Michael J. Barlow [b], Boyd M. Goodson [f,g], Eduard Y. Chekmenev [a,h,*]

[a] Department of Chemistry, Integrative Biosciences (Ibio), Wayne State University, Karmanos Cancer Institute (KCI), Detroit, MI 48202, United States
[b] Sir Peter Mansfield Imaging Centre, University of Nottingham, Nottingham NG7 2RD, United Kingdom
[c] XeUS Technologies LTD, Nicosia, Cyprus
[d] International Tomography Center SB RAS, Institutskaya Street 3A, Novosibirsk 630090, Russia
[e] Novosibirsk State University, Pirogova Street 2, Novosibirsk 630090, Russia
[f] Department of Chemistry and Biochemistry, Southern Illinois University, Carbondale, IL 62901, United States
[g] Materials Technology Center, Southern Illinois University, Carbondale, IL 62901, United States
[h] Russian Academy of Sciences, Leninskiy Prospekt 14, Moscow 119991, Russia

ARTICLE INFO

Article history:
Received 11 March 2020
Revised 21 May 2020
Accepted 25 May 2020
Available online 29 May 2020

Keywords:
Xenon
Hyperpolarization
SEOP
Hyperpolarizer
Automation
Quality assurance

ABSTRACT

We present a pilot quality assurance (QA) study of spin-exchange optical pumping (SEOP) performed on two nearly identical second-generation (GEN-2) automated batch-mode clinical-scale ^{129}Xe hyperpolarizers, each utilizing a convective forced air oven, high-power (~170 W) continuous pump laser irradiation, and xenon-rich gas mixtures (~1.30 atm partial pressure). In one study, the repeatability of SEOP in a 1000 Torr Xe/900 Torr N_2/100 Torr ^{4}He (2000 Torr total pressure) gas mixture is evaluated over the course of ~700 gas loading cycles, with negligible decrease in performance during the first ~200 cycles, and with high ^{129}Xe polarization levels (avg. $\%P_{Xe}$ = 71.7% with standard deviation σ_{PXe} = 1.5%), build-up rates (avg. γ_{SEOP} = 0.019 min^{-1} with standard deviation σ_γ = 0.003 min^{-1}) and polarization lifetimes (avg. T_1 = 90.5 min with standard deviation σ_T = 10.3 min) reported at moderate oven temperature of ~70 °C. Although the SEOP cell in this study exhibited a detectable performance decrease after 400 cycles, the cell continued to produce potentially useable HP ^{129}Xe with $\%P_{Xe}$ = 42.3 ± 0.6% even after nearly 700 refill cycles. The possibility of "regenerating" "dormant" (*i.e.*, not used for an extended period of time) SEOP cells using repeated temperature cycling methods to recover $\%P_{Xe}$ is also demonstrated. The quality and consistency of results show significant promise for translation to clinical-scale production of hyperpolarized ^{129}Xe contrast agents for imaging and bio-sensing applications.

© 2020 Elsevier Inc. All rights reserved.

1. Introduction

Nuclear spin polarization (P)—the degree of spin alignment with an applied static magnetic field—is generally very low (10^{-6}-10^{-5}) for biomedically relevant spin-½ nuclei (^{1}H, ^{31}P, ^{129}Xe, ^{13}C, ^{15}N) at clinically relevant conditions and the several-Tesla magnetic fields of modern MRI scanners. However, hyperpolarization can boost P to the order of unity, with corresponding gains in the detection sensitivity of MR spectroscopic and imaging techniques by 4–5 orders of magnitude [1–4]. This sensitivity gain enables detection of dilute fluids [5–8] including inhalable hyperpolarized (HP) gases such as ^{3}He and ^{129}Xe [9–19].

^{129}Xe gas is traditionally hyperpolarized by the Spin Exchange Optical Pumping (SEOP) process [20,21]. Two SEOP variants exist: continuous-flow [22–26] and stopped-flow (or batch-mode) production approaches [27–34]. Both methods have their own merits and limitations [35], and both approaches have been developed to enable production of HP ^{129}Xe on a clinical scale, *i.e.* in sufficiently large quantities and high P to enable inhalation and functional ^{129}Xe MRI of human subjects or animals. Indeed, the inhaled ^{129}Xe gas can be employed for a wide range of functional and metabolic MRI exams, including studies of the lung [10,36–40], brain imaging [41–44], brown fat imaging [45,46], receptor imaging [47–50] and potentially others. Moreover, HP ^{129}Xe can be employed for other non-biomedical applications [13,51–53].

* Corresponding authors at: Department of Chemistry, Integrative Biosciences (Ibio), Wayne State University, Karmanos Cancer Institute (KCI), Detroit, MI 48202, United States (E.Y. Chekmenev).

E-mail addresses: jonathan.birchall@wayne.edu (J.R. Birchall), chekmenev@wayne.edu (E.Y. Chekmenev).

https://doi.org/10.1016/j.jmr.2020.106755
1090-7807/© 2020 Elsevier Inc. All rights reserved.

The ultimate use of HP ^{129}Xe in the vast majority of applications (including most prominently biomedical applications with HP ^{129}Xe considered as a drug) requires good production consistency from one production cycle to the next, to ensure a high level of reproducibility and scientific rigor of the studies. The SEOP process is a two-step process requiring an alkali metal (typically Rb) to act as an intermediary for inducing ^{129}Xe nuclear spin polarization originating from circularly-polarized laser light [20,21]. Rb metal is placed inside a sealed vessel (the "SEOP cell"), which is refilled with a ^{129}Xe-containing gas mixture, either on a continuous- or batch-filling basis [27]. The Rb quality may degrade over time as residual O_2, moisture, and other impurities slowly react with Rb, which leads to two undesirable effects. First and foremost, a reduced equilibrium Rb vapor density is observed (because of the colligative properties), which in turn results in lower-than-anticipated laser light absorption by the SEOP cell at a set temperature. This reduced optical pumping rate consequently leads to a decreased overall ^{129}Xe polarization level ($\%P_{Xe}$). The second deleterious effect is a reduction of the apparent ^{129}Xe longitudinal spin relaxation time (T_1) within the SEOP cell, which may lead to lower values of steady-state $\%P_{Xe}$. The combined outcome of both effects is thus a reduction in $\%P_{Xe}$. Once SEOP cell performance becomes unacceptably poor, a replacement of the SEOP cell is required, which may be costly, laborious, and disruptive to day-to-day operation—especially in the context of *in vivo* studies.

Here, we report a first-in-kind pilot quality assurance (QA) study of the reproducibility of the stopped-flow ^{129}Xe SEOP production process. The reported study was conducted using a second generation (GEN-2) stopped-flow, clinical-scale ^{129}Xe hyperpolarizer [54–56], operational at two sites: Wayne State University (Detroit, MI, USA) and The University of Nottingham (Nottingham, UK). Specifically, we investigate the longevity of SEOP cells filled with Rb metal in the context of multiple gas mixture refills. Since each SEOP cell can be refilled many hundreds of times, and because Xe gas mixtures are relatively costly, two studies have been performed. In one, we performed a series of SEOP cell refills with a Xe-containing gas mixture (25 times). In the other study, we interleaved Xe gas mixture fills with SEOP cell refills using an inert gas (N_2) to simulate the effects of hundreds of total SEOP cell refills. Overall, we conclude that the SEOP cell can be successfully refilled over ~200 times without any observable degradation in SEOP performance, and nearly 700 times with non-terminal reduction of hyperpolarization performance—demonstrating that clinical-scale batch-mode hyperpolarizers are robust in their operation under good laboratory practices. The described approaches should be of interest because they comprise a straightforward way to perform QA studies in a reasonable amount of time (~3 weeks) and that can be readily adopted by multiple sites.

2. Materials and methods

Two second-generation (GEN-2) automated batch-mode hyperpolarizers with nominally identical configuration were utilized to perform ^{129}Xe SEOP in this work. The first of these devices was in operation at Wayne State University, USA, with the second at the University of Nottingham, UK. The GEN-2 hyperpolarizer (Fig. 1) is contained within an aluminum chassis (Quote #17177 & 18025, MiniTec, Farmington, NY). The device operates in the Xe-rich gas mixture regime, *i.e.*, high Xe partial pressure, under conditions of high-power, frequency-narrowed pump laser irradiation. The pump laser used to perform optical pumping of Rb electrons was a BrightLock Ultra-500 continuous-wave device, with a 2″ beam expanding telescope and a λ/4 waveplate providing >98% purity circular photon polarization (QPC Laser Technologies, Sylmar, CA). Power output from the optical train was ~170 W, with

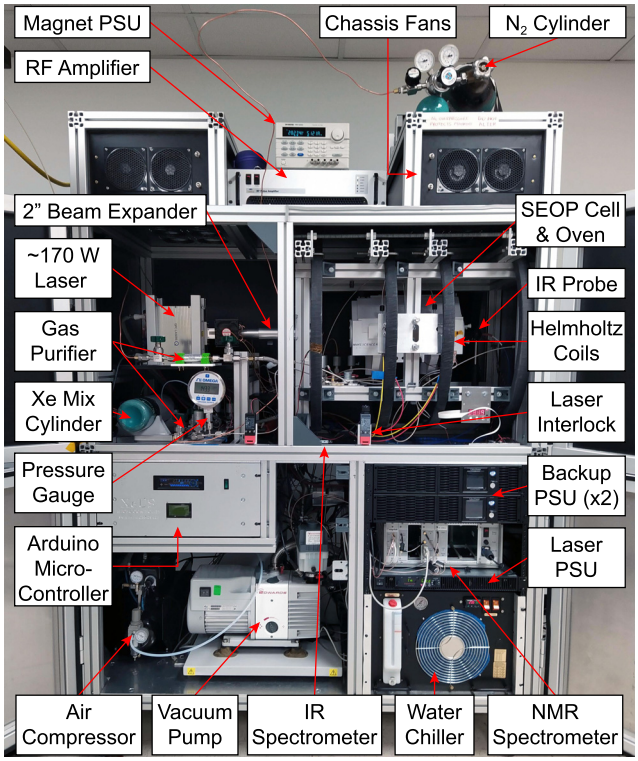


Fig. 1. Annotated photograph of the GEN-2 hyperpolarizer device and chassis, outlining the key components and their orientation. The gas-handling manifold (center of photograph) is illustrated in detail in Fig. 2 and in the Supporting Information (SI).

a spectral full width at half maximum (FWHM) of 0.154 nm. Photon emission was tuned to the Rb D_1 wavelength (λ = 794.77 nm) using a high-capacity water chiller (K-O Concepts DMC-14-G2, Titusville, FL), operating at a flow rate of 6 L/min with 1.4 kW cooling power. SEOP was performed inside a sealed, cylindrical glass vessel with a diameter of 2″ (matched to the diameter of the beam-expanding telescope) and a volume of ~500 cubic centimeters (cc) using a 3D-printed Temperature Electric Cooler (TEC) oven, described in detail previously [56]. The oven maintained the SEOP cell temperature with a thermocouple attached to the SEOP cell surface. The SEOP cell and the oven were placed inside four parallel magnet coils providing a homogeneous magnetic field of up to 40 Gauss (4.0 mT) during SEOP process, with some RF shielding by the hyperpolarizer chassis. A low-frequency Kea2 NMR spectrometer (Magritek, Wellington, New Zealand) and butterfly-orientation RF-coil, tuned to a 40.8 kHz resonance frequency for both ^{1}H and ^{129}Xe spins was used for NMR polarimetry. The homogeneous magnetic field was configured to be ~3.6 times stronger when performing ^{129}Xe NMR, in order to account for the lower gyromagnetic ratio (-11.777 MHz·T^{-1}) of ^{129}Xe nuclei relative to protons (42.576 MHz·T^{-1}) and satisfy the matching condition for resonance of both spins at 40.8 kHz. The complete design and all details of RF coil and other hardware and electronics of this open-source hyperpolarizer is presented in detail elsewhere [57].

Following preparation, cleaning, and Rb loading of SEOP cells [58], desired gas mixtures were loaded into the SEOP cell *in situ* on the GEN-2 hyperpolarizer manifold. This manifold incorporated a pair of gas purifiers (Eliminator CAG-VR4-1-PF-ISV, NuPure, Ottawa, ON, Canada) to ensure efficient removal of potential contaminants.

Evacuation of SEOP cells was performed using a rotary vane vacuum pump (RV5, Edwards, Burgess Hill, UK), capable of achiev-

ing vacuum levels of less than 1×10^{-2} Torr inside the SEOP cell in under 10 min (under 2 min when evacuating the manifold only), as measured using a vacuum gauge (APG100-XLC Active Pirani NW16, Edwards, Burgess Hill, UK) rated to 10^{-4} Torr. Loading and evacuation of the manifold was performed in stages, using a DR-150 air compressor (Silentaire Technology, Houston, TX) operating at 45 PSI to independently actuate a series of pneumatic bellows valves (SS-BNV51-C/O, Swagelok, Solon, OH). Unless stated otherwise, all SEOP cells were filled to a total pressure of 2000 Torr, as measured using a digital pressure gauge installed in series along the manifold inlet path (DPG4000, Omega Engineering, Norwalk, CT). An additional filter (Wafergard GT-Plus, Entegris, Billerica, MA) was positioned in the gas exit path from the SEOP cell, to ensure the HP ^{129}Xe contrast agent could be collected in a temporary storage vessel, *e.g.*, Tedlar bag [54], with negligible (<5 ng) Rb content. All details pertaining to the design of the gas-loading manifold (including bill of materials)—the performance of which is tested in the presented study—are provided in the Supporting Information (SI): Figure S1 and Figure S2.

Operation of the gas manifold and control over other hyperpolarizer functions such as oven temperature, magnetic field strength, and laser current were conducted using a USB-connected graphical user interface (GUI) written in JavaScript p5.js using Processing v3.5.3 software, and communicating with an Arduino IDE Mega 2560 micro-controller. A schematic summary of the gas-handling manifold is presented, as shown in the Processing GUI, in Fig. 2.

Standard operation of the GEN-2 hyperpolarizer device for performing SEOP of ^{129}Xe commenced with switching on the B_0 magnetic field (5.12 A to achieve a resonance frequency of 40.8 kHz in ^{129}Xe spins), water chiller (20.7 °C to ensure pump laser photon emission at the Rb D_1 wavelength of 794.77 nm), and laser diode array (LDA) (40 A to achieve ~170 W output) power supply units (PSUs) via the Processing USB interface. Spectroscopic IR measurements were performed on the pump laser at maximum current before heating the SEOP cell, providing a point of reference to ensure stable and consistent power output over subsequent days of experimental operation. Additionally, a baseline measurement of pump laser intensity without optical pumping (due to negligible Rb vapor density at low SEOP cell temperatures) facilitated the calculation of fractional pump laser photon absorption and electronic rubidium polarization, P_{Rb}. This value is calculated under steady-state conditions using

$$|P_{Rb}| = \frac{A}{A_0} - 1 = \left|\frac{\ln(I_{hot}) - \ln(I_{cold})}{\ln(I_0) - \ln(I_{cold})}\right| - 1 \quad (1)$$

where A and A_0 are calculated as the absorbance values of the SEOP cell, with and without application of the homogeneous B_0 magnetic field, respectively, defined as $A = -\ln(I/I_{cold})$. The peak integral I corresponds to the respective steady-state ("hot" SEOP cell) spectra, while I_{cold} represents the same peak integral for the baseline ("cold" SEOP cell) spectrum. This process is summarized in Fig. 3c, and is described in greater detail in previous studies and in the SI [58]. After recording an average measurement of stable laser power and wavelength at maximum driver current, the pump laser current was reduced to move the photon emission away from the Rb D_1 wavelength. This ensured that no optical pumping would take place while the temperature of the forced air oven (set via the Processing USB interface) was raised to values at which SEOP was to be performed (between 60 and 72.5 °C in this study).

At the end of each polarization build-up experiment, steady-state ^{129}Xe polarization was determined using an exponential curve-fitting of NMR spectral integrals. These signals were acquired at six-minute intervals using low flip-angle (~45°) RF pulses to ensure sufficient signal-to-noise ratio (SNR) while conserving net ^{129}Xe polarization. Calculation of P_{Xe} as a function of time takes the form

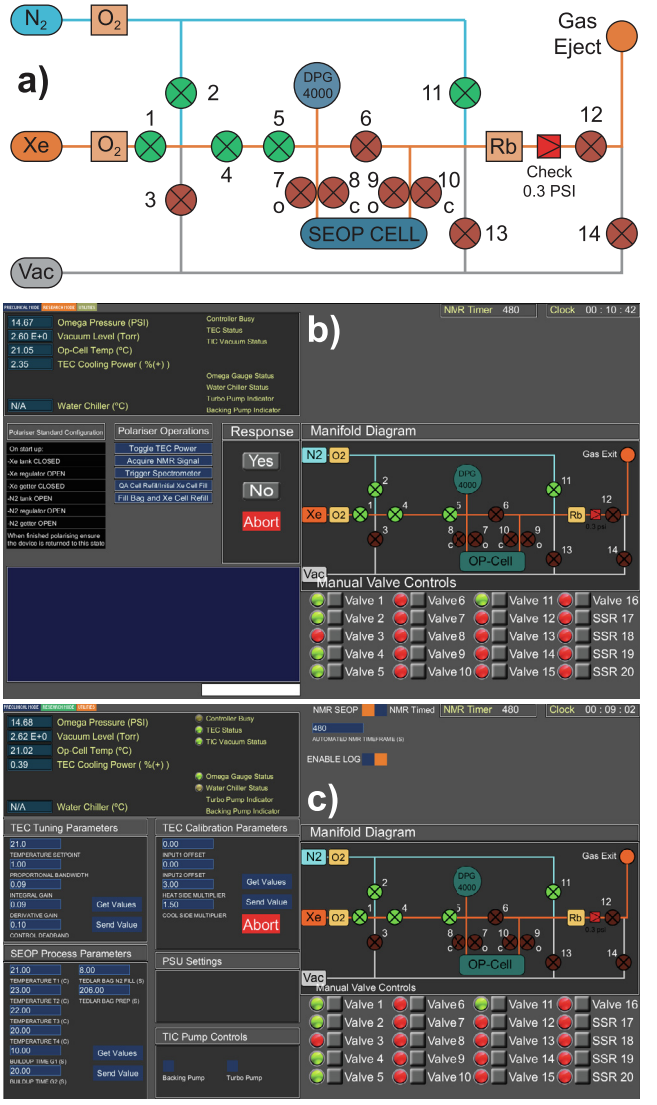


Fig. 2. Schematic of the gas handling manifold employed on the second-generation (GEN-2) batch-mode hyperpolarizer device, as shown schematically on the Processing graphical user interface (GUI) in both (b) Research Mode and (c) Utilities Mode (more details provided elsewhere) [57]. Individual valves are numbered as shown in the Processing graphical user interface (GUI), as either normally open (NO, green circle) or normally closed (NC, brown circle). Helical valves used to rotate the SEOP cell stopcocks (7–10) are labelled as either "o" (opening via anticlockwise rotation) or "c" (closing via clockwise rotation). Purifiers and filters are denoted with brown rectangles. A one-way check valve to prevent the gas backflow inside the SEOP cell is represented with a red square. The orange ellipse labelled "Xe" represents the Xe gas mixture cylinder, containing a preset mixture of natural abundance Xe, N_2 and ^{4}He content. (For interpretation of the references to colour in this figure legend, the reader is referred to the web version of this article.)

$$P_{Xe} = P_{\max}[1 - \exp(-\gamma_{SEOP} \cdot t] + P_{Xe}(0) \quad (2)$$

Here, γ_{SEOP} represents the polarization build-up rate constant given by

$$\gamma_{SEOP} = \frac{1}{T_b} = \gamma_{SE} + \Gamma_{Xe} = \gamma_{SE} + \frac{1}{T_1} \quad (3)$$

where T_b is the exponential polarization build-up time constant, γ_{SE} is the ^{87}Rb-^{129}Xe spin-exchange rate, Γ_{Xe} is HP ^{129}Xe spin destruction rate (given as $1/T_1$) and T_1 is the longitudinal spin-relaxation

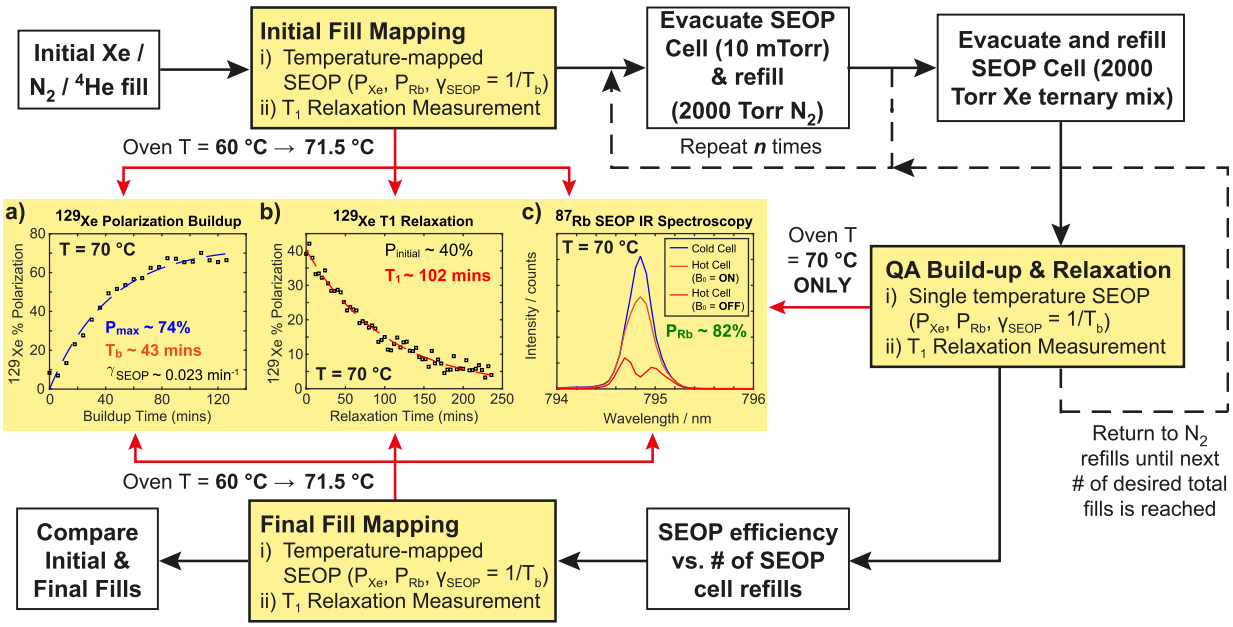


Fig. 3. Flow chart outlining the QA study process, from initial filling and SEOP study of the 1000 Torr Xe/900 Torr N_2/100 Torr ^{4}He gas mixture, to evacuation of SEOP cells and gas mixture refill procedures on the GEN-2 hyperpolarizer and eventual data comparison and analysis. The inset boxes provide examples NMR spectroscopic data acquired during the ^{129}Xe polarization (a) build-up and (b) relaxation processes, as well as IR spectroscopic data of the pump laser emission profile before and during ^{129}Xe polarization build-up (c). Key performance indicators of SEOP efficiency ($\%P_{Xe\ (max)}$, $\%P_{Rb}$, T_b, and T_1) in this example dataset are colored to match their respective QA study results presented in Fig. 5c.

time constant. Steady-state ^{129}Xe polarization, P_{Xe}, can be calculated using

$$P_{Xe} = P_H\left(\frac{S_{Xe}}{S_H}\cdot\frac{C_H}{C_{Xe}}\cdot\frac{\gamma_H}{\gamma_{Xe}}\right)\cdot Corr(T_2^*) \quad (4)$$

where P_H represents a known thermal ^{1}H polarization of H_2O phantom (containing 10 mM $CuSO_4$) at 40.8 kHz resonance frequency, C_H and C_{Xe} represent the respective proton phantom and ^{129}Xe concentrations, γ_H and γ_{Xe} the proton and ^{129}Xe gyromagnetic ratios, and S_{Xe} and S_H are the HP ^{129}Xe signal and the reference signals from water phantom respectively. A correction factor, $Corr(T_2^*)$ is used to account for the differing rates of NMR signal decay (T_2^*) between ^{1}H and ^{129}Xe [55,58]. In our study, exponential fitting of NMR peak integral data for the purposes of P_{Xe}, γ_{SEOP} and T_1 calculation was performed in MATLAB using previously described protocols—the copy of the MATLAB processing code is provided in Ref. # [58]. For the purpose of this study, all error bar values presented in the Results and Discussion section were derived for two-sigma bounds corresponding to ~95% confidence intervals.

The oven temperature was then adjusted to perform build-up experiments under various conditions, Fig. 3a. Elevated temperatures result in increased vaporization of Rb, contributing to increased optical pumping rates [55]. However, at excessively high oven temperatures, the combined effect of heating due to the oven and pump laser may result in a "runaway" effect (and the SEOP cell temperature becomes unmanageable), whereby the Rb vapor density increases exponentially [25,59–61]. It was therefore necessary to determine an optimal temperature for performing SEOP that achieves a balance of high levels of ^{129}Xe polarization at appreciable build-up rates, while avoiding the Rb runaway regime—termed "temperature mapping" [55]. While waiting for the temperature to stabilize at a new set-point, the pump laser was again shifted off-resonance from the Rb D_1 wavelength by reducing the current to 25 A, effectively halting optical pumping. Accompanied by the application of 2000 high-flip-angle "crushing" RF pulses, the ^{129}Xe polarization was rapidly zeroed out before beginning the following SEOP build-up experiment to ensure comparability between trials.

Alternatively, the hyperpolarizer could be switched to a cool-down state, whereby the temperature set-point was returned to ambient (~25 °C) and pump laser current was reduced to 15 A (just above the lasing threshold) until the SEOP cell surface temperature had dropped below 35 °C. This practice prevented Rb vapor from condensing on the front and rear windows of the SEOP cell. ^{129}Xe polarization T_1 relaxation measurements were performed after cooling down the SEOP cell to ambient temperature, Fig. 3b. During this time, the pump laser and oven were switched off, with the homogeneous magnetic field maintained at a current of 5.12 A. NMR spectra were acquired at four-minute intervals over the span of four hours. This sequence was performed before each gas mixture refill procedure, since the ability to maintain a long T_1 relaxation time after each refill is a key performance indicator for quality assurance purposes, highlighting that the SEOP cell has been successfully refilled without introducing depolarizing contaminants.

Once all necessary data had been acquired from the initial ternary 1000 Torr Xe/900 Torr N_2/100 Torr ^{4}He gas mixture load—^{129}Xe polarization ($\%P_{Xe}$), polarization build-up time ($T_b = 1/\gamma_{SEOP}$), rubidium polarization ($\%P_{Rb}$), and T_1 relaxation measurements—it was necessary to evacuate and refill the SEOP cell and repeat for the purposes of quality assurance. To minimizing wastage of expensive Xe gas mixtures, all "intermediate" refills in this first study were performed with ultra-high purity grade nitrogen (>99.999%) to simulate intended clinical-scale operation, and a final fill was performed with the desired Xe-containing ternary gas mixture. Heating and cooling of the SEOP cell by the forced air oven and pump laser was not performed on intermediate N_2 fills to facilitate significantly more rapid data acquisition and to reduce pump laser degradation. For example, the addition of the required heating and cooling with lengthen the total duration of the QA study by 690 working hours. This additional experimental time duration would require 17 weeks of extra time and would also add a further 690 h of run time to LDA with rated lifetime ~10,000 h. These are

clear limitations of the reported QA study at Wayne State University site, which is in part addressed by the mini-study at the University of Nottingham (see below). The overall experimental procedure is described in Fig. 3. The SEOP cell filling and evacuation procedure is displayed schematically in Fig. 4.

Following a complete temperature-dependent SEOP mapping procedure of a given gas mixture, the SEOP cell underwent a series of *in situ* evacuation and N_2 filling procedures on the GEN-2 hyperpolarizer manifold, before being refilled with an identical gas mixture composition as described in Fig. 4. For the purposes of the quality assurance study, the Xe gas mixture was comprised of 1000 Torr Xe/900 Torr N_2/100 Torr ^{4}He, and was loaded during the 1st, 17th, 69th, 180th, 437th, and 694th SEOP cell fills, with all other refills being performed with N_2 only. The QA study comprised identical SEOP experiments, with NMR data acquired at six-minute intervals until achieving steady-state ^{129}Xe polarization at a SEOP cell surface temperature of 70 °C in these six Xe gas mixture fills. Following each SEOP experiment at 70 °C, the SEOP cell was cooled to room temperature (~25 °C) and the pump laser switched off to allow T_1 relaxation measurements to be performed.

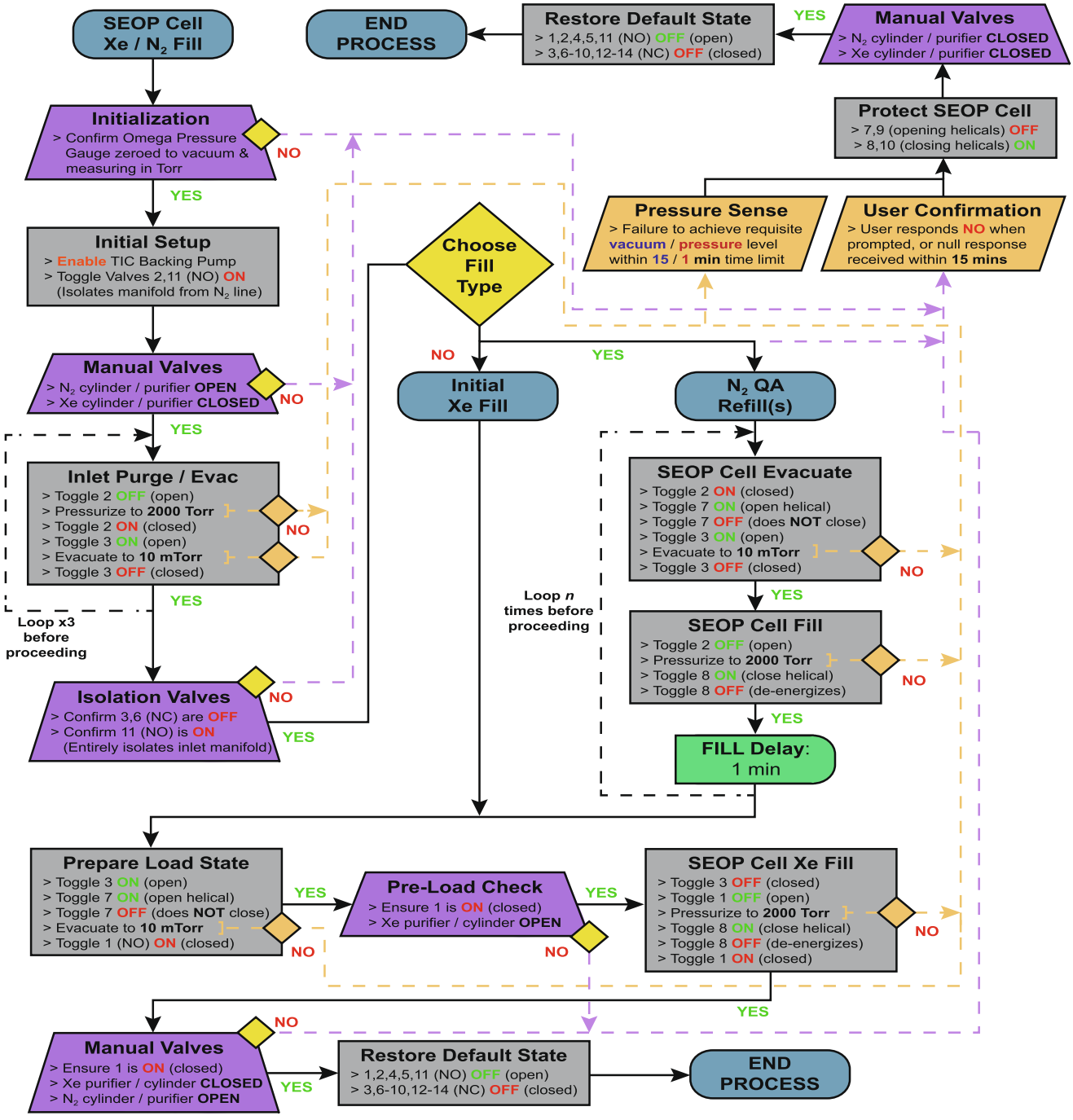


Fig. 4. Process flowchart depicting the automated quality assurance (QA) refill sequence coded into the Arduino Mega 2560 microcontroller for the purpose of evacuating and refilling SEOP cells. Purple trapezia represent manual/user-led confirmations or actions. Grey rectangles are automated processes. Yellow diamonds are decisions the user can choose between or confirm through the GUI. Orange parallelograms represent active sensing and response to parameters observed outside of acceptable range.

3. Results and discussion

Before embarking on a protracted QA study, it was necessary to determine a set of optimal conditions that would yield the most reliable comparisons—particularly with regards to the oven temperature at which SEOP is performed. The SEOP cell was therefore first studied at a range of oven temperatures (termed mapping [55]) following initial loading of the 1000 Torr Xe/900 Torr N_2/100-Torr ^{4}He gas mixture (Fig. 5a), before any refilling took place during the QA study.

A maximum ^{129}Xe polarization of 73.6 ± 4.6% was observed during this initial mapping processes at an oven temperature of 70 °C, after which $\%P_{Xe}$ values began to decrease (it was not possible to maintain a stable SEOP cell surface temperature over 71.5 °C due to the thermal effects of rubidium runaway, so no SEOP data above this temperature was recorded). This level of ^{129}Xe polarization was achieved at a modest build-up rate γ_{SEOP} of 0.023 ± 0.004 min^{-1}. Based on the observations from this initial study, we elected to proceed with an oven temperature of 70 °C. However, it should be noted that build-up rates approaching ~0.05 min^{-1} (a ~2-fold increase relative to those observed at maximum value of $\%P_{Xe}$) can be achieved with only a modest reduction in $\%P_{Xe}$ (65.2 ± 2.4% at γ_{SEOP} = 0.049 ± 0.007 min^{-1}). Such high build-up rate is of significant clinical relevance. For example, assuming 1.0-hour production cycle (*e.g.*, 30 mins for temperature manipulation and ejection and 30 min. of polarization build-up), this yields dose equivalent (DE) rate [35] of 0.16 L/hour at 0.8 L of gas mixture per 1.0-h-cycle at ejection using total 2000 Torr SEOP cell pressure and 50% Xe content using 100% enriched ^{129}Xe (natural abundance Xe employed here lowers DE rate to 0.042 L/hour) of ~41%-hyperpolarized Xe (estimated after ejection from the hyperpolarizer after 24 mins of cooldown [54]).

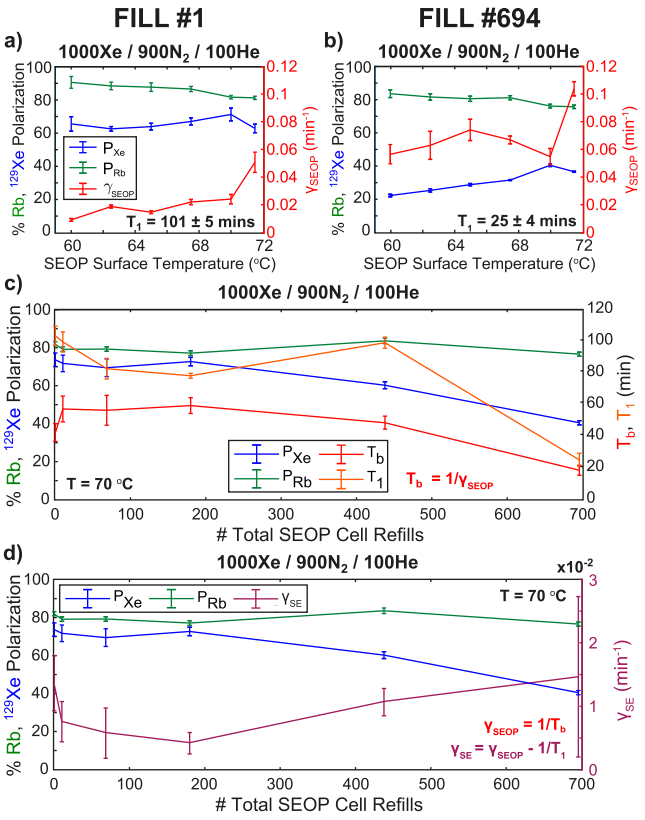


Fig. 5. (a) Steady-state $\%P_{Xe}$, γ_{SEOP}, and $\%P_{Rb}$ measurements as a function of SEOP cell surface temperature following fill #1 (the initial 1000 Torr Xe/900 Torr N_2/100 Torr ^{4}He gas mixture fill at the commencement of the QA study). (b) Steady-state $\%P_{Xe}$, γ_{SEOP}, and $\%P_{Rb}$ measurements as a function of SEOP cell surface temperature following fill #694 (the final 1000 Torr Xe/900 Torr N_2/100 Torr ^{4}He gas mixture fill at the conclusion of the QA study); note the shorter ^{129}Xe T_1 value. (c) Steady-state $\%P_{Xe}$, $\%P_{Rb}$, and T_b measurements after polarization build-up at a SEOP cell surface temperature of 70 °C, as well as post-build-up T_1 relaxation measurements, as a function of the number of total gas mixture refills. (d) ^{87}Rb-^{129}Xe spin-exchange rate, γ_{SE}, as a function of the number of the number of total gas mixture refills compared to associated steady-state $\%P_{Xe}$ and T_b measurements. The solid lines are added to guide the eye. Note that data in display b) was taken after the last point (694th total fill) in displays (c) and (d).

A temperature-dependent SEOP build-up map of the sixth and final Xe gas mixture fill (694th total fill) is shown in Fig. 5b, providing a comparison of SEOP process efficiency between the start and end points of the QA study under otherwise identical experimental conditions. We note a significant decrease in maximum achievable ^{129}Xe polarization values across the entire range of oven temperatures studied, ranging from roughly a factor of three reduction at lower oven temperatures ($\%P_{Xe}$ = 67.7 ± 4.5% → 22.2 ± 0.6% at 60 °C) to slightly under a factor of two reduction at higher oven temperatures ($\%P_{Xe}$ = 73.6 ± 4.6% → 42.4 ± 1.1% at 70 °C). The effects of SEOP cell "poisoning" due to accumulated oxidizing impurities likely suppress the Rb vapor density inside the SEOP cell, resulting in reduced spin-exchange rate (*e.g.*, γ_{SE} = 0.013 ± 0.004 min^{-1}, γ_{SE} = 0.008 ± 0.003 min^{-1}, γ_{SE} = 0.006 ± 0.003 min^{-1}, and γ_{SE} = 0.004 ± 0.001 min^{-1} for the refill numbers 1st, 17th, 69th, and 180th respectively, as calculated from the measured values for γ_{SEOP} and Γ_{Xe}). Indeed, the more-than-doubled build-up rate at the end of the QA study actually occurs as a consequence of the severe limitations on maximum achievable ^{129}Xe polarization in "end-of-lifetime" SEOP cells: In such cases, steady-state $\%P_{Xe}$ can actually be achieved faster, albeit at a lower overall value. This occurs because the increase in HP ^{129}Xe relaxation rate more than compensates for the reduction in the spin exchange rate. Additionally, while higher temperatures may be utilized to mitigate the effects of Rb vapor density suppression in aging SEOP cells where Rb oxidation becomes prevalent, naturally they cannot counteract the increase in ^{129}Xe spin-relaxation rate. Despite these results strongly indicating a decrease in SEOP cell performance and Rb quality, no visible signs of Rb oxidation were observed at the conclusion of the quality assurance study.

In addition to the initial and final states of the SEOP cell, complete results of the QA study are summarized in Fig. 5c, with steady-state ^{129}Xe and Rb polarization values, as well as polarization build-up ($T_b = 1/\gamma_{SEOP}$) and T_1 relaxation times from each Xe gas mixture fill at 70 °C, presented for comparison.

From Fig. 5c, it can first be seen that no significant decrease in steady-state ^{129}Xe polarization was observed during the first 180 total SEOP cell refills, with $\%P_{Xe}$ values of 73.6 ± 4.6% and 72.3 ± 2.3% for the first Xe gas mixture fill and the 180th total fill (the 4th Xe-containing fill), respectively. The 5th Xe gas mixture fill corresponded to the 437th total fill, marking a substantial jump in the total number of refills—256 N_2 refills between Xe gas mixture fills, compared to 110 refills between the previous two Xe runs. This resulted in a small decrease in steady-state ^{129}Xe polarization to $\%P_{Xe}$ = 60.0 ± 1.8%. This change indicates that SEOP cell purity and subsequent SEOP performance began to be negatively impacted at some point between these two experiments (the 180th and 437th fills). This trend appears to continue in a roughly linear fashion, with an additional 256 N_2 refills further reducing the maximum achievable ^{129}Xe polarization to 42.4 ± 1.1%.

When comparing polarization build-up timescales, a small (but within error bars) increase in the exponential build-up time constant T_b was observed after the initial set of N_2 refills, increasing from 42.7 ± 7.0 mins (γ_{SEOP} = 0.023 ± 0.004 min^{-1}) during SEOP performed on the first Xe gas mixture fill to 56.8 ± 8.2 mins (γ_{SEOP} = 0.018 ± 0.003 min^{-1}) when undertaking SEOP in the second Xe gas mixture fill (17th total fill). This result indicates that there is no

appreciable negative effect on maximum achievable ^{129}Xe polarization at this stage, and considering the consistently high T_1 values observed, any increase in build-up time T_b would likely not be attributed to SEOP cell or Rb quality degradation. Indeed, the build-up time constant remained remarkably similar over the third and fourth Xe gas mixture refills: after SEOP in the third (69th total fill), T_b = 56.0 ± 9.4 mins, γ_{SEOP} = 0.018 ± 0.003 min^{-1}, whereas after SEOP in the fourth (180th total fill), T_b = 58.9 ± 5.0 mins, γ_{SEOP} = 0.017 ± 0.001 min^{-1}. Although the computed γ_{SE} values had relatively large error bars due to corresponding error propagation (from T_1 and T_b), the general trend over the first 180 refills was the relative stability of γ_{SE} within the error bars (Fig. 5d). In subsequent Xe gas mixture fills, however, the polarization build-up time constant is substantially reduced, reflecting not an increase in the spin-exchange rate, but in the ^{129}Xe spin destruction rate Γ_{Xe} (=1/T_1); $\gamma_{SEOP} = \gamma_{SE} + \Gamma_{Xe}$. This change is also reflected by the significantly lower maximum achievable ^{129}Xe polarization. Indeed, after SEOP on the sixth and final Xe gas mixture fill (694th total fill), the build-up time constant was further reduced to 18.3 ± 2.0 mins (γ_{SEOP} = 0.055 ± 0.006 min^{-1}), corresponding to a build-up rate that is significantly faster than even the first Xe gas mixture fill where spin-destruction processes were least prevalent. Looking more directly at the ^{129}Xe T_1 relaxation time, it was first observed to decrease gradually with the number of total SEOP cell refills, from 101.8 ± 4.9 mins following the initial fill, to 78.1 ± 1.5 mins after the fourth Xe gas mixture fill (180 total SEOP cell refills). This observation is consistent with slow accumulation of impurities over the course of a large number of refills. The increased T_1 of 99.2 ± 3.5 mins observed in the fifth Xe gas mixture fill (437th total SEOP cell fill) appears to be anomalous with respect to the observations of $\%P_{Xe\ (max)}$ and T_b at this stage of the study. This anomalous appearance may be potentially explained through the increase in γ_{SE} value: 0.011 ± 0.002 mins^{-1} for the 437th refill versus 0.00 4 ± 0.002 mins^{-1} for the180th refill, Fig. 5d and Table 1—the latter can be rationalized as Rb metal quality regeneration due to SEOP cell temperature cycling (see additional evidence provided in the section below). For the sixth and final Xe gas mixture refill, however (694th total SEOP cell fill), a drastic reduction in T_1 was observed: 24.9 ± 4.2 mins (note the large error bars in γ_{SE} on Fig. 5d make γ_{SE} unusable in determination of trend). This explains the marked downturn in maximum achievable ^{129}Xe polarization levels and polarization-build-up times as a result of increased spin-relaxation effects. Results from individual runs are provided in more detail in Table 1.

In addition to the QA study undertaken at Wayne State University (WSU), USA, a second study was conducted using an identical GEN-2 hyperpolarizer device at the University of Nottingham, UK. This study investigated repeatability of ^{129}Xe hyperpolarization in a 1000 Torr Xe/1000 Torr N_2 gas mixture (no ^{4}He fraction present). Unlike the QA study conducted at WSU, all refills in this study were performed using the binary Xe/N_2 gas mixture, with no intermediate re-filling of the SEOP cell using N_2-only gas mixtures. Additionally, SEOP was conducted for thirty minutes only at an oven temperature of 60 °C (meaning $\%P_{Xe}$ values were not necessarily representative of the steady state), which is unfortunately a limitation of this aspect of the study. However, the key aim of this second QA study was not to quantitatively determine the SEOP cells' ultimate polarization, but to provide an additional study of polarizer consistency over the course of a few days versus a few weeks. The results investigating the variation in ^{129}Xe polarization, over back-to-back Xe gas mixture refill and polarization build-up runs, are summarized in Fig. 6.

It can be demonstrated from these results that the ^{129}Xe NMR peak integral, and by extension, ^{129}Xe polarization, varied somewhat between successive refills/SEOP build-up runs (to a degree just above the magnitude of the uncertainty). This likely reflects the fact that steady-state conditions were not achieved after only 30 min of SEOP [61]. However, extrapolation of the linear fit with 95% confidence bounds yields an estimate of 109–452 SEOP cell refills needed to reduce the NMR peak integral to half of its initial value (65.3 a.u.), which is noticeably less than the ~700 SEOP refill lifetime observed in the first pilot QA study at Wayne State University. This discrepancy may be the result of several compounding effects. First, temperature-cycling was performed during SEOP on all cell refills in this second study, which was not the case during the first study at Wayne State University where N_2 substitute was used in many SEOP cell refills. Second, it may also be a consequence of a slight differences in the SEOP cell preparation: *e.g.*, cell coating, Rb quantity: 0.25 g (University of Nottingham) versus 0.5 g (Wayne State University). Therefore, we conclude that in the second pilot QA study the overall qualitative trend of ^{129}Xe NMR peak integral indicates that there was only minimal decrease in performance attributable to the gas mixture refill process, and that useful SEOP cell lifetime was again on the order of several hundred gas mixture refills.

Finally, we comment on the possibility of improving the efficiency of ^{129}Xe SEOP in "dormant" SEOP cells using temperature-cycled regeneration. Following the conclusion of the first GEN-2 hyperpolarizer QA study, the device and SEOP cell were left in a state of non-use for a period of four weeks. The SEOP cell underwent a further two refills with N_2 and one with the same 1000 Torr Xe/900 Torr N_2/100 Torr ^{4}He gas mixture utilized in the QA study (697th total fill), using the same protocol as dictated in Fig. 4. An identical SEOP build-up experiment at 70 °C was conducted on this SEOP cell until steady-state ^{129}Xe polarization conditions were reached. A significant decrease in $\%P_{Xe}$ (42.3 ± 0.6% → 23.4 ± 0.8%) was observed.

Following this step, the SEOP cell underwent two cycles of heating and cooling between ambient temperature and 70 °C for 90 min each, under pump laser illumination at maximum driver current to provide more efficient temperature cycling and also to avoid Rb metal deposition on optical windows. A further series of temperature mapping experiments were then performed at SEOP cell surface temperatures between 60 °C and 71.5 °C, with NMR and IR spectroscopic measurements recorded in identical fashion to the first pilot QA study. The temperature-dependent SEOP build-up map of this final Xe gas mixture fill can be found in Fig. S5. A comparison of ^{129}Xe polarization build-up curves for

Table 1
Summary of SEOP results (P_{Xe}, γ_{SEOP}, P_{Rb}, T_1 and Γ_{SE}) from all six Xe gas mixture refills conducted on the GEN-2 ^{129}Xe hyperpolarizer during the single-SEOP-cell quality assurance study at Wayne State University, Detroit, MI, USA.

Xe fill #	Total fill #	$\%P_{Xe}$ max.	γ_{SEOP} @ max $\%P_{Xe}$ (min^{-1})	$\%P_{Rb}$ @ max $\%P_{Xe}$	T_1 (min)	γ_{SE} (min^{-1})
1	1	73.6 ± 4.6	0.023 ± 0.004	81.7 ± 1.1	101.8 ± 4.9	0.014 ± 0.004
2	17	71.6 ± 4.4	0.018 ± 0.003	78.8 ± 1.2	99.5 ± 6.4	0.008 ± 0.003
3	69	69.4 ± 4.4	0.018 ± 0.003	78.9 ± 1.2	82.6 ± 6.5	0.006 ± 0.004
4	180	72.3 ± 2.3	0.017 ± 0.001	76.7 ± 1.2	78.1 ± 1.5	0.004 ± 0.002
5	437	60.0 ± 1.8	0.021 ± 0.002	83.3 ± 1.5	99.2 ± 3.5	0.011 ± 0.002
6	694	42.4 ± 1.1	0.055 ± 0.006	78.4 ± 1.1	24.9 ± 4.2	0.015 ± 0.013

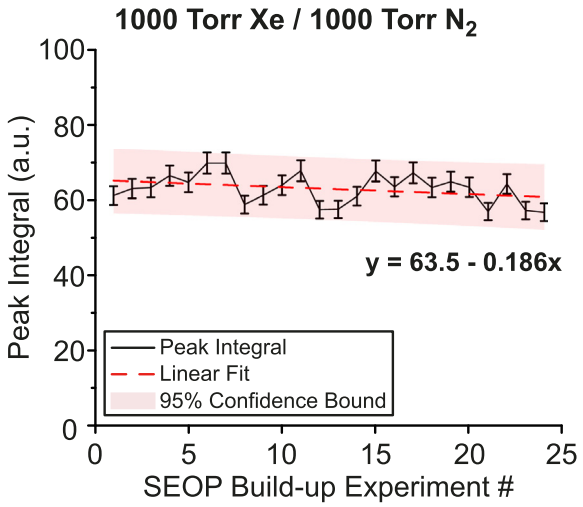


Fig. 6. HP ^{129}Xe NMR signal (arbitrary units, a.u.) recorded after 30 min of polarization build-up of SEOP in a 1000 Torr Xe/1000 Torr N_2 SEOP cell, as a function of number of SEOP cell refills. The shaded region represents a two-sigma (95%) confidence bound on the linear fit (dashed red line). This data was obtained using the second GEN-2 hyperpolarizer at the University of Nottingham, UK.

SEOP at 70 °C following the QA study conclusion (694th total fill), the post-study refills (697th total fill) and thermal regeneration is shown in Fig. 7.

From this data, it can be seen that the process of thermal cycling has the potential to recover a significant fraction of P_{Xe} in "dormant" SEOP cells that have not been used for extended periods of time (*e.g.*, four weeks, as in the present case). Following two cycles of raising and lowering the oven temperature, a steady-state polarization value of $\%P_{Xe}$ = 35.8 ± 1.1% was recorded, a ~1.5-fold increase with respect to the ^{129}Xe polarization observed immediately following the final gas mixture refill. It should be noted that the thermal regeneration process also facilitated a significant increase in polarization build-up rate (γ_{SEOP} = 0.029 ± 0.003 min^{-1} → 0.062 ± 0.008 min^{-1}), while also resulting in no noticeable change in T_1 (all ~25 mins). This increase likely arises as a consequence of better re-distribution of impurities into the bulk of Rb metal pool following temperature-cycling, and subsequent elevation in Rb vapor density (and hence γ_{SE}).

Further regeneration cycles yielded no significant additional benefit in our experiments, indicating that it is likely not possible

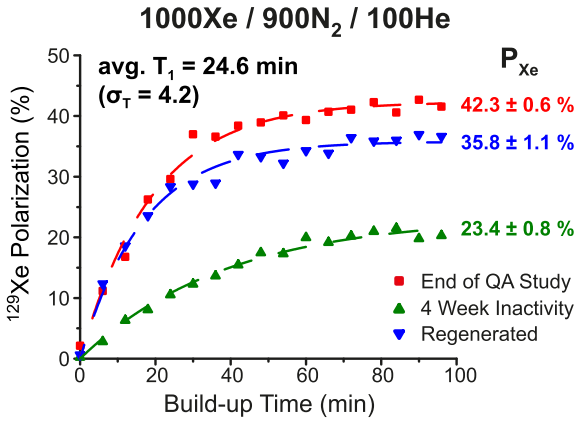


Fig. 7. Comparison of ^{129}Xe polarization build-up during SEOP experiments conducted at the conclusion of the QA study (red), following additional gas mixture refills and a period of experimental inactivity (green) and thermally-cycled SEOP cell regeneration (blue). (For interpretation of the references to colour in this figure legend, the reader is referred to the web version of this article.)

to entirely reverse the consequences of Rb oxidation. However, considering that the cleaning of spent SEOP cells (and the preparation of new ones) is typically a time-intensive and costly exercise [58], any potential options for extending SEOP cell lifetime should be welcome in both biomedical and basic-science applications of HP ^{129}Xe.

4. Conclusions

The results of this first-in-kind quality assurance study demonstrate the high reproducibility of clinical-scale ^{129}Xe hyperpolarization via batch-mode spin-exchange optical pumping using an automated, second-generation (GEN-2) hyperpolarizer across nearly 700 SEOP cell refills. Using high Xe densities (1000 Torr Xe, 2000 Torr total pressure), consistently high levels of ^{129}Xe polarization (avg. $\%P_{Xe}$ = 71.7% with standard deviation σ_P = 1.52%) were observed over the span of the first ~200 gas mixture refills. These consistently high levels of ^{129}Xe polarization were accompanied by correspondingly small variation in build-up rate (avg. γ_{SEOP} = 0.019 min^{-1} with standard deviation σ_γ = 0.003-min^{-1}) and polarization lifetime (avg. T_1 = 90.5 min with standard deviation σ_T = 10.3 min) for the first ~200 gas mixture refills. Reduced (yet still useful) levels of polarization ($\%P_{Xe}$ = 42.3 ± 0.6 %) were observed following a further ~500 gas mixture refills at the conclusion of the study (694 fills in total). When using a second near-identical apparatus performing Xe gas mixture refills only, there was again no significant reduction in the recorded NMR peak integral across 25 total SEOP cell refills. We note that three out of four metrics ($\%P_{Xe}$, γ_{SEOP}, T_1) are indicative quantitative metrics of SEOP cell overall "health" and overall SEOP process performance; however, interestingly $\%P_{Rb}$ provided essentially no indication of reduced cell performance, Fig. 5. For example, at the last SEOP cell fill, the changes in the first three parameters were significantly greater than their corresponding error bars. The fact that $\%P_{Rb}$ does not track reduced cell performance likely reflects the fact that while Rb gas phase concentration (at fixed temperature, *e.g.*, 70 °C) may decrease with cell degradation, Rb *polarization* remains relatively high as the LDA maintains efficient electron excitation of Rb atoms in the gas phase as the Rb vapor electron spin polarization is relatively insensitive to cell degradation processes (and the "photon-to-Rb ratio" may even increase [33]). We have also shown the ability to recover a significant fraction of $\%P_{Xe}$ otherwise lost to cell degradation and dormancy via thermally cycling of SEOP cells to improve optical pumping efficiency. This observation indicates that our methodology of merely refilling the SEOP cell with N_2 without performing heating and cooling (as would be done under normal clinical-scale production) may represent "less harsh" conditions, which is a clear limitation of this study, and should be quantified in further studies. However, these combined observations should prove beneficial in directing further clinical-scale HP ^{129}Xe production studies in the future. The described pilot study is of N = 1 SEOP cells studied at each site, which we hope to expand in the future to more SEOP cells, and also to extend this approach to newer batch-mode clinical-scale hyperpolarizer designs [58].

Associated content

Itemized schematic and bill of materials of the GEN-2 hyperpolarizer gas handling manifold, supplementary QA study results and figures. PDF.

Notes

We dedicate this Article to the memory of Dr. Kirill V. Kovtunov (PhD, 1983-2020), friend, colleague, and mentor. PN, BMG, and EYC declare the stake of ownership in XeUS Technologies, LTD.

Declaration of Competing Interest

The authors declare that they have no known competing financial interests or personal relationships that could have appeared to influence the work reported in this paper.

Acknowledgment

This work was supported by DOD CDMRP under BRP W81XWH-12-1-0159/BC112431, W81XWH-15-1-0271 and W81XWH-15-1-0272. BMG acknowledges a Cottrell SEED grant from Research Corporation for Science Advancement. EVP, KVK, and IVK thank Russian Science Foundation (grant #19-13-00047) for financial support.

Appendix A. Supplementary material

Supplementary data to this article can be found online at https://doi.org/10.1016/j.jmr.2020.106755.

References

[1] B.M. Goodson, N. Whiting, A.M. Coffey, P. Nikolaou, F. Shi, B.M. Gust, M.E. Gemeinhardt, R.V. Shchepin, J.G. Skinner, J.R. Birchall, M.J. Barlow, E.Y. Chekmenev, Hyperpolarization methods for MRS, Emagres 4 (2015) 797–810.
[2] K.V. Kovtunov, E.V. Pokochueva, O.G. Salnikov, S. Cousin, D. Kurzbach, B. Vuichoud, S. Jannin, E.Y. Chekmenev, B.M. Goodson, D.A. Barskiy, I.V. Koptyug, Hyperpolarized NMR: d-DNP, PHIP, and SABRE, Chem. Asian J. 13 (2018) 1857–1871.
[3] P. Nikolaou, B.M. Goodson, E.Y. Chekmenev, NMR hyperpolarization techniques for biomedicine, Chem. Eur. J. 21 (2015) 3156–3166.
[4] J.H. Ardenkjaer-Larsen, B. Fridlund, A. Gram, G. Hansson, L. Hansson, M.H. Lerche, R. Servin, M. Thaning, K. Golman, Increase in signal-to-noise ratio of > 10,000 times in liquid-state NMR, Proc. Natl. Acad. Sci. U. S. A. 100 (2003) 10158–10163.
[5] J. Kurhanewicz, D.B. Vigneron, K. Brindle, E.Y. Chekmenev, A. Comment, C.H. Cunningham, R.J. DeBerardinis, G.G. Green, M.O. Leach, S.S. Rajan, R.R. Rizi, B.D. Ross, W.S. Warren, C.R. Malloy, Analysis of cancer metabolism by imaging hyperpolarized nuclei: prospects for translation to clinical research, Neoplasia 13 (2011) 81–97.
[6] K. Golman, O. Axelsson, H. Johannesson, S. Mansson, C. Olofsson, J.S. Petersson, Parahydrogen-induced polarization in imaging: Subsecond C-13 angiography, Magn. Reson. Med. 46 (2001) 1–5.
[7] E. Johansson, L.E. Olsson, S. Månsson, J.S. Petersson, K. Golman, F. Ståhlberg, R. Wirestam, Perfusion assessment with bolus differentiation: A technique applicable to hyperpolarized tracers, Magn. Reson. Med. 52 (2004) 1043–1051.
[8] K. Golman, R. In't Zandt, M. Thaning, Real-time metabolic imaging, Proc. Natl. Acad. Sci. U. S. A. 103 (2006) 11270–11275.
[9] B.M. Goodson, Nuclear magnetic resonance of laser-polarized noble gases in molecules, materials, and organisms, J. Magn. Reson. 155 (2002) 157–216.
[10] J.P. Mugler, T.A. Altes, Hyperpolarized ^{129}Xe MRI of the human lung, J. Magn. Reson. Imaging 37 (2013) 313–331.
[11] L. Schroder, Xenon for NMR biosensing - Inert but alert, Phys. Medica 29 (2013) 3–16.
[12] C. Witte, L. Schroder, NMR of hyperpolarised probes, NMR Biomed. 26 (2013) 788–802.
[13] D.A. Barskiy, A.M. Coffey, P. Nikolaou, D.M. Mikhaylov, B.M. Goodson, R.T. Branca, G.J. Lu, M.G. Shapiro, V.-V. Telkki, V.V. Zhivonitko, I.V. Koptyug, O.G. Salnikov, K.V. Kovtunov, V.I. Bukhtiyarov, M.S. Rosen, M.J. Barlow, S. Safavi, I.P. Hall, L. Schröder, E.Y. Chekmenev, NMR Hyperpolarization Techniques of Gases, Chem. Eur. J. 23 (2017) 725–751.
[14] K.V. Kovtunov, I.V. Koptyug, M. Fekete, S.B. Duckett, T. Theis, B. Joalland, E.Y. Chekmenev, Parahydrogen-induced Hyperpolarization of Gases, Angew. Chem. Int. Ed. (2020), https://doi.org/10.1002/anie.201915306.
[15] E. Babcock, I. Nelson, S. Kadlecek, B. Driehuys, L.W. Anderson, F.W. Hersman, T. G. Walker, Hybrid spin-exchange optical pumping of He-3, Phys. Rev. Lett. 91 (2003) 4.
[16] I.C. Ruset, L.L. Tsai, R.W. Mair, S. Patz, M.I. Hrovat, M.S. Rosen, I. Muradian, J. Ng, G.P. Topulos, J.P. Butler, R.L. Walsworth, F.W. Hersman, A system for open-access He-3 human lung imaging at very low field, Concept Magnetic Res. B 29B (2006) 210–221.
[17] M.S. Albert, G.D. Cates, B. Driehuys, W. Happer, B. Saam, C.S. Springer, A. Wishnia, Biological magnetic-resonance-imaging using laser polarized Xe-129, Nature 370 (1994) 199–201.
[18] S.S. Kaushik, Z.I. Cleveland, G.P. Cofer, G. Metz, D. Beaver, J. Nouls, M. Kraft, W. Auffermann, J. Wolber, H.P. McAdams, B. Driehuys, Diffusion-weighted hyperpolarized Xe-129 MRI in healthy volunteers and subjects with chronic obstructive pulmonary disease, Magn. Reson. Med. 65 (2011) 1155–1165.
[19] D.M.L. Lilburn, G.E. Pavlovskaya, T. Meersmann, Perspectives of hyperpolarized noble gas MRI beyond ^{3}He, J. Magn. Reson. 229 (2013) 173–186.
[20] T.G. Walker, W. Happer, Spin-exchange optical pumping of noble-gas nuclei, Rev. Mod. Phys. 69 (1997) 629–642.
[21] T.G. Walker, Fundamentals of spin-exchange optical pumping, J. Phys. Conf. Ser. 294 (2011) 012001.
[22] I.C. Ruset, S. Ketel, F.W. Hersman, Optical pumping system design for large production of hyperpolarized Xe-129, Phys. Rev. Lett. 96 (2006) 053002.
[23] B. Driehuys, G.D. Cates, E. Miron, K. Sauer, D.K. Walter, W. Happer, High-volume production of laser-polarized Xe-129, Appl. Phys. Lett. 69 (1996) 1668–1670.
[24] A.L. Zook, B.B. Adhyaru, C.R. Bowers, High capacity production of > 65% spin polarized xenon-129 for NMR spectroscopy and imaging, J. Magn. Reson. 159 (2002) 175–182.
[25] M.S. Freeman, K. Emami, B. Driehuys, Characterizing and modeling the efficiency limits in large-scale production of hyperpolarized ^{129}Xe, Phys. Rev. A 90 (2014) 023406.
[26] D.J. Kennedy, S.J. Seltzer, R. Jiménez-Martínez, H.L. Ring, N.S. Malecek, S. Knappe, E.A. Donley, J. Kitching, V.S. Bajaj, A. Pines, An optimized microfabricated platform for the optical generation and detection of hyperpolarized ^{129}Xe, Sci. Rep. 7 (2017) 43994.
[27] M.S. Rosen, T.E. Chupp, K.P. Coulter, R.C. Welsh, S.D. Swanson, Polarized Xe-129 optical pumping/spin exchange and delivery system for magnetic resonance spectroscopy and imaging studies, Rev. Sci. Instrum. 70 (1999) 1546–1552.
[28] G. Norquay, G.J. Collier, M. Rao, N.J. Stewart, J.M. Wild, ^{129}Xe-Rb spin-exchange optical pumping with high photon efficiency, Phys. Rev. Lett. 121 (2018) 153201.
[29] P. Nikolaou, N. Whiting, N.A. Eschmann, K.E. Chaffee, B.M. Goodson, Generation of laser-polarized xenon using fiber-coupled laser-diode arrays narrowed with integrated volume holographic gratings, J. Magn. Reson. 197 (2009) 249–254.
[30] N. Whiting, P. Nikolaou, N.A. Eschmann, M.J. Barlow, R. Lammert, J. Ungar, W. Hu, L. Vaissie, B.M. Goodson, Using frequency-narrowed, tunable laser diode arrays with integrated volume holographic gratings for spin-exchange optical pumping at high resonant fluxes and xenon densities, Appl. Phys. B-Lasers Opt. 106 (2012) 775–788.
[31] P. Nikolaou, A.M. Coffey, L.L. Walkup, B.M. Gust, N. Whiting, H. Newton, S. Barcus, I. Muradyan, M. Dabaghyan, G.D. Moroz, M. Rosen, S. Patz, M.J. Barlow, E.Y. Chekmenev, B.M. Goodson, Near-unity nuclear polarization with an 'open-source' ^{129}Xe hyperpolarizer for NMR and MRI, Proc. Natl. Acad. Sci. U. S. A. 110 (2013) 14150–14155.
[32] P. Nikolaou, A.M. Coffey, L.L. Walkup, B.M. Gust, N.R. Whiting, H. Newton, I. Muradyan, M. Dabaghyan, K. Ranta, G. Moroz, S. Patz, M.S. Rosen, M.J. Barlow, E.Y. Chekmenev, B.M. Goodson, XeNA: An automated 'open-source' ^{129}Xe hyperpolarizer for clinical use, Magn. Reson. Imaging 32 (2014) 541–550.
[33] J.G. Skinner, K. Ranta, N. Whiting, A.M. Coffey, P. Nikolaou, M.S. Rosen, E.Y. Chekmenev, P.G. Morris, M.J. Barlow, B.M. Goodson, High Xe density, high photon flux, stopped-flow spin-exchange optical pumping: simulations versus experiments, J. Magn. Reson. 312 (2020) 106686.
[34] T. Hughes-Riley, J.S. Six, D.M.L. Lilburn, K.F. Stupic, A.C. Dorkes, D.E. Shaw, G.E. Pavlovskaya, T. Meersmann, Cryogenics free production of hyperpolarized ^{129}Xe and ^{83}Kr for biomedical MRI applications, J. Magn. Reson. 237 (2013) 23–33.
[35] M. He, S.H. Robertson, S.S. Kaushik, M.S. Freeman, R.S. Virgincar, J. Davies, J. Stiles, W.M. Foster, H.P. McAdams, B. Driehuys, Dose and pulse sequence considerations for hyperpolarized ^{129}Xe ventilation MRI, Magn. Reson. Imaging 33 (2015) 877–885.
[36] J.P. Mugler III, B. Driehuys, J.R. Brookeman, G.D. Cates, S.S. Berr, R.G. Bryant, T. M. Daniel, E.E. De Lange, J.H. Downs, C.J. Erickson, W. Happer, D.P. Hinton, N.F. Kassel, T. Maier, C.D. Phillips, B.T. Saam, K.L. Sauer, M.E. Wagshu, MR imaging and spectroscopy using hyperpolarized ^{129}Xe gas: preliminary human results, Magn. Reson. Med. 37 (1997) 809–815.
[37] J.P. Mugler, T.A. Altes, I.C. Ruset, I.M. Dregely, J.F. Mata, G.W. Miller, S. Ketel, J. Ketel, F.W. Hersman, K. Ruppert, Simultaneous magnetic resonance imaging of ventilation distribution and gas uptake in the human lung using hyperpolarized xenon-129, Proc. Natl. Acad. Sci. U. S. A. 107 (2010) 21707–21712.
[38] I. Dregely, I.C. Ruset, J.F. Mata, J. Ketel, S. Ketel, J. Distelbrink, T.A. Altes, J.P. Mugler, G.W. Miller, F.W. Hersman, K. Ruppert, Multiple-Exchange-Time Xenon Polarization Transfer Contrast (MXTC) MRI: initial results in animals and healthy volunteers, Magn. Reson. Med. 67 (2012) 943–953.
[39] S. Patz, F.W. Hersman, I. Muradian, M.I. Hrovat, I.C. Ruset, S. Ketel, F. Jacobson, G.P. Topulos, H. Hatabu, J.P. Butler, Hyperpolarized Xe-129 MRI: A viable functional lung imaging modality?, Eur. J. Radiol. 64 (2007) 335–344.
[40] I. Muradyan, J.P. Butler, M. Dabaghyan, M. Hrovat, I. Dregely, I. Ruset, G.P. Topulos, E. Frederick, H. Hatabu, W.F. Hersman, S. Patz, Single-breath xenon polarization transfer contrast (SB-XTC): Implementation and initial results in healthy humans, J. Magn. Reson. Imaging 37 (2013) 457–470.
[41] M.R. Rao, N.J. Stewart, P.D. Griffiths, G. Norquay, J.M. Wild, Imaging human brain perfusion with inhaled hyperpolarized ^{129}Xe MR imaging, Radiology 286 (2018) 659–665.
[42] S.D. Swanson, M.S. Rosen, B.W. Agranoff, K.P. Coulter, R.C. Welsh, T.E. Chupp, Brain MRI with laser-polarized ^{129}Xe. Magnetic resonance in medicine, Magn. Reson. Med. 38 (1997) 695–698.

[43] B. Driehuys, S. Martinez-Jimenez, Z.I. Cleveland, G.M. Metz, D.M. Beaver, J.C. Nouls, S.S. Kaushik, R. Firszt, C. Willis, K.T. Kelly, J. Wolber, M. Kraft, H.P. McAdams, Chronic Obstructive pulmonary disease: safety and tolerability of hyperpolarized Xe-129 MR imaging in healthy volunteers and patients, Radiology 262 (2012) 279–289.
[44] B. Driehuys, Crossing the chasm(s): demonstrating the clinical value of hyperpolarized Gas MRI, Acad. Radiol. 24 (2017) 1–3.
[45] R.T. Branca, T. He, L. Zhang, C.S. Floyd, M. Freeman, C. White, A. Burant, Detection of brown adipose tissue and thermogenic activity in mice by hyperpolarized xenon MRI, Proc. Natl. Acad. Sci. U. S. A. 111 (2014) 18001–18006.
[46] M.A. Antonacci, C. McHugh, M. Kelley, A. McCallister, S. Degan, R.T. Branca, Direct detection of brown adipose tissue thermogenesis in UCP1−/− mice by hyperpolarized ^{129}Xe MR thermometry, Sci. Rep. 9 (2019) 14865.
[47] C. Witte, V. Martos, H.M. Rose, S. Reinke, S. Klippel, L. Schröder, C.P.R. Hackenberger, Live-cell MRI with Xenon Hyper-CEST Biosensors targeted to metabolically labeled cell-surface Glycans, Angew. Chem. Int. Ed. 54 (2015) 2806–2810.
[48] F.T. Hane, T. Li, P. Smylie, R.M. Pellizzari, J.A. Plata, B. DeBoef, M.S. Albert, In vivo detection of cucurbit[6]uril, a hyperpolarized xenon contrast agent for a xenon magnetic resonance imaging biosensor, Sci. Rep. 7 (2017) 41027.
[49] Y. Wang, B.W. Roose, E.J. Palovcak, V. Carnevale, I.J. Dmochowski, A genetically encoded β-lactamase reporter for ultrasensitive ^{129}Xe NMR in mammalian cells, Angew. Chem. Int. Ed. 55 (2016) 8984–8987.
[50] Y. Wang, I.J. Dmochowski, An expanded palette of Xenon-129 NMR biosensors, Acc. Chem. Res. 49 (2016) 2179–2187.
[51] K. Knagge, J. Prange, D. Raftery, A continuously recirculating optical pumping apparatus for high xenon polarization and surface NMR studies, Chem. Phys. Lett. 397 (2004) 11–16.
[52] K. Knagge, J.R. Smith, L.J. Smith, J. Buriak, D. Raftery, Analysis of porosity in porous silicon using hyperpolarized ^{129}Xe two-dimensional exchange experiments, Solid State Nucl. Magn. Reson. 29 (2006) 85–89.
[53] A.J. Moulé, M.M. Spence, S.-I. Han, J.A. Seeley, K.L. Pierce, S. Saxena, A. Pines, Amplification of xenon NMR and MRI by remote detection, Proc. Natl. Acad. Sci. U. S. A. 100 (2003) 9122–9127.
[54] P. Nikolaou, A.M. Coffey, M.J. Barlow, M. Rosen, B.M. Goodson, E.Y. Chekmenev, Temperature-ramped ^{129}Xe spin exchange optical pumping, Anal. Chem. 86 (2014) 8206–8212.
[55] P. Nikolaou, A.M. Coffey, K. Ranta, L.L. Walkup, B. Gust, M.J. Barlow, M.S. Rosen, B.M. Goodson, E.Y. Chekmenev, Multi-dimensional mapping of spin-exchange optical pumping in clinical-scale batch-mode ^{129}Xe hyperpolarizers, J. Phys. Chem. B 118 (2014) 4809–4816.
[56] P. Nikolaou, A.M. Coffey, L.L. Walkup, B. Gust, C. LaPierre, E. Koehnemann, M.J. Barlow, M.S. Rosen, B.M. Goodson, E.Y. Chekmenev, A 3D-printed high power nuclear spin polarizer, J. Am. Chem. Soc. 136 (2014) 1636–1642.
[57] J.R. Birchall, R.K. Irwin, P. Nikolaou, A.M. Coffey, B.E. Kidd, M. Murphy, M. Molway, L.B. Bales, K. Ranta, M.J. Barlow, B.M. Goodson, M.S. Rosen, E.Y. Chekmenev, XeUS: a second-generation automated 'open-source' batch-mode clinical-scale hyperpolarizer, J. Magn. Reson. (2020) Manuscript submitted for review.
[58] J.R. Birchall, P. Nikolaou, A.M. Coffey, B.E. Kidd, M. Murphy, M. Molway, L.B. Bales, B.M. Goodson, R.K. Irwin, M.J. Barlow, E.Y. Chekmenev, Batch-mode clinical-scale optical hyperpolarization of Xenon-129 using an aluminum jacket with rapid temperature ramping, Anal. Chem. 92 (2019) 4309–4316.
[59] C. Witte, M. Kunth, F. Rossella, L. Schröder, Observing and preventing rubidium runaway in a direct-infusion xenon-spin hyperpolarizer optimized for high-resolution hyper-CEST (chemical exchange saturation transfer using hyperpolarized nuclei) NMR, J. Chem. Phys. 140 (2014) 084203.
[60] M.A. Antonacci, A. Burant, W. Wagner, R.T. Branca, Depolarization of nuclear spin polarized ^{129}Xe gas by dark rubidium during spin-exchange optical pumping, J. Magn. Reson. 279 (2017) 8.
[61] J.R. Birchall, N. Whiting, J.G. Skinner, M.J. Barlow, B.M. Goodson, Using Raman spectroscopy to improve hyperpolarized noble gas production for clinical lung imaging techniques, in: K. Maaz (Ed.), Raman Spectroscopy and Applications, InTechOpen, 2017, pp. 247–268.

ACS EARTH AND SPACE CHEMISTRY

http://pubs.acs.org/journal/aesccq

Letter

Parahydrogen-Induced Magnetization of Jovian Planets?

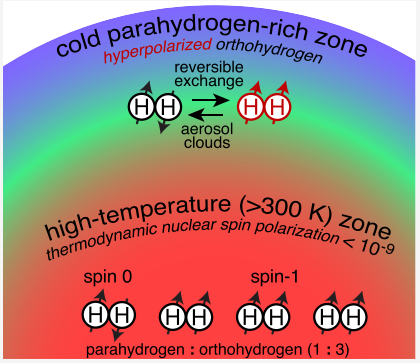
Eduard Y. Chekmenev*

Cite This: *ACS Earth Space Chem.* 2020, 4, 495−498

Read Online

ACCESS | Metrics & More | Article Recommendations | Supporting Information

ABSTRACT: A long-overdue hypothesis on the origin of the magnetic field of Jovian planets is presented. It is proposed that rapid parahydrogen ↔ orthohydrogen exchange catalyzed by aerosol clouds of parahydrogen-rich planetary layers renders a hyperpolarized nuclear spin state of orthohydrogen (and potentially other proton-containing compounds). This enhancement of nuclear spin polarization by several orders of magnitude (termed hyperpolarization) significantly enhances otherwise negligible proton magnetization. It is hypothesized that this persistent exchange process produces planetary magnetism on Jovian planets. This hypothesis builds on recent experimental evidence that parahydrogen exchange may indeed produce hyperpolarized orthohydrogen.



KEYWORDS: *parahydrogen, planetary magnetism, Jovian planet, hyperpolarization, nuclear spin, hydrogen, exchange, Uranus*

Downloaded via WAYNE STATE UNIV on June 9, 2020 at 03:31:08 (UTC).
See https://pubs.acs.org/sharingguidelines for options on how to legitimately share published articles.

All Jovian planets possess a magnetic field, and their magnetic fields are so large that these fields dominate the weather of the planet, their moons, and beyond.[1] Jupiter's magnetic moment is estimated to be approximately 20 000 times greater than that of the Earth. The existence of Jupiter's magnetic field was first predicted by the observations of a variable radio source[2] and verified later by the Pioneer 10 space probe in 1973. The origin of a magnetic field of Jupiter and other Jovian planets remains unconfirmed to this day. Shortly after the discovery of magnetism of Jovian planets, the hypothesis of an electrically conductive metallic hydrogen planetary core was introduced on the basis of the prior theoretical predictions (ca. 1935) of metallic hydrogen modifications at ultrahigh pressures.[3] According to this theory, the magnetic field of Jovian planets is created by the electric currents of the planetary metallic core composed of compressed hydrogen. Although several experimental studies have reported the creation of metallic hydrogen on a subsecond time scale,[4,5] these reports are disputed and the experimental results have not been reproduced by other laboratories, thereby raising some concerns about the validity of the metallic hydrogen existence in Jovian planets.

The lack of experimental validation is not the only challenge for the metallic hydrogen theory. Some smaller Jovian planets (e.g., Neptune and Uranus) cannot generate sufficiently high pressures to theoretically create the metallic hydrogen inside the planetary core. As a result of this fundamental theoretical gap, the variant of dynamo theory was proposed for smaller Jovian planets, where a combination of ammonia, methane, and water is responsible for generating electrically conductive planetary layers.[1,6] However, to the best of my knowledge, there has been no experimental evidence for creating strong electrical conductivity in such mixtures. Moreover, any dynamo theories fall short of explaining the large tilt of the magnetic field axis with respect to the rotation axis of Neptune and Uranus by approximately 47° and 59°, respectively.[1] Furthermore, recent flybys' magnetic analysis of Jovian planets clearly shows a very complex multipolar (i.e., quadrupolar and octapolar) structure of the magnetosphere of Neptune and Uranus[7,8] and more recently of Jupiter,[9,10] which is inconsistent with the expectation of a predominant dipolar structure predicted by the convectional planetary dynamo theory.

A magnetic field can be generally created in two ways. The moving electric charge is the first mechanism for inducing planetary magnetism. The second common source of the permanent magnetism is planetary components themselves. The key striking characteristic of all Jovian planets is their high content (90% or more) of hydrogen. Molecular dihydrogen dominates their upper planetary layers. The dihydrogen molecule exists in two spin isomer forms: parahydrogen (nuclear singlet, spin 0) and orthohydrogen (nuclear triplet, spin 1).[11] In the high-temperature limit, the equilibrium ratio of the two isomers is 1:3. Parahydrogen is the lower energy spin isomer. As a result, at low temperatures, the equilibrium shifts to the para state. In 1986, Bowers and Weitekamp demonstrated that the symmetry of the parahydrogen singlet can be revealed as a large nuclear spin magnetization in the non-symmetric hydrogenation

Received: December 24, 2019
Revised: February 21, 2020
Accepted: March 9, 2020
Published: March 18, 2020



ACS Publications

© 2020 American Chemical Society

product of parahydrogen and unsaturated compounds through chemical symmetry breaking of the parahydrogen nuclear singlet.[12] As a result, nuclear spins gain a high degree of polarization, i.e., degree of alignment of nuclear spins. Consequently, these highly polarized nuclear spin states are called hyperpolarized. The parahydrogen-derived nuclear spin polarization can reach the order of unity, and these highly magnetized non-equilibrium spin states are employed in nuclear magnetic resonance (NMR) spectroscopy and magnetic resonance imaging (MRI) as a source of significant (by orders of magnitude) signal enhancement.[13,14] This magnetic resonance hyperpolarization technique has been called parahydrogen-induced polarization (PHIP),[15] signifying that it is the NMR-silent parahydrogen state that can in fact serve as a source of massive nuclear spin hyperpolarization. In 2009, the non-hydrogenative variant of PHIP was introduced.[16] This relatively new technique [called signal amplification by reversible exchange (SABRE)] employs parahydrogen exchange for nuclear spin hyperpolarization of small molecules.[16] The dihydrogen molecule is not chemically depleted in the SABRE process; instead, it is released in the form of hyperpolarized orthohydrogen.[17−19] This finding[17] does not yet have practical implications for the field of MRI and NMR applications but can have immense implications for planetary science, because it shows that the interconversion of the two spin isomers (parahydrogen and orthohydrogen) can lead to production of hyperpolarized nuclear spins in orthohydrogen. Unlike parahydrogen (spin 0), orthohydrogen (spin 1) possesses net magnetic moment, and therefore, hyperpolarized orthohydrogen molecules may produce large magnetization (especially on the planetary scale, as discussed here), with the overall value being the sum of all hyperpolarized dipoles. It should be made abundantly clear that proton spin polarization at thermodynamic equilibrium is negligible (and, thus, commonly discarded), e.g., less than 10^{-9} at the Earth's magnetic field (ca. 50 μT) and 77 K.

The spontaneous interconversion between orthohydrogen and parahydrogen is an extremely slow process; i.e., equilibration time for pure H_2 is $\sim 10^8$ s, because this is a forbidden transition.[11] However, the interconversion process can be accelerated by a wide range of catalysts.[11,13] In all Jovian planets, the para-/orthohydrogen ratio is 1:3 in high-temperature (>300 K) zones[20,21] corresponding to thermodynamic nuclear spin polarization of protons.[13] In colder layers, catalysis by aerosols consisting of NH_3, CH_4, H_2S, and other compounds renders the para-/orthohydrogen ratio in accordance with thermodynamic equilibrium,[20] which otherwise (i.e., in the absence of such catalysis) would be close to that of the high-temperature limit of 1:3 as a result of efficient mixing of colder and hot planetary zones on the time scale significantly shorter than the spontaneous process of para-/orthohydrogen conversion.[21] Although departures from thermodynamic equilibrium of the para-/orthohydrogen ratio exist in the Jovian planets,[22] the areas of thermodynamically equilibrated para-/orthohydrogen have been linked to ammonia-rich clouds,[20,23] indicating that aerosol-based catalysis plays a crucial role in para-/orthohydrogen interconversion. Moreover, of all Jovian planets, the para-/orthohydrogen ratio of Uranus is the most thermodynamically equilibrated,[24] and the magnetosphere of Uranus is the most "anomalous"; i.e., (i) the magnetic field axis has the largest tilt from the rotation axis, (ii) the magnetic field at the equator of ~23 μT is greater than that of two other heavier Jovian planets, Saturn (~6.6-fold greater mass) at ~22 μT and Neptune (~1.2-fold greater mass) at ~13 μT, and (iii) the magnetic field has the highest asymmetry, e.g., ~10 μT strength at the South pole, ~110 μT at the North pole, etc.,[25] indicating that fast interconversion of para- and orthohydrogen may be an important factor influencing the magnetosphere of Jovian planets.

Here, it is hypothesized that these parahydrogen-rich layers in the troposphere can undergo a sufficiently fast parahydrogen ↔ orthohydrogen exchange process catalyzed by aerosols rendering a persistent existence of hyperpolarized proton nuclei in orthohydrogen (and potentially other more dilute proton-containing compounds). I note that, although atmosphere of Jovian planets consists of many layers, it is the troposphere, i.e., the lower layer, that is important in the context of the hyperpolarization process discussed here, because troposphere layers have a low temperature; for example, the Uranus troposphere (ca. 350 km thick) has temperature ranging from 50 to 120 K, and the troposphere of Jovian planets accounts for most of their atmospheric mass balance. Nuclear spin hyperpolarization of orthohydrogen protons is induced by cooling of dihydrogen gas, which forms a parahydrogen-rich mixture acting as the fundamental source of hyperpolarization (Figure 1). The

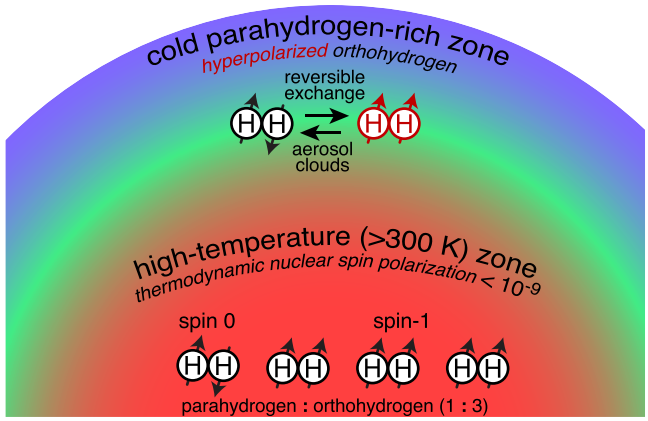


Figure 1. Overall schematic of dihydrogen nuclear spin polarization. The high-temperature (>300 K) zone exhibits a high-temperature thermodynamic distribution of para- and orthohydrogen (1:3) corresponding to thermodynamic nuclear spin polarization of protons, i.e., $<10^{-9}$.[13] In the colder zone in troposphere layers, chemical exchange between para- and orthohydrogen (on aerosol clouds) results in (i) thermodynamic equilibrium of the para-/orthohydrogen ratio (corresponding to a parahydrogen-rich condition, e.g., 50% para at 77 K) and (ii) non-thermodynamic nuclear spin polarization of orthohydrogen corresponding to the hyperpolarized nuclear spin state of orthohydrogen.[17]

excess of parahydrogen at a low temperature (well above the thermodynamic 1:3 equilibrium distribution at the high-temperature limit; Figure 2b) leads to production of hyperpolarized orthohydrogen (Figure 2a). Hyperpolarization of orthohydrogen protons leads to enhanced net magnetization, which generates a fraction or the entire static magnetism of Jovian planets. Note that nuclear spin relaxation may lead to depolarization of hyperpolarized orthohydrogen to thermally polarized hydrogen, and the corresponding relaxation rate (k_3) must not be significantly larger than the back conversion rate (k_2) of orthohydrogen to parahydrogen (Figure 2a). In other words, the parahydrogen ↔ orthohydrogen exchange rate must be significantly greater than the relaxation rate of the hyperpolarized state. Although it is the parahydrogen singlet

https://dx.doi.org/10.1021/acsearthspacechem.9b00326
ACS Earth Space Chem. 2020, 4, 495−498

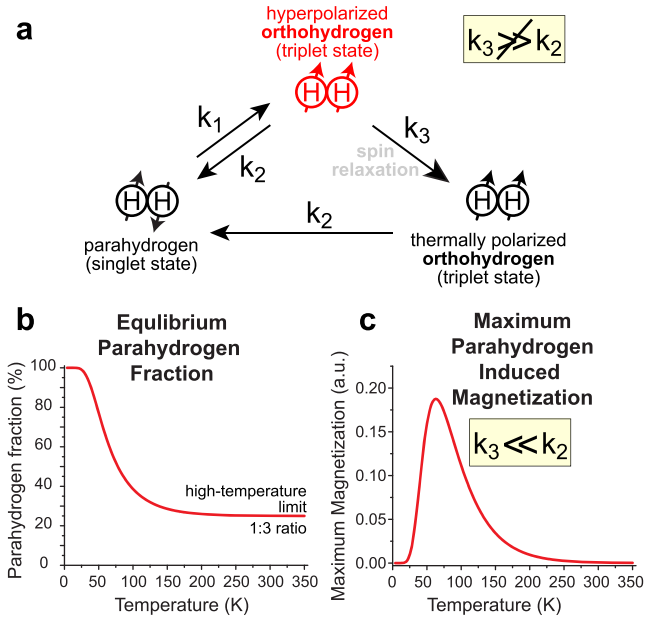


Figure 2. (a) Schematic of dihydrogen transformation as a result of the rapid parahydrogen ↔ orthohydrogen exchange process catalyzed by aerosols and nuclear spin relaxation. Hyperpolarized orthohydrogen is created as a result of spin conversion from parahydrogen. The produced hyperpolarized state may undergo a relaxation process, resulting in parahydrogen-induced magnetization depletion. The corresponding relaxation rate (k_3) of the hyperpolarized state must not be significantly greater than the rate of orthohydrogen conversion to parahydrogen (k_2); otherwise, the level of parahydrogen-induced magnetization will be significantly reduced. (b) Equilibrium parahydrogen percentage fraction (χ) as a function of the temperature. (c) Maximum fractional parahydrogen-induced magnetization [defined as $(\chi - 25\%)(100\% - \chi)/75\%/100\%$] as a function of the temperature under conditions of $k_3 \ll k_2$.

state that provides the source of nuclear spin polarization in this model, parahydrogen itself is not magnetized and it is hyperpolarized orthohydrogen that acts as a carrier of magnetization. As a result, the maximum fractional magnetization dependence upon the temperature (Figure 2c) exhibits a clear maximum at ∼63 K. The quantity of dihydrogen in all Jovian planets is certainly large enough to generate a sufficient quantity of hyperpolarized protons to account for a fraction or the entire planetary magnetism (see the Supporting Information for details).

The key strength of the proposed hypothesis is the possibility to explain the complex magnetic field structure of Jovian planets, because it is likely modulated by the heterogeneously distributed catalytic aerosols. Unlike many other theories, the proposed hypothesis can be potentially readily tested by probing the troposphere of a Jovian planet by NMR spectroscopy during future flyby missions.

The described hypothesis here will clearly benefit from future quantitative modeling, which will likely require the development of a new kind of nuclear magnetic spin physics to describe nuclear spin dynamics on the planetary scale.

■ ASSOCIATED CONTENT

Supporting Information

The Supporting Information is available free of charge at https://pubs.acs.org/doi/10.1021/acsearthspacechem.9b00326.

Computation of planetary magnetic moments as a result of nuclear spin polarization (Table S1) (PDF)

■ AUTHOR INFORMATION

Corresponding Author

Eduard Y. Chekmenev − *Department of Chemistry, Integrative Biosciences (Ibio), Karmanos Cancer Institute (KCI), Wayne State University, Detroit, Michigan 48202, United States; Russian Academy of Sciences, 119991 Moscow, Russia;* orcid.org/0000-0002-8745-8801; Email: chekmenev@wayne.edu

Complete contact information is available at: https://pubs.acs.org/10.1021/acsearthspacechem.9b00326

Notes

The author declares no competing financial interest.

■ ACKNOWLEDGMENTS

The author thanks the National Science Foundation (NSF) under Grants CHE-1836308 and CHE-1904780, the National Cancer Institute under 1R21CA220137 and 1U01CA202229, and the Department of Defense (DOD) Congressionally Directed Medical Research Programs (CDMRP) under W81XWH-12-1-0159/BC112431 and W81XWH-15-1-0271 for funding sources. The author thanks Dr. Panayiotis Nikolaou for proofreading the manuscript.

■ REFERENCES

(1) Kivelson, M. G.; Bagenal, F. Planetary Magnetospheres. In *Encyclopedia of the Solar System*, 2nd ed.; McFadden, L.-A., Johnson, T., Weissman, P., Eds.; Academic Press: Cambridge, MA, 2007; Chapter 28, pp 519−540, DOI: 10.1016/B978-012088589-3/50032-3.

(2) Burke, B. F.; Franklin, K. L. Observations of a variable radio source associated with the planet Jupiter. *J. Geophys. Res.* **1955**, *60* (2), 213−217.

(3) Wigner, E.; Huntington, H. B. On the Possibility of a Metallic Modification of Hydrogen. *J. Chem. Phys.* **1935**, *3* (12), 764−770.

(4) Dias, R. P.; Silvera, I. F. Observation of the Wigner-Huntington transition to metallic hydrogen. *Science* **2017**, *355* (6326), 715−718.

(5) Zaghoo, M.; Salamat, A.; Silvera, I. F. Evidence of a first-order phase transition to metallic hydrogen. *Phys. Rev. B: Condens. Matter Mater. Phys.* **2016**, *93* (15), 155128.

(6) Stanley, S.; Bloxham, J. Convective-region geometry as the cause of Uranus' and Neptune's unusual magnetic fields. *Nature* **2004**, *428* (6979), 151−153.

(7) Stanley, S.; Bloxham, J. Numerical dynamo models of Uranus' and Neptune's magnetic fields. *Icarus* **2006**, *184* (2), 556−572.

(8) Stanley, S.; Bloxham, J. On the secular variation of Saturn's magnetic field. *Phys. Earth Planet. Inter.* **2016**, *250*, 31−34.

(9) Moore, K. M.; Yadav, R. K.; Kulowski, L.; Cao, H.; Bloxham, J.; Connerney, J. E. P.; Kotsiaros, S.; Jørgensen, J. L.; Merayo, J. M. G.; Stevenson, D. J.; Bolton, S. J.; Levin, S. M. A complex dynamo inferred from the hemispheric dichotomy of Jupiter's magnetic field. *Nature* **2018**, *561* (7721), 76−78.

(10) Connerney, J. E. P.; Adriani, A.; Allegrini, F.; Bagenal, F.; Bolton, S. J.; Bonfond, B.; Cowley, S. W. H.; Gerard, J.-C.; Gladstone, G. R.; Grodent, D.; Hospodarsky, G.; Jorgensen, J. L.; Kurth, W. S.; Levin, S. M.; Mauk, B.; McComas, D. J.; Mura, A.; Paranicas, C.; Smith, E. J.; Thorne, R. M.; Valek, P.; Waite, J. Jupiter's magnetosphere and aurorae observed by the Juno spacecraft during its first polar orbits. *Science* **2017**, *356* (6340), 826−832.

(11) Farkas, A. *Orthohydrogen, Parahydrogen, and Heavy Hydrogen*; Cambridge University Press: Cambridge, U.K., 1935.

(12) Bowers, C. R.; Weitekamp, D. P. Transformation of Symmetrization Order to Nuclear-Spin Magnetization by Chemical-

Reaction and Nuclear-Magnetic-Resonance. *Phys. Rev. Lett.* **1986**, *57* (21), 2645−2648.
(13) Hövener, J.-B.; Pravdivtsev, A. N.; Kidd, B.; Bowers, C. R.; Glöggler, S.; Kovtunov, K. V.; Plaumann, M.; Katz-Brull, R.; Buckenmaier, K.; Jerschow, A.; Reineri, F.; Theis, T.; Shchepin, R. V.; Wagner, S.; Bhattacharya, P.; Zacharias, N. M.; Chekmenev, E. Y. Parahydrogen-based Hyperpolarization for Biomedicine. *Angew. Chem., Int. Ed.* **2018**, *57* (35), 11140−11162.
(14) Golman, K.; Axelsson, O.; Johannesson, H.; Mansson, S.; Olofsson, C.; Petersson, J. S. Parahydrogen-induced polarization in imaging: Subsecond C-13 angiography. *Magn. Reson. Med.* **2001**, *46* (1), 1−5.
(15) Eisenschmid, T. C.; Kirss, R. U.; Deutsch, P. P.; Hommeltoft, S. I.; Eisenberg, R.; Bargon, J.; Lawler, R. G.; Balch, A. L. Para Hydrogen Induced Polarization In Hydrogenation Reactions. *J. Am. Chem. Soc.* **1987**, *109* (26), 8089−8091.
(16) Adams, R. W.; Aguilar, J. A.; Atkinson, K. D.; Cowley, M. J.; Elliott, P. I. P.; Duckett, S. B.; Green, G. G. R.; Khazal, I. G.; Lopez-Serrano, J.; Williamson, D. C. Reversible Interactions with para-Hydrogen Enhance NMR Sensitivity by Polarization Transfer. *Science* **2009**, *323* (5922), 1708−1711.
(17) Barskiy, D. A.; Kovtunov, K. V.; Koptyug, I. V.; He, P.; Groome, K. A.; Best, Q. A.; Shi, F.; Goodson, B. M.; Shchepin, R. V.; Coffey, A. M.; Waddell, K. W.; Chekmenev, E. Y. The feasibility of formation and kinetics of NMR Signal Amplification by Reversible Exchange (SABRE) at high magnetic field (9.4 T). *J. Am. Chem. Soc.* **2014**, *136* (9), 3322−3325.
(18) Gloggler, S.; Muller, R.; Colell, J.; Emondts, M.; Dabrowski, M.; Blumich, B.; Appelt, S. Para-hydrogen induced polarization of amino acids, peptides and deuterium-hydrogen gas. *Phys. Chem. Chem. Phys.* **2011**, *13* (30), 13759−13764.
(19) Truong, M. L.; Theis, T.; Coffey, A. M.; Shchepin, R. V.; Waddell, K. W.; Shi, F.; Goodson, B. M.; Warren, W. S.; Chekmenev, E. Y. ^{15}N Hyperpolarization By Reversible Exchange Using SABRE-SHEATH. *J. Phys. Chem. C* **2015**, *119* (16), 8786−8797.
(20) Massie, S. T.; Hunten, D. M. Conversion of para and ortho hydrogen in the Jovian planets. *Icarus* **1982**, *49* (2), 213−226.
(21) Smith, W. H. On the ortho-para equilibrium of H_2 in the atmospheres of the Jovian planets. *Icarus* **1978**, *33* (1), 210−216.
(22) Conrath, B. J.; Gierasch, P. J.; Ustinov, E. A. Thermal Structure and Para Hydrogen Fraction on the Outer Planets from Voyager IRIS Measurements. *Icarus* **1998**, *135* (2), 501−517.
(23) Carlson, B. E.; Lacis, A. A.; Rossow, W. B. Ortho-para-hydrogen Equlibration on Jupiter. *Astrophys. J.* **1992**, *393* (1), 357−372.
(24) Fouchet, T.; Lellouch, E.; Feuchtgruber, H. The hydrogen ortho-to-para ratio in the stratospheres of the giant planets. *Icarus* **2003**, *161* (1), 127−143.
(25) Ness, N. F.; Acuna, M. H.; Behannon, K. W.; Burlaga, L. F.; Connerney, J. E. P.; Lepping, R. P.; Neubauer, F. M. Magnetic Fields at Uranus. *Science* **1986**, *233* (4759), 85−89.

https://dx.doi.org/10.1021/acsearthspacechem.9b00326
ACS Earth Space Chem. 2020, 4, 495−498

Journal of Magnetic Resonance 315 (2020) 106739

Contents lists available at ScienceDirect

Journal of Magnetic Resonance

journal homepage: www.elsevier.com/locate/jmr

Helium-rich mixtures for improved batch-mode clinical-scale spin-exchange optical pumping of Xenon-129

Jonathan R. Birchall [a], Panayiotis Nikolaou [b], Robert K. Irwin [c], Michael J. Barlow [c], Kaili Ranta [d], Aaron M. Coffey [e], Boyd M. Goodson [d,f], Ekaterina V. Pokochueva [g,h], Kirill V. Kovtunov [g,h], Igor V. Koptyug [g,h], Eduard Y. Chekmenev [a,i,*]

[a] Department of Chemistry, Integrative Biosciences (Ibio), Wayne State University, Karmanos Cancer Institute (KCI), 5101 Cass Ave, Detroit, MI 48202, United States
[b] XeUS Technologies, G. Karaiskaki 2A, P. Lakatamia, Nicosia 2312, Cyprus
[c] Sir Peter Mansfield Imaging Centre, University of Nottingham, Nottingham NG7 2RD, United Kingdom
[d] Department of Chemistry and Biochemistry, Southern Illinois University, 1245 Lincoln Drive, Carbondale, IL 62901, United States
[e] Department of Radiology, Vanderbilt University Institute of Imaging Science (VUIIS), 1161 21st Ave South, Nashville, TN 37232, United States
[f] Materials Technology Center, Southern Illinois University, 1245 Lincoln Drive, Carbondale, IL 62901, United States
[g] International Tomography Center SB RAS, Institutskaya Street 3A, Novosibirsk 630090, Russia
[h] Novosibirsk State University, Pirogova Street 2, Novosibirsk 630090, Russia
[i] Russian Academy of Sciences, Leninskiy Prospekt 14, Moscow 119991, Russia

ARTICLE INFO

Article history:
Received 21 April 2020
Accepted 24 April 2020
Available online 30 April 2020

Keywords:
Hyperpolarization
Xenon-129
Spin exchange optical pumping
Batch-mode hyperpolarizer

ABSTRACT

We present studies of spin-exchange optical pumping (SEOP) using ternary xenon-nitrogen-helium gas mixtures at high xenon partial pressures (up to 1330 Torr partial pressure at loading, out of 2660 Torr total pressure) in a 500-mL volume SEOP cell, using two automated batch-mode clinical-scale ^{129}Xe hyperpolarizers operating under continuous high-power (~170 W) pump laser irradiation. In this pilot study, we explore SEOP in gas mixtures with up to 45% ^{4}He content under a wide range of experimental conditions. When an aluminum jacket cooling/heating design was employed (GEN-3 hyperpolarizer), ^{129}Xe polarization ($\%P_{Xe}$) of 55.9 ± 0.9% was observed with mono-exponential build-up rate γ_{SEOP} of 0.049 ± 0.001 min^{-1} for the ^{4}He-rich mixture (1000 Torr Xe/900 Torr He, 100 Torr N_2), compared to $\%P_{Xe}$ of 49.3 ± 3.3% at γ_{SEOP} of 0.035 ± 0.004 min^{-1} for the N_2-rich gas mixture (1000 Torr Xe/100 Torr He, 900 Torr N_2). When forced-air cooling/heating was used (GEN-2 hyperpolarizer), $\%P_{Xe}$ of 83.9 ± 2.7% was observed at γ_{SEOP} of 0.045 ± 0.005 min^{-1} for the ^{4}He-rich mixture (1000 Torr Xe/900 Torr He, 100 Torr N_2), compared to $\%P_{Xe}$ of 73.5 ± 1.3% at γ_{SEOP} of 0.028 ± 0.001 min^{-1} for the N_2-rich gas mixture (1000 Torr Xe and 1000 Torr N_2). Additionally, $\%P_{Xe}$ of 72.6 ± 1.4% was observed at a build-up rate γ_{SEOP} of 0.041 ± 0.003 min^{-1} for a super-high-density ^{4}He-rich mixture (1330 Torr Xe/1200 Torr ^{4}He/130 Torr N_2), compared to $\%P_{Xe}$ = 56.6 ± 1.3% at a build-up rate of γ_{SEOP} of 0.034 ± 0.002 min^{-1} for an N_2-rich mixture (1330 Torr Xe/1330 Torr N_2) using forced air cooling/heating. The observed SEOP hyperpolarization performance under these conditions corresponds to $\%P_{Xe}$ improvement by a factor of 1.14 ± 0.04 at 1000 Torr Xe density and by up to a factor of 1.28 ± 0.04 at 1330 Torr Xe density at improved SEOP build-up rates by factors of 1.61 ± 0.18 and 1.21 ± 0.11 respectively. Record $\%P_{Xe}$ levels have been obtained here: 83.9 ± 2.7% at 1000 Torr Xe partial pressure and 72.6 ± 1.4% at 1330 Torr Xe partial pressure. In addition to improved thermal stability for SEOP, the use of ^{4}He-rich gas mixtures also reduces the overall density of produced inhalable HP contrast agents; this property may be desirable for HP ^{129}Xe inhalation by human subjects in clinical settings—especially in populations with heavily impaired lung function. The described approach should enjoy ready application in the production of inhalable ^{129}Xe contrast agent with near-unity ^{129}Xe nuclear spin polarization.

© 2020 Elsevier Inc. All rights reserved.

1. Introduction

NMR hyperpolarization can be used to increase the net nuclear spin polarization (P) of nuclear spins far beyond thermal equilibrium levels [1–3], even approaching unity in some cases [4]. This

* Corresponding author at: Department of Chemistry, Integrative Biosciences (Ibio), Wayne State University, Karmanos Cancer Institute (KCI), 5101 Cass Ave, Detroit, MI 48202, United States.
E-mail address: chekmenev@wayne.edu (E.Y. Chekmenev).

https://doi.org/10.1016/j.jmr.2020.106739
1090-7807/© 2020 Elsevier Inc. All rights reserved.

vast increase in available magnetization results in substantially improved signal-to-noise ratio (SNR) and facilitates structural and functional Magnetic Resonance Imaging (MRI) of nuclear spins with otherwise inherently low thermal polarization [5,6]. Target nuclei for hyperpolarization are frequently prepared for ultimate use either in a liquid state (e.g., utilizing a bolus injection of a biocompatible molecule, such as spin-labeled [1-^{13}C]-pyruvate [7–11] or [$^{15}N_3$]-metronidazole [12]), or in a gaseous state (utilizing inhalation of a non-reactive noble gas, such as ^{3}He [13–15], ^{83}Kr [16], and ^{129}Xe [17,18]). These approaches open the way for a swath of applications in the field of biomedical imaging, from characterization of metabolic pathways [11,19], to monitoring respiratory function [5,20–27].

^{129}Xe hyperpolarization is typically performed using spin-exchange optical pumping (SEOP) in the gaseous phase [28,29]. In this two-stage process, circularly polarized "pump" laser photons are used to first transfer spin angular momentum to rubidium electrons (optical pumping), followed by transfer of this accumulated electron spin angular momentum to ^{129}Xe nuclei via Fermi contact interactions (spin exchange) [28]. A nitrogen (N_2) buffer gas performs collisional quenching of the excited Rb electrons, minimizing radiative spin relaxation from absorption of spontaneously emitted omnidirectional photons (fluorescence) [30,31]. Varying the composition of this binary $^{129}Xe/N_2$ gas mixture greatly affects the dynamics of the process, such as maximum achievable ^{129}Xe polarization ($\%P_{Xe}$), rates of polarization build-up (γ_{SEOP}) and decay ($1/T_1$), and even how the desired end product of hyperpolarized (HP) ^{129}Xe is collected—such as in the case of batch-mode versus continuous-flow production modalities [30,32–36].

In addition to nitrogen, helium has also seen wide use in SEOP as a buffer gas (particularly in continuous-flow setups) [30], acting to pressure broaden the Rb D_1 absorption profile and thereby increase the proportion of laser photons able to successfully induce optical pumping [37,38]. In such cases, ^{4}He is chosen because it has a much lower collisional spin destruction (*i.e.*, spin-depolarization) rate compared to N_2 and Xe [39–42]. With recent advancements in pump laser technology such as high-power, frequency-narrowed laser diode arrays (LDAs) [4,43–47], inclusion of helium in the gas mixture for this purpose has become increasingly redundant. Despite this trend, helium still possesses a substantially higher thermal conductivity (~17.77 * 10^{-2} W m^{-1} K^{-1}) than either nitrogen (~3.09 * 10^{-2} W m^{-1} K^{-11}) or xenon (~0.70 * 10^{-2} W m^{-1} K^{-1}) [48], in principle resulting in gas mixtures that are significantly more stable to thermal fluctuations, with minimal impact on radiation trapping efficiency (provided sufficient N_2 is still present—typically ~100–200 Torr partial pressure) [31]. This property could potentially prove useful in mitigating the effects of temperature-induced alkali metal "runaway", which otherwise can become especially prevalent at high pump laser powers typically utilized in modern SEOP experiments [32,49–51].

Both continuous-flow and batch-mode hyperpolarization approaches have their own respective advantages. In continuous-flow SEOP, the employed mixture of Xe is usually very dilute, necessitating that the produced HP ^{129}Xe be pre-concentrated via cryo-collection. Once thawed, the concentrated HP gas can then be administered via inhalation [18]. However, because Xe is a heavy gas with anesthetic properties, concerns exist about safety and tolerability of pure HP ^{129}Xe inhalation—indeed, a number of studies focused on this aspect of HP ^{129}Xe imaging technology [18,52,53]. One approach to mitigate potential challenges associated with inhalation of dense Xe gas is to dilute it with other lighter buffer gases. The disadvantage of HP contrast gas dilution is the reduction of the HP ^{129}Xe concentration, which ultimately decreases the usable MRI scan signal obtained. In batch-mode (or stopped-flow) SEOP, the mixture of ^{129}Xe and other buffering gases is hyperpolarized at elevated pressure first (*e.g.*, ~3 atm), and typically higher ^{129}Xe polarization is obtained at lower ^{129}Xe densities. Once the SEOP process is completed, the resulting mixture is simply expanded into a temporary storage Tedlar bag without the use of cryo-collection [4,54] (representing a potential translational advantage over continuous-flow SEOP). To achieve low density of HP ^{129}Xe in the final mixture stored in the Tedlar bag, two approaches can be envisioned. In one approach, the produced HP mixture can be diluted with buffering gases to reduce the overall density and enhance inhalation tolerability by the subjects after the SEOP process (*e.g.*, from 50% Xe concentration to Xe 25% concentration by two-fold dilution) after the SEOP process for example using light ^{4}He gas. For example, batch-mode SEOP has been previously shown to yield a typical maximum value of 60 ± 4% using 1000 Torr Xe mixture (total SEOP cell pressure of 2000 Torr). A hypothetical two-fold dilution of such a mixture by ^{4}He gas after gas ejection from the hyperpolarizer would therefore yield 25% Xe content in the Tedlar bag. In the second approach, the Xe-containing gas mixture can be diluted before to the process of batch-mode SEOP hyperpolarization. Gas mixture dilution before performing SEOP renders nominally higher $\%P_{Xe}$ achieved in the batch-mode SEOP process, because leaner Xe mixtures have been demonstrated to produce higher $\%P_{Xe}$ previously [4,35], *e.g.*, the gas mixture containing 500 Torr Xe partial pressure (in the SEOP cell with 2000 Torr pressure) yielded 73 ± 4% versus 60 ± 4% in gas mixture 1000 Torr Xe partial pressure (in the SEOP cell with 2000 Torr pressure) [35]. If the target Xe fraction is 25% in the gas mixture after ejection from the hyperpolarizer device, the use of a diluted Xe mixture (*i.e.*, second approach with 500 Torr Xe in 2000 Torr total pressure) for SEOP would therefore yield higher $\%P_{Xe}$ (by ~1.14-fold as seen in Ref. # [35]) compared to the first approach. Therefore, the approach of diluting SEOP gas mixtures with buffering gases before undertaking SEOP can be advantageous in the context of obtaining the higher value $\%P_{Xe}$ in diluted Xe gas mixture in the Tedlar bag storage.

Historically, batch-mode SEOP has employed mixtures rich in N_2 gas. In the pilot study presented here, we explore the utility of SEOP buffering using ^{4}He, which is the lightest inert gas able to be employed. The results described here represent a feasibility study to employ ^{4}He buffering gas in clinical-scale stopped-flow SEOP, a practice which can make the HP ^{129}Xe gas contrast agent mixture lighter, among other potential advantages. Specifically, when an aluminum jacket cooling/heating design is employed, $\%P_{Xe}$ of 55.9 ± 0.9% is observed at γ_{SEOP} of 0.049 ± 0.001 min^{-1} for the ^{4}He-rich mixture (1000 Torr Xe/900 Torr He, 100 Torr N_2), compared to $\%P_{Xe}$ of 49.3 ± 3.3% at γ_{SEOP} of 0.035 ± 0.004 min^{-1} for the N_2-rich gas mixture (1000 Torr Xe/100 Torr He, 900 Torr N_2). Where forced-air heating/cooling is used, $\%P_{Xe}$ of 83.9 ± 2.7% is observed at γ_{SEOP} of 0.045 ± 0.005 min^{-1} for the ^{4}He-rich ternary gas mixture (1000 Torr Xe/900 Torr He, 100 Torr N_2), compared to $\%P_{Xe}$ of 73.5 ± 1.3% at γ_{SEOP} of 0.028 ± 0.001 min^{-1} for the N_2-rich binary gas mixture (1000 Torr Xe and 1000 Torr N_2). Moreover, the ^{4}He-rich mixture renders better thermal stability of the SEOP hyperpolarization process.

2. Materials and methods

For most of the data presented in this work, the ^{129}Xe hyperpolarizer used in our SEOP experiments was a third-generation (GEN-3), automated batch-mode device, intended for operation under conditions of high-power continuous pump laser irradiation (BrightLock Ultra-500, QPC Laser Technologies, Sylmar, CA) and high Xe densities. The output from the optical train at maximum driver current of ~170 W (nominal frequency-narrowed spectral width 0.154 nm) was tuned to the Rb D_1 wavelength of

794.77 nm using a high-capacity water chiller (Termotek P312, Baden-Baden, Germany), possessing 930 W of cooling power and a flow rate of >4 L/min. A telescope and collimating lens (QPC Laser Technologies, Sylmar, CA) facilitate beam expansion to a diameter of 2″, while a λ/4 waveplate in the optical train ensures circular polarization of purity >98%. SEOP is performed inside a sealed, cylindrical glass vessel (termed "SEOP cell") with a volume of ~500 cubic centimeters (cc) (XET010, XeUS Technologies LTD, Cyprus). An aluminum jacket encloses the SEOP cell, allowing vaporization of Rb via direct thermal transfer from a pair of replaceable cartridge heaters to the cell surface [55], rather than using a forced-air oven common in previous hyperpolarizer designs [56–58]. A layer of Arctic Alumina thermal paste coats the SEOP cell and jacket, facilitating rapid and uniform distribution of thermal energy into the cell and maintaining an optimal Rb vapor density equilibrium throughout the cell [55]. A homogeneous magnetic field of up to 40 Gauss (4 mT) is provided by a solenoid coil, fully enclosing the SEOP cell [55]. Radio frequency (RF) pulsing and NMR signal acquisition is performed using a Kea2 NMR spectrometer (Magritek, New Zealand) at a 40.8 kHz resonance frequency for both ^{1}H or ^{129}Xe spins. The experimental SEOP configuration utilized in this work is summarized in Fig. 1.

Some experiments as detailed below have been performed using a previously described second-generation (GEN-2), automated batch-mode device [35,56,57]—the LDA module was upgraded by a module of the same power but with more spectrally narrowed output: FWHM of 0.195 nm versus 0.24 nm employed previously.

We mitigate the effects of proximal contact of HP ^{129}Xe with paramagnetic impurities within the SEOP cell walls [59–61] by utilizing SurfaSil™ siliconizing fluid coating (Thermo Fisher Scientific, Waltham MA). This forms a buffering layer between the gas mixture and the SEOP cell walls, helping to reduce ^{129}Xe spin destruction rates.

After preparation with SurfaSil™ siliconizing fluid, SEOP cells were filled with ~0.5 g Rb in an N_2-rich controlled-environment cabinet, to ensure sufficient Rb vapor density for SEOP to occur without requiring unreasonably high temperature elevation. Following this step, loading of desired ^{129}Xe/N_2/^{4}He gas mixtures was performed either on a custom gas-loading manifold or *in situ* on the hyperpolarizers' manifolds. Two ternary gas mixtures of differing composition were utilized for the bulk of the work conducted in this study. Both contained the same partial pressure of 1000 Torr non-enriched Xe (^{129}Xe isotopic natural abundance ≈ 26.4%). The remainder was comprised of 900 Torr ^{4}He/100 Torr N_2 in the first gas mixture, and the inverse 900 Torr N_2/100 Torr ^{4}He in the second—both equating to a total pressure of 2000 Torr (unless noted otherwise). A step-by-step procedure detailing the cleaning, preparation, and loading of SEOP cells with Rb and gas mixtures is described elsewhere [55].

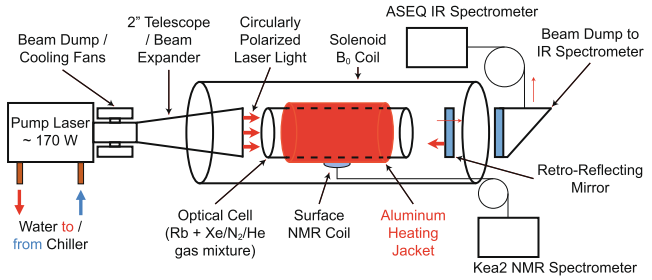


Fig. 1. Schematic drawing outlining the device diagram employed for ^{129}Xe SEOP process as performed on the third-generation (GEN-3) batch-mode hyperpolarizer device.

In order to determine $\%P_{Xe}$, it is first necessary to calibrate the NMR signal against a known reference, typically a thermally polarized water sample. Doping the sample with 10 mM $CuSO_4$ facilitates shortened relaxation times, allowing short repetition times on the order of 0.3 s or less—greatly accelerating signal averaging. ^{1}H NMR peaks from a signal reference phantom (filled in an otherwise identical SEOP cell) are visible after as few as 2,000 scans; however, we have employed 20,000 – 100,000 scans for the sake of improved reliability at higher SNR (Fig. 2a).

After NMR acquisition (Prospa v3.12 software, Magritek, New Zealand), each spectrum undergoes phase- and baseline-correction, before calculation of the peak area integral [55]. Because hyperpolarization increases the NMR signal intensity by several orders of magnitude, ^{129}Xe NMR data (Fig. 2b) can be acquired in a single shot. To ensure reliable direct comparison, the homogeneous B_0 magnetic field strength is adjusted by a factor of ~3.6 to account for the differing gyromagnetic ratios of the ^{1}H phantom calibration source and hyperpolarized ^{129}Xe. This practice allows receiver detection of both nuclear species at the same Larmor precession frequency of 40.8 kHz. For RF excitation, an identical pulse length of 150 μs was used for both nuclei, but a lower RF pulse amplitude (again by a factor of ~3.6, corresponding to the ratio of the two gyromagnetic ratios) was employed for the ^{1}H nucleus versus the ^{129}Xe nucleus. Comparing the ratio of peak integrals provides a signal enhancement factor, which can then be multiplied by the known thermal polarization to calculate $\%P_{Xe}$. The end-point of this analysis is shown in Equation (1) below,

$$P_{Xe} = P_H\left(\frac{C_H}{C_{Xe}}\cdot\frac{\gamma_H}{\gamma_{Xe}}\cdot\frac{S_{Xe}}{S_H}\right)\cdot Corr(T_2^*), \tag{1}$$

where P_H is the thermal proton polarization at 40.8 kHz resonance frequency (note the equilibrium thermal polarization values of ^{129}Xe and ^{1}H spins are identical at identical detection frequency),

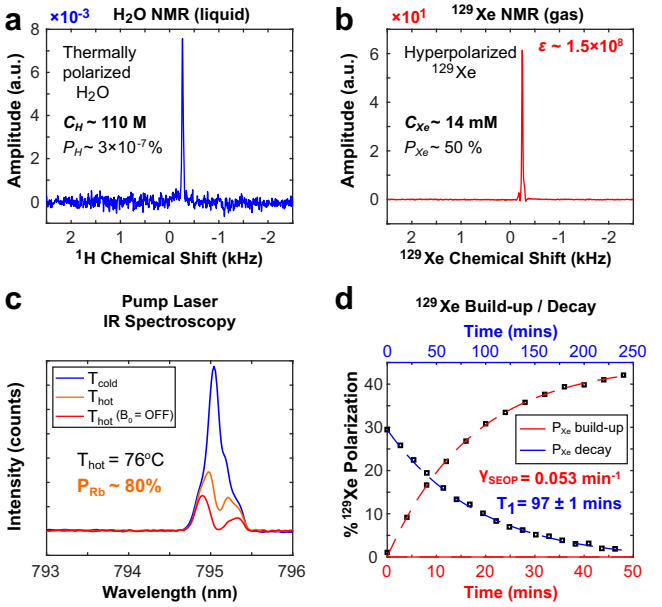


Fig. 2. Example spectra showing (a) ^{1}H NMR spectrum (200,000 scans) of thermally polarized reference H_2O phantom (doped with 10 mM $CuSO_4$) containing ~110 M (C_H) concentration of proton spins, and (b) ^{129}Xe NMR spectrum (single scan) of HP ^{129}Xe gas at ^{129}Xe concentration (denoted as C_{Xe}) of ~14 mM, respectively. (c) NIR optical absorption spectroscopy of Rb D_1 pump laser under various stages of SEOP, and (d) typical experimental SEOP results showing ^{129}Xe polarization build-up and decay as a function of time. The polarization build-up data (red) yields build-up rate (γ_{SEOP}) and the $\%P_{Xe}$ maximum value at $5/\gamma_{SEOP}$. The polarization decay data (blue) yields the T_1 decay constant of HP ^{129}Xe in the SEOP cell at room temperature and with the laser powered off.

γ_{Xe} and γ_H represent the gyromagnetic ratios of ^{129}Xe and ^{1}H respectively, C_{Xe} and C_H represent the concentrations of ^{129}Xe and ^{1}H spins respectively, S_{Xe} and S_H represent the observed peak integral values of ^{129}Xe and ^{1}H spins respectively (see Ref. [55]), and $Corr(T_2^*)$ is a correction factor accounting for the differing rates of ^{129}Xe and ^{1}H NMR signal decay (the detailed analysis of $Corr(T_2^*)$ is provided in the Supporting Information of Ref. # [35]).

In addition to NMR spectroscopy, optical near-infrared (NIR) spectroscopy is used to determine pump laser photon absorption and infer Rb electron polarization ($\%P_{Rb}$) [35,44]. This was performed using a high resolution optical spectrometer (HR1, ASEQ Instruments, Vancouver, Canada). Given sufficient Rb vapor density and incident photon flux, it is possible to see a dramatic, frequency-localized reduction in pump laser intensity at the Rb D_1 transition wavelength, even with exceptionally frequency-narrowed pump lasers (Fig. 2c). The Rb polarization was calculated using modified Beer's Law as described previously (Eq. (2)) [44],

$$|P_{Rb}| = \left|\frac{\ln(I_{hot}) - \ln(I_{cold})}{\ln(I_0) - \ln(I_{cold})}\right| - 1, \quad (2)$$

where I_{hot} and I_0 represent the peak integrals of the optical absorption spectrum during SEOP with the homogeneous B_0 magnetic field powered on and off, respectively and I_{cold} represents the peak integral of the cold (*ca.* room temperature) SEOP cell. Before each day of experimentation, an optical spectrum of the pump laser was acquired at maximum power (~170 W) and room temperature, serving as a reference signal under conditions of no optical pumping (owing to negligible Rb vapor density), denoted by the value I_{cold} in Equation (2). This acquisition was performed five times and an average intensity spectrum plotted to ensure reliability against random fluctuations. Optical absorption spectra were also acquired at the same time as NMR spectra acquisition (Fig. 2d) to record the pump laser absorption profile signal, denoted by I_{hot} in Eq. (2).

Equation (2) provides an estimate for the average Rb polarization throughout the cell. Because the transmitted IR light is sampled only from the central point behind the rear of the cell, the resulting $\%P_{Rb}$ value may tend to be an overestimate of the "true" average $\%P_{Rb}$ throughout the cell. In addition to variances in Rb polarization across the cell, variances in Rb density may also cause systematic errors, but the effects on the estimated cell-average $\%P_{Rb}$ are likely to be mitigated by the fact that the Xe NMR data are taken from the longitudinal center of the cell. On the other hand, Eq. (2) also assumes that the magnetic field (when the magnetic field is turned off) is effectively zero; a non-zero field along the direction of the cell under these conditions could instead lead to an underestimate of $\%P_{Rb}$. Nevertheless, the value in this facile estimate of $\%P_{Rb}$ is in checking for internal consistency of the various measured values concerning the xenon hyperpolarization process. Indeed, despite these systematic contributions we have previously found that the resulting $\%P_{Rb}$ estimates can give reasonable internal agreement, particularly when SEOP is performed near optimal conditions. For example, we previously reported [57] a ratio of $\%P_{Rb}$ to $\%P_{Xe}$ that offered excellent internal agreement with a simplistic expectation calculated from the ratio of the spin-exchange rate (γ_{SE}) to $\gamma_{SEOP} = \gamma_{SE} + \Gamma_{Xe}$, (where $\Gamma_{Xe} = 1/T_1$): 0.77 versus 0.79, respectively [57].

Before each day of experimentation, when acquiring dynamic $\%P_{Xe}$ and $\%P_{Rb}$ data in this study, the heating jacket/forced air SEOP oven was first allowed to reach a desired temperature set-point, with large flip-angle "crusher" NMR pulses applied continuously (~3 per second) throughout to prevent any significant ^{129}Xe polarization build-up, helping to ensure repeatability. Once a stable jacket/SEOP oven temperature was achieved, the crusher pulses were halted (setting the zero of time) and $\%P_{Xe}$ was allowed to build up via SEOP. Using small flip-angle RF pulses, ^{129}Xe NMR spectra were acquired at 4-minute intervals to observe the build-up of magnetization until an eventual steady state was achieved where a stable maximum $\%P_{Xe}$ was maintained. Similarly, the effective lifetime of a hyperpolarized ^{129}Xe sample can be determined from an exponential T_1 relaxation curve, whereby regular application of low-intensity RF pulses when no SEOP can take place (no photon flux and negligible Rb vapor density) allows observation of the decaying NMR signal (Fig. 2d).

Build-up experiments were continuously monitored until near-steady-state ^{129}Xe polarization was achieved, typically on the order of 40–60 min when using the GEN-3 hyperpolarizer, or 120–150 min when using the GEN-2 hyperpolarizer. At the end of each build-up run, an optical spectrum was acquired with the magnetic field switched off, with profile signal denoted by (I_0) in Equation (2), to enable later determination of Rb polarization. Large flip-angle NMR crusher pulses were then applied once again to destroy the ^{129}Xe magnetization as the jacket temperature was increased prior to initiation of the subsequent run. The overall process was repeated until a suitable temperature range had been investigated.

For each temperature and SEOP cell, $\%P_{Xe}$ and $\%P_{Rb}$ were calculated using integrals of NMR magnitude spectra and optical absorption spectra, and Equations (1) and (2) respectively (we note that in some cases, $\%P_{Rb}$ data was not recorded and therefore is not plotted on the corresponding maps below). A ^{129}Xe polarization build-up curve was constructed for each experiment by plotting $\%P_{Xe}$ as a function of time, and both the ^{129}Xe polarization build-up time (T_b) and build-up rate ($\gamma_{SEOP} = 1/T_b$) were determined using exponential fitting of the build-up curve at each temperature. Taking the steady state $\%P_{Xe}$ and (where available) $\%P_{Rb}$ values, as well as γ_{SEOP} from each set of experiments, a temperature-dependent map was constructed, illustrating the complex dynamics of the SEOP process.

Results obtained from the second generation (GEN-2) hyperpolarizer device for the purposes of comparison with previous studies were obtained using a previously described setup without any modifications using the similar overall approach described for the GEN-3 device above [35,56,57].

The error bar values correspond to 95% confidence intervals.

3. Results and discussion

First, we provide the comparative analysis of a "^{4}He-rich" gas mixture in the context of batch-mode SEOP for the hyperpolarizer design employing the new generation-3 (GEN-3) aluminum jacket (which surrounds SEOP cell to provide fast cooling and heating during SEOP process). This design provides the advantages of fast and more robust temperature manipulation for SEOP cells [55]. Next, we provide the same comparative analysis for more established hyperpolarizer designs employing forced air oven configurations surrounding the SEOP chamber [58], where forced air is employed for cooling and heating during SEOP process: these results were obtained on a previous generation (GEN-2) hyperpolarizer [57].

3.1. GEN-3 experimentations with SEOP cells with "fast" build-up rates.

Results from two different SEOP cells exhibiting "rapid" ^{129}Xe polarization build-up (defined as $\gamma_{SEOP} > 0.1$ min^{-1} at temperature below 80 °C) are presented in Fig. 3, comparing the efficiency of the SEOP process in both the ^{4}He-rich and the N_2-rich gas mixtures. In contrast, experimental results from SEOP cells exhibiting "slow" (defined as $\gamma_{SEOP} < 0.1$ min^{-1} at temperature below 80 °C) ^{129}Xe polarization build-up are outlined in Fig. 4. The data is presented

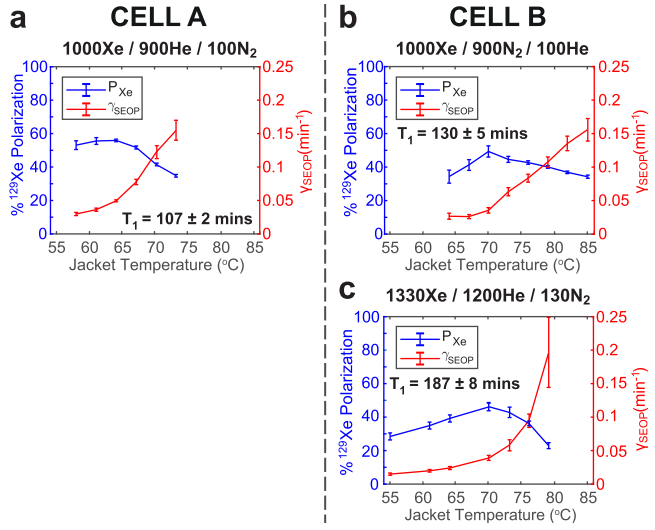


Fig. 3. Temperature maps of steady-state $\%P_{Xe}$, $\%P_{Rb}$ and γ_{SEOP} values in SEOP cells with "fast" build-up rates (*i.e.*, γ_{SEOP} exceeding 0.1 min^{-1} at jacket temperatures below 80 °C). Note two different color-coded y-axes for $\%P_{Xe}/\%P_{Rb}$ and γ_{SEOP}. (a) temperature map of SEOP cell containing "^{4}He-rich" mixture composed of 1000 Torr Xe/900 Torr ^{4}He/100 Torr N_2 gas mixture (labeled as cell A), (b) temperature map of SEOP cell containing "N_2-rich" mixture composed of 1000 Torr Xe/900 Torr N_2/100 Torr ^{4}He (labeled as cell B), (c) temperature map of SEOP cell B containing "^{4}He-rich" mixture composed of 2660 Torr 1330 Torr Xe/1200 Torr ^{4}He/130 Torr N_2) total pressure.

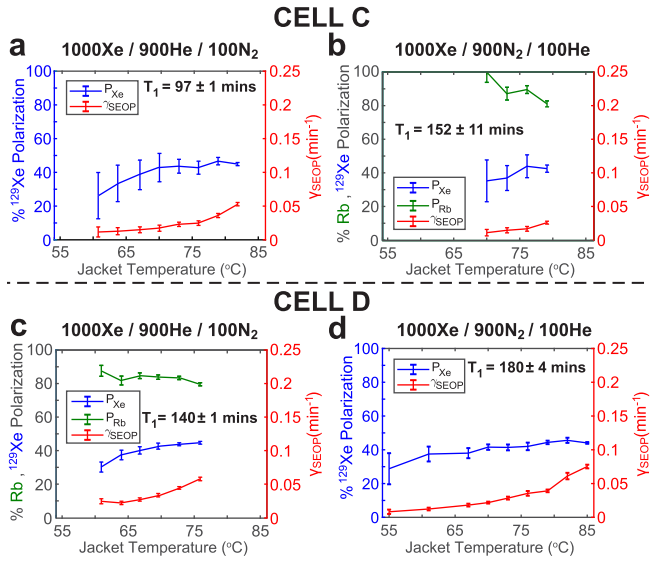


Fig. 4. Temperature maps of steady-state $\%P_{Xe}$, γ_{SEOP} and (where available) $\%P_{Rb}$ values in SEOP cells with "slow" build-up rates (*i.e.*, γ_{SEOP} less 0.1 min^{-1} at jacket temperatures below 80 °C). Results presented in Fig. 4a and Fig. 4b were obtained from the same SEOP cell (labeled as cell C), whereas those presented in Fig. 4c and Fig. 4d were acquired from a second SEOP cell (labeled as cell D). Note two different color-coded y-axes for $\%P_{Xe}/\%P_{Rb}$ and γ_{SEOP}. (a) temperature map of SEOP cell C containing "^{4}He-rich" mixture composed of 1000 Torr Xe/900 Torr ^{4}He/100 Torr N_2 gas mixture, (b) temperature map of SEOP cell C containing "N_2-rich" mixture composed of 1000 Torr Xe/900 Torr N_2/100 Torr ^{4}He, (c) temperature map of SEOP cell D containing "^{4}He-rich" mixture composed of 1000 Torr Xe/900 Torr ^{4}He/100 Torr N_2 gas mixture, (d) temperature map of SEOP cell D containing "N_2-rich" mixture composed of 1000 Torr Xe/900 Torr N_2/100 Torr ^{4}He.

in two different sub-groups because we have observed different γ_{SEOP} trends for various SEOP cells—specifically, we see an apparent temperature shift from one SEOP cell to another, which is likely attributed to the variable degree of Rb metal spread over the interior cell surface. The comparison of SEOP cells points that although the temperature dependence may be shifted from one cell to another due to Rb metal distribution (under otherwise identical conditions and most importantly the composition of the gas mixture), γ_{SEOP} is likely a significantly better proxy for the gas-phase Rb metal concentration in the regime when $\gamma_{SEOP} > 1/T_1$. Therefore, more rigorous comparative analysis of the results from physically different Rb-spread SEOP cells should compare $\%P_{Xe}$ and $\%P_{Rb}$ at similar or identical values of γ_{SEOP} rather than at the same temperature due to Rb-spread-induced temperature shift of the curves.

The absolute rates of SEOP are highly important in the context of clinical applications as faster build-up rates translate directly into greater dose equivalent (DE) [62] production rates of the contrast agent. Although the definition of "fast" versus "slow" is indeed artificial in this case, in this limited pilot set of SEOP cells, we clearly see clusters of SEOP cells that in fact exhibit significantly higher maximum build-up rates: *e.g.*, cells A and B both have max. γ_{SEOP} of ~0.16–0.19 min^{-1} (Fig. 3), whereas the cells C and D represent a significantly different cluster with max. γ_{SEOP} of ~0.05–0.08 min^{-1} (Fig. 4). As a result of such significantly different SEOP dynamics, these two clusters were analyzed independently. Our future efforts will certainly be focused on investigating the underlying causes of this clustering.

All data presented in Figs. 3 and 4 exhibited long T_1 relaxation time constants—defined for the purposes of this study as those SEOP cells with T_1 > 90 min. In such cases, even when the build-up rate γ_{SEOP} is modest (e.g. ~0.02 min^{-1}), the effects of T_1 relaxation on maximum $\%P_{Xe}$ (*i.e.*, the $\%P_{Xe}$ after $5/\gamma_{SEOP}$) [35] are minute.

In Fig. 3, it was observed that the ^{4}He-rich mixture (loaded in SEOP cell A) performed well compared to the more traditional N_2-rich mixture (loaded in SEOP cell B), exhibiting slightly faster build-up rates and slightly higher maximum $\%P_{Xe}$ values across the range of temperatures investigated. The maximum $\%P_{Xe}$ was achieved at a higher build-up rate in ^{4}He-rich mix (55.9 ± 0.9% at 0.049 ± 0.001 min^{-1} for the ^{4}He-rich mix, compared to 49.3 ± 3.3% at 0.035 ± 0.004 min^{-1} for the N_2-rich gas mixture). Although these two sets of data were acquired from physically different SEOP cells (which may have slightly different photon transmission and/or paramagnetic impurity characteristics), it is also important to note that the maximum $\%P_{Xe}$ value for ^{4}He-rich mixture was obtained at a faster γ_{SEOP}. This effect (of higher polarization at faster build-up rates) may be attributed to the higher thermal conductivity of ^{4}He resulting in more efficient thermalization of the overall gas mixture in different regions of the cell.

From the data presented in Fig. 3a and Fig. 3b, we draw two preliminary conclusions in this pilot study. First, SEOP in the ^{4}He-rich gas mixture resulted in a small increase in the maximum achievable $\%P_{Xe}$ (55.9 ± 0.9% at a jacket temperature of 64 °C), relative to the N_2-rich mixture (49.3 ± 3.3% at a jacket temperature of 70 °C). This result corresponds to the overall improvement in $\%P_{Xe}$ by a factor of 1.13 ± 0.08 and γ_{SEOP} increase by a factor 1.40 ± 0.16. Secondly, ^{4}He-rich SEOP experienced a significantly more stable maximum $\%P_{Xe}$ as a function of changing jacket temperature, with a flatter plateau illustrating ^{129}Xe polarization values between 50% and 60% being achieved over a range of temperatures from 58 °C to 67 °C. By contrast, the N_2-rich gas mixture began to show a steady decline in $\%P_{Xe}$ when performing SEOP above 69 °C. The latter observation has practical implications in that it means that it should generally enable more stable automation for the hyperpolarizer instrumentation, with easier avoidance of Rb runaway. All of these observations present clear evidence that inclusion of ^{4}He in the SEOP gas mixture offers practical benefits to HP ^{129}Xe contrast agent production, in terms of improved $\%P_{Xe}$ and polarization build-up and production rates.

In addition to different fractional gas mixture compositions, we also examined the SEOP dynamics of the He-rich regime at higher

total SEOP cell pressure (loaded in the SEOP cell B). Fig. 3c highlights the results from ^{129}Xe polarization build-up following SEOP in a 50% Xe/45% ^{4}He/5% N_2 SEOP cell, containing 1330 Torr Xe (2660 Torr total pressure), relative to that of an identical composition with 2000 Torr total cell pressure presented in Fig. 3a. The feasibility of efficient ^{129}Xe polarization build-up in high-density, He-rich mixtures is demonstrated with relatively high levels of $\%P_{Xe}$ (46.1 ± 2.4% at 70 °C) and modest build-up rates (γ_{SEOP} ~ 0.04-min^{-1}). Note that when the build-up accelerates (γ_{SEOP} ~ 0.2 min^{-1} at 79 °C), $\%P_{Xe}$ decreases substantially to ~20%. This decrease by a factor of ~2 is significantly more pronounced than that seen in Fig. 3a. The reason for this observation is that as the gas mixture density (particularly the Xe density) inside the SEOP cell increases, the probability of Rb electrons experiencing binary Rb/Xe spin-destruction collisions increases, subsequently resulting in lower $\%P_{Rb}$ values—although $\%P_{Rb}$ values are not reported in Fig. 3, this effect has been studied in details in our recent simulation work [63].

3.2. GEN-3 experiments with SEOP cells with "slow" build-up rates.

Fig. 4 provides the comparative analysis of ^{4}He-rich gas mixtures versus N_2-rich mixtures for SEOP cells that exhibited slower polarization build-up (here defined as γ_{SEOP} < 0.1 min^{-1}, generally observed at 80 °C jacket temperatures or below). We attribute such "slower" γ_{SEOP} values (*e.g.*, Fig. 4a versus Fig. 3a) at the same temperature as a result of worse Rb metal distribution in the SEOP cells C and D, as discussed in depth above. Results presented in Fig. 4a and Fig. 4b were obtained from the same SEOP cell (labeled as cell C), whereas those presented in Fig. 4c and Fig. 4d were acquired from a second SEOP cell (labeled as cell D). Performance of ^{4}He-rich gas mixtures versus N_2-rich mixtures was comparable in terms of both build-up rate and maximum observed $\%P_{Xe}$ (on the order of 40%), as shown in Fig. 4. For both gas mixture compositions, the slow rate of polarization build-up results in a more stable SEOP system, with less pronounced performance-temperature dependence and a larger temperature range at which high levels of $\%P_{Xe}$ can be achieved. It should be noted again that all of these SEOP cells possessed long T_1 relaxation times (>90 min.), allowing for a more critical evaluation of reproducibility between SEOP cells.

The two pairs of data sets (Fig. 4a/Fig. 4b and Fig. 4c/Fig. 4d) again appear to be in good agreement and indicate that the presence of additional ^{4}He (or concurrent reduction in N_2 fraction) demonstrates no significant improvements or deterioration in performance for ^{4}He-rich gas mixtures relative to the more traditional N_2-rich SEOP. We conclude that the gains (if any) seen in Fig. 4 versus those seen in Fig. 3 are lower due to overall lower quality of Rb metal distribution for the data in Fig. 4 (seen as significantly slower build-up rates at the same temperatures) versus the gains seen in Fig. 3a/Fig. 3b in the context of this pilot study. Table 1 provides more detailed and quantitative comparative data analysis for all SEOP cells and gas mixture compositions studied.

Where $\%P_{Rb}$ was estimated and recorded, SEOP cells demonstrated a moderate reduction in $\%P_{Rb}$ at elevated temperatures (given an approximately 20% decrease at the highest temperature studied for each gas mixture). The ability for Rb polarization to be maintained at such a high level is indicative of the global optical pumping rate exceeding the rate of Rb spin-destruction, which in turn reflects high resonant laser photon flux throughout the SEOP cell [35].

However, the data presented here for the GEN-3 hyperpolarizer indicates some degree of mismatch between the very high levels of Rb polarization and the unexpectedly modest $\%P_{Xe}$ values. For example, in Fig. 4b and Fig. 4c $\%P_{Rb}$ is greater than $\%P_{Xe}$ by approximately a factor of two, even under conditions of elevated build-up rates, *e.g.*, γ_{SEOP} > 0.05 min^{-1} at 76 °C (Fig. 4c). We note that previous studies with a second generation (GEN-2) hyperpolarizer revealed a much smaller difference (less than a factor of 1.3, also see Fig. 5) between $\%P_{Rb}$ and $\%P_{Xe}$ under similar build-up rates and Xe densities in binary Xe/N_2 gas mixtures—and that the difference between $\%P_{Rb}$ and $\%P_{Xe}$ values could be quantifiably explained by the measured values for γ_{SEOP} and Γ_{Xe} [35]. We are currently investigating these discrepancies, which may be attributed to the different heating/cooling design of the GEN-3 hyperpolarizer [55]. We speculate that the GEN-3 design has colder (front and back) regions of the SEOP cell, which do not significantly contribute to the SEOP process due to low local Rb vapor density [55].

3.3. GEN-2 experiments with SEOP cells

The experiments described in this section were performed using forced air cooling/heating design in the previously described GEN-2 hyperpolarizer [35,56,57]. Note that the key difference between GEN-3 [55] and GEN-2 [35,56,57] designs is the use of a different method for temperature control of the SEOP cell: an aluminum jacket versus forced air respectively. In order to compare applicability of ^{4}He-rich mixtures for ^{129}Xe SEOP on the GEN-2 hyperpolarizer device, we have performed further temperature mapping of the SEOP process using a 1000 Torr Xe/900 Torr ^{4}He/100 Torr N_2 gas mixture (Fig. 5a) and a 1330 Torr Xe/1200 Torr ^{4}He/130 Torr N_2 gas mixture (Fig. 5b), where we find much better quantitative agreement between $\%P_{Xe}$ and $\%P_{Rb}$—in line with previous studies [35]. For the sake of optimal comparability with previous studies, we also present temperature maps of the

Table 1
Summary of experimental results.

SEOP Cell	Polarizer	Xe:N_2:^{4}He ratio	Xe Pressure (Torr)	Maximum % P_{Xe} (%)	γ_{SEOP} @ max $\%P_{Xe}$ (min^{-1})	$\%P_{Rb}$ @ max % P_{Xe}	DE rate (L/hour)	Figure	Temperature (°C)
A	GEN-3	50/5/45	1000	55.9 ± 0.8	0.049 ± 0.001	N/A	~0.29	Fig. 3a	64
B	GEN-3	50/5/45	1000	49.3 ± 3.3	0.035 ± 0.004	N/A	~0.29	Fig. 3b	70
B	GEN-3	50/5/45	1330	56.1 ± 2.9	0.039 ± 0.004	N/A	~0.32	Fig. 3c	70
C	GEN-3	50/5/45	1000	44.9 ± 0.9	0.053 ± 0.003	N/A	~0.24	Fig. 4a	82
C	GEN-3	50/45/5	1000	42.5 ± 2.2	0.026 ± 0.002	81.0 ± 1.8	~0.14	Fig. 4b	79
D	GEN-3	50/5/45	1000	44.7 ± 0.8	0.058 ± 0.003	79.6 ± 0.9	~0.25	Fig. 4c	76
D	GEN-3	50/45/5	1000	44.1 ± 0.5	0.075 ± 0.003	N/A	~0.29	Fig. 4d	85
E	GEN-2	50/5/45	1000	83.9 ± 2.7	0.045 ± 0.005	82.8 ± 1.3	~0.20	Fig. 5a	70
F	GEN-2	50/50/0	1000	73.5 ± 1.3	0.028 ± 0.001	80.4 ± 1.9	~0.13	Fig. 5b	65
E	GEN-2	50/5/45	1330	72.6 ± 1.4	0.041 ± 0.003	74.9 ± 1.2	~0.27	Fig. 5c	67.5
F	GEN-2	50/50/0	1330	56.6 ± 1.3	0.034 ± 0.002	70.0 ± 1.5	~0.19	Fig. 5d	65

*DE rate values are provided using the following parameters: (i) 100% enriched ^{129}Xe use; (ii) GEN-2 production cycle of 1.0 h with 24 min. cooldown period and GEN-3 production cycle of 25 min. with 4 min. cooldown; (iii) a corresponding set of $\%P_{Xe}$ and γ_{SEOP} corresponding to the highest build-up rate was used – see the corresponding figures for details. Temperature corresponds to the condition of the SEOP process for which maximum values of $\%P_{Xe}$ is reported under the corresponding values γ_{SEOP} and $\%P_{Rb}$.

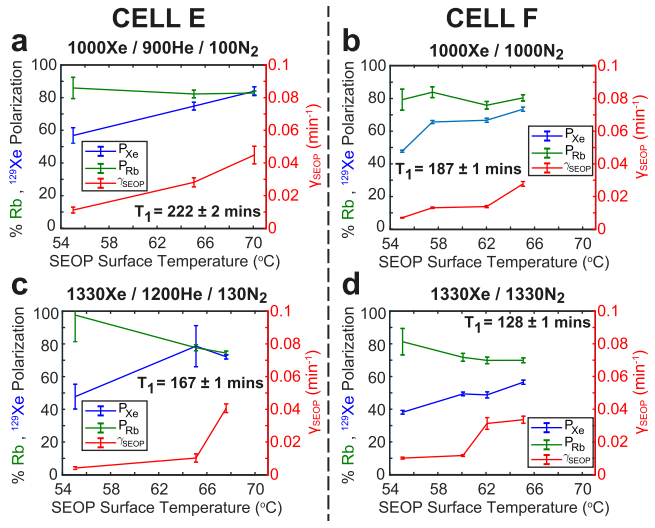


Fig. 5. Temperature maps of steady-state $\%P_{Xe}$, γ_{SEOP}, and $\%P_{Rb}$ values in SEOP cells C and D using a GEN-2 hyperpolarizer with forced air cooling/heating. Results presented in figure (a and c) were obtained from the same SEOP cell (labeled as cell E) using the same Rb distribution. Results presented in figure (b and d) were obtained from the same SEOP cell (labeled as cell F) using the same Rb distribution. Note two different color-coded y-axes for $\%P_{Xe}/\%P_{Rb}$ and γ_{SEOP}. (a) temperature map of SEOP cell E containing "^{4}He-rich" mixture composed of 1000 Torr Xe/900 Torr ^{4}He/100 Torr N_2 gas mixture (this gas composition was obtained by decreasing the total gas pressure of the cell content shown in figure (c) via partial evacuation of the SEOP cell), (b) temperature map of SEOP cell F containing "N_2-rich" mixture composed of 1000 Torr Xe/1000 Torr N_2 (this gas composition was obtained by decreasing the total gas pressure of the cell content shown in figure (d) via partial evacuation of the SEOP cell), (c) temperature map of SEOP cell E containing "^{4}He-rich" mixture composed of 1330 Torr Xe/1200 Torr ^{4}He/130 Torr N_2 gas mixture, (d) temperature map of SEOP cell F containing "N_2-rich" mixture composed of 1330 Torr Xe/1330 Torr N_2.

^{129}Xe SEOP hyperpolarization process in the corresponding binary gas mixtures—1000 Torr Xe/1000 Torr N_2 (Fig. 5c) and 1330 Torr Xe/1330 Torr N_2 (Fig. 5d), also on the GEN-2 hyperpolarizer.

The maximum $\%P_{Xe}$ values achieved following SEOP on the GEN-2 hyperpolarizer device in Fig. 5a and Fig. 5b compare favorably to those obtained from the GEN-3 hyperpolarizer under similar conditions, shown in Fig. 3a and Fig. 3c respectively. However, we note significantly slower ^{129}Xe polarization build-up rates seen across the range of SEOP cell surface temperatures investigated in both Fig. 5a and Fig. 5b compared to those seen in Fig. 3a and Fig. 3c respectively. Also note the convergence of high ^{129}Xe and Rb polarization measurements (~84% and 73% in the 2000 Torr and 2660 Torr SEOP cells, respectively) at high oven temperatures, $T \rightarrow 70$ °C, qualitatively in accordance with previous studies [35,57]. This observation demonstrates that the more modest $\%P_{Xe}$ values and discrepancy between $\%P_{Xe}/\%P_{Rb}$ observed in the GEN-3 SEOP studies shown previously can likely be attributed to the design of the GEN-3 hyperpolarizer [55] (specifically the heating jacket, which of course warrants further investigation), but does not arise as a negative consequence of employing ^{4}He-rich gas mixtures.

The values for average $\%P_{Rb}$, $\%P_{Xe}$, γ_{SEOP}, and Γ_{Xe} can also be used to check for internal consistency [57]. For example, the agreement between the measured P_{Xe} values in Fig. 5b and the product $[\%P_{Rb}\cdot\gamma_{SE}/\gamma_{SEOP}]$ grows with temperature, giving reasonable agreement at 65 °C (~73%, and ~65%, respectively). The worse agreement at lower temperatures may in part reflect an underestimate of the γ_{SE} rate at those lower temperatures (*e.g.*, because magnetization losses due to pulsing are not included in the exponential fits for the build-up dynamics), as well as the reliance on a fixed value for $\Gamma_{Xe} = T_1^{-1}$.

The maximum $\%P_{Xe}$ value shown in Fig. 5b exceeded that obtained previously with the GEN-2 hyperpolarizer device under similar conditions. For example, a binary gas mixture comprising 1000 Torr Xe and 1000 Torr N_2 previously yielded a $\%P_{Xe}$ of ~60% [35], while in this work we report on $\%P_{Xe}$ of 73.5 ± 1.3% at a build-up rate of $\gamma_{SEOP} = 0.028 \pm 0.001$ min^{-1} and an oven temperature of 65 °C in Fig. 5b. We attribute the improvement in polarization levels in part due to more spectrally narrowed LDA. The maximum $\%P_{Xe}$ values shown in Fig. 5a and Fig. 5c (*i.e.*, ^{4}He-rich mixtures) exceeded those obtained in Fig. 5b and Fig. 5d (*i.e.*, N_2-rich mixtures) respectively. Fig. 5a features a 1000 Xe/900 ^{4}He/100 N_2 mixture with maximum $\%P_{Xe}$ of 83.9 ± 2.7% at a build-up rate γ_{SEOP} of 0.045 ± 0.005 min^{-1} versus Fig. 5b featuring a 1000 Xe/1000 N_2 mixture with $\%P_{Xe}$ of 73.5 ± 1.3% at γ_{SEOP} of 0.028 ± 0.001 min^{-1}. This corresponds to approximately a factor of 1.14 ± 0.04 improvement in $\%P_{Xe}$ value at the factor of 1.61 ± 0.18 increase in the γ_{SEOP}. Note the overall improvement in $\%P_{Xe}$ (when using ^{4}He-rich mixture versus N_2-rich mixture) is very similar to that of the GEN-3 hyperpolarizer (data shown in Fig. 3a and Fig. 3b).

We have also investigated the feasibility of SEOP at higher Xe densities using the GEN-2 device: 1330 Torr Xe partial pressure (Fig. 5c and Fig. 5d). Fig. 5c demonstrated a maximum $\%P_{Xe}$ of 72.6 ± 1.4% at a build-up rate γ_{SEOP} of 0.041 ± 0.003 min^{-1} and an oven temperature of 67.5 °C, significantly exceeding that observed in the similarly dense binary gas mixture (*i.e.*, without inclusion of He), giving $\%P_{Xe} = 56.6 \pm 1.3\%$ at a build-up rate of $\gamma_{SEOP} = 0.034 \pm 0.002$ min^{-1} and an oven temperature of 65 °C in Fig. 5d. We note that SEOP of the ^{4}He-rich mixture in Fig. 5c was performed at a higher temperature, which was challenging to perform in the N_2-rich mixture (Fig. 5d) due to Rb runaway [35,49–51]. This observation corresponds to an overall improvement in $\%P_{Xe}$ by a factor of 1.28 ± 0.04 and an increase of γ_{SEOP} by a factor of 1.21 ± 0.11. A better ^{129}Xe magnetization payload (defined as the product of Xe fraction and polarization) is achieved at 1330 Torr partial pressure. Taken together, the GEN-2 results clearly indicate the benefits of using ^{4}He-rich mixtures in that (1) somewhat better $\%P_{Xe}$ values can be achieved under otherwise similar conditions; (2) better magnetization payload can be achieved with a higher density mixture (up to 1330 Torr); and (3) somewhat faster build-up rates can be attained due to a better thermal management of the SEOP cell (allowing stable SEOP at higher temperatures and over a wider temperature range).

Despite the high-density 2660 Torr ternary gas mixture presenting lower maximum $\%P_{Xe}$ values as observed in Fig. 3c, Fig. 5c and Fig. 5d, the increased quantity of Xe nuclei in the higher-density regime results in equivalent or greater net magnetization being achieved under optimal SEOP conditions. It is normally to be expected that near-unity polarization would be easier to achieve in a system with fewer target nuclei (*e.g.*, low-density regime) [35].

3.4. Dose-equivalent (DE) production rates.

In the context of clinical applications, an important metrics of the SEOP performance is the dose equivalent (DE) [62], *i.e.*, the production rate per unit time of 100% hyperpolarized 100% enriched pure ^{129}Xe gas. Gen-3 hyperpolarizer design enables much faster production cycle [55]. Using the information provided in Fig. 3a and b, we conclude that the production rate is approximately the same for ^{4}He-rich and N_2-rich mixtures with DE rate value of ~0.29 L/h of 100% hyperpolarized 100% enriched pure ^{129}Xe gas (assuming production cycle of 25 min. (8 mins for temperature manipulation and ejection and 17 min. of polarization build-up ($\gamma_{SEOP} \rightarrow 0.16$ min^{-1}). These values correspond to a production rate of 1.9 L/hour (0.8 L/dose per 0.42 h at ejection using total 2000 Torr

SEOP cell pressure and 50% Xe content) of ~29%-hyperpolarized (estimated after ejection from the hyperpolarizer) in 1000 Torr Xe mixtures using 100% enriched ^{129}Xe (natural abundance Xe employed here lowers DE rate to 0.073 L/hour). The GEN-2 hyperpolarizer has slower production rates despite nominally higher % P_{Xe} values due to overall significantly slower rate of the SEOP process and overall longer production cycle (*e.g.*, 30 mins for temperature manipulation and ejection and 30 min. of polarization build-up ($\gamma_{SEOP} \rightarrow 0.041$ min^{-1}). This yields DE rate of 0.27 L/hour at 1.28 L/dose per 1.0 h at ejection using total 2660 Torr SEOP cell pressure (Fig. 5c) and 50% Xe content using 100% enriched ^{129}Xe (natural abundance Xe employed here lowers DE rate to 0.070 L/hour) of ~42%-hyperpolarized Xe (estimated after ejection from the hyperpolarizer) in ^{4}He-rich 1330 Torr Xe mixture. The respective DE rate metrics for Fig. 5a ($\gamma_{SEOP} \rightarrow 0.045$ min^{-1}) for 2000 Torr ^{4}He-rich mixture is 0.20 L/hour for 100% enriched ^{129}Xe (natural abundance Xe employed here lowers DE rate to 0.052 L/hour). The corresponding numbers for N_2-rich mixtures shown in Fig. 5b and Fig. 5d respectively are ~0.13 L/h and ~0.19 L/h respectively using 100% enriched ^{129}Xe when production cycle of 1.0 h is employed. Thus, DE rate performance clearly demonstrates the enhanced production rates in the context of GEN-2 hyperpolarizer due to use of ^{4}He-rich mixtures.

4. Conclusion

Based on the results presented in this work, we observe modest (by a factor of 1.14 ± 0.04 to 1.28 ± 0.04) increases for GEN-2 device and on-par performance to small increase (by a factor of 1.13 ± 0.08) for GEN-3 device in maximum achievable HP ^{129}Xe polarization when utilizing ^{4}He-rich gas mixtures, and that these values can be reached at somewhat faster polarization build-up rates when compared to corresponding N_2-rich binary gas mixtures. For example, when the aluminum jacket cooling/heating was employed (GEN-3 device), $\%P_{Xe}$ of 55.9 ± 0.9% was observed at γ_{SEOP} of 0.049 ± 0.001 min^{-1} for the ^{4}He-rich mixture (1000 Torr Xe/900 Torr ^{4}He/100 Torr N_2), compared to $\%P_{Xe}$ of 49.3 ± 3.3% at γ_{SEOP} of 0.035 ± 0.004 min^{-1} for the N_2-rich gas mixture (1000 Torr Xe/100 Torr ^{4}He/900 Torr N_2). In the case where forced-air heating/cooling was employed (GEN-2 device), $\%P_{Xe}$ of 83.9 ± 2.7% was observed at γ_{SEOP} of 0.045 ± 0.005 min^{-1} for the ^{4}He-rich mixture (1000 Torr Xe/900 Torr ^{4}He/ 100 Torr N_2), compared to $\%P_{Xe}$ of 73.5 ± 1.3% at γ_{SEOP} of 0.028 ± 0.001 min^{-1} for the N_2-rich gas mixture (1000 Torr Xe and 1000 Torr N_2). Of note, $\%P_{Xe}$ of 83.9 ± 2.7% represents record number at such high Xe density (1000 Torr) for a clinical-scale apparatus.

Additionally, rapid build-up rates of $\gamma_{SEOP} > 0.1$ min^{-1} in these ^{4}He-rich gas mixtures may be achieved, and have a substantially larger window of high performance across a broader range of temperatures (facilitating automation), likely arising as a consequence of improved thermal conductivity and better management of thermal transport processes within the SEOP cell. The comparable-or-greater performance of ^{4}He-rich mixes in SEOP hyperpolarization is of particular interest for clinical studies, where the reduction in gaseous contrast agent density has the potential to improve patient tolerability to inhaled HP contrast agents.

It should also be emphasized that the presented pilot study has a number of limitations (including performed GEN-2-based experiments in physically different cells E and F, Fig. 5), which should be addressed in the future including a small number of SEOP cells studied (which may not be sufficient for determining the statistical significance of the results obtained) and the lack of certain control experiments.

In summary, we believe that substituting a significant proportion of the N_2 buffer gas with ^{4}He results in similar or somewhat better ^{129}Xe polarization levels and similar or better build-up rates compared to those of corresponding N_2-rich mixtures. Additionally, ^{4}He-rich gas mixtures appear to be more resistant to thermal instability and present a larger "window" for performing efficient SEOP (*e.g.*, Fig. 5b versus Fig. 5d), while also presenting a key practical advantage of greater ease of automation. Therefore, attention can be turned to expanding the scope of this study to a wider range of lighter ^{4}He-containing gas mixtures and any potential applications of this new regime. Presented in Table 2 is a theoretical comparison of binary Xe/N_2 gas mixtures and their hypothetical ternary $Xe/N_2/^4$He counterparts, accompanied by their respective densities relative to air that could be readily employed in SEOP for the production of HP ^{129}Xe contrast agents.

Table 2
Compositional density comparison of the binary Xe gas mixtures commonly used in Xe-rich batch-mode SEOP, and the envisioned ternary gas mixture equivalents utilizing ^{4}He.

Binary Mix Composition (%)	Density (g·L^{-1})**	Ternary (^{4}He) Mix Composition (%)	Density (g·L^{-1})**
20Xe/80N_2	1.7	20Xe/75He/5N_2	1.3
25Xe/75N_2	1.9	25Xe/70He/5N_2	1.6
30Xe/70N_2	2.2	30Xe/65He/5N_2	1.9
40Xe/60N_2	2.7	40Xe/55He/5N_2	2.4
50Xe/50N_2	3.3	50Xe/45He/5N_2	3.0
75Xe/25N_2	4.5	75Xe/20He/5N_2	4.4
100Xe*	5.8	not applicable	
air	1.3	air	1.3

* At natural abundance of Xe isotopes.
** At sea level pressure and 273 K.

5. Notes

PN, BMG, and EYC declare the stake of ownership in XeUS Technologies, LTD.

Acknowledgment

This work was supported by DOD CDMRP under BRP W81XWH-12-1-0159/BC112431, W81XWH-15-1-0271, and W81XWH-15-1-0272. The Russian team thanks RSF grant (19-13-00047).

References

[1] P. Nikolaou, B.M. Goodson, E.Y. Chekmenev, NMR hyperpolarization techniques for biomedicine, Chem. Eur. J. 21 (2015) 3156–3166.
[2] D.A. Barskiy, A.M. Coffey, P. Nikolaou, D.M. Mikhaylov, B.M. Goodson, R.T. Branca, G.J. Lu, M.G. Shapiro, V.-V. Telkki, V.V. Zhivonitko, I.V. Koptyug, O.G. Salnikov, K.V. Kovtunov, V.I. Bukhtiyarov, M.S. Rosen, M.J. Barlow, S. Safavi, I.P. Hall, L. Schröder, E.Y. Chekmenev, NMR hyperpolarization techniques of gases, Chem. Eur. J. 23 (2017) 725–751.
[3] B.M. Goodson, N. Whiting, A.M. Coffey, P. Nikolaou, F. Shi, B.M. Gust, M.E. Gemeinhardt, R.V. Shchepin, J.G. Skinner, J.R. Birchall, M.J. Barlow, E.Y. Chekmenev, Hyperpolarization methods for MRS, Emagres 4 (2015) 797–810.

[4] P. Nikolaou, A.M. Coffey, L.L. Walkup, B.M. Gust, N. Whiting, H. Newton, S. Barcus, I. Muradyan, M. Dabaghyan, G.D. Moroz, M. Rosen, S. Patz, M.J. Barlow, E.Y. Chekmenev, B.M. Goodson, Near-unity nuclear polarization with an 'open-source' ^{129}Xe hyperpolarizer for NMR and MRI, Proc. Natl. Acad. Sci. USA 110 (2013) 14150–14155.

[5] J.P. Mugler, T.A. Altes, Hyperpolarized ^{129}Xe MRI of the human lung, J. Magn. Reson. Imaging 37 (2013) 313–331.

[6] B.M. Goodson, Nuclear magnetic resonance of laser-polarized noble gases in molecules, materials, and organisms, J. Magn. Reson. 155 (2002) 157–216.

[7] K. Golman, R. in't Zandt, M. Thaning, Real-time metabolic imaging, Proc. Natl. Acad. Sci. USA 103 (2006) 11270–11275.

[8] S.E. Day, M.I. Kettunen, F.A. Gallagher, D.E. Hu, M. Lerche, J. Wolber, K. Golman, J.H. Ardenkjaer-Larsen, K.M. Brindle, Detecting tumor response to treatment using hyperpolarized C-13 magnetic resonance imaging and spectroscopy, Nat. Med. 13 (2007) 1382–1387.

[9] J.H. Ardenkjaer-Larsen, B. Fridlund, A. Gram, G. Hansson, L. Hansson, M.H. Lerche, R. Servin, M. Thaning, K. Golman, Increase in signal-to-noise ratio of > 10,000 times in liquid-state NMR, Proc. Natl. Acad. Sci. USA 100 (2003) 10158–10163.

[10] E. Cavallari, C. Carrera, M. Sorge, G. Bonne, A. Muchir, S. Aime, F. Reineri, The ^{13}C hyperpolarized pyruvate generated by ParaHydrogen detects the response of the heart to altered metabolism in real time, Sci. Rep. 8 (2018) 8366.

[11] S.J. Nelson, J. Kurhanewicz, D.B. Vigneron, P.E.Z. Larson, A.L. Harzstark, M. Ferrone, M. van Criekinge, J.W. Chang, R. Bok, I. Park, G. Reed, L. Carvajal, E.J. Small, P. Munster, V.K. Weinberg, J.H. Ardenkjaer-Larsen, A.P. Chen, R.E. Hurd, L.I. Odegardstuen, F.J. Robb, J. Tropp, J.A. Murray, Metabolic imaging of patients with prostate cancer using hyperpolarized 1-C-13 pyruvate, Sci. Transl. Med. 5 (2013) 198ra108.

[12] R.V. Shchepin, J.R. Birchall, N.V. Chukanov, K.V. Kovtunov, I.V. Koptyug, T. Theis, W.S. Warren, J.G. Gelovani, B.M. Goodson, S. Shokouhi, M.S. Rosen, Y.-F. Yen, W. Pham, E.Y. Chekmenev, Hyperpolarizing concentrated metronidazole $^{15}NO_2$ group over six chemical bonds with more than 15% polarization and 20 minute lifetime, Chem. Eur. J. 25 (2019) 8829–8836.

[13] J.M. Wild, K. Teh, N. Woodhouse, M.N.J. Paley, S. Fichele, N. de Zanche, L. Kasuboski, Steady-state free precession with hyperpolarized He-3: experiments and theory, J. Magn. Reson. 183 (2006) 13–24.

[14] E. Babcock, I. Nelson, S. Kadlecek, B. Driehuys, L.W. Anderson, F.W. Hersman, T. G. Walker, Hybrid spin-exchange optical pumping of He-3, Phys. Rev. Lett. 91 (2003) 4.

[15] W.C. Chen, T.R. Gentile, Q. Ye, T.G. Walker, E. Babcock, On the limits of spin-exchange optical pumping of He-3, J. Appl. Phys. 116 (2014) 6.

[16] G.E. Pavlovskaya, Z.I. Cleveland, K.F. Stupic, R.J. Basaraba, T. Meersmann, Hyperpolarized krypton-83 as a contrast agent for magnetic resonance imaging, Proc. Natl. Acad. Sci. USA 102 (2005) 18275–18279.

[17] M.S. Albert, G.D. Cates, B. Driehuys, W. Happer, B. Saam, C.S. Springer, A. Wishnia, Biological magnetic-resonance-imaging using laser polarized Xe-129, Nature 370 (1994) 199–201.

[18] B. Driehuys, S. Martinez-Jimenez, Z.I. Cleveland, G.M. Metz, D.M. Beaver, J.C. Nouls, S.S. Kaushik, R. Firszt, C. Willis, K.T. Kelly, J. Wolber, M. Kraft, H.P. McAdams, Chronic obstructive pulmonary disease: safety and tolerability of hyperpolarized Xe-129 MR imaging in healthy volunteers and patients, Radiology 262 (2012) 279–289.

[19] J. Kurhanewicz, D.B. Vigneron, K. Brindle, E.Y. Chekmenev, A. Comment, C.H. Cunningham, R.J. DeBerardinis, G.G. Green, M.O. Leach, S.S. Rajan, R.R. Rizi, B.D. Ross, W.S. Warren, C.R. Malloy, Analysis of cancer metabolism by imaging hyperpolarized nuclei: prospects for translation to clinical research, Neoplasia 13 (2011) 81–97.

[20] I. Muradyan, J.P. Butler, M. Dabaghyan, M. Hrovat, I. Dregely, I. Ruset, G.P. Topulos, E. Frederick, H. Hatabu, W.F. Hersman, S. Patz, Single-breath xenon polarization transfer contrast (SB-XTC): Implementation and initial results in healthy humans, J. Magn. Reson. Imaging 37 (2013) 457–470.

[21] J.P. Butler, S.H. Loring, S. Patz, A. Tsuda, D.A. Yablonskiy, S.J. Mentzer Evidence for Adult Lung Growth in Humans, N. Engl. J. Med. 367 (2012) 244–247.

[22] S. Patz, I. Muradian, M.I. Hrovat, I.C. Ruset, G. Topulos, S.D. Covrig, E. Frederick, H. Hatabu, F.W. Hersman, J.P. Butler, Human pulmonary imaging and spectroscopy with hyperpolarized Xe-129 at 0.2T, Acad. Radiol. 15 (2008) 713–727.

[23] J.M. Wild, H. Marshall, X. Xu, G. Norquay, S.R. Parnell, M. Clemence, P.D. Griffiths, J. Parra-Robles, Simultaneous imaging of lung structure and function with triple-nuclear hybrid MR imaging, Radiology 267 (2013) 251–255.

[24] S.S. Kaushik, Z.I. Cleveland, G.P. Cofer, G. Metz, D. Beaver, J. Nouls, M. Kraft, W. Auffermann, J. Wolber, H.P. McAdams, B. Driehuys, Diffusion-weighted hyperpolarized Xe-129 MRI in healthy volunteers and subjects with chronic obstructive pulmonary disease, Magn. Reson. Med. 65 (2011) 1155–1165.

[25] B. Driehuys, Crossing the chasm(s): demonstrating the clinical value of hyperpolarized gas MRI, Acad. Radiol. 24 (2017) 1–3.

[26] C. Witte, L. Schroder, NMR of hyperpolarised probes, NMR Biomed. 26 (2013) 788–802.

[27] L.L. Walkup, J.C. Woods, Translational applications of hyperpolarized ^{3}He and ^{129}Xe, NMR Biomed. 27 (2014) 1429–1438.

[28] T.G. Walker, Fundamentals of spin-exchange optical pumping, J. Phys. Conf. Ser. 294 (2011) 012001.

[29] T.G. Walker, W. Happer, Spin-exchange optical pumping of noble-gas nuclei, Rev. Mod. Phys. 69 (1997) 629–642.

[30] B. Driehuys, G.D. Cates, E. Miron, K. Sauer, D.K. Walter, W. Happer, High-volume production of laser-polarized Xe-129, Appl. Phys. Lett. 69 (1996) 1668–1670.

[31] I. Saha, P. Nikolaou, N. Whiting, B.M. Goodson, Characterization of violet emission from Rb optical pumping cells used in laser-polarized xenon NMR experiments, Chem. Phys. Lett. 428 (2006) 268–276.

[32] A.L. Zook, B.B. Adhyaru, C.R. Bowers, High capacity production of > 65% spin polarized xenon-129 for NMR spectroscopy and imaging, J. Magn. Reson. 159 (2002) 175–182.

[33] I.C. Ruset, S. Ketel, F.W. Hersman, Optical pumping system design for large production of hyperpolarized Xe-129, Phys. Rev. Lett. 96 (2006) 053002.

[34] G. Schrank, Z. Ma, A. Schoeck, B. Saam, Characterization of a low-pressure high-capacity Xe-129 flow-through polarizer, Phys. Rev. A 80 (2009) 063424.

[35] P. Nikolaou, A.M. Coffey, K. Ranta, L.L. Walkup, B. Gust, M.J. Barlow, M.S. Rosen, B.M. Goodson, E.Y. Chekmenev, Multi-dimensional mapping of spin-exchange optical pumping in clinical-scale batch-mode ^{129}Xe hyperpolarizers, J. Phys. Chem. B 118 (2014) 4809–4816.

[36] G. Norquay, G.J. Collier, M. Rao, N.J. Stewart, J.M. Wild, ^{129}Xe-Rb spin-exchange optical pumping with high photon efficiency, Phys. Rev. Lett. 121 (2018) 153201.

[37] C. Ottinger, R. Scheps, G.W. York, A. Gallagher, Broadening of the Rb resonance lines by the noble gases, Phys. Rev. A 11 (1975) 14.

[38] A.H. Couture, T.B. Clegg, B. Driehuys, Pressure shifts and broadening of the Cs D1 and D2 lines by He, N_2, and Xe at densities used for optical pumping and spin exchange polarization, J. Appl. Phys. 104 (2008) 6.

[39] A.B.-A. Baranga, S. Appelt, C.J. Erickson, A.R. Young, W. Happer, Alkali-metal-atom polarization imaging in high-pressure optical-pumping cells, Phys. Rev. A 58 (1998) 2282.

[40] M.E. Wagshul, T.E. Chupp, Laser optical pumping of high-density Rb in polarized ^{3}He targets, Phys. Rev. A 49 (1994) 3854–3869.

[41] W.C. Chen, T.R. Gentile, T.G. Walker, E. Babcock, Spin-exchange optical pumping of ^{3}He with Rb-K mixtures and pure K, Phys. Rev. A 75 (2007) 013416.

[42] I.A. Nelson, T.G. Walker, Rb-Xe spin relaxation in dilute Xe mixtures, Phys. Rev. A 65 (2001) 012712.

[43] H. Zhu, I.C. Ruset, F.W. Hersman, Spectrally narrowed external-cavity high-power stack of laser diode arrays, Opt. Lett. 30 (2005) 1342–1344.

[44] P. Nikolaou, N. Whiting, N.A. Eschmann, K.E. Chaffee, B.M. Goodson, Generation of laser-polarized xenon using fiber-coupled laser-diode arrays narrowed with integrated volume holographic gratings, J. Magn. Reson. 197 (2009) 249–254.

[45] B. Chann, I. Nelson, T.G. Walker, Frequency-narrowed external-cavity diode-laser-array bar, Opt. Lett. 25 (2000) 1352–1354.

[46] E. Babcock, B. Chann, I.A. Nelson, T.G. Walker, Frequency-narrowed diode array bar, Appl. Opt. 44 (2005) 3098–3104.

[47] J.N. Zerger, M.J. Lim, K.P. Coulter, T.E. Chupp, Polarization of ^{129}Xe with high power external-cavity laser diode arrays, Appl. Phys. Lett. 76 (2000) 1798–1800.

[48] G.W.C. Kaye, T.H. Laby, Tables of physical and chemical constants and some mathematical functions, Longman Sci. Tech. (1995).

[49] C. Witte, M. Kunth, F. Rossella, L. Schröder, Observing and preventing rubidium runaway in a direct-infusion xenon-spin hyperpolarizer optimized for high-resolution hyper-CEST (chemical exchange saturation transfer using hyperpolarized nuclei) NMR, J. Chem. Phys. 140 (2014) 084203.

[50] M.S. Freeman, K. Emami, B. Driehuys, Characterizing and modeling the efficiency limits in large-scale production of hyperpolarized ^{129}Xe, Phys. Rev. A 90 (2014) 023406.

[51] M.A. Antonacci, A. Burant, W. Wagner, R.T. Branca, Depolarization of nuclear spin polarized ^{129}Xe gas by dark rubidium during spin-exchange optical pumping, J. Magn. Reson. 279 (2017) 60–67.

[52] N.J. Stewart, H.-F. Chan, P.J.C. Hughes, F.C. Horn, G. Norquay, M. Rao, D.P. Yates, R.H. Ireland, M.Q. Hatton, B.A. Tahir, P. Ford, A.J. Swift, R. Lawson, H. Marshall, G.J. Collier, J.M. Wild, Comparison of ^{3}He and ^{129}Xe MRI for evaluation of lung microstructure and ventilation at 1.5T, J. Magn. Reson. Imaging 48 (2018) 632–642.

[53] L.L. Walkup, R.P. Thomen, T.G. Akinyi, E. Watters, K. Ruppert, J.P. Clancy, J.C. Woods, Z.I. Cleveland, Feasibility, tolerability and safety of pediatric hyperpolarized ^{129}Xe magnetic resonance imaging in healthy volunteers and children with cystic fibrosis, Pediatr. Radiol. 46 (2016) 1651–1662.

[54] J.S. Six, T. Hughes-Riley, K.F. Stupic, G.E. Pavlovskaya, T. Meersmann, Pathway to cryogen free production of hyperpolarized Krypton-83 and Xenon-129, PLoS ONE 7 (2012) 16.

[55] J.R. Birchall, P. Nikolaou, A.M. Coffey, B.E. Kidd, R.K. Irwin, M. Murphy, M. Molway, L.B. Bales, B.M. Goodson, M.J. Barlow, E.Y. Chekmenev, Batch-mode clinical-scale optical hyperpolarization of Xenon-129 using an aluminum jacket with rapid temperature ramping, Anal. Chem. 92 (2020) 4309–4316.

[56] P. Nikolaou, A.M. Coffey, M.J. Barlow, M. Rosen, B.M. Goodson, E.Y. Chekmenev, Temperature-ramped ^{129}Xe spin exchange optical pumping, Anal. Chem. 86 (2014) 8206–8212.

[57] P. Nikolaou, A.M. Coffey, L.L. Walkup, B. Gust, C. LaPierre, E. Koehnemann, M.J. Barlow, M.S. Rosen, B.M. Goodson, E.Y. Chekmenev, A 3D-printed high power nuclear spin polarizer, J. Am. Chem. Soc. 136 (2014) 1636–1642.

[58] P. Nikolaou, A.M. Coffey, L.L. Walkup, B.M. Gust, N.R. Whiting, H. Newton, I. Muradyan, M. Dabaghyan, K. Ranta, G. Moroz, S. Patz, M.S. Rosen, M.J. Barlow,

E.Y. Chekmenev, B.M. Goodson, XeNA: an automated 'open-source' ^{129}Xe hyperpolarizer for clinical use, Magn. Reson. Imaging 32 (2014) 541–550.
[59] H. Fujiwara, A. Kimura, Y. Yanagawa, T. Kamiya, M. Hattori, T. Hiraga, Relaxation behavior of laser-polarized ^{129}Xe gas: size dependency and wall effect of the T_1 relaxation time in glass and gelatin bulbs, J. Magn. Reson. 150 (2001) 156–160.
[60] S.R. Breeze, S. Lang, I. Moudrakovski, C.I. Ratcliffe, J.A. Ripmeester, B. Simard, G. Santyr, Coatings for optical pumping cells and extending the lifetime of hyperpolarized xenon, J. Appl. Phys. 86 (1999) 4040–4042.
[61] S.R. Breeze, S. Lang, I. Moudrakovski, C.I. Ratcliffe, J.A. Ripmeester, G. Santyr, B. Simard, I. Zuger, Coatings for optical pumping cells and short-term storage of hyperpolarized xenon, J. Appl. Phys. 87 (2000) 8013–8017.
[62] M. He, S.H. Robertson, S.S. Kaushik, M.S. Freeman, R.S. Virgincar, J. Davies, J. Stiles, W.M. Foster, H.P. McAdams, B. Driehuys, Dose and pulse sequence considerations for hyperpolarized ^{129}Xe ventilation MRI, Magn. Reson. Imaging 33 (2015) 877–885.
[63] J.G. Skinner, K. Ranta, N. Whiting, A.M. Coffey, P. Nikolaou, M.S. Rosen, E.Y. Chekmenev, P.G. Morris, M.J. Barlow, B.M. Goodson, High Xe density, high photon flux, stopped-flow spin-exchange optical pumping: simulations versus experiments, J. Magn. Reson. 312 (2020) 106686.
[64] Y. Shukla, A. Wheatley, M. Kirby, S. Svenningsen, A. Farag, G.E. Santyr, N.A.M. Paterson, D.G. McCormack, G. Parraga, Hyperpolarized ^{129}Xe magnetic resonance imaging: tolerability in healthy volunteers and subjects with pulmonary disease, Acad. Radiol. 19 (2012) 941–951.

Journal of Magnetic Resonance 312 (2020) 106686

Contents lists available at ScienceDirect

Journal of Magnetic Resonance

journal homepage: www.elsevier.com/locate/jmr

High Xe density, high photon flux, stopped-flow spin-exchange optical pumping: Simulations versus experiments

Jason G. Skinner [a,1], Kaili Ranta [b,2], Nicholas Whiting [c], Aaron M. Coffey [d], Panayiotis Nikolaou [e], Matthew S. Rosen [f,g,h], Eduard Y. Chekmenev [i,j], Peter G. Morris [k], Michael J. Barlow [a], Boyd M. Goodson [b,*]

[a] Division of Respiratory Medicine, School of Medicine, Queen's Medical Centre, University of Nottingham, Nottingham, NG7 2UH, UK
[b] Department of Chemistry and Biochemistry, Southern Illinois University Carbondale, Carbondale, IL, 62901, USA
[c] Department of Physics & Astronomy and Department of Molecular & Cellular Biosciences, Rowan University, Glassboro, NJ 08028, USA
[d] Vanderbilt University Institute of Imaging Science (VUIIS), Department of Radiology and Radiological Sciences, Vanderbilt-Ingram Cancer Center (VICC), Department of Biomedical Engineering, Department of Physics and Astronomy, Vanderbilt University Medical Center, Nashville, TN, 37232, USA
[e] XeUS Technologies LTD, Pano Lakatamia, Nicosia 2312, Cyprus
[f] Athinoula A. Martinos Center for Biomedical Imaging, Department of Radiology, Massachusetts General Hospital, 149 13th Street, Charlestown, MA 02129, USA
[g] Department of Radiology, Harvard Medical School, Boston, MA 02115, USA
[h] Department of Physics, Harvard University, Cambridge, MA 02138, USA
[i] Russian Academy of Sciences, Leninskiy Prospekt 14, 119991 Moscow, Russia
[j] Department of Chemistry, Integrative Biosciences (Ibio), Wayne State University, Karmanos Cancer Institute (KCI), Detroit, MI, 48202, United States
[k] Sir Peter Mansfield Imaging Centre, School of Physics & Astronomy, University of Nottingham, Nottingham, NG7 2RD, UK

ARTICLE INFO

Article history:
Received 31 December 2019
Accepted 7 January 2020
Available online 16 January 2020

Keywords:
Xenon
SEOP
Lung imaging
Hyperpolarised

ABSTRACT

Spin-exchange optical pumping (SEOP) can enhance the NMR sensitivity of noble gases by up to five orders of magnitude at Tesla-strength magnetic fields. SEOP-generated hyperpolarised (HP) ^{129}Xe is a promising contrast agent for lung imaging but an ongoing barrier to widespread clinical usage has been economical production of sufficient quantities with high ^{129}Xe polarisation. Here, the 'standard model' of SEOP, which was previously used in the optimisation of continuous-flow ^{129}Xe polarisers, is modified for validation against two Xe-rich stopped-flow SEOP datasets. We use this model to examine ways to increase HP Xe production efficiency in stopped-flow ^{129}Xe polarisers and provide further insight into the underlying physics of Xe-rich stopped-flow SEOP at high laser fluxes.

© 2020 Elsevier Inc. All rights reserved.

1. Introduction

Spin-exchange optical pumping (SEOP), a method of nuclear spin hyperpolarisation [1,2], can be used to enhance the NMR detection sensitivity of noble gases by up to five orders of magnitude at Tesla-strength magnetic fields [3]. Noble gas isotopes polarised by SEOP include ^{21}Ne, [4] ^{83}Kr [5], ^{131}Xe [6], ^{131m}Xe [7], ^{3}He [8], and ^{129}Xe [1–3]. For biomedical applications, hyperpolarised (HP) ^{129}Xe has emerged as a versatile and viable agent, with current MR based biomedical applications and drivers for the technology including lung imaging [9–16], brain imaging [17–19], the study of brown adipose tissue (BAT) [20], and various functionalised host-guest biosensors [21–32], a number of which are currently reaching a high level of maturity in *in vitro* studies of disease [33,34]. Each of these applications take advantage of various properties of ^{129}Xe including its moderate tissue solubility, exquisite chemical shift sensitivity, avidity for binding to proteins and other molecular hosts, its lipophilic tendencies, non-toxic nature, and sufficiently long *in vivo* T_1 relaxation times that permit delivery to distal tissues–all of which have been discussed previously in a number of reviews [35–40].

Production of HP ^{129}Xe by SEOP begins with the optical pumping of alkali metal (typically Rb) valence electrons using circularly polarised light resonant at the D_1 transition. This process quickly leads to a highly polarised Rb electronic ground state that subsequently polarises the ^{129}Xe nuclear spins through a combination of binary and molecular van der Waals (vdW) collisions wherein spin-exchange occurs, mediated by the Fermi contact hyperfine interaction [41,35,3,42,2].

A major barrier to generating high ^{129}Xe polarisations at high concentrations – of particular value for lung imaging – is the high

* Corresponding author.
E-mail address: bgoodson@chem.siu.edu (B.M. Goodson).
[1] Present address: Department of Nuclear Medicine, Klinikum rechts der Isar, The Technical University of Munich (TUM), Munich, Germany.
[2] Present address: The Ohio State University College of Medicine, Columbus, OH, USA.

https://doi.org/10.1016/j.jmr.2020.106686
1090-7807/© 2020 Elsevier Inc. All rights reserved.

rate of Xe-induced Rb spin order destruction (hereafter referred to as spin destruction (SD)) that scales with Xe density [3]. Continuous-flow (CF) polarisers – the original method for producing large (~liter*atm) quantities of polarised ^{129}Xe [43] – usually approach this issue by polarising at low Xe concentrations (i.e. typically 1 or 2% of the gas mix, with helium forming the dominant part because of its low SD rate [44,43,45–48]. See Ref [49] for a notable exception), using cryogenic separation methods to increase the HP Xe concentration post-SEOP [43]. Historically however, this method has not produced the ^{129}Xe polarisations predicted by theory e.g. with Norquay et al. producing 12% polarisation against a predicted 24% during an optimisation study [45], among other cases [43,47].

In 2014, this discrepancy between theory and experiment in the CF approach was addressed by Freeman et al. [46] after they hypothesized that the continuous flow of a cold noble gas over molten Rb may inherently promote the formation of deleterious Rb clusters within the optical pumping (OP) cell [46]. The Rb clusters were expected to impact the system by depolarising both the Rb and Xe spins, and by scattering the incident light of the OP laser. Additionally, it was anticipated that the use of high resonant flux at the D_1 transition may accelerate Rb cluster formation [46]. By incorporating Rb clusters into the existing theoretical framework [50,45], the authors were able to more accurately model CF SEOP over a range of OP cell sizes and a range of laser linewidths [46]. Additionally, after modifying the experiment to minimise the formation of the clusters – primarily via a Rb pre-saturator (precedent for which existed with the rationale that it maintains a more stable Rb density [44]) – they were able to substantially improve their production rates and bring P_{Xe} performance in line with the model. While Rb clusters have yet to be detected *in situ* [51], that work provided both compelling evidence for the existence of Rb clusters in CF polarisers, and a pathway through which to improve performance.

Clinical-scale Xe-rich stopped-flow (SF) SEOP, an alternate approach to producing large volumes of HP ^{129}Xe, is now well-established in the literature [52–58], and has been used to produce very high P_{Xe} values (up to 90.9% ± 5.2% [53]) – even at high Xe concentrations i.e. 74% ± 7% at 1000 Torr [55], despite the prevailing high rates of Xe-induced SD. At the cost of having the HP Xe diluted by the presence of buffer gases (which are minimised for Xe-rich gas mixtures), the ability to avoid cryo-collection makes SEOP devices simpler and easier to automate, and reduces the concern of ^{129}Xe hyperpolarisation depletion during storage or phase changes. SF SEOP has been modelled previously (e.g., [59,60]), but rarely in the Xe-rich regime [61,62], particularly in the context of optical pumping with high resonant flux. Here, two sets of simulations of SF SEOP – hereafter referred to as 'Sim1' and 'Sim2' – are presented and compared to two literature datasets. Sim1 [61,62] is a 2D (z,r) Mathematica-based approach that was originally conducted to aid interpretation of our collaboration's initial SF results [52] (dubbed 'Dataset1' in this contribution). Sim2 is a 1D (z) Python-based approach that draws on the theoretical framework used in the optimisation of the CF ^{129}Xe polarisers described above [45,46]. In the present work, both Sim1 and Sim2 are used to model Dataset1 [52]; Sim2 alone is used to model 'Dataset2', which are the experimental results of a multi-parameter optimisation study using our consortium's 'XeUS' SF polariser [56].

Sim1 and Sim2 are found to provide excellent qualitative and quantitative descriptions of Xe-rich SF SEOP, including the inverse relationship between the optimal (externally measured) cell temperature for SEOP (T_{opt}) and Xe density ([Xe]) that characterises this regime – an effect that was previously exploited to achieve high polarisations [52,56]. Furthermore, Sim2 results revealed that under certain conditions the simulations trended towards a 'universally optimal' amount of laser absorption at P_{max}, and these results may i) help provide both an explanation for the observed interplay of laser linewidth, T_{opt}, and [Xe], in the context of optimising the photon-to-[Rb] ratio (discussed below), and ii) provide a new way to quickly optimise SF polarisers. Finally, the validated Sim2 is used to investigate how to modify the design and operation of clinical-scale SF polarisers to further improve their performance. The simulations considered cell temperature, cell geometry, laser linewidth, laser power, gas mixture, and gas pressure, with results including that reduction of laser linewidth (and therefore increasing resonant intensity) improves P_{Xe} disproportionately more at higher [Xe].

2. Theory

A theoretical framework for SEOP by Wagshul and Chupp [50] was updated and used as the basis for modelling of CF polarisers by Norquay et al. in 2013 [45], with Freeman et al. introducing the Rb cluster terms in 2014 [46]. Sim2 is based largely on these models, and as such the pertinent aspects are recounted here. Sim1 drew on earlier literature sources, detailed at the end of the theory section.

2.1. Optical Pumping

The optical pumping rate, γ_{OP}, is dependent on the overlap of the Rb absorption cross section, σ_s, and the photon flux of the laser, Φ, as it traverses the length, z, of the optical pumping cell:

$$\gamma_{OP}(z,\nu) = \int \Phi(z,\nu)\sigma_s(\nu)d\nu. \tag{1}$$

σ_s is commonly approximated with a Lorentzian line-shape[3] that varies as a function of frequency, ν, in the following way:

$$\sigma_s(\nu) = \sigma_0 \frac{\Gamma_{Rb}^2}{4(\nu-\nu_{D_1})^2+\Gamma_{Rb}^2}, \tag{2}$$

where Γ_{Rb} is the FWHM of the pressure-broadened Rb cross section which has an (air-referenced) centre frequency ν_{D_1} of c/794.77 nm [64]. The peak amplitude σ_0 is given by:

$$\sigma_0 = \frac{2r_e c f}{\Gamma_{Rb}}, \tag{3}$$

where r_e is the classical electron radius, c is the speed of light, and f is the oscillator strength of the D_1 transition, which has been shown to have a value of 0.337 [65,45].

Xe, N_2, and He – gases often present in SEOP OP cells – pressure-broaden the Rb transition at different rates. These values were measured by Romalis et al. to be 18.9, 17.8, and 18 GHz/amagat for ^{129}Xe, N_2, and He, respectively [63]. The total broadening in the presence of all three gases is thus:

$$\Gamma_{Rb}[\text{GHz}] = 18.9[\text{Xe}] + 17.8[\text{N}_2] + 18.0[\text{He}], \tag{4}$$

where square brackets indicate the density of the gas in amagats.

The spectral profile of the laser was approximated with a Gaussian line-shape and varies with frequency according to:

$$I(\nu) = I_0 e^{-\left(\frac{\nu-\nu_{Las}}{\Gamma_{Las}}\right)^2}, \tag{5}$$

where ν_{Las} is the centre frequency of the laser, Γ_{Las} is the standard deviation of the Gaussian laser spectrum,[4] and I_0 is the beam intensity at the cell front given by:

[3] Out of simplicity, deviations from a Lorentzian line-shape of the Rb absorption profile [63] were not included in the present simulations.

[4] conversion of FWHM to standard deviation was performed using: $\Gamma_{Las} = \frac{Las_{FWHM}}{[2\sqrt{2\ln(2)}]}$

$$I_0 = \frac{P}{Ah\sqrt{\pi}\Gamma_{\mathrm{Las}} v_{\mathrm{Las}}}, \tag{6}$$

where h is the Planck constant, P is the power, and A is the area of laser illumination which is assumed here to be equal to the cross sectional area of the OP cell. The photon flux Φ through the OP cell has been estimated as [45]:

$$\Phi(z,\nu) = I(\nu)e^{[-\lambda^{-1}(z,\nu)z]}, \tag{7}$$

where λ^{-1} is the position-dependent absorption length. For a cell illuminated by a circularly polarised beam of positive helicity σ^+, λ^{-1} is defined as [50]:

$$\lambda^{-1}(z,\nu) = \sigma_s(\nu)[\mathrm{Rb}](1 - P_{\mathrm{Rb}}(z)), \tag{8}$$

in which [Rb] is the Rb vapour number density in cm^{-3} and $P_{\mathrm{Rb}}(z)$ is the position dependent Rb polarisation. [Rb] in this case was modelled as [66]:

$$[\mathrm{Rb}] = \frac{10^{26.180-(\frac{4040}{T})}}{T}, \tag{9}$$

where T is the temperature in Kelvin.

2.2. Rubidium Polarisation

The Rb polarisation, $P_{\mathrm{Rb}}(z)$, is a function of the optical pumping rate, $\gamma_{\mathrm{OP}}(z,\nu)$, and the Rb spin destruction Γ_{SD}:

$$P_{\mathrm{Rb}}(z) = \frac{\gamma_{\mathrm{OP}}(z,\nu)}{\gamma_{\mathrm{OP}}(z,\nu) + \Gamma_{\mathrm{SD}}}. \tag{10}$$

Away from the walls of the OP cell, Γ_{SD} can occur by two mechanisms: (1) binary collisions with atoms or (2) via the formation of short-lived Rb-Xe vdW molecules. The binary term is:

$$\Gamma_{\mathrm{SD}}^{\mathrm{BC}} = \sum_i [\mathrm{G_i}]\kappa_{\mathrm{SD}}^{\mathrm{Rb-i}}, \tag{11}$$

where $\kappa_{\mathrm{SD}}^{\mathrm{Rb-i}}$ is the Rb SD cross section for Rb binary collisions with each of the gas atoms present in the cell, and $[\mathrm{G_i}]$ is the atomic number density of each gas. Cross section values used in each simulation can be found in Table 1.

The Rb SD rate due to vdW Rb-Xe molecules has been estimated as [45][5]:

$$\Gamma_{\mathrm{SD}}^{\mathrm{vdW}} = \left(\frac{66183}{1 + 0.92\frac{[\mathrm{N_2}]}{[\mathrm{Xe}]} + 0.31\frac{[\mathrm{He}]}{[\mathrm{Xe}]}}\right)\left(\frac{T}{423}\right)^{-2.5} \tag{12}$$

where square brackets indicate gas number density in m^{-3}. Gathering expressions (11) and (12), the total Rb SD is then:

$$\Gamma_{\mathrm{SD}} = \Gamma_{\mathrm{SD}}^{\mathrm{BC}} + \Gamma_{\mathrm{SD}}^{\mathrm{vdW}}. \tag{13}$$

2.3. Xenon Polarisation

The Rb-Xe spin-exchange (SE) rate, γ_{SE}, is the sum of binary and vdW terms, and is given by the following expression [45,46]:

$$\gamma_{\mathrm{SE}} = \gamma_{\mathrm{SE}}^{\mathrm{vdW}} + \gamma_{\mathrm{SE}}^{\mathrm{BC}} = \left(\frac{1}{\sum_i \left(\frac{[\mathrm{G_i}]}{\xi_i}\right)} + \kappa_{\mathrm{SE}}^{\mathrm{Rb-Xe}}\right)[\mathrm{Rb}] \tag{14}$$

$$= (\kappa_{\mathrm{SE}}^{\mathrm{vdW}} + \kappa_{\mathrm{SE}}^{\mathrm{BC}})[\mathrm{Rb}], \tag{15}$$

[5] based on works by Ruset [72] and Nelson et al. [71]

Table 1
Gas-specific binary SD rates as used in Sim1 and Sim2. Units are $\mathrm{cm}^3\ \mathrm{s}^{-1}$.

Cross section	Sim1 value	Sim2 value
$\kappa_{\mathrm{SD}}^{\mathrm{Rb-Rb}}$	–	4.2×10^{-13} [67]
$\kappa_{\mathrm{SD}}^{\mathrm{Rb-He}}$	–	$3.45 \times 10^{-19}(T/298\ \mathrm{K})^{4.26}$ [67]
$\kappa_{\mathrm{SD}}^{\mathrm{Rb-N_2}}$	9.4×10^{-18} [68]	$3.44 \times 10^{-18}(T/298\ \mathrm{K})^{3}$ [69]
$\kappa_{\mathrm{SD}}^{\mathrm{Rb-Xe}}$	5.2×10^{-15} [70]	$6.02 \times 10^{-15}(T/298\ \mathrm{K})^{1.17}$ [71]

where ξ_i is the vdW rate for each gas atom, with number density again given by $[\mathrm{G_i}]$. The vdW rates are in Table 2. $\kappa_{\mathrm{SE}}^{\mathrm{BC}}$ is the binary collision SE cross section and has been reported to be $2.17 \times 10^{-16}\mathrm{cm}^3\mathrm{s}^{-1}$ [75,45].

In a CF SEOP polariser, the nuclear spin polarisation of ^{129}Xe generated through SE with polarised Rb atoms after a given residence time t_{res} is [43]:

$$P_{\mathrm{Xe}}(t_{\mathrm{res}}) = \frac{\gamma_{\mathrm{SE}}}{\gamma_{\mathrm{SE}} + \Gamma}\langle P_{\mathrm{Rb}}\rangle(1 - \exp^{-(\gamma_{\mathrm{SE}}+\Gamma)t_{\mathrm{res}}}), \tag{16}$$

where t_{res} is the average amount of time Xe atoms spend in the OP cell as they flow from the gas cylinder to the cold finger, Γ is the ^{129}Xe SD rate, and $\langle P_{\mathrm{Rb}}\rangle$ is the spatially averaged Rb polarisation within the OP cell. In most CF SEOP setups, Γ is dominated by wall relaxation and equal to $\frac{1}{T_1}$, therefore experimentally measured in-cell T_1 values can be used in the simulations to calculate Γ.

In SF SEOP, the SEOP gas mixture is held static within the OP cell, therefore t_{res} becomes the total OP time t:

$$P_{\mathrm{Xe}}(t) = \frac{\gamma_{\mathrm{SE}}}{\gamma_{\mathrm{SE}} + \Gamma}\langle P_{\mathrm{Rb}}\rangle(1 - \exp^{-(\gamma_{\mathrm{SE}}+\Gamma)t}), \tag{17}$$

and the ^{129}Xe nuclear spin polarisation P_{Xe} will reach steady state as t tends to infinity (~1 h in practice). Under this condition the terminal polarisation can be calculated as:

$$\lim_{t\to\infty} P_{\mathrm{Xe}} = \frac{\gamma_{\mathrm{SE}}}{\gamma_{\mathrm{SE}} + \Gamma}\langle P_{\mathrm{Rb}}\rangle. \tag{18}$$

Note that $\gamma_{\mathrm{SE}} + \Gamma$ is equal to–and quoted as–γ_{SEOP} in a number of publications.

2.4. Alternative Equation Forms Used in Sim1

Sim1 is an earlier simulation that used alternative forms for a number of the equations given above and these are detailed here. For the calculation of the D_1 linewidth a lineshift contribution was also considered [63]:

$$\nu_{D_1}[\mathrm{GHz}] = 377107.4 - 8.5[\mathrm{N_2}] - 5.05[\mathrm{Xe}] + 4.3[\mathrm{He}], \tag{19}$$

where the number densities of the gas species are in amagats. Line broadening (cf. Eq. (4)) was calculated as:

$$\Gamma_{\mathrm{Rb}}[\mathrm{GHz}] = 0.04 + 18.9[\mathrm{Xe}] + 17.8[\mathrm{N_2}] + 18.0[\mathrm{He}]. \tag{20}$$

[Rb] (cf. Eq. (9)) was calculated via:

$$P_V[\mathrm{Torr}] = 10^{(7.193-\frac{4040}{T})}, \tag{21}$$

Table 2
Gas-specific vdW rates (used only in Sim2).

Atomic species	vdW rate
ξ_{Xe}	5230 s^{-1} [73]
ξ_{N_2}	5700 s^{-1} [74]
ξ_{He}	17000 s^{-1} [43]

with T given in Kelvin and P_V standing for Rb vapour pressure. A comparison plot of Eqs. (9) and (21) is available in the ESI. Rb SD (cf. Eqs. (12) and (13)) was determined without the vdW contribution:

$$\Gamma_{SD} = \kappa_{SD}^{Rb-Xe}[Xe] + \kappa_{SD}^{Rb-N_2}[N_2], \tag{22}$$

using temperature independent binary cross section values of $\kappa_{SD}^{Rb-Xe} = 5.2 \times 10^{-15}$ cm^{3}s^{-1} and $\kappa_{SD}^{Rb-N_2} = 9.4 \times 10^{-18}$ cm^{3}s^{-1}, introduced by Bouchiat et al. and Wagshul et al. respectively [70,68].

The SE rate equation (cf. Eq. (14)) took the form of that given by Cates et al. [73,62]:

$$\gamma_{SE} = \left(\langle\sigma v\rangle + \frac{\gamma_M \zeta}{[Xe](1+br)}\right)[Rb], \tag{23}$$

where $\langle\sigma v\rangle = 3.7 \times 10^{-16}$ cm^{3}s^{-1} is the velocity-averaged binary SE cross section, $\gamma_M = 2.94 \times 10^4$ s^{-1} is an experimentally determined constant, $\zeta = 0.1791$ is a value that corresponds to Rb isotope distribution, and $br = 0.275[N_2]/[Xe]$ is a correction factor to account for the differential capacity of N_2 to facilitate formation and break-up of vdW complexes compared to Xe [73].

3. Methods

3.1. Dataset1

To collect Dataset1 [52], ^{129}Xe NMR signal intensity was measured as a function of external cell temperature (T_{cell}) and [Xe] using low-field *in situ* NMR spectroscopy. [Xe] ranged from 50 to 1400 Torr. Gas mixes were backfilled with N_2 to 2000 Torr total pressure at loading and contained in a 1" diameter cylindrical 'Rosen' style OP cell [60] with 75 cc inner cell volume. The B_0-field (32 G) was generated using a Helmholtz coil pair of 22" inner diameter and a Magritek Aurora NMR spectrometer was used for low-field NMR (^{129}Xe frequency: 37.5 kHz).

OP was performed using a TEC-cooled prototype 'Comet' (Newport/Spectra-Physics) fixed-frequency laser diode array (LDA). [76] Output at the OP cell was ~29 W with a spectral linewidth of 0.27 nm centred at 794.66 nm. The laser was specifically driven to have a 'blue-side' spectral offset from the Rb D_1 line to achieve maximum P_{Xe} under those conditions [76]. The LDA was fibre-coupled to the OP cell and a binocular circular polariser box (Coherent) which yielded a 85/15 straight/angled beam ratio was used to circularly polarise the light. A 2" mirror was present behind the cell to retro-reflect excess transmitted laser light back into the OP cell. This practice was found to provide up to a ~29% 'free' increase in P_{Xe} (under nominal conditions; dependent on T_{cell}) [77].

3.2. Dataset2

For Dataset2 [56], ^{129}Xe NMR signal intensity was measured as a function of T_{cell}, [Xe] (275 to 2000 Torr Xe, backfilled with N_2), *and* laser power (100, 125, 142 and 170 W). The laser had a spectral width of 0.3 nm and was centered at 794.8 nm. The measurements were made on board a clinical-scale polariser that has been described previously [56,55]. A Magritek Kea2 low-field NMR spectrometer was used to perform *in situ* NMR polarimetry at 47 kHz. The resulting ^{129}Xe spectra were calibrated against a doped (10 mM $CuSO_4$), thermally polarised water ^{1}H NMR spectrum (acquired with 200,000 averages) that was obtained at the same frequency and in a vessel of the same shape and volume (2"-diameter (500 cc) cell) [56].

Once steady-state ^{129}Xe polarisation curves were obtained, γ_{SEOP} (= $\gamma_{SE} + \Gamma$) values were extracted by fitting the data to Eq. (17). After SEOP, in-cell room-temperature (rt) measurements of T_1 were made by quickly cooling the OP cell down to rt (to minimise the Rb gas-phase concentration), turning off the laser, and acquiring *in situ* NMR spectra while P_{Xe} decayed.

3.3. Sim1

Sim1 simulations were performed using Mathematica (version 8.0.0.0) on a PC. For a given simulation, D_1 spectral width and center were calculated via Eqs. (19) and (20) with a Lorentzian frequency distribution. The simulated laser output was kept centered on the Rb D_1 line with a variable spectral width of 0.25–10 nm. A cylindrical cell was assumed (z, r) and light flux incident on the front of the cell, Φ, was amplitude-modulated in space using a flat 'top-hat' cross-sectional profile and modelled to decay with a Gaussian spatial profile near the cell walls (see Fig. 1). [Rb] was determined solely based on Eq. (21), and was kept homogeneous throughout the cell as no temperature gradients were included in the simulations. Only binary mixtures of Xe and N_2 were considered. [Xe] and [N_2] were determined assuming ideal gases loaded at 293 K.

P_{Rb} at a given position in the cell was determined as an instantaneous function of light flux according to Eq. (10). Light propagation through the cell cannot be calculated directly using Beer's law because polarised Rb atoms [↑] are transparent to circularly polarised light; therefore, light absorption must be determined based on the density of available absorbers, [↓], since the D_1 absorption cross section, σ_s, in Eq. (1) is defined using unpolarised light:

$$[\downarrow] = \frac{[Rb]}{2}(1 - P_{Rb}). \tag{24}$$

Light flux at a given position within the cell was calculated based on a finite number (~200–300) of discrete modified 'Beer's cell layers', where γ_{OP} in the first Beer's cell layer was calculated using Eq. (7) with the integration implemented by Riemann sum using 100–300 steps over ±250 GHz from center (~10 x FWHM), and used to calculate: i) the P_{Rb} value assigned to the first layer as a function of position across the face of the cell, ii) the resulting light attenuation, and iii) [↓] for the next 'Beer's cell layer'. The attenuated input

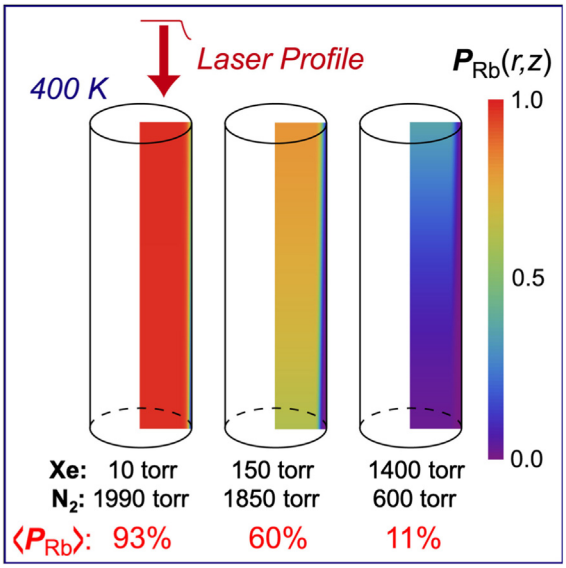


Fig. 1. Three selected simulation plots of P_{Rb} from Sim1: 10, 150, and 1400 Torr Xe with constant T_{cell} and total cell pressure (400 K and 2000 Torr). Each plot was generated with an input radial resolution of 200 with 199 total recursions representing the Rb cell polarisation at any one azimuthal angle. These values were then cylindrically integrated to estimate average Rb polarisation, $\langle P_{Rb} \rangle$, throughout the cell [62].

flux Φ_1 is then applied to the next layer (one step deeper into the cell) and that process is repeated over a total of 100–300 layers in the cell. Finally, the calculated P_{Rb} values can then be volume-averaged across the cell for the quantity $\langle P_{Rb}\rangle$ used to calculate P_{Xe}. Example output of such calculations can be seen in Fig. 1.

3.4. Sim2

Sim2 was written in Python (2.7.13) using the freely available Spyder editor (3.0.2) as contained in the Anaconda distribution. For a given simulation, the Rb D_1 was modelled to experience pressure broadening as given in Eq. (4) and assumed a Lorentzian spectral profile (Eq. (2)). Lineshift was not simulated, and the laser line – modelled with a Gaussian profile (Eq. (2)) – was centred on the D_1 transition at 794.77 nm. Incident light is assumed to be 100% polarised. A 1D cell was assumed (z), equivalent to considering the laser to have no cross-sectional variation in intensity. [Rb] was calculated via Eq. (9) and was modelled as constant throughout the cell. Binary mixtures of Xe and N_2 were considered in the simulation of Dataset1 and Dataset2. He was included in later exploratory simulations of Dataset2. [Xe], [N_2], and [He] were determined assuming ideal gases loaded at 293 K.

Due to the fact that P_{Rb} and γ_{OP} are functions of each other [P_{Rb} depends on γ_{OP} by Eq. (10), and γ_{OP} depends on P_{Rb} by Eqs. (1), (7) and (8)], $\langle P_{Rb}\rangle$ and γ_{OP} were determined using an equilibrium function approach: Eqs. (1), (2), (7), and (8) were combined to give the following integral [in accordance with Eqn. (1)] and solved numerically using the Trapezoid rule over a given frequency range $[\nu_{min}, \nu_{max}]$ for 300 discrete values of z:

$$\gamma_{OP}(z,\nu) = \int_{\nu_{min}}^{\nu_{max}} I_0 e^{-\left(\frac{\nu-\nu_{Las}}{\Gamma_{Las}}\right)^2} e^{(-\lambda^{-1}z)} \sigma_0 \frac{\Gamma_{Rb}^2}{4(\nu-\nu_{D_1})^2+\Gamma_{Rb}^2} d\nu, \qquad (25)$$

where $\nu_{min} = \nu_{Las} - 5\Gamma_{Las}$ and $\nu_{max} = \nu_{Las} + 5\Gamma_{Las}$.

To calculate a cell averaged P_{Rb} value, an initial 'guess' (P_{Rb} = 0) is firstly substituted into Eq. (25) for z = 0. An output value of P_{Rb} is calculated for the given experimental conditions. The new value is then compared to the initial P_{Rb} value (the guess). If the difference between the values is greater than 1×10^{-8}, the equilibrium function condition is not satisfied, and the new P_{Rb} value is fed back into the calculation in place of the previous value and a further new P_{Rb} is calculated. This process continues until the equilibrium condition is satisfied, at which point the value is accepted as the true P_{Rb} value for z = 0. The resulting P_{Rb} is then used as the initial guess for the next z and the process is repeated for the length of the OP cell which is divided into 300 discrete z values. The 300 $P_{Rb}(z)$ points are averaged to obtain the spatially averaged P_{Rb} value, $\langle P_{Rb}\rangle$, as used in the calculation of P_{Xe}.

3.4.1. Exploratory Simulations with Sim2

For the exploratory simulations of Dataset2, modifications to the OP cell geometry, gas mix composition, laser linewidth, and/or total cell pressure were made within Sim2. The modified parameters used for the OP cell geometry (Figs. 9 and 10) and laser linewidth (Figs. 9–11) are shown in Table 3. For simulations including He (Fig. 10), the gas mix was modified such that He constituted 90% of the buffer gas balance that would otherwise be completely N_2. For simulations with a modified geometry, in-cell T_1 relaxation was scaled according to the surface-area to volume (S/V) ratio. For simulations that modulated the total gas pressure (Figs. 9 and 11), the constituent gases were multiplied by the factors: 0.25, 0.5, 1, 2, 10. In some cases, multiple modifications were simulated simultaneously (e.g., a 3" cell, with He, and a 0.015 nm FWHM laser – Fig. 10). Simulations at 0.015 nm were performed due to the recent emergence of lasers with this linewidth at the Rb D_1.

3.5. Phenomena not modelled

Rb cluster terms were not included in Sim1 or Sim2 because the previously calculated higher efficiencies of the SF polarisers do not indicate a loss pattern that could be explained by Rb clusters [54]; furthermore, flow conditions suspected of driving Rb cluster formation [46] are absent in SF polarisers. Other effects not incorporated include: Collision-induced Rb spectral line asymmetries (that have their own dependencies on gas partial pressures and temperatures [63]); choice of alkali metal besides Rb [78,79]; gas motion from either diffusion or convection [59]; any potential effects of laser detuning [80]; or greatly elevated gas temperatures that have been observed via in-situ Raman spectroscopy [81–83].

4. Results and discussion

4.1. Comparison of Sim1 and Sim2 to Dataset1

Fig. 2(a) summarises Dataset1: the results of the SEOP experiments where the Xe-rich SF regime was first probed under high resonant flux conditions [52]. ^{129}Xe NMR signal intensity is plotted as a function of T_{cell} for the gas mixes investigated: 50, 100, 300, 500, 950, 1400 Torr Xe, each backfilled to 2000 Torr with N_2. The maximum signal intensity for each gas mix occurs at a different T_{cell} value, and as [Xe] increases, its respective peak value was observed to shift to lower temperatures. This inverse relationship

Table 3
Key experimental parameters. Entries in Dataset1 marked with an asterisk are those used in the simulations only. Sim1 and Sim2 simulations of Dataset1 and Dataset2 used the entries in the Dataset1 and Dataset2 columns. Parameters for the exploratory simulations of Dataset2 with Sim2 are displayed in the 5 rightmost columns. The 'Linewidth' column shows the values used in simulations in which the pump laser FWHM was modulated. The final four columns show the values used in simulations in which the OP cell diameter or OP cell length was modulated.

	Experimental data		Exploratory Sim2 simulations				
Parameter	Dataset1 [52]	Dataset2 [56]	Laser FWHM Linewidth	D = 3 "	D = 1 "	L = 50 cm	L = 100 cm
Cell radius [cm]	1.27	2.54	2.54	3.81	1.27	2.54	2.54
Cross-sectional area [cm^2]	5.07	20.3	20.3	45.6	5.07	20.3	20.3
Cell length [cm]	15.0	25.0	25.0	25.0	25.0	50.0	100.0
Cell volume [cm^3]	76.0	507	507	1140	127	1010	2030
Surface area [cm^2]	130	440	440	690	209	839	1640
S/V ratio [cm^{-1}]	1.71	0.87	0.87	0.61	1.65	0.83	0.807
In-cell T_1 [hrs]	0.16	2.5	2.5	3.56	3.63	2.62	2.7
(Xe)$\Gamma = \frac{1}{T_1}$ [s^{-1}]	1.66×10^{-3}	1.11×10^{-4}	1.11×10^{-4}	7.8×10^{-5}	7.65×10^{-5}	1.06×10^{-4}	1.03×10^{-4}
Laser power [W]	29	100, 125, 142, 170	100, 125, 142, 170	100, 125, 142, 170	100, 125, 142, 170	100, 125, 142, 170	100, 125, 142, 170
Laser FWHM [nm]	0.25*, 0.27, 3.0*, 10.0*	0.3	0.015, 0.15, 0.3, 10.0	0.015, 0.15, 0.3	0.15, 0.3	0.15, 0.3	0.15, 0.3

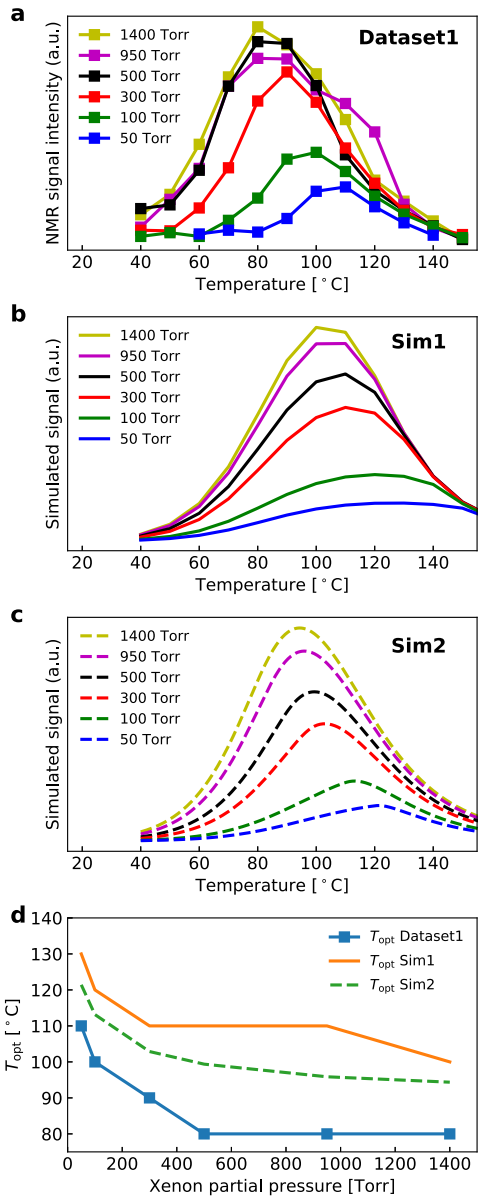


Fig. 2. Dataset1 and corresponding Sim1 and Sim2 simulations. (a) HP ^{129}Xe NMR signal intensity as a function of T_{cell} for 50, 100, 300, 500, 950, and 1400 Torr of Xe, back filled to 2000 Torr with N_2 in a L = 15 cm, r = 1.27 cm OP cell illuminated with a 29 W, 0.27 nm FWHM laser at 794.66 nm. In-cell T_1 = 0.16 h. Sim1 and Sim2 simulation results appear in (b) and (c) respectively. (d) Simulated and experimental optimal temperature, T_{opt}, plotted as a function of [Xe]. Dataset1 in (a) reproduced with permission from reference [52]. Simulations in (b) reproduced from references [62,61]. See Table 3 for further parameters.

can be seen more clearly in Fig. 2 – a plot of optimal temperature, T_{opt}, against [Xe]. Fig. 2(b) and (c) show the results of Sim1 and Sim2, respectively, for these experimental conditions. For Sim1 and Sim2, the product of the P_{Xe} and [Xe] is plotted, proportional to the NMR signal intensity, as is shown for Dataset1 in (a).

Sim1 and Sim2 quantitatively recapture much of the inverse relationship exhibited by T_{opt} and [Xe] in Dataset1, exhibiting only a vertical offset from Dataset1 (of 30 °C at its worst) that is likely explained by a difference between the true gas temperature within the OP cell and that measured experimentally using a thermocouple at the cell exterior. The reality is that within the cell a range of temperatures exist – extreme temperatures under some conditions [58], driving convective or turbulent flow patterns that have been observed with Raman spectroscopy [81]. But the agreement shown here indicates that even a simplistic 1D model is able to provide an adequate description of the prevailing SEOP physics under the high-[Xe], high-photon-flux SF regime when averaging over the entire cell. As an aside, there have been instances where P_{Xe} has been greater at higher [Xe] than at lower [Xe] [76,52]. This experimental result was not reproduced by either simulation.

The overall inverse temperature trend can be explained in terms of the Xe-induced Rb SD rate which is mediated by the Xe-Rb spin-rotation interaction: Higher [Xe] results in greater rates of Xe-induced Rb spin destruction, which in turn increases opacity in the OP cell. By reducing the OP cell temperature at higher [Xe], [Rb] is reduced, leading to an increase in photon flux throughout the cell and thus increased P_{Rb} and P_{Xe} values, albeit at the expense of γ_{SEOP}. In the limit where the in-cell ^{129}Xe T_1 is long (approaching infinity), optimising the 'photon-to-[Rb] ratio' is central to achieving a high P_{Xe} value. In separate simulations with Sim1, the same trends with only a slight temperature shift were borne out when the 3-body contributions were removed, further emphasising the central role of the photon-to-[Rb] ratio. In experiments, the effect was also found to be independent from [N_2] and the xenon nuclear spin destruction rate [58].

4.2. Investigations of laser linewidth effects using Sim1 and Sim2

By considering P_{Xe} as a function of laser linewidth, the results from the Sim1 and Sim2 simulations in Figs. 3 and 4 provide insight into how Xe-rich mixes can perform so well in spite of the high accompanying rate of Rb spin destruction, and provide

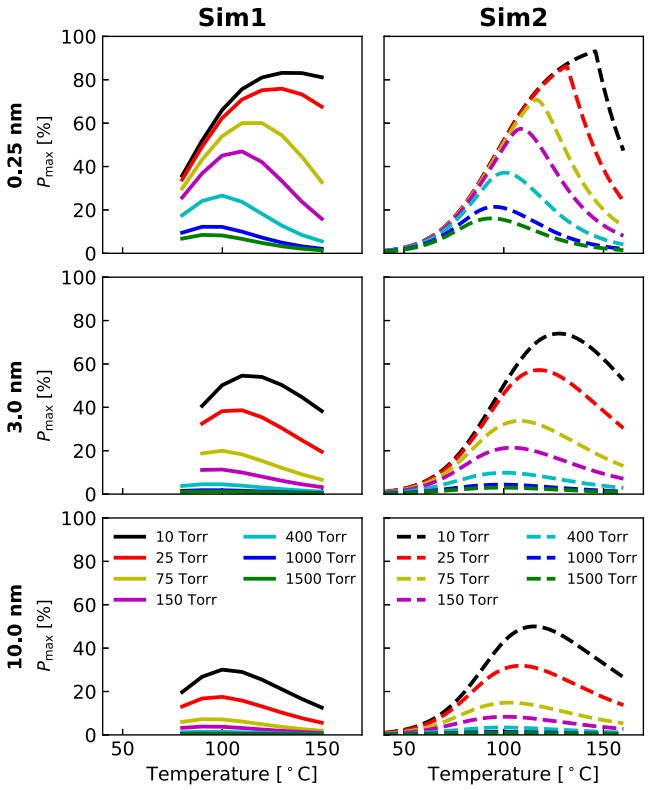


Fig. 3. Simulations of SF SEOP as a function of OP laser linewidth (0.25, 3, 10 nm FWHM) for seven Xe:N_2 gas mixes: 10, 25, 75, 150, 400, 1000 and 1500 Torr Xe, back-filled to 2000 Torr with N_2 in a L = 15 cm, r = 1.27 cm OP cell illuminated with a 29 W laser. Simulated laser and D_1 spectral lines were aligned in both simulations. In-cell T_1 = 0.16 h. As the laser linewidth increases, P_{max} for a given gas mix drops, and the distribution (particularly its peak, T_{opt}) becomes less sensitive to temperature. T_{opt} decreases with increasing [Xe], and the polarisation increases with narrowing linewidth at a greater relative rate for higher [Xe] mixes.

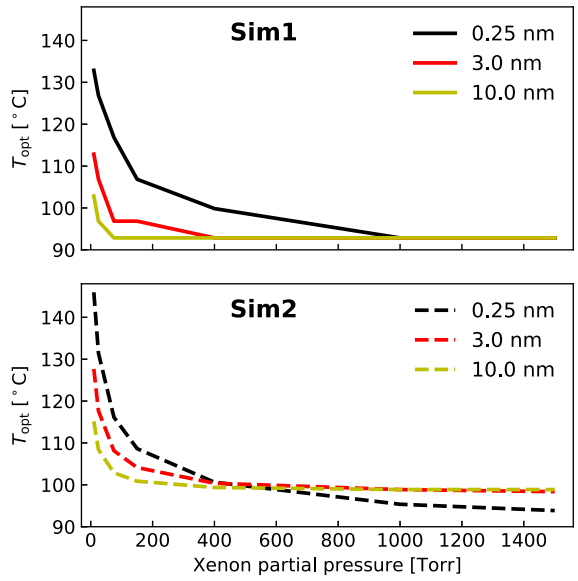


Fig. 4. Comparison of T_{opt} behaviour for Sim1 and Sim2 as a function of laser linewidth (cf. Fig. 2(d)) for seven Xe:N_2 gas mixes: 10, 25, 75, 150, 400, 1000 and 1500 Torr Xe, back-filled to 2000 Torr with N_2 in a L = 15 cm, r = 1.27 cm OP cell illuminated with a 29 W laser. Simulated laser and D_1 spectral lines were aligned in both simulations. In-cell T_1 = 0.16 h. In both Sim1 and Sim2, T_{opt} decreases with increasing [Xe], and as linewidth increases, P_{max} becomes less sensitive to T. Sim1 results reproduced from reference [62].

further support to the importance of optimizing the 'photon-to-[Rb]' ratio. Both simulations indicate that as the spectral linewidth of the laser is increased (while keeping total incident laser power constant), both P_{Xe} *and* T_{opt} decrease; P_{Xe} also becomes less sensitive to T, as manifested by the broadening distributions. Looking at it the other way, as P_{Xe} becomes more sensitive to T as the laser linewidth is reduced, richer [Xe] mixes enjoy a disproportionally greater gain in signal intensity. The effect at the highest Xe densities is striking: note particularly the 1500 Torr mix, which sees P_{Xe} increase from ~1% to almost 10% and 20% in Sim1 and Sim2 respectively as the spectral linewidth is reduced from 10 nm to 0.25 nm FWHM. This disproportionally greater gain in P_{Xe} at higher [Xe] is because there is more potential at higher [Xe] to recover P_{Xe} by reducing T (reducing the Rb density), countering the Rb-SD induced optical opacity that causes P_{Rb} – and consequently P_{Xe} – to plummet.

The P_{max} values of the lowest two Sim2 [Xe] curves peak sharply in the 0.25 nm FWHM simulations. Likely origins for this 'effect' include (i) the 'simplistic' 1D nature of the model combined with (ii) performing the simulations at the 'extreme' conditions of very narrow laser spectral widths, and with (iii) the assumption of 100% polarised light; under these conditions, we are closer to the limit of effectively zero Xe-induced Rb spin destruction, so the effect of narrowing the laser linewidth (and coupling increasingly to the Rb D_1 and the temperature dependent Rb vapour density) dominates the behaviour of both P_{Rb} and P_{Xe}. Indeed, there is a sharp transition from complete in-cell optical transparency to partial transparency as T_{cell} is increased, which manifests here as a sharpening spike in the P_{Xe} curves in the upper right hand corner of Fig. 3. This effect is apparent in Sim2 (a 1D model) and not in Sim1 (a 2D model), because Sim1 also includes a polarised-light attenuation function at the walls, reducing susceptibility to this effect under such extreme conditions. Implementing a lower incident light polarisation in Sim2 (e.g. ~95%) correspondingly softens the P_{Xe} curves. (Similar behaviour is apparent later in some Sim2 simulations of Dataset2 conditions with extreme laser narrowing to 0.015 nm FWHM; cf. Fig. 9).

Fig. 4 summarises the T_{opt} behaviour across these simulated data sets. Although normalised differently, both sets of simulations show increased sensitivity to temperature at narrower linewidths. This result likely explains why – before such narrow, high-powered lasers were used for SEOP – the temperature-sensitive nature of P_{Xe} as a function of [Xe] (which in turn led to HP Xe preparations with high P_{Xe} at high [Xe] by exploiting T_{opt}) [52,56] had not been previously noticed. Indeed, studies using broadband lasers have tended to report little or no dependence of T_{opt} on [Xe] [78].

4.3. Comparison of Sim2 to Dataset2

Fig. 5 summarises Dastaset2, the results of the XeUS multidimensional study [56]. In these experiments, P_{Xe} and γ_{SEOP} were measured as a function of T_{cell}, incident laser power, and [Xe]. For each gas mix, the maximum measured values are plotted as colour contour maps in panels (c), (e), (g), (i), and (k) for P_{Xe} and panels (d), (f), (h), (j), and (l) for γ_{SEOP}. Fig. 5(a) shows a cross-section of the P_{Xe} and γ_{SEOP} data from panel (g) as an example – the 1000 Torr mix at ~100 W of lasing power – and panel (b) shows the optimal values of P_{Xe} and γ_{SEOP} for each gas mix. P_{Xe} and γ_{SEOP} values were obtained from fits to a form of Eq. (17).

As discussed in the original publication [56], the data exhibit several trends, most of which are borne out in the Sim2 results in Fig. 6. For instance, when considering the γ_{SEOP} data (panels (d), (f), (h), (j) and (l)) it can be seen that increasing T_{cell} gives rise to an expected exponential increase in γ_{SEOP}, reflecting the dependence on [Rb] (by Eqs. (14) and (23)) which increases exponentially with T (Eq. (9)). However, hints of laser-induced heating are evident in the experimental data that are absent in Sim2. A pure dependence on [Rb] would mean that the colour contours would run purely vertically – as is the case in the simulations – but in Dataset2, as the laser power is increased, γ_{SEOP} begins to elevate at lower T_{cell}. The relative contributions of γ_{SE}^{BC} & γ_{SE}^{vdW} to γ_{SEOP} predicted by Sim2 across the whole of Dataset2 can be seen in the ESI. γ_{SE}^{BC} provides the greater contribution in every case under the conditions studied.

P_{Xe} follows a different trend throughout. Taking panel (a) in both Figs. 5 and 6 as an example, it can be seen that as T_{cell} is increased, P_{Xe} initially grows until P_{max} is reached, as given by Eq. (18). $\langle P_{Rb} \rangle$ here is given by Eq. (10). These eqns show that P_{Xe} approaches $\langle P_{Rb} \rangle$ when γ_{SE} is much greater than Γ, which occurs at higher temperatures (by Eq. (14)); however, this also leads to a higher density of absorbers, which reduces photon flux through the rear regions of the OP cell, lowering γ_{OP} across the cell and thus $\langle P_{Rb} \rangle$, placing a limit on the achievable xenon polarisation (P_{max}). In other words, P_{max} initially grows with increasing T as more Rb is vaporised, but once [Rb] becomes too high, overall $\langle P_{Rb} \rangle$ decreases, resulting in the lower P_{max} values at higher T_{cell} values. (This interplay between P_{max}, $\langle P_{Rb} \rangle$, and light absorption is shown in Fig. 8.).

There are regions of no data in Dataset2 (Fig. 5). This absence is because: i) either γ_{SEOP} was excessively low (resulting in impractically long experiments for the prevailing time constraints), or ii) it was not possible to measure P_{max} without inducing 'Rb runaway', which occurs when undissipated heat from laser absorption or cell heating rapidly compounds the amount of Rb in the vapour phase over a short time [47,80,84]; the uncontrolled growth of [Rb] results in decreasing P_{Rb} in more poorly illuminated regions of the OP cell and hence more laser absorption and heat dissipation from the gas into the inner surface of the cell (and Rb pools) in a self-reinforcing pattern. Rb runaway is more common at higher [Xe] because the rates of Xe-induced Rb spin destruction are higher and (likely) because the thermal conductivity of the gas mixture is lower due to the increased presence of Xe.

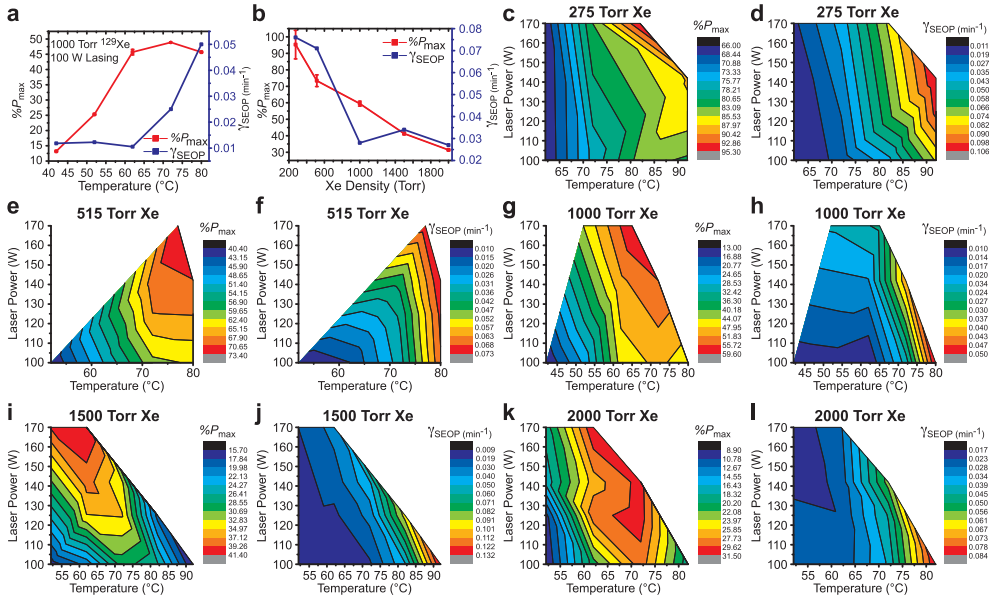


Fig. 5. Dataset2: results of the XeUS multi-parameter study. P_{Xe} and γ_{SEOP} were measured as a function of T_{cell}, incident laser power, and [Xe] for five Xe:N_2 gas mixtures contained within a L = 25 cm, r = 2.54 cm OP cell. The maximum values for P_{Xe} and γ_{SEOP} for each gas mix at each temperature and laser power are plotted in colour contour maps (c), (e), (g), (i), and (k) for P_{Xe} and (d), (f), (h), (j), and (l) for γ_{SEOP}. P_{Xe} and γ_{SEOP} were determined from fits to a form of Eq. (17). (a) shows a cross-section of panel (g): P_{Xe} and γ_{SEOP} for the 1000 Torr mix at 100 W. (b) shows $P_{max} - P_{Xe}$ at the optimal temperature T_{opt} for each gas mix – and the corresponding γ_{SEOP} values. Reprinted with permission from Ref. [56] Copyright (2014) American Chemical Society.

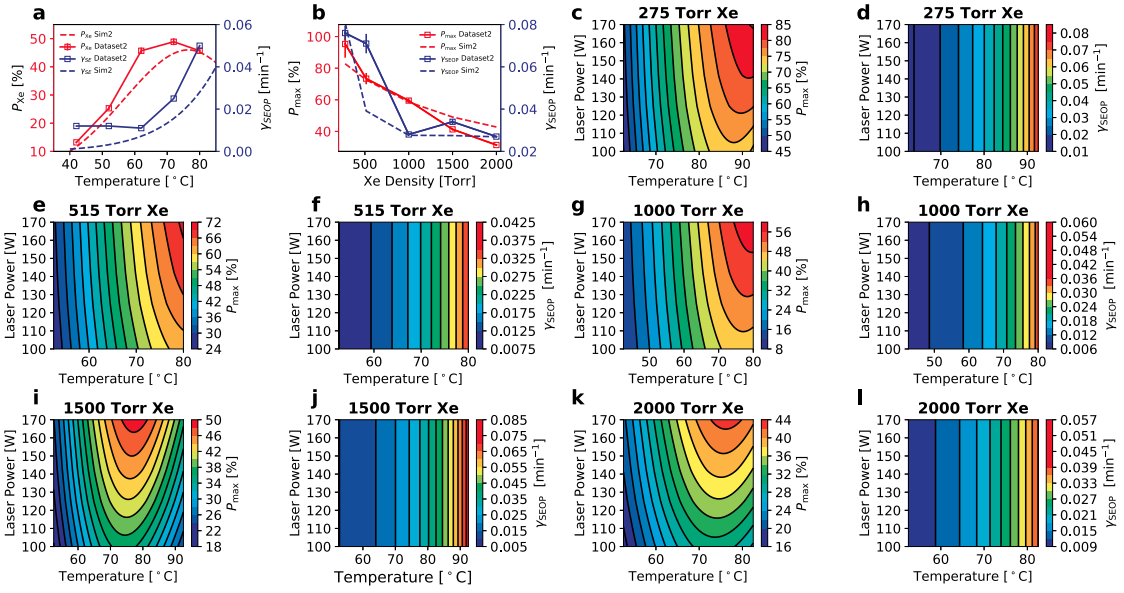


Fig. 6. Sim2 simulations of Dataset2 (c.f. Fig. 5). P_{Xe} and γ_{SEOP} simulated as a function of T_{cell}, incident laser power, and [Xe] for five Xe:N_2 gas mixtures contained within a L = 25 cm, r = 2.54 cm OP cell. Maximum values for P_{Xe} and γ_{SEOP} for each gas mix at each temperature and laser power are plotted in colour contour maps (c), (e), (g), (i), and (k) for P_{Xe} and (d), (f), (h), (j), and (l) for γ_{SEOP}. (a) shows a cross-section of panel (g): simulations P_{Xe} and γ_{SEOP} for the 1000 Torr gas mix at P = 100 W. Simulations (dashed lines) are plotted with the corresponding experimental data (solid lines, square markers). (b) shows simulation derived (dashed lines) and experimentally measured (solid lines, square markers) $P_{max} - P_{Xe}$ at the optimal temperature T_{opt} for each gas mix – as well as the corresponding γ_{SEOP} values. Further parameters are summarised in Table 3.

Panel (b) of Fig. 6 shows the optimal P_{Xe} values from Dataset2 as a function of [Xe], plotted for comparison against the corresponding Sim2 predictions. Overall, good qualitative and quantitative agreement is observed: in particular, Sim2 predicts the P_{max} of the 515 Torr and 1000 Torr mixtures to within 1%. The model underestimates P_{max} at 275 Torr, but the experimental error is large. At higher [Xe] the experimental data are lower than that predicted by Sim2, and this discrepancy may be due to thermal effects that are not considered by the model that worsen at higher [Xe] for at least two possible reasons: i) increased rates of non-radiative de-excitation of the Rb via the resulting heat-generating Rb-N_2 collisions (due to greater Xe-induced Rb-SD at higher [Xe]), and ii) the bulk thermal conductivity reduces because more-thermally-conductive N_2 is replaced by Xe.

As [Xe] is increased from 275 Torr to 2000 Torr, the same inverse relationship with T_{opt} present in Dataset1 is again apparent: T_{opt} decreases from 82 °C to 62 °C (a drop of 20 °C) in Dataset2, and 93.8 °C to 76.3 °C (a drop of 17.5 °C) in Sim2 (Fig. 7). Both Sim2 and Dataset2 exhibited higher Xe polarisations with increasing laser power throughout the tested range. Thus, the use

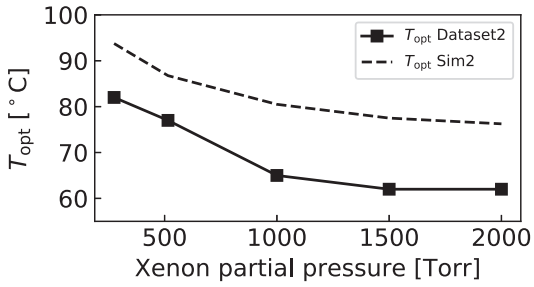


Fig. 7. T_{opt} as a function of [Xe] for Dataset2 (solid lines, square markers) and Sim2 (dashed lines), c.f. Figs. 5(b) and 6(b). As with Dataset1 (Fig. 2(d)), the temperature at which P_{max} occurs for a given gas mix (T_{opt}) decreases with increasing [Xe]. The offset is likely explained by a difference between the true gas temperature within the OP cell and that measured experimentally using a thermocouple at the cell exterior. Experimental data from the SI of Ref. [56].

of LDA powers greater than 170 W (and/or more spectrally-narrowed output) should lead to further increases in P_{max}, particularly at higher xenon loadings. The specification of the laser confined Dataset2 experiments to the 100 W to 170 W power range, but the simulations shown in Fig. 6 have no such limitation. Thus, extrapolated variants (laser powers of 25–1000 W) of displays Fig. 6 are presented in the ESI. If the increased heat load could be mitigated, greater LDA power would allow for operation in the regimes with higher [Rb], thereby increasing γ_{SEOP} and HP Xe production rates. A way to mitigate thermal issues that are exacerbated by high fluxes and high [Xe] may be the addition of more-thermally-conductive He to the SEOP mixture (this prospect is considered later with Sim2).

4.4. Optimal absorption trend

Upon examining the results of Sim2 it became clear that there was a distinct pattern in the amount of power absorption that occurred at P_{max} for a given gas mix at a given set of experimental conditions. For instance, at Dataset2 conditions – that is for a D = 2", L = 25 cm cell containing a binary gas mixture at a pressure of 2000 Torr irradiated with a 0.3 nm FWHM laser – optimal power absorption was constant at approximately ~63%; this is shown in Fig. 8. Here, P_{Xe}, $\langle P_{Rb}\rangle$, and % power absorbed are shown (blue, green, and red, respectively) for four selected Sim2 simulations of Dataset2 experimental conditions: 100 W of lasing power at 275 & 1000 Torr Xe ((a) & (c)); and 170 W of lasing power at 275 and 1000 Torr Xe ((b) & (d)). The blue vertical dashed lines indicate P_{max}, and the red horizontal dashed lines indicate the amount of laser absorption at P_{max}. Laser absorption in every case is ~63% regardless of power and [Xe] (62.88%, 63.34%, 62.41% and 62.88% for (a), (b), (c), and (d) respectively). Fig. 9 shows that this result holds for all of the gas mixes (275, 515, 1000, 1500, 2000 Torr Xe) and laser powers (100, 125, 142, 170 W) simulated under at Dataset2 (XeUS) conditions (solid lines with squares).

A similar pattern was observed when the simulation was taken beyond the ranges of conditions explored in Dataset2. For example, Fig. 9 shows % power absorbed as a function of [Xe] for the P_{max} values at various laser spectral widths (0.015, 0.15, 10 nm FWHM) and at various total gas pressures (0.25, 2 and 10 times the Dataset2 total gas pressure). Each group was simulated at four laser powers (100, 125, 142, 170 W) and 5 Xe fractions: 275, 515, 1000, 1500, and 2000 Torr (or equivalent fraction if the total gas pressure was modulated). In all cases but one, the plots indicate that the % absorption at P_{max} is independent of incident laser power, and virtually independent of [Xe] (only a very minor decrease with increasing [Xe] is evident). Indeed, simulating Dataset2 for a fixed Rb absorption linewidth, i.e. in the absence of pressure broadening (cf. Eq. (4)), largely eliminated this slight

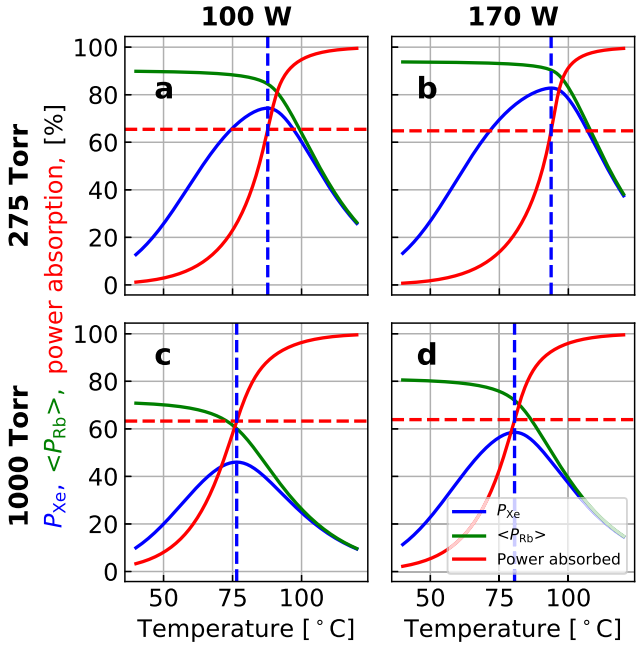


Fig. 8. Four selected Sim2 simulations of SF SEOP in a 2" cell with a total gas pressure of 2000 Torr and OP laser linewidth of 0.3 nm FWHM. Top and bottom rows are 275 and 1000 Torr of Xe respectively, backfilled with N_2. Left and right columns are 100 W and 170 W of incident OP laser power, respectively. Blue, green, and red, curves respectively show $\%P_{Xe}$, $\%P_{Rb}$, and % power absorbed, as functions of T. At P_{max} for each condition (vertical blue dashed lines), the % power absorbed is always ~63% (horizontal red dashed lines), i.e. virtually independent of [Xe] and laser power.

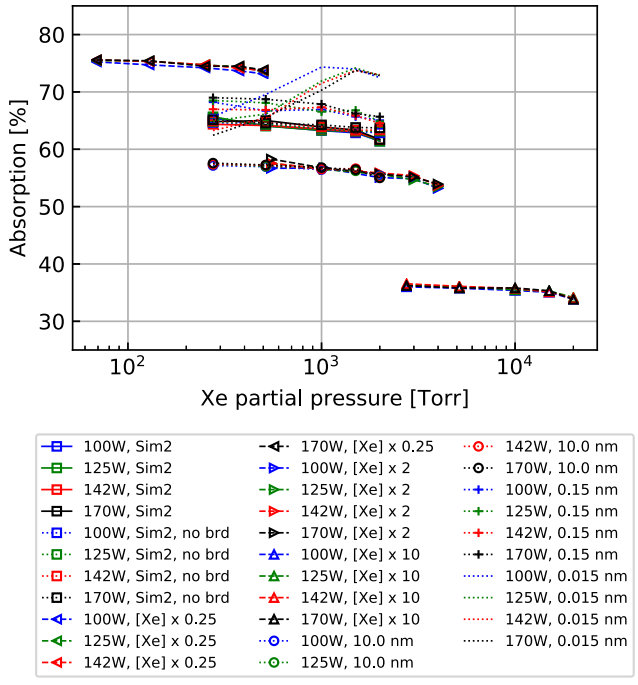


Fig. 9. Sim2 simulations of SF SEOP at 8 groups of conditions: 'Sim2' (Dataset2 conditions); 'Sim2, no brd' (explained below); Sim2 conditions but with 0.5, 2, and 10 times the Sim2 partial and total pressures; Sim2 conditions but with laser FWHM linewidths of 10, 0.15 and 0.015 nm. The plots show % laser power absorption at P_{max} (and thus T_{opt}) as a function of [Xe], here quantified using the partial pressure at loading at 25 °, for given variations of total pressure and laser spectral FWHM. 'Sim2, no brd' simulations are obtained using Sim2 but with an artificially fixed Rb D_1 linewidth such that no broadening is allowed to occur as a function of gas mix. Taken together, the plots indicate that % optimal power absorption is virtually independent of both incident laser power and [Xe] and for each group of conditions.

decrease with [Xe] (cf. Fig. 9 'Sim2, no brd')), supporting the conclusion that this slight dependence on [Xe] merely reflects a differential increase in pressure-broadening of the Rb line with increasing Xe. Only the 'ultra-narrow' 0.015 nm simulation at low [Xe] deviated from the absorption trend, exhibiting a lower absorption at P_{max}. This is likely because at low [Xe], we are closer to the limit of no Xe-induced Rb SD, so the effect of narrowing the laser linewidth (and coupling increasingly to the Rb D_1 and the temperature dependent Rb vapour density) dominates the behaviour of both P_{Rb} and P_{Xe} (in exactly the same way as for Sim2 simulations in Fig. 3). Further similar results – where cell geometry simulations are also plotted – are available in the ESI.

While the amount of laser absorption needed to achieve P_{max} is effectively constant for any given set of conditions examined (bar the ultra-narrow 0.015 nm case), the optimal absorption value changes as other experimental conditions are varied. For instance, considering first the total pressure modulation, there is a clear trend: As total pressure is increased from 0.25·[Xe] to 10·[Xe], the optimal absorption value decreases from ~75% to ~35%. For linewidth FWHM modulations (0.015, 0.15, 0.3, 10 nm) there is also a clear trend: 10 nm has the lowest optimal absorption value. This increases through ~63% for Dataset2 (XeUS) conditions (0.3 nm) to ~67% for 0.15 nm. This continues through to ~74% for 0.015 nm at higher [Xe], but at low [Xe] the optimal absorption at P_{max} is suppressed for reasons discussed above. Thus optimal absorption increases for decreasing linewidth. Again, further similar results for cell geometry simulations are available in the ESI.

4.5. Exploratory simulations: cell geometry, laser linewidth, total pressure, and addition of helium

Sim2 was used explore the parameter space surrounding Dataset2 and considered scenarios that could be readily implemented on, e.g., the XeUS line of SF SEOP polarisers [53–57,85]. In the results that follow, P_{Xe} is presented as a function of (1) buffer gas composition (Fig. 10); (2) cell geometry (Fig. 10); (3) laser linewidth (Figs. 10 and 11)); and (4) total gas pressure (Fig. 11). Dataset2 and the Sim2 simulations of Dataset2 are used as references in order to make comparisons. Table 3 summarises relevant parameters for each new simulation examined in this section.

For case (1), the simulations included a gas mixture wherein He comprised 90% of the buffer gas balance. As expected, replacing 90% of the N_2 buffer gas with He has ostensibly no impact on P_{Xe} when compared to the non-He simulations – in fact the curves in Fig. 10 overlap completely. Given this fact, He is likely a strong candidate to mitigate thermal issues that prevail during SEOP at high Xe density, high-photon-flux conditions because it is 28- and 6-fold more thermally conductive than Xe and N_2 respectively [86]. Indeed this outcome was observed in separate experiments that used *in situ* Raman spectroscopy to monitor in-cell SEOP temperatures [83]. Furthermore, the practice of using He as the dominant buffer gas could enable an increase in the operational duty cycle of SF polarisers via faster heating and cooling of the cells. Note however, that He cannot replace all of the N_2 within the cell

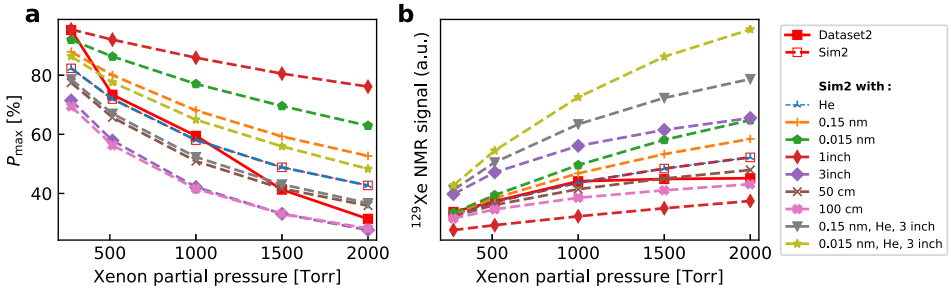


Fig. 10. Results of Sim2 simulations predicting (a) P_{max} (at T_{opt}) and (b) magnetisation (proportional to the NMR signal) as a function of modifications to Dataset2 conditions. Results include variations (and in some cases also combinations) of: (1) buffer gas (He comprising 90% of the buffer gas balance), (2) cell geometry (1, 2, and 3 inch cell diameters), and (3) OP laser spectral FWHM (0.015, 0.15, 0.3 nm FHWM). The solid red line with square markers is Dataset2. For each simulation, experimental parameters (e.g. cell length, area, T_1) were scaled appropriately and are summarised in Table 3.

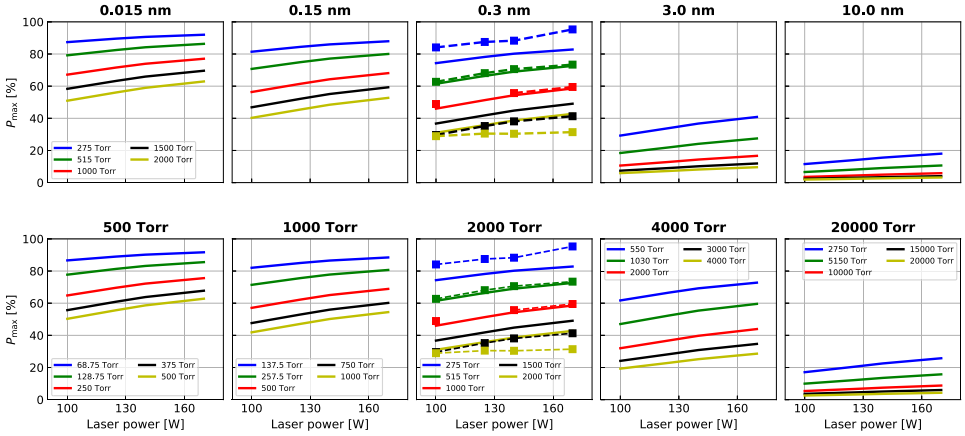


Fig. 11. Top row: P_{Xe} as a function of laser power and partial pressure for 5 different total pressures (corresponding to multiplying the Dataset2 total pressure by factors of 0.25, 0.5, 1.0, 2.0 and 10.0, respectively), as predicted by Sim2. Xe partial pressures correspond to 14, 26, 50, 75 and 90% of the total pressure indicated by the blue, green, red, black and gold lines respectively. Dashed lines with squares are experimental values (Dataset2). Bottom row: Optimal P_{Xe} as a function of laser power and Xe partial pressure at 5 laser FWHM linewidths: 0.015, 0.15, 0.3, 3, and 10 nm, as predicted by Sim2. [Xe] = 275, 515, 1000, 1500, and 2000 Torr are indicated by the blue, green, red, black, and yellow lines respectively. Dashed lines show corresponding values from Dataset2.

because N_2 provides a non-radiative pathway for the de-excitation of Rb atoms, ultimately preventing polarisation loss [87,43].

In case (2) 1" and 3" diameter OP cells were considered, along with 2" OP cells with increased L = 50 & 100 cm. Cell geometry determines i) how OP light is distributed throughout the cell, ii) the volume of gas to be polarised, and iii) the rate of wall induced relaxation (via the S/V ratio); a large S/V ratio will result in greater relaxation. Relative to the 2" cell, P_{Xe} in the 3" cell drops due to the dilution of incident flux, but magnetisation rises due to the larger cell volume. The 3" cell provides almost twice the signal of the 2" XeUS cell because increasing the diameter from 2" to 3" while keeping the length constant actually increases the cell volume by more than a factor of two. Using a 3" diameter cell will increase the net magnetisation generated, but unless cryo-collection or extraction methods other than positive pressure expansion (the current method) are employed (e.g. using large syringe pumps that can extract most of the contents of the cell after hyperpolarisation [60]), a significant fraction of HP gas will remain in the OP cell. The 3" cell may also run hotter than the 2" cell due to the reduced S/V ratio, increasing it's susceptibility to Rb runaway, though this effect could potentially be mitigated with the addition of He. A 1" cell enables high P_{Xe} values but the reduced volume results in low magnetisation. Both the 50 cm cell and the 100 cm cell fair worse than the Sim2 simulation of Dataset2 in terms of both P_{Xe} and magnetisation due to poorer light penetration. Correspondingly, T_{opt} becomes lower for these cells as the cell length increases in order to lower [Rb], and subsequently recover P_{Rb} at the back of the cell (that was low due to the poor light penetration).

For case (3) Dataset2 conditions were simulated for a range of incident pump laser spectral widths: 0.015, 0.15, 0.3, 3.0, and 10.0 nm FWHM. Reducing the laser linewidth from 0.3 nm to 0.15 and 0.015 nm (Fig. 10) increases both P_{Xe} and magnetisation, and disproportionally greater so for the higher [Xe] loadings, consistent with the Sim1 and Sim2 results shown previously in Fig. 3. Fig. 11 shows how P_{Xe} is expected to behave as a function of [Xe] and laser power for each of the laser FWHM listed. Again, as shown earlier in Fig. 3, greater P_{max} values can be expected at narrower linewidths.

Fig. 10 also shows the expected P_{Xe} and magnetisation trends with select cases of (1), (2), and (3) implemented simultaneously. The combination of a He-buffered, 3" OP cell, pumped with a 170 W, 0.015 nm FHWM laser gives the greatest magnetisation, thus investigations of this configuration are highly encouraged. While the thermal effects of He are not modelled here, its use is recommended on the grounds of its greater thermal conductivity that will likely be valuable in a 3 inch cell (with a lower S/V ratio) pumped with an ultra narrow 0.015 nm laser.

For case (4), Xe-rich SEOP is simulated as a function of the total pressure, with 5 total pressures considered – 500, 1000, 2000, 4000, and 20000 Torr – shown in Fig. 11. Xe partial pressures correspond to 14, 26, 50, 75 and 90% of the total pressure indicated by the blue, green, red, light blue and purple dashed lines respectively – the same proportions as Dataset2. Fig. 11 shows P_{max} decreases with pressure – a consequence of Γ_{SD}^{BC}.

5. Conclusions

High Xe density, high-photon-flux SF SEOP was simulated using two different simulation implementations, both of which draw on existing SEOP theory. Both validate well against Dataset1, reproducing the inverse relationship between T_{opt} and [Xe] with good quantitative agreement. Additionally, both implementations indicate that the possibility to polarise Xe to high levels at high [Xe] derives from the use of narrowed lasers and the exploitation of the T_{opt} relationship that maximises the photon-to-[Rb] ratio, and that the use of narrower linewidths should lead to further gains in HP Xe production. Sim2 was also compared to Dataset2 – a dataset that covered larger regions of parameter space at clinically-relevant production scales [56]. The simulation closely reproduces experimental P_{Xe}, γ_{SEOP}, and T_{opt} values over most of the parameter space and is thus considered to provide an excellent description of behaviour within the Xe-rich, high-photon-flux SF regime.

Exploratory simulations with Sim2 indicate a number of readily implementable options exist for increasing the magnetisation output – the product of the moles of Xe prepared and its polarisation– of clinical-scale SF (e.g. XeUS-type) polarisers. Of these, inclusion of He within the gas mixtures would likely be easiest to implement. Experimentally, this practice should increase thermal control – particularly at higher [Xe] where the greatest potential exists to increase magnetisation output if thermal issues can be addressed – and potentially increase the duty cycle of HP gas production due to the higher bulk thermal conductivity of the gas mixture. A 3" cell should double magnetisation output relative to the current 2" cell but require modification to parts of the polariser including: the optical train, the AR-coated windows, retro-reflector, and the 3D printed oven, all of which would be relatively easy to implement. However, for optimal results, a new gas extraction protocol may be required. Narrower laser linewidths will likely bring further gains in polariser output, particularly at Xe-rich mixtures with relatively low total pressures. Combining a He back-loaded, 3" cell (the largest considered here) with the narrowest possible laser should provide the best results.

Finally, scrutiny of the laser absorption revealed for the first time that in the SF configuration under the conditions examined, achieving the maximum P_{Xe} trends towards an optimal, fixed level of absorption that is effectively independent of laser power and [Xe] for a given laser linewidth, cell geometry, and total cell pressure, thereby providing a new method to rapidly optimise – and automate – SF Xe polarisers: For example, once P_{Xe} for one partial pressure has been maximised, all Xe partial pressures can be optimised by simply matching the integral of the laser power absorption spectrum to that obtained with the first optimisation. Implementation of the above improvements will be the subject of future efforts. Readers of this paper may also find of interest the results of a new simulation platform for CF SEOP created by Schrank (Ref. [88]).

Declaration of Competing Interest

The authors declare the following financial interests/personal relationships which may be considered as potential competing interests: Eduard Chekmenev, Boyd Goodson and Panayiotis Nikolaou each declare they have a stake in XeUS Technologies LTD. All other authors declare they have no conflict of interest.

Acknowledgements

We gratefully acknowledge the support of EPSRC, the School of Medicine, University of Nottingham, the NSF (CHE-1905341, CHE-1904780, CHE-1416432, CHE-1836308 and CHE-1416268), the NIH (1R21EB018014, 1F32EB021840, 1R21EB020323, 1R21CA220137), the NSF/DoD ASSURE Program (DMR-1757954), and the DOD (W81XWH-15–1-0271, W81XWH-15–1-0272, OISE-0966393, and W81XWH-12–1-0159/BC112431).

Appendix A. Supplementary material

Supplementary data associated with this article can be found, in the online version, at https://doi.org/10.1016/j.jmr.2020.106686.

References

[1] B.M. Goodson, N. Whiting, A.M. Coffey, P. Nikolaou, F. Shi, B.M. Gust, M.E. Gemeinhardt, R.V. Shchepin, J.G. Skinner, J.R. Birchall, et al., Hyperpolarization methods for MRS, eMagRes 4 (2015) 797–810.

[2] P. Nikolaou, B.M. Goodson, E.Y. Chekmenev, NMR hyperpolarization techniques for biomedicine, Chemistry–A, Eur. J. 21 (8) (2015) 3156–3166.

[3] T. Walker, W. Happer, Spin-exchange optical pumping of noble-gas nuclei, Rev. Mod. Phys. 69 (2) (1997) 629–642.

[4] T. Chupp, K. Coulter, Polarization of ^{21}Ne by spin exchange with optically pumped Rb vapor, Phys. Rev. Lett. 55 (10) (1985) 1074.

[5] G.E. Pavlovskaya, Z.I. Cleveland, K.F. Stupic, R.J. Basaraba, T. Meersmann, Hyperpolarized krypton-83 as a contrast agent for magnetic resonance imaging, Proc. Natl. Acad. Sci. USA 102 (51) (2005) 18275–18279.

[6] K.F. Stupic, Z.I. Cleveland, G.E. Pavlovskaya, T. Meersmann, Hyperpolarized ^{131}Xe NMR spectroscopy, J. Magn. Reson. 208 (1) (2011) 58–69.

[7] Y. Zheng, G.W. Miller, W.A. Tobias, G.D. Cates, A method for imaging and spectroscopy using γ-rays and magnetic resonance, Nature 537 (7622) (2016) 652.

[8] T. Chupp, M. Wagshul, K. Coulter, A. McDonald, W. Happer, Polarized, high-density, gaseous ^{3}He targets, Phys. Rev. C 36 (6) (1987) 2244.

[9] J.P. Mugler, B. Driehuys, J.R. Brookeman, G.D. Cates, S.S. Berr, R.G. Bryant, T.M. Daniel, E.E. De Lange, J.H. Downs, C.J. Erickson, W. Happer, D.P. Hinton, N.F. Kassel, T. Maier, C.D. Phillips, B.T. Saam, K.L. Sauer, M.E. Wagshul, MR imaging and spectroscopy using hyperpolarized ^{129}Xe gas: preliminary human results, Magn. Reson. Med. 37 (6) (1997) 809–815, https://doi.org/10.1002/mrm.1910370602.

[10] I. Dregely, J.P. Mugler, I.C. Ruset, T.A. Altes, J.F. Mata, G.W. Miller, J. Ketel, S. Ketel, J. Distelbrink, F. Hersman, et al., Hyperpolarized xenon-129 gas-exchange imaging of lung microstructure: first case studies in subjects with obstructive lung disease, J. Magn. Reson. Imaging 33 (5) (2011) 1052–1062.

[11] J.P. Mugler, T.A. Altes, Hyperpolarized ^{129}Xe MRI of the human lung, J. Magn. Reson. Imaging 37 (2) (2013) 313–331.

[12] K. Qing, K. Ruppert, Y. Jiang, J.F. Mata, G.W. Miller, Y.M. Shim, C. Wang, I.C. Ruset, F.W. Hersman, T.A. Altes, J.P. Mugler, Regional mapping of gas uptake by blood and tissue in the human lung using hyperpolarized xenon-129 MRI, J. Magn. Reson. Imaging 39 (2) (2014) 346–359, https://doi.org/10.1002/jmri.24181.

[13] L.L. Walkup, J.C. Woods, Translational applications of hyperpolarized ^{3}He and ^{129}Xe, NMR Biomed. 27 (12) (2014) 1429–1438.

[14] Z. Wang, S.H. Robertson, J. Wang, M. He, R.S. Virgincar, G.M. Schrank, E.A. Bier, S. Rajagopal, Y.C. Huang, T.G. O'Riordan, et al., Quantitative analysis of hyperpolarized ^{129}Xe gas transfer MRI, Med. Phys. 44 (6) (2017) 2415–2428.

[15] Y.V. Chang, MOXE: A model of gas exchange for hyperpolarized ^{129}Xe magnetic resonance of the lung, Magn. Reson. Med. 69 (3) (2013) 884–890, https://doi.org/10.1002/mrm.24304.

[16] I. Muradyan, J.P. Butler, M. Dabaghyan, M. Hrovat, I. Dregely, I. Ruset, G.P. Topulos, E. Frederick, H. Hatabu, W.F. Hersman, S. Patz, Single-breath xenon polarization transfer contrast (SB-XTC): implementation and initial results in healthy humans, J. Magn. Reson. Imaging 37 (2) (2013) 457–470, https://doi.org/10.1002/jmri.23823.

[17] S.D. Swanson, M.S. Rosen, B.W. Agranoff, K.P. Coulter, R.C. Welsh, T.E. Chupp, Brain MRI with laser-polarized ^{129}Xe, Magn. Reson. Med. 38 (5) (1997) 695–698.

[18] M. Rao, N.J. Stewart, G. Norquay, P.D. Griffiths, J.M. Wild, High resolution spectroscopy and chemical shift imaging of hyperpolarized ^{129}Xe dissolved in the human brain in vivo at 1.5 tesla, Magn. Reson. Med. 75 (6) (2016) 2227–2234.

[19] X. Zhou, Y. Sun, M. Mazzanti, N. Henninger, J. Mansour, M. Fisher, M. Albert, MRI of stroke using hyperpolarized ^{129}Xe, NMR Biomed. 24 (2) (2011) 170–175, https://doi.org/10.1002/nbm.1568.

[20] R.T. Branca, T. He, L. Zhang, C.S. Floyd, M. Freeman, C. White, A. Burant, Detection of brown adipose tissue and thermogenic activity in mice by hyperpolarized xenon MRI, Proc. Nat. Acad. Sci. 111 (50) (2014) 18001–18006.

[21] M.M. Spence, S.M. Rubin, I.E. Dimitrov, E.J. Ruiz, D.E. Wemmer, A. Pines, S.Q. Yao, F. Tian, P.G. Schultz, Functionalized xenon as a biosensor, Proc. Nat. Acad. Sci. 98 (19) (2001) 10654–10657.

[22] M.G. Shapiro, R.M. Ramirez, L.J. Sperling, G. Sun, J. Sun, A. Pines, D.V. Schaffer, V.S. Bajaj, Genetically encoded reporters for hyperpolarized xenon magnetic resonance imaging, Nat. Chem. 6 (7) (2014) 629–634.

[23] F.T. Hane, T. Li, P. Smylie, R.M. Pellizzari, J.A. Plata, B. DeBoef, M.S. Albert, In vivo detection of cucurbit [6] uril, a hyperpolarized xenon contrast agent for a xenon magnetic resonance imaging biosensor, Sci. Rep. 7 (2017) 41027.

[24] B.A. Riggle, Y. Wang, I.J. Dmochowski, A "smart" ^{129}Xe NMR biosensor for pH-dependent cell labeling, J. Am. Chem. Soc. 137 (16) (2015) 5542–5548.

[25] C. Boutin, E. Léonce, T. Brotin, A. Jerschow, P. Berthault, Ultrafast z-spectroscopy for ^{129}Xe NMR-based sensors, J. Phys. Chem. Lett. 4 (23) (2013) 4172–4176.

[26] R.M. Fairchild, A.I. Joseph, K.T. Holman, H.A. Fogarty, T. Brotin, J.-P. Dutasta, C. Boutin, G. Huber, P. Berthault, A water-soluble Xe@ cryptophane-111 complex exhibits very high thermodynamic stability and a peculiar ^{129}Xe NMR chemical shift, J. Am. Chem. Soc. 132 (44) (2010) 15505–15507.

[27] V. Roy, T. Brotin, J.-P. Dutasta, M.-H. Charles, T. Delair, F. Mallet, G. Huber, H. Desvaux, Y. Boulard, P. Berthault, A cryptophane biosensor for the detection of specific nucleotide targets through xenon NMR spectroscopy, ChemPhysChem 8 (14) (2007) 2082–2085.

[28] G. Huber, T. Brotin, L. Dubois, H. Desvaux, J.-P. Dutasta, P. Berthault, Water soluble cryptophanes showing unprecedented affinity for xenon: candidates as NMR-based biosensors, J. Am. Chem. Soc. 128 (18) (2006) 6239–6246.

[29] M. Kunth, C. Witte, A. Hennig, L. Schröder, Identification, classification, and signal amplification capabilities of high-turnover gas binding hosts in ultra-sensitive NMR, Chem. Sci. 6 (11) (2015) 6069–6075.

[30] S. Klippel, C. Freund, L. Schröder, Multichannel MRI labeling of mammalian cells by switchable nanocarriers for hyperpolarized xenon, Nano Lett. 14 (10) (2014) 5721–5726.

[31] Y. Wang, B.W. Roose, E.J. Palovcak, V. Carnevale, I.J. Dmochowski, A genetically encoded β-lactamase reporter for ultrasensitive ^{129}Xe NMR in mammalian cells, Angew. Chem. 128 (31) (2016) 9130–9133.

[32] E. Mari, P. Berthault, ^{129}Xe NMR-based sensors: biological applications and recent methods, Analyst 142 (18) (2017) 3298–3308.

[33] K. Jeong, C. Netirojjanakul, H.K. Munch, J. Sun, J.A. Finbloom, D.E. Wemmer, A. Pines, M.B. Francis, Targeted molecular imaging of cancer cells using MS2-based ^{129}Xe NMR, Bioconjug. Chem. 27 (8) (2016) 1796–1801.

[34] K.K. Palaniappan, R.M. Ramirez, V.S. Bajaj, D.E. Wemmer, A. Pines, M.B. Francis, Molecular imaging of cancer cells using a bacteriophage-based ^{129}Xe NMR biosensor, Angew. Chem. 125 (18) (2013) 4949–4953.

[35] B.M. Goodson, Nuclear magnetic resonance of laser-polarized noble gases in molecules, materials, and organisms, J. Magn. Reson. 155 (2002) 157.

[36] A. Oros, N. Shah, Hyperpolarized xenon in NMR and MRI, Phys. Med. Biol. 49 (20) (2004) R105–R153.

[37] A. Cherubini, A. Bifone, Hyperpolarised xenon in biology, Prog. Nucl. Magn. Reson. Spectrosc. 42 (1) (2003) 1–30.

[38] L. Schroeder, Xenon for NMR biosensing: Inert but alert, Physica Med. 29 (1) (2013) 3–16, https://doi.org/10.1016/j.ejmp.2011.11.001. http://www.sciencedirect.com/science/article/pii/S1120179711001384.

[39] B.M. Goodson, K. Ranta, J.G. Skinner, A.M. Coffey, P. Nikolaou, M. Gemeinhardt, D. Anthony, S. Stephenson, S. Hardy, J. Owers-Bradley, M.J. Barlow, E.Y. Chekmenev, The Physics of Hyperpolarized Gas MRI, Elsevier, 2017, pp. 23–46.

[40] D.A. Barskiy, A.M. Coffey, P. Nikolaou, D.M. Mikhaylov, B.M. Goodson, R.T. Branca, G.J. Lu, M.G. Shapiro, V.-V. Telkki, V.V. Zhivonitko, et al., NMR hyperpolarization techniques of gases, Chem.-A Eur. J. 23 (4) (2017) 725–751.

[41] M. Bouchiat, T. Carver, C. Varnum, Nuclear polarization in He-3 gas induced by optical pumping and dipolar exchange, Phys. Rev. Lett. 5 (8) (1960) 373–375, https://doi.org/10.1103/PhysRevLett. 5.373.

[42] S. Parnell, M. Deppe, J. Parra-Robles, J. Wild, Enhancement of ^{129}Xe polarization by off-resonant spin exchange optical pumping, J. Appl. Phys. 108 (6) (2010) 064908.

[43] B. Driehuys, G.D. Cates, E. Miron, K. Sauer, D.K. Walter, W. Happer, High-volume production of laser-polarized ^{129}Xe, Appl. Phys. Lett. 96 (12) (1996) 1668–1670.

[44] I.C. Ruset, S. Ketel, F. Hersman, Optical pumping system design for large production of hyperpolarized ^{129}Xe, Phys. Rev. Lett. 96 (2006) 053002.

[45] G. Norquay, S.R. Parnell, X. Xu, J. Parra-Robles, J.M. Wild, Optimized production of hyperpolarized ^{129}Xe at 2 bars for in vivo lung magnetic resonance imaging, J. Appl. Phys. 113 (4) (2013) 044908.

[46] M. Freeman, K. Emami, B. Driehuys, Characterizing and modeling the efficiency limits in large-scale production of hyperpolarized ^{129}Xe, Phys. Rev. A 90 (2) (2014) 023406.

[47] A.L. Zook, B.B. Adhyaru, C.R. Bowers, High capacity production of >65% spin polarized xenon-129 for NMR spectroscopy and imaging, J. Magn. Reson. 159 (2) (2002) 175–182.

[48] G. Schrank, Z. Ma, A. Schoeck, B. Saam, Characterization of a low-pressure high-capacity Xe-129 flow-through polarizer, Phys. Rev. A 80 (6) (2009) 063424, https://doi.org/10.1103/PhysRevA.80.063424.

[49] M.G. Mortuza, S. Anala, G.E. Pavlovskaya, T.J. Dieken, T. Meersmann, Spin-exchange optical pumping of high-density xenon-129, J. Chem. Phys. 118 (4) (2003) 1581–1584.

[50] M. Wagshul, T. Chupp, Optical pumping of high-density Rb with a broadband dye laser and GaAlAs diode laser arrays: application to ^{3}he polarization, Phys. Rev. A 40 (8) (1989) 4447.

[51] C. Flower, M. Freeman, M. Plue, B. Driehuys, Electron microscopic observations of Rb particles and pitting in ^{129}Xe spin-exchange optical pumping cells, J. Appl. Phys. 122 (2) (2017) 024902.

[52] N. Whiting, P. Nikolaou, N.A. Eschmann, B.M. Goodson, M.J. Barlow, Interdependence of in-cell xenon density and temperature during Rb/Xe-129 spin-exchange optical pumping using VHG-narrowed laser diode arrays, J. Magn. Reson. 208 (2) (2011) 298–304, https://doi.org/10.1016/j.jmr.2010.11.016.

[53] P. Nikolaou, A.M. Coffey, L.L. Walkup, B.M. Gust, N. Whiting, H. Newton, I. Muradyan, M. Dabaghyan, K. Ranta, G.D. Moroz, et al., Xena: An automated 'open-source' ^{129}Xe hyperpolarizer for clinical use, Magn. Reson. Imaging 32 (5) (2014) 541–550.

[54] P. Nikolaou, A.M. Coffey, L.L. Walkup, B.M. Gust, N. Whiting, H. Newton, S. Barcus, I. Muradyan, M. Dabaghyan, G.D. Moroz, M.S. Rosen, S. Patz, M.J. Barlow, E.Y. Chekmenev, B.M. Goodson, Near-unity nuclear polarization with an open-source ^{129}Xe hyperpolarizer for NMR and MRI, Proc. Natl. Acad. Sci. arXiv:http://www.pnas.org/content/early/2013/08/13/1306586110.full.pdf+html, doi:https://doi.org/10.1073/pnas.1306586110. http://www.pnas.org/content/early/2013/08/13/1306586110.abstract.

[55] P. Nikolaou, A.M. Coffey, L.L. Walkup, B.M. Gust, C.D. LaPierre, E. Koehnemann, M.J. Barlow, M.S. Rosen, B.M. Goodson, E.Y. Chekmenev, A 3D-printed high power nuclear spin polarizer, J. Am. Chem. Soc. 136 (4) (2014) 1636–1642.
[56] P. Nikolaou, A.M. Coffey, K. Ranta, L.L. Walkup, B.M. Gust, M.J. Barlow, M.S. Rosen, B.M. Goodson, E.Y. Chekmenev, Multidimensional mapping of spin-exchange optical pumping in clinical-scale batch-mode ^{129}Xe hyperpolarizers, J. Phys. Chem. B 118 (18) (2014) 4809–4816.
[57] P. Nikolaou, A.M. Coffey, M.J. Barlow, M.S. Rosen, B.M. Goodson, E.Y. Chekmenev, Temperature-ramped ^{129}Xe spin-exchange optical pumping, Anal. Chem. 86 (16) (2014) 8206–8212.
[58] B.M. Goodson, N. Whiting, H. Newton, J.G. Skinner, K. Ranta, P. Nikolaou, M.J. Barlow, E.Y. Chekmenev, Spin-exchange optical pumping at high xenon densities and laser fluxes: principles and practice, Royal Soc. Chem. (2015) 96–121.
[59] A. Fink, D. Baumer, E. Brunner, Production of hyperpolarized xenon in a static pump cell: numerical simulations and experiments, Phys. Rev. A 72 (5) (2005) 053411.
[60] M.S. Rosen, T.E. Chupp, K.P. Coulter, R.C. Welsh, S.D. Swanson, Polarized ^{129}Xe optical pumping/spin exchange and delivery system for magnetic resonance spectroscopy and imaging studies, Rev. Sci. Instrum. 70 (2) (1999) 1546–1552.
[61] K. Ranta, L. Walkup, N. Whiting, P. Nikolaou, M. Barlow, B. Goodson, Interplay of temperature, Xe density, and laser linewidth during Rb-Xe spin-exchange optical pumping: simulation vs. experiment, in: 52nd Experimental Nuclear Magnetic Resonance Conference 2011, Boston, USA, 2011.
[62] K. Ranta, Clinical-scale hyperpolarization of ^{129}Xe and ^{131}Xe via stopped-flow spin exchange optical pumping, Ph.D. thesis, Southern Illinois University Carbondale, 2016.
[63] M.V. Romalis, E. Miron, G.D. Cates, Pressure broadening of Rb D_1 and D_2 lines by ^{3}He, ^{4}He, N_2, and Xe. line cores and near wings, Phys. Rev. A 56 (1997) 4569–4578, https://doi.org/10.1103/PhysRevA.56.4569.
[64] D.A. Steck, Rubidium 85 D line data, 2008.
[65] B. Larson, O. Häusser, P. Delheij, D. Whittal, D. Thiessen, Optical pumping of Rb in the presence of high-pressure ^{3}He buffer gas, Phys. Rev. A 44 (5) (1991) 3108.
[66] C. Alcock, V. Itkin, M. Horrigan, Vapour pressure equations for the metallic elements: 298–2500 K, Can. Metall. Q. 23 (3) (1984) 309–313.
[67] A.B.-A. Baranga, S. Appelt, M. Romalis, C. Erickson, A. Young, G. Cates, W. Happer, Polarization of ^{3}He by spin exchange with optically pumped Rb and K vapors, Phys. Rev. Lett. 80 (13) (1998) 2801.
[68] M.E. Wagshul, T. Chupp, Laser optical pumping of high-density Rb in polarized ^{3}He targets, Phys. Rev. A 49 (5) (1994) 3854.
[69] W. Chen, T. Gentile, T. Walker, E. Babcock, Spin-exchange optical pumping of He-3 with Rb-K mixtures and pure K, Phys. Rev. A 75 (1) (2007) 013416.
[70] M. Bouchiat, J. Brossel, L. Pottier, Evidence for Rb-rare-gas molecules from the relaxation of polarized Rb atoms in a rare gas. experimental results, J. Chem. Phys. 56 (7) (1972) 3703–3714.
[71] I. Nelson, T. Walker, Rb-Xe spin relaxation in dilute Xe mixtures, Phys. Rev. A 65 (1) (2001) 012712.
[72] I.C. Ruset, Hyperpolarized ^{129}Xe production and applications, Ph.D. thesis, University of New Hampshire, 1999.
[73] G. Cates, R. Fitzgerald, A. Barton, P. Bogorad, M. Gatzke, N. Newbury, B. Saam, Rb-^{129}Xe spin-exchange rates due to binary and three-body collisions at high Xe pressures, Phys. Rev. A 45 (7) (1992) 4631.
[74] C.V. Rice, D. Raftery, Rubidium – xenon spin exchange and relaxation rates measured at high pressure and high magnetic field, J. Chem. Phys. 117 (12) (2002) 5632.
[75] Y.-Y. Jau, N.N. Kuzma, W. Happer, Magnetic decoupling of 129-Xe-Rb and 129-Xe-Cs binary spin exchange, Phys. Rev. A 67 (2) (2003) 022720.
[76] P. Nikolaou, N. Whiting, N.A. Eschmann, K.E. Chaffee, B.M. Goodson, M.J. Barlow, Generation of laser-polarized xenon using fiber-coupled laser-diode arrays narrowed with integrated volume holographic gratings, J. Magn. Reson. 197 (2) (2009) 249–254, https://doi.org/10.1016/j.jmr.2008.12.015.
[77] N. Whiting, P. Nikolaou, N. Eschmann, M. Barlow, B. Goodson, Effects of laser power, linewidth, and component gas densities on the polarization of xenon with fixed-frequency volume holographic grating (VHG)-narrowed laser diode arrays, in: 49th Exptl., Nucl. Magn. Reson. Conf., Asilomar, CA, 2008.
[78] N. Whiting, N.A. Eschmann, B.M. Goodson, M.J. Barlow, ^{129}Xe-Cs (D1, D2) versus ^{129}Xe-Rb (D_1) spin-exchange optical pumping at high xenon densities using high-power laser diode arrays, Phys. Rev. A 83 (2011) 053428.
[79] A. Couture, T. Clegg, B. Driehuys, Pressure shifts and broadening of the Cs D1 and D2 lines by He, N_2, and Xe at densities used for optical pumping and spin exchange polarization, J. Appl. Phys. 104 (9) (2008) 094912.
[80] N. Whiting, P. Nikolaou, N.A. Eschmann, M.J. Barlow, R. Lammert, J. Ungar, W. Hu, L. Vaissie, B.M. Goodson, Using frequency-narrowed, tunable laser diode arrays with integrated volume holographic gratings for spin-exchange optical pumping at high resonant fluxes and xenon densities, Appl. Phys. B: Lasers Opt. 106 (2012) 775–788, https://doi.org/10.1007/s00340-012-4924-x.
[81] D.K. Walter, W. Griffith, W. Happer, Energy transport in high-density spin-exchange optical pumping cells, Phys. Rev. Lett. 86 (15) (2001) 3264–3267.
[82] H. Newton, L.L. Walkup, N. Whiting, L. West, J. Carriere, F. Havermeyer, L. Ho, P. Morris, B.M. Goodson, M.J. Barlow, Comparative study of in situ N_2 rotational Raman spectroscopy methods for probing energy thermalisation processes during spin-exchange optical pumping, Appl. Phys. B: Lasers Opt. (2013), https://doi.org/10.1007/s00340-013-5588-x.
[83] J. Birchall, N. Whiting, J. Skinner, M.J. Barlow, B.M. Goodson, Using Raman Spectroscopy to Improve Hyperpolarized Noble Gas Production for Clinical Lung Imaging Techniques, InTech, 2017, pp. 247–268.
[84] C. Witte, M. Kunth, F. Rossella, L. Schröder, Observing and preventing rubidium runaway in a direct-infusion xenon-spin hyperpolarizer optimized for high-resolution hyper-CEST (chemical exchange saturation transfer using hyperpolarized nuclei) NMR, J. Chem. Phys. 140 (8) (2014) 084203.
[85] J.G. Skinner, Optimisation of xenon rich stopped flow spin-exchange optical pumping for functional lung imaging, Ph.D. thesis, University of Nottingham, 2017.
[86] G. Kaye, T. Laby, Tables of Physical and Chemical Constants, Longman Sc & Tech, 1995.
[87] I. Saha, P. Nikolaou, N. Whiting, B.M. Goodson, Characterization of violet emission from Rb optical pumping cells used in laser-polarized xenon NMR experiments, Chem. Phys. Lett. 428 (2006) 268–276.
[88] G.M. Schrank, A Novel, Finite-Element Model for Spin-Exchange Optical Pumping Using an Open-Source Code, arXiv:1911.01574 (2019).

analytical chemistry

pubs.acs.org/ac Article

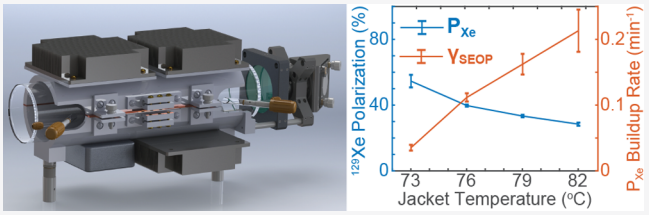
Batch-Mode Clinical-Scale Optical Hyperpolarization of Xenon-129 Using an Aluminum Jacket with Rapid Temperature Ramping

Jonathan R. Birchall, Panayiotis Nikolaou,* Aaron M. Coffey, Bryce E. Kidd, Megan Murphy, Michael Molway, Liana B. Bales, Boyd M. Goodson, Robert K. Irwin, Michael J. Barlow, and Eduard Y. Chekmenev*

Cite This: *Anal. Chem.* 2020, 92, 4309−4316 Read Online

ACCESS | Metrics & More | Article Recommendations | Supporting Information

ABSTRACT: We present spin-exchange optical pumping (SEOP) using a third-generation (GEN-3) automated batch-mode clinical-scale ^{129}Xe hyperpolarizer utilizing continuous high-power (~170 W) pump laser irradiation and a novel aluminum jacket design for rapid temperature ramping of xenon-rich gas mixtures (up to 2 atm partial pressure). The aluminum jacket design is capable of heating SEOP cells from ambient temperature (typically 25 °C) to 70 °C (temperature of the SEOP process) in 4 min, and perform cooling of the cell to the temperature at which the hyperpolarized gas mixture can be released from the hyperpolarizer (with negligible amounts of Rb metal leaving the cell) in approximately 4 min, substantially faster (by a factor of 6) than previous hyperpolarizer designs relying on air heat exchange. These reductions in temperature cycling time will likely be highly advantageous for the overall increase of production rates of batch-mode (i.e., stopped-flow) ^{129}Xe hyperpolarizers, which is particularly beneficial for clinical applications. The additional advantage of the presented design is significantly improved thermal management of the SEOP cell. Accompanying the heating jacket design and performance, we also evaluate the repeatability of SEOP experiments conducted using this new architecture, and present typically achievable hyperpolarization levels exceeding 40% at exponential build-up rates on the order of 0.1 min^{-1}.



Hyperpolarized noble gases such as ^{3}He, ^{83}Kr, and ^{129}Xe have seen use in a multitude of NMR and magnetic resonance imaging (MRI) applications, including spectroscopic biosensing, spectroscopic studies of porous media, theranostic imaging of the lungs and brain, and others.[1−25] NMR signal is directly proportional to the degree of nuclear spin alignment with the applied static magnetic field or nuclear spin polarization, *P*. The low *P* of such isotopes possessing nonzero spin intrinsically limits the achievable signal-to-noise ratio (SNR) for use in spectroscopic or imaging applications. It is therefore necessary to increase the net nuclear spin polarization of these systems to several orders of magnitude above those found at thermal equilibrium,[23,26,27] with near-unity polarization becoming more accessible with recent advancements in hyperpolarizer design.[28]

Circularly polarized photons can be employed for electron spin hyperpolarization of a vaporized alkali metal (such as rubidium). Hyperpolarization of ^{129}Xe is usually achieved by transferring angular momentum from the hyperpolarized (HP) electron of the vaporized alkali metal via Fermi contact interactions.[29−31] This two-stage spin-exchange optical pumping (SEOP) process creates a population excess in a particular ^{129}Xe spin state, significantly increasing the net ^{129}Xe polarization and hence NMR signal intensity. Production of HP ^{129}Xe contrast agent typically occurs in either a batch-mode (stopped-flow) or continuous flow modality, both of which present substantial differences in ^{129}Xe *P* build-up and energy transport dynamics.[32−38]

In addition to ^{129}Xe target nuclei, molecular nitrogen (N_2) is typically included in the gas mixture to quench radiative, randomly polarized emission (fluorescence) from excited Rb atoms via gas-phase collisions, thus mitigating what would otherwise be a major source of electron spin-relaxation.[32,39] Helium-4 has also seen some use as a buffer gas, particularly in continuous-flow polarizer designs,[32,40,41] to perform pressure broadening of the Rb absorption lines (D_1 ~795 nm, D_2 ~780 nm)[42−44] and thus increase the optical pumping efficiency. The advent of frequency-narrowed, high-power laser diode arrays (LDAs)[28,45−49] has made the inclusion of ^{4}He less critical in batch-mode hyperpolarizer designs. Despite these advances, the significant increases in thermal conductivity and specific heat capacity afforded by He-rich ternary gas mixtures relative to their binary Xe/N_2 counterparts may make them

Received: November 6, 2019
Accepted: February 19, 2020
Published: February 19, 2020

Downloaded via VANDERBILT UNIV on March 17, 2020 at 20:13:49 (UTC).
See https://pubs.acs.org/sharingguidelines for options on how to legitimately share published articles.

© 2020 American Chemical Society

attractive for future studies, considering the pursuit of even higher laser powers and narrower spectral profiles will undoubtedly present a new series of challenges in the thermal management of alkali metal "runaway" processes.[50−53]

Because SEOP hyperpolarization utilizes gas-phase collisions between vaporized Rb and Xe atoms, elevated temperatures (~70 °C for batch-mode,[28,54] ~120 °C for continuous-flow configurations) are required to maintain sufficient Rb vapor densities for effective optical pumping. Continuous-flow hyperpolarizers, typically employing extremely dilute Xe gas mixtures, require a cryo-collection stage to remove buffering gases,[32] allowing the HP Xe to be accumulated in the solid state, where the spin−lattice relaxation time (T_1) is a few hours.[55,56] Rapid thawing of the frozen Xe then takes place, before expansion into a temporary storage vessel,[32] for example, Tedlar bag. By contrast, hyperpolarization in the batch-mode modality is typically performed using Xe-rich gas mixtures, and thus can be performed without the use of cryo-collection,[28,57] but still necessitates a "cool-down" stage where the reaction vessel (termed "SEOP cell") is reduced to ~25−50 °C before the gaseous HP contrast agent can be extracted, for example, for intended clinical use.[54] The temperature reduction results in the Rb condensation in the SEOP cell and negligible (less than 5 ng) presence of Rb metal excipient in the Tedlar bag.[54]

Our previous batch-mode hyperpolarizer designs employ a forced air oven to heat and cool the SEOP cell,[28,54,58,59] which is somewhat inefficient due to low thermal conductivity and heat capacity of air. For example, long times (~up to 24 min) for heating up/cooling down the cell are therefore necessary in such a design,[54] inherently limiting the rate and duty cycle of HP ^{129}Xe production. Moreover, the useable ^{129}Xe net spin polarization decreases during the SEOP cell cooldown due to a period of spin-relaxation before eventual transfer of HP^{129}Xe into the Tedlar bag. Here, we address these issues by incorporating a novel aluminum jacket design, whereby direct thermal contact with the SEOP cell ensures rapid transfer of heat during heating/cooling cycles. As a result, temperature ramping of the SEOP cell can be accomplished in ~4 min, that is, approximately 6 times faster than the previous designs. The results described in this study aim to both realize the efficiency and applicability of the new design for the purposes of increasing HP ^{129}Xe contrast agent production rates for clinical use. Specifically, we demonstrate $\%P_{Xe}$ of 54.8 ± 3.8% at γ_{SEOP} of 0.035 ± 0.004 min^{-1} and $\%P_{Xe}$ of ~40% at γ_{SEOP} of ~0.1 min^{-1} for 1000 Torr Xe mixture. $\%P_{Xe}$ of ~30% is achieved at γ_{SEOP} of ~0.06 min^{-1} for 1500 Torr Xe mixture. Moreover, high γ_{SEOP} of 0.2 min^{-1} may enable new approaches for clinical-scale SEOP.

MATERIALS AND METHODS

In this study, ^{129}Xe hyperpolarization via SEOP was performed using an automated, third-generation (GEN-3) device, operating in the batch mode under conditions of high Xe partial pressures (i.e., Xe-rich mixtures) and high laser power (~170 W). Optical pumping was performed using a Bright-Lock Ultra-500 continuous-wave pump laser source, with a 2" beam expanding telescope and a $^1/_4$-λ waveplate providing circular polarization of purity >98% (QPC Laser Technologies, Sylmar, CA). Frequency-narrowing was employed to achieve a spectral width of 0.154 nm, with wavelength tuning onto the Rb D_1 transition wavelength facilitated by a thermistor and high-capacity *P*312 water chiller (Termotek, Baden−Baden, Germany) operating at 930 W cooling power and a flow rate of >4 L/min. The aluminum jacket design for heating and cooling of SEOP cells (Figure 1a and Figure 1d) consisted of four 50

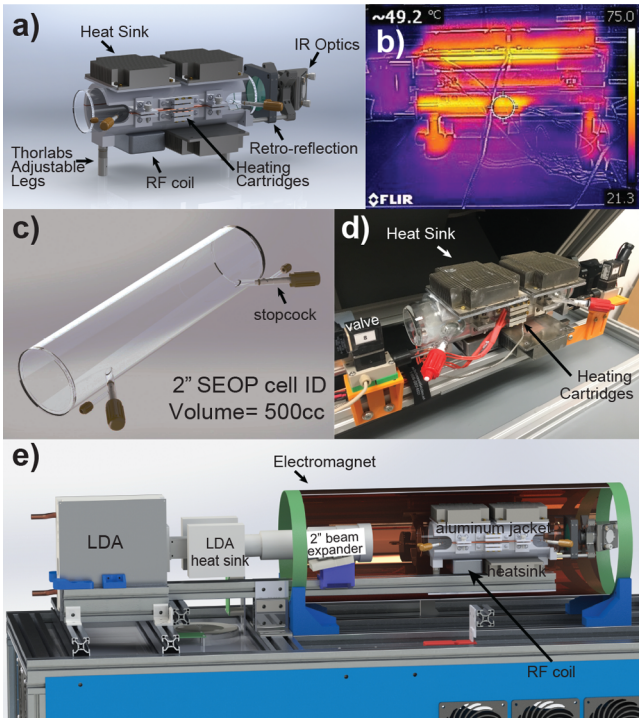


Figure 1. (a) 3D rendering of the aluminum heating jacket. (b) Thermal photo illustrating localized temperature of the heating elements, heat sinks and SEOP cell. (c) 3D rendering of the SEOP cell designed for the GEN-3 hyperpolarizer. (d) Photo showing aluminum heating jacket implementation on the GEN-3 hyperpolarizer. (e) 3D rendering of the GEN-3 hyperpolarizer upper chassis, illustrating the alignment of the pump laser, SEOP cell aluminum heating jacket, and NMR solenoid magnet coil (large horizontal cylinder shown as a cut-away to depict internal components).

W cartridge heaters in contact with a cylindrical aluminum frame. A series of three heat sinks were used to effectively dissipate heat during the cooling process, venting it to the main body of the GEN-3 hyperpolarizer chassis where it could be easily removed by a cluster of independently operated fans. A pair of ThorLabs adjustable pillars were utilized to perform pump laser alignment, with a retro-reflecting mirror situated at the rear of the SEOP cell increasing the optical pumping efficiency and allowing IR spectroscopy to be performed. A small rectangular opening was included at the bottom of the jacket structure to allow insertion of the NMR surface coil, for RF transmit pulses and receiving the NMR signal. A layer of Arctic Alumina thermal paste (thermal conductivity >4 W/(m·K)) coated the interior surface of the jacket for rapid heat transfer (Figure 1b). The use of thermal paste adds a negligible additional time (ca. 10 min) during the SEOP cell replacement process compared to previous designs.[58−60] Although we do not have the metrics for how often the cell needs to be changed on this device yet, we are currently completing the quality assurance study for a previous-generation device (with similar geometry of the SEOP cell),[58,60] and we find that the SEOP cell can be used for more than 500 refills or more than 1 year (whichever comes sooner), so the additional 10 min time

https://dx.doi.org/10.1021/acs.analchem.9b05051
Anal. Chem. 2020, 92, 4309−4316

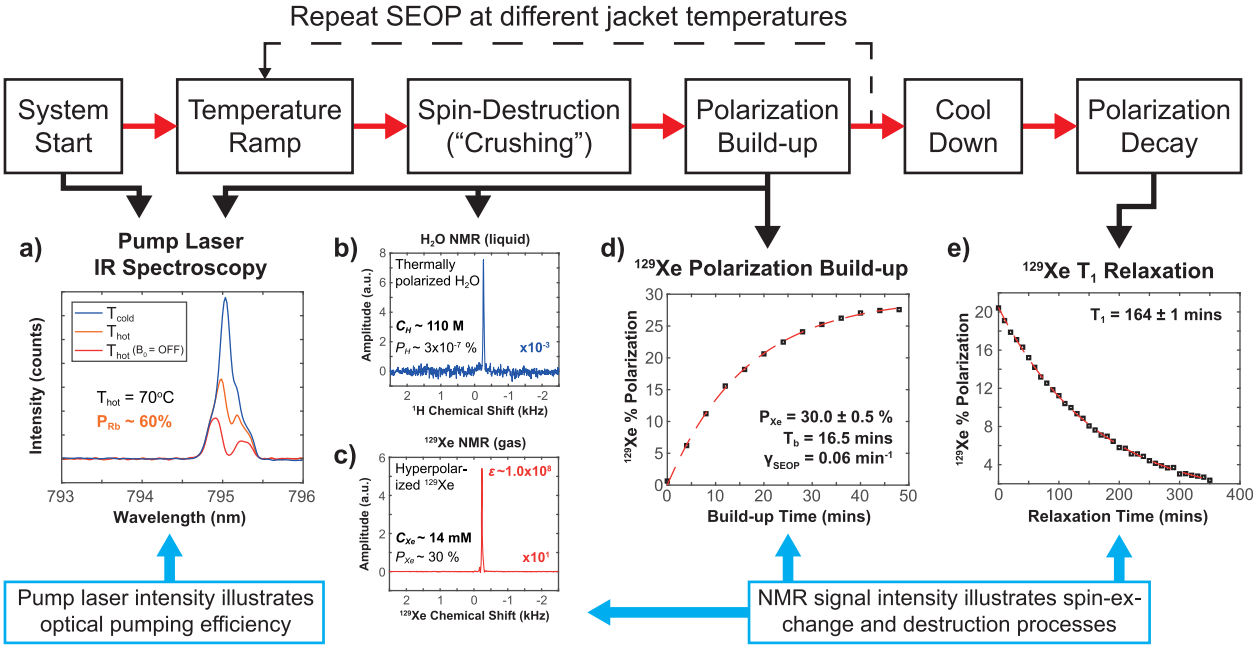


Figure 2. Flowchart describing the typical stages of operation of the GEN-3 hyperpolarizer device. Example data acquired during each stage of the SEOP process for the purposes of determining (a) Pump laser light absorption spectra employed for estimation of Rb electron polarization (P_{Rb}); (b) ^{1}H NMR spectroscopy of thermally polarized ^{1}H nuclei of a water phantom (doped with 10 mM $CuSO_4$. of the same geometry shown in display (c); (c) ^{129}Xe NMR spectroscopy employed to measure nuclear spin polarization (P_{Xe}) relative to that of proton phantom; (d) ^{129}Xe polarization build-up curve employed to compute ^{129}Xe build-up rate (γ_{SEOP}) and steady-state $\%P_{Xe}$; (e) ^{129}Xe polarization relaxation curve employed to compute the ^{129}Xe T_1 decay rate— see SI Figure S1a for details.

required for application of thermal paste does not impact the process significantly.

The diameter of the SEOP cell (Figure 1c) matches size of the beam expander (2" o.d.). The SEOP cell has an internal volume of 0.5 L (Mid Rivers Glassblowing, Saint Peters, MO). The SEOP cell cleaning, preparation, and Rb loading processes are described in the Supporting Information (SI). A solenoid coil surrounded the SEOP cell and heating jacket, providing a homogeneous (~300 ppm over 5 cm sphere according to the design specifications) B_0 magnetic field of up to 40 G (4 mT). The tuning of the RF coil was performed with it already inserted inside the aluminum case shown in Figure 1a, and the attachment to the aluminum jacket does not result in any observable RF coil detuning. The aluminum casing of the RF coil and the jacket provide excellent radio frequency (RF) screening of outside noise sources, resulting in improved NMR signal-to-noise ratio (SNR) compared to previous designs.[53] RF pulse transmission and NMR detection were performed using a Kea2 NMR spectrometer (Magritek, New Zealand) at a 40.8 kHz B_1 resonance frequency for both ^{1}H or ^{129}Xe spins. Since ^{129}Xe possesses a substantially lower gyromagnetic ratio (−11.777 MHz/T) relative to ^{1}H (42.576 MHz/T), it was necessary to increase the B_0 field strength by the ratio of proton and ^{129}Xe gyromagnetic ratios (ca. factor of ~3.6) when acquiring ^{129}Xe to match these resonance frequencies at 40.8 kHz. Figure 1e shows 3D rendering of the hyperpolarizer upper chassis.

A Wi-Fi-enabled user interface allowed independently actuating solenoid valves and chassis fans, isolating various stages of the inlet, outlet, and vacuum lines and well as monitoring and tuning of laser power and wavelength, heating jacket temperature. Operation of the GEN-3 hyperpolarizer commenced with the enabling of the B_0 magnetic field (3.08 A), water chiller (20.4 °C), and LDA. To ensure repeatability, IR spectroscopic measurements were performed on the pump laser at maximum current (37 A, ~170 W) before any SEOP cell heating took place (Figure 2a). LDA power output was stable over different days of experimental operation, and it provided a baseline measurement of photon flux under conditions of zero optical pumping (owing to negligible Rb vapor density at low temperatures). Once stable on-resonance laser power was achieved, the Wi-Fi interface was used to perform programmed temperature ramping and achieve the desired jacket temperature. This resulted in vaporization of Rb and sufficient absorption of pump laser photons, enabling the SEOP process to commence. Calibration of RF pulses and computation of nuclear ^{129}Xe and electron Rb polarization levels is provided in the SI.

NMR and IR spectroscopic data were acquired at regular intervals throughout each experiment to determine SEOP parameters as functions of jacket temperature, build-up time, gas mixture composition, etc. After reaching steady-state polarization and data acquisition at a given temperature, the jacket temperature could be altered to repeat experiments at different temperatures, or the hyperpolarizer could be switched to a cool-down state, whereby all fans were enabled and pump laser power was reduced. Until sufficiently low cell temperatures were observed, the laser current was maintained just above the lasing threshold (~10 A) to minimize the effect of Rb vapor condensing on the front and rear windows of the SEOP cell.

After the cool-down stage had been completed, the gas mixture could either be expanded into a Tedlar bag for storage, transport, and/or clinical research use, or retained inside the SEOP cell for further experimentation. This time period was typically used to perform T_1 relaxation measurements, since ^{129}Xe polarization could be maintained inside the solenoid coil B_0 field to a reasonably high level for several hours (Figure 2e).

https://dx.doi.org/10.1021/acs.analchem.9b05051
Anal. Chem. 2020, 92, 4309−4316

RESULTS AND DISCUSSION

Results from this study have been subdivided into two sections. The first of these pertains to the operational performance efficiency of the aluminum heating jacket for performing automated SEOP cell temperature ramping (Figure 3), and

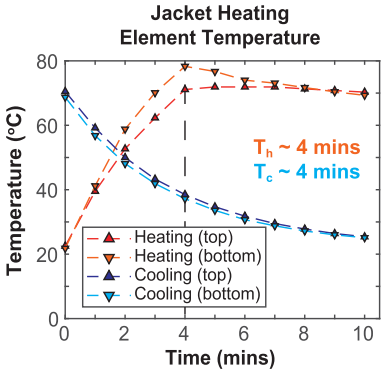


Figure 3. Temperature measurements of upper and lower jacket heating elements during a heating and cooling cycle between 22 and 70 °C, with associated exponentially fitted heating (T_h) and cooling (T_c) times included.

illustrates the rapid time scales on which SEOP cell heating and cooling can be performed. Individual measurements of the upper and lower heating element temperatures were recorded over the span of 10 min during a heating and cooling cycle, along with exponential curve-fitted parameters of the respective temperature build-up and decay processes. This facilitated an estimation of the heating and cooling time constants (T_h and T_c, respectively). From room temperature (~22 °C), the jacket temperature was raised to a set-point of 70 °C using the Wi-Fi-enabled controller. After stabilization of temperature was achieved, the temperature set-point was returned to 20 °C and all fans were enabled. During temperature ramp-up, all four (50 W each) heating elements within the jacket reached the set-point of 70 °C in <4 min (T_h). The slightly slower temperature build-up rate at the top heating element may be a result of its closer proximity to the cooling fans mounted on the top of the hyperpolarizer chassis, which naturally experienced greater airflow and more effective temperature dissipation. During the corresponding cooling cycle, both upper and lower parts of the jacket exhibited very similar temperature readings due to the significantly greater airflow throughout the chassis with all cooling fans enabled. A temperature of ~38 °C (deemed as sufficient for release of HP ^{129}Xe gas mixture in the Tedlar bag in our previous studies[54]) was recorded on both heating elements after 4 min of cooling (Tc). This is an important threshold, because it is below the melting point of Rb (39.3 °C), ensuring that the Rb vapor density is sufficiently low to allow collection of HP ^{129}Xe contrast agent with very low (few nanograms) Rb content in the temporary storage container (e.g., Tedlar bag).[54]

Rapid heating and cooling in this way decreases the overall time required for the production rates of a batch of HP ^{129}Xe (while increasing the duty cycle), as there is a reduced turn-around time between collecting one sample of HP contrast agent and commencing polarization within the next. The design presented here compares very favorably with our previous forced-air design, where the cool-down rate (for SEOP cell temperature reduction of 30 °C from 72 to 42 °C) was ~24 min[54]—a factor of 6 overall improvement. Rapid and efficient cooling of the SEOP cell is also important in the clinical setting, as it results in a shorter period of spin-relaxation between reaching steady-state ^{129}Xe polarization and delivery of HP ^{129}Xe contrast agent to subjects, allowing the ^{129}Xe to retain more polarization for the purposes of clinical imaging. For example, in our previous studies, 24 min long cool-down delay resulted in a 14.1 ± 0.7% absolute polarization loss.[54]

In addition to demonstration of rapid heating and cooling rates, we have performed the dynamic polarization build-up with the SEOP cell completely closed (Figure 4a) and SEOP

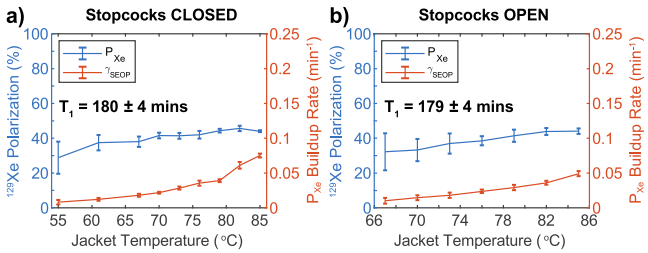


Figure 4. Steady-state $\%P_{Xe}$ and γ_{SEOP} measurements during long-lifetime (high T_1) SEOP in cells with identical 1000 Torr Xe/900 Torr N_2/100 Torr ^{4}He gas mixtures, with gas manifold stopcocks (a) closed and (b) open, as a function of the cell jacket temperature.

cell isolated from the rest of the gas loading manifold by a pair of nonmagnetic normally closed solenoid valves (Type 6126, Bürkert Fluid Control Systems, Huntersville, NC) (Figure 4b), mounted to a baseplate constructed from polyetheretherketone (PEEK). We note that the SEOP cell stopcocks (Figure 1) are not accessible while the hyperpolarizer upper chassis is sealed, and therefore the automatic SEOP cell refill can only be performed via opening of the solenoid valves. Figure 4 shows steady-state maximum $\%P_{Xe}$ and γ_{SEOP} data (obtained using the method described in Figure 2d) from ^{129}Xe polarization build-up as a function of temperature in the same SEOP cell, containing a 1000 Torr Xe/900 Torr N_2/100 Torr ^{4}He gas mixture; the only difference between the experiments is whether or not the manual stopcocks on the cell are open or closed. Importantly, the steady-state ^{129}Xe polarization, build-up rates, and ^{129}Xe T_1 values are either nearly identical for the two experiments or follow similar trends, with the only major difference being a shift in the temperature value: for the experiments where the SEOP cell stopcocks were left open (Figure 4b), there is a noticeable decrease in both measurements at a given jacket temperature relative to that in Figure 4a, where the stopcocks remained closed. This results in a temperature differential $\Delta T \approx 4$ °C between the two regimes for comparable performance (e.g., steady-state $\%P_{Xe} \approx 40\%$, $\gamma_{SEOP} \approx 0.02$ min^{-1} were observed after SEOP at jacket temperatures of ~70 and 75 °C when stopcocks were open and closed, respectively). Considering the long and nearly identical T_1 relaxation times (~3 h), differing rates of spin-relaxation can be ruled out as a contributing factor to the observed difference in performance. There may be additional thermal coupling effects of the SEOP cell contents to the PEEK bases upon which the manifold gas-handling valves are mounted, resulting in greater heat dissipation and concomitant Rb vapor density reduction. Consequently, polarization build-up dynamics are slower as a result of reduced frequency of spin-exchanging collisions at the same nominal temperature.

https://dx.doi.org/10.1021/acs.analchem.9b05051
Anal. Chem. 2020, 92, 4309−4316

These effects require additional investigation to quantify their effect on SEOP.

Another important consideration for clinical-scale HP ^{129}Xe contrast agent production is repeatability. Here, we provide pilot results with our new PEEK-based gas-loading manifold. Sparse temperature maps of $\%P_{Xe}$ and γ_{SEOP} recorded from two sequential in situ gas mixture refills (both 1000 Torr Xe/900 Torr N_2/100 Torr ^{4}He) on the GEN-3 hyperpolarizer manifold in an identical SEOP cell are displayed in Figure 5.

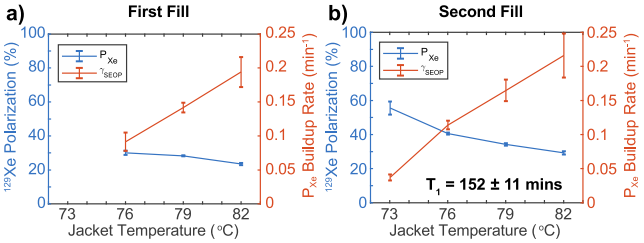


Figure 5. Pilot study on repeatability of steady-state $\%P_{Xe}$ and γ_{SEOP} measurements in SEOP cells following long-lifetime (high T_1) SEOP in two separate refills of an identical 1000 Torr Xe/900 Torr N_2/100 Torr ^{4}He gas mixture as a function of optical cell jacket temperature. T_1 relaxation time was measured once only after temperature-mapping the second gas mixture load, shown in (b).

The results from the second gas mixture refill were actually better than those observed from the first, with an increase in $\%P_{Xe}$ most pronounced at lower jacket temperatures ($\%P_{Xe}$ value of 54.8 ± 3.8% at γ_{SEOP} of 0.035 ± 0.004 min^{-1}, Figure 5b), and a modest increase in γ_{SEOP}, which was more noticeable at higher jacket temperatures (the reason for omission of the results recorded at 73 °C in the first refill is that an especially low build-up rate led to a near-linear increase in $\%P_{Xe}$ over the 60 min experimental duration, i.e., insufficient data). One explanation for the improved performance of the second fill is that heating and cooling multiple times sufficiently temperature-cycled the SEOP cell and yielded a more evenly distributed Rb spread across the interior walls (the stopcocks were closed during these experiments). This "curing" process would have given a higher Rb vapor density (as discussed previously regarding Figure 4) and a higher spin-exchange rate resulting in the improved ^{129}Xe polarization levels and build-up rates. A T_1 relaxation measurement was performed immediately after acquiring results from the second fill and cooling the SEOP cell, yielding a long lifetime of $T_1 \approx 2.5$ h. Since ^{129}Xe spin-relaxation processes are independent of the spin-exchange rate, the significance discrepancy in performance of the two SEOP runs is unlikely to be the result of some rapid change in T_1. Additionally, later SEOP cells that underwent additional heating and cooling cycles before being utilized in experiments did not experience this effect, so pre-SEOP "cell-curing" via temperature-cycling ($N > 4$) has become an important step in our methodology for improving reliability.

Figure 6a shows a selection of results from SEOP experiments performed on the GEN-3 hyperpolarizer under a variety of experimental conditions, including different gas mixtures and at different stages of SEOP cell life cycle. Rb polarization data is included where available. Figure 6a demonstrates that the maximum $\%P_{Xe}$ values were consistently between 30% and 50% (in a wide range of temperatures ranging from 64 to 85 °C) for the 1000 Torr Xe/900 Torr N_2/100 Torr ^{4}He ternary gas mixture used in the majority of work

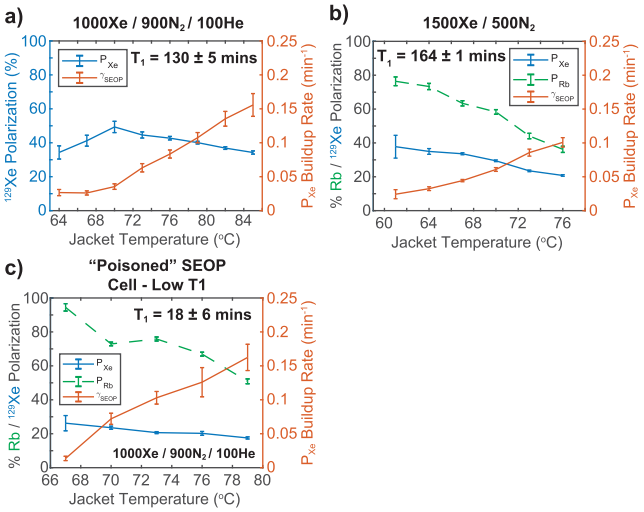


Figure 6. Temperature-dependent SEOP maps showing steady-state $\%P_{Xe}$, γ_{SEOP} and (where available) $\%P_{Rb}$ measurements following long-lifetime (high T_1) SEOP in various experimental regimes as a function of jacket temperature. (a) 1000 Torr Xe/900 Torr N_2/100 Torr ^{4}He ternary gas mixture, (b) 1500 Torr Xe/500 Torr N_2 binary gas mixture. Display (c) illustrates polarization build-up in a "poisoned" cell (i.e., where the Rb has been partially oxidized and where ^{129}Xe T_1 is low) containing a 1000 Torr Xe/900 Torr N_2/100 Torr ^{4}He gas mixture.

for this study, peaking at $\%P_{Xe} \sim 49.3 \pm 3.3\%$ (at γ_{SEOP} of 0.035 ± 0.004 min^{-1}) for 70 °C build-up in the experiment described in Figure 6a.

A build-up rate exceeding 0.15 min^{-1} was observed at a maximum jacket temperature of 85 °C, albeit under conditions far from T_{OPT} (corresponding to maximum $\%P_{Xe}$) at ~70 °C, where γ_{SEOP} was approximately 4.5 times slower. While these effects resulted in a reduction in $\%P_{Xe}$ from 49.3 ± 3.3% at 70 °C to 34.3 ± 0.9% at 85 °C (i.e., approximately a factor of 1.30 decrease), it is very interesting to note that a significantly faster buildup of polarization in Xe-rich gas mixtures is still possible. We also note that Figure 5a showed an even faster γ_{SEOP} value of 0.214 ± 0.032 min^{-1} at these elevated jacket temperatures, clearly indicating that minor decreases in maximum $\%P_{Xe}$ can be traded for significant gains in SEOP rates. For clinical-scale production, it may be beneficial to operate in these "hotter" conditions to facilitate more rapid hyperpolarization build-up and greater throughput of HP ^{129}Xe contrast agent, at the expense of slightly reduced net magnetization and image contrast. Moreover, these ultrafast build-up rates in excess of 0.20 min^{-1}—corresponding to spin up times of only ~5 min.—compare favorably to the highest build-up rates achieved using the forced-air oven hyperpolarizer design. For example, 1000 Torr Xe and 1000 Torr N_2 binary mixtures exhibited γ_{SEOP} of 0.050 ± 0.005 min^{-1} using similar laser power and SEOP cell dimensions[53], a more than a factor of 4 increase in the build-up rate. We attribute these significant gains in γ_{SEOP} to better thermal handling of the SEOP cell provided by the metal jacket. Furthermore, these fast build-up rates potentially pave the way to new modes of operation of high-pressure SEOP hyperpolarizers.[61] For example, we envision an approach of employing automated temperature ramping (the concept described previously[54]) of the SEOP cell during polarization build-up process with faster build-up rates at the beginning of the cycle and slower build-up rates (corresponding to higher $\%P_{Xe}$) at the end of the SEOP

https://dx.doi.org/10.1021/acs.analchem.9b05051
Anal. Chem. 2020, 92, 4309−4316

process. We also envision continuous-flow operation mode for this design at high Xe partial pressures, to mitigate the issue of cryo-collection *and* provide high production rates with acceptable $\%P_{Xe}$ levels.

We also compare three temperature maps of three SEOP cells presented in Figures 4a, 5b, and 6a filled with the same 1000 Torr Xe/900 Torr N_2/100 Torr ^{4}He gas mixture. All three SEOP cells performed similarly in terms of $\%P_{Xe}$ as a function of γ_{SEOP}, in all three cases, $\%P_{Xe}$ peaks (45.6 ± 1.5%, 43.8 ± 3.1%, and 49.3 ± 3.3%, respectively) at γ_{SEOP} of 0.03−0.04 min^{-1}. However, the significant variability of γ_{SEOP} as a function of temperature, which we attribute to variable Rb distribution during SEOP cell preparation. Since T_1 relaxation times were appreciably long in all cases (i.e., the spin destruction term (SI eq 5) Γ_{Xe} $(1/T_1)$ is significantly smaller compared to the build-up rates, we ignore T_1-limiting effects. Thus, we conclude that it is insufficient/nonuniform Rb distribution on the cell surfaces (affecting the Rb vapor density and spin-exchange rate) that leads to significant shifting in the temperature response, but no appreciable change in maximum $\%P_{Xe}$.

Another desirable avenue for investigation for clinical-scale production of HP ^{129}Xe contrast agents is highly rich Xe gas mixtures. An increased Xe fraction results in a greater number of polarizable target nuclei, and thus a larger theoretical limit for magnetization and SNR if similar $\%P_{Xe}$ values and spin-exchange rates can be achieved. Figure 6b displays results from a SEOP cell (with good ^{129}Xe T_1 > 2.5 h) using a 1500 Torr Xe/500 Torr N_2 binary gas mixture. The maximum $\%P_{Xe}$ is achieved at significantly lower temperatures than in the 1000 Torr Xe mixtures (e.g., Figure 6a), having already reached begun to decrease with temperature at 61 °C: 37.8 ± 6.7% versus 49.3 ± 3.3%, respectively. This is not surprising, because similar trends have been observed using previous forced-air oven designs.[53,62] We also note very similar trends in γ_{SEOP} of the two mixtures shown in Figure 6a and b. However, when taking into account the 50% increase in Xe fraction (Figure 6b versus Figure 6a; resulting from the increased Xe-dependent Rb spin-destruction rate[63,64]), a decrease in $\%P_{Xe}$ from 49.3 ± 3.3% to 37.8 ± 6.7%, will generate 15% more magnetization, by virtue of the greater quantity of ^{129}Xe nuclei. From this perspective, the super-rich 75% Xe mixture compares favorably at many of the jacket temperatures investigated during the study, only starting to suffer significant performance loss at high temperatures (64−76 °C, Figure 6b) where the Rb polarization begins to markedly decrease, $\%P_{Rb}$ fell to roughly 40% at a jacket temperature of 76 °C in the 75% Xe gas mixture.

Figure 6c also shows a temperature map of the SEOP cell at the end its operational lifetime, that is, relatively short T_1 due to Rb "poisoning" (i.e., partial oxidation) by atmospheric oxygen or water vapor. Over the course of multiple gas mixture refills and accidental SEOP cell exposure, oxidizing impurities such as O_2 and H_2O may accumulate inside the SEOP cell, reacting to form Rb oxides. This condition serves to not only suppress the Rb vapor density, but also contributes actively to spin-destruction rate $(1/T_1)$ from Xe-wall collisions. The maximum ^{129}Xe polarization observed from the SEOP cell employed in this experiment was substantially lower (26.2 ± 4.5% at T_{OPT} = 67 °C and a build-up rate γ_{SEOP} = 0.014 ± 0.003 min^{-1}) and steadily decreased with increasing jacket temperature. The observation that high levels of ^{129}Xe polarization cannot be recovered by simply increasing the temperature further to achieve an equivalent Rb vapor density (besides decreased $\%P_{Rb}$ at elevated Rb gas-phase densities) is likely due to increased spin-relaxation effects due to the presence of paramagnetic impurities. Further evidence for this effect can be obtained from the build-up rate in this cell, γ_{SEOP}, which rapidly increases even as $\%P_{Xe}$ remains low. While such a short relaxation time would traditionally render such "poisoned" SEOP cells useless to clinical-scale HP ^{129}Xe contrast agent production (because lengthy (e.g., 24 min-long[54]) cool-down process renders significant ^{129}Xe polarization loss), the rapid cooling potential of the GEN-3 hyperpolarizer aluminum jacket (ca. 4 min) means that useful magnetization can still be observed even after cooling the SEOP cell before HP ^{129}Xe gas mixture ejection. The fast build-up rates and fast temperature cycling may potentially allow the completion of polarization cycles in as little as 25 min, which may be desirable in clinical settings (8 min for temperature manipulation and ejection and 17 min of polarization build-up (γ_{SEOP} → 0.2 min^{-1}), resulting in a production rate of 1.9 L/hour of ∼25%-hyperpolarized (estimated) Xe:N_2 (50:50) mixture, corresponding to the dose equivalent (DE[65]) of ∼0.24 L of 100% hyperpolarized 100% enriched pure ^{129}Xe gas (assuming that 100% enriched ^{129}Xe is employed).

Lastly, we note that the presented data indicates a greater-than-expected difference between $\%P_{Xe}$ and $\%P_{Rb}$ recorded measurements (roughly a factor of 1.8 when considering Figure 6b and c), which previous studies have suggested should not typically exceed a factor of 1.3 in equally dense binary Xe/N_2 gas mixtures under conditions of similar polarization build-up rates, for example, γ_{SEOP} > 0.1 min^{-1} at 73 °C (Figure 6c) and similar (long) ^{129}Xe relaxation times.[53] More generally, the steady-state xenon polarization should in principle approach that of the Rb, once multiplied by the ratio of the spin-exchange rate to the SEOP build-up rate (i.e., $\%P_{Xe} = \%P_{Rb} \cdot (\gamma_{SE}/\gamma_{SEOP})$).[53,58] We believe the present deviation from this expectation is a consequence of the GEN-3 hyperpolarizer design: Specifically, we note that the ends (approximately 1" in the front and 1" in the back) of the SEOP cell are not covered by the aluminum jacket (Figure 1a), because the very ends of the SEOP cell have ∼$^1/_8$" greater diameter as a result of the fusion (i.e., glass welding) process of the optical windows and 2" glass tubing. Figure 2b shows that the ends of the SEOP cell (not covered by the jacket) may indeed be significantly colder than the rest of the SEOP cell due to contact with ambient air. We speculate that these colder regions of the cell do not constructively contribute to the SEOP process because of very low local density of Rb vapor atoms—leading to negligible regional build-up rates, even though Rb polarization appears to be high as estimated from the average $\%P_{Rb}$ along the length of the OP cell—as a consequence of having these cold and therefore "inert" regions, the gas convection may effectively average out ^{129}Xe polarization and would lead to apparent lowering of ^{129}Xe polarization values. Our future studies are aimed at improving this aspect of the aluminum jacket while maintaining the key benefits of this new design.

CONCLUSIONS

This work demonstrates the use of the cartridge-heated aluminum jacket design for rapid SEOP cell heating and cooling, with heating and cooling times reduced several-fold, down to ∼4 min, and improved thermal stability of the

https://dx.doi.org/10.1021/acs.analchem.9b05051
Anal. Chem. 2020, 92, 4309−4316

polarization process. The reduced preparation time during heating (to ensure sufficiently dense Rb vapor) and cool-down time (to minimize T_1 spin-relaxation losses) of this design has the potential to significantly scale-up production rates of HP ^{129}Xe contrast agent clinical-scale production compared to the previous forced-air designs.[45,53,54,58,59] The preliminary quality assurance studies performed on the GEN-3 ^{129}Xe hyperpolarizer indicate high levels of polarization are achievable in Xe-rich gas mixtures on clinically relevant time scales and quantities: for example, $\%P_{Xe}$ value of 54.8 ± 3.8% at γ_{SEOP} of 0.035 ± 0.004 min^{-1} at 1000 Torr Xe pressure. Moreover, high ∼40% P_{Xe} is maintained at ∼0.1 min^{-1} γ_{SEOP} for 1000 Torr Xe mixture, and ∼30% P_{Xe} is maintained at 0.06 min^{-1} γ_{SEOP} for 1500 Torr Xe mixture. The initial results show good repeatability. Furthermore, production rates with γ_{SEOP} as high as 0.2 min^{-1} have been demonstrated, which may enable more efficient approaches for clinical-scale SEOP at high Xe densities.

■ ASSOCIATED CONTENT

Supporting Information

The Supporting Information is available free of charge at https://pubs.acs.org/doi/10.1021/acs.analchem.9b05051.

Methodologies for cleaning, preparation, and loading of SEOP cells for use on the GEN-3 hyperpolarizer device; procedures for performing NMR/IR data analysis using MATLAB and associated MATLAB code; comparison of MATLAB data processing with previous manual calculation methods to demonstrate integrity and reliability of presented results and conclusions (PDF)

■ AUTHOR INFORMATION

Corresponding Authors

Eduard Y. Chekmenev − *Department of Chemistry, Integrative Biosciences (Ibio), Wayne State University, Karmanos Cancer Institute (KCI), Detroit, Michigan 48202, United States; Russian Academy of Sciences, Moscow 119991, Russia;* orcid.org/0000-0002-8745-8801; Email: chekmenev@wayne.edu

Panayiotis Nikolaou − *XeUS Technologies LTD, Nicosia 2312, Cyprus*; Email: peternikolaou78@gmail.com

Authors

Jonathan R. Birchall − *Department of Chemistry, Integrative Biosciences (Ibio), Wayne State University, Karmanos Cancer Institute (KCI), Detroit, Michigan 48202, United States*

Aaron M. Coffey − *Department of Radiology, Vanderbilt University Institute of Imaging Science (VUIIS), Nashville, Tennessee 37232, United States*

Bryce E. Kidd − *Department of Chemistry and Biochemistry, Southern Illinois University, Carbondale, Illinois 62901, United States*

Megan Murphy − *Department of Chemistry and Biochemistry, Southern Illinois University, Carbondale, Illinois 62901, United States*

Michael Molway − *Department of Chemistry and Biochemistry, Southern Illinois University, Carbondale, Illinois 62901, United States*

Liana B. Bales − *Department of Chemistry and Biochemistry, Southern Illinois University, Carbondale, Illinois 62901, United States*

Boyd M. Goodson − *Department of Chemistry and Biochemistry and Materials Technology Center, Southern Illinois University, Carbondale, Illinois 62901, United States;* orcid.org/0000-0001-6079-5077

Robert K. Irwin − *Sir Peter Mansfield Imaging Centre, University of Nottingham, Nottingham NG7 2RD, United Kingdom*

Michael J. Barlow − *Sir Peter Mansfield Imaging Centre, University of Nottingham, Nottingham NG7 2RD, United Kingdom*

Complete contact information is available at: https://pubs.acs.org/10.1021/acs.analchem.9b05051

Notes

The authors declare the following competing financial interest(s): P.N., B.M.G., and E.Y.C. declare the stake of ownership in XeUS Technologies, Ltd.

■ ACKNOWLEDGMENTS

This work was supported by DOD CDMRP W81XWH-12-1-0159/BC112431, W81XWH-15-1-0271, W81XWH-15-1-0272.

■ REFERENCES

(1) Raftery, D.; Reven, L.; Long, H.; Pines, A.; Tang, P.; Reimer, J. A. *J. Phys. Chem.* **1993**, *97* (8), 7.

(2) Spence, M. M.; Rubin, S. M.; Dimitrov, I. E.; Ruiz, E. J.; Wemmer, D. E.; Pines, A.; Yao, S. Q.; Tian, F.; Schultz, P. G. *Proc. Natl. Acad. Sci. U. S. A.* **2001**, *98* (19), 10654−10657.

(3) Nossov, A.; Haddad, E.; Guenneau, F.; Mignon, C.; Gedeon, A.; Grosso, D.; Babonneau, F.; Bonhomme, C.; Sanchez, C. *Chem. Commun.* **2002**, No. 21, 2476−2477.

(4) Pavlovskaya, G. E.; Cleveland, Z. I.; Stupic, K. F.; Basaraba, R. J.; Meersmann, T. *Proc. Natl. Acad. Sci. U. S. A.* **2005**, *102*, 18275−18279.

(5) Schroder, L.; Lowery, T. J.; Hilty, C.; Wemmer, D. E.; Pines, A. *Science* **2006**, *314* (5798), 446−449.

(6) Berthault, P.; Huber, G.; Desvaux, H. *Prog. Nucl. Magn. Reson. Spectrosc.* **2009**, *55*, 35−60.

(7) Boutin, C.; Stopin, A.; Lenda, F.; Brotin, T.; Dutasta, J.; Jamin, N.; Sanson, A.; Boulard, Y.; Leteurtre, F.; Huber, G.; Bogaert-Buchmann, A.; Tassali, N.; Desvaux, H.; Carrière, M.; Berthault, P. *Bioorg. Med. Chem.* **2011**, *19* (13), 9.

(8) Albert, M. S.; Cates, G. D.; Driehuys, B.; Happer, W.; Saam, B.; Springer, C. S.; Wishnia, A. *Nature* **1994**, *370* (6486), 199−201.

(9) Salerno, M.; de Lange, E. E.; Altes, T. A.; Truwit, J. D.; Brookeman, J. R.; Mugler, J. P. *Radiology* **2002**, *222*, 252−260.

(10) Wild, J. M.; Teh, K.; Woodhouse, N.; Paley, M. N. J.; Fichele, S.; de Zanche, N.; Kasuboski, L. *J. Magn. Reson.* **2006**, *183* (1), 13−24.

(11) Patz, S.; Muradian, I.; Hrovat, M. I.; Ruset, I. C.; Topulos, G.; Covrig, S. D.; Frederick, E.; Hatabu, H.; Hersman, F. W.; Butler, J. P. *Acad. Radiol.* **2008**, *15* (6), 713−727.

(12) Kaushik, S. S.; Cleveland, Z. I.; Cofer, G. P.; Metz, G.; Beaver, D.; Nouls, J.; Kraft, M.; Auffermann, W.; Wolber, J.; McAdams, H. P.; Driehuys, B. *Magn. Reson. Med.* **2011**, *65* (4), 1155−1165.

(13) Driehuys, B.; Martinez-Jimenez, S.; Cleveland, Z. I.; Metz, G. M.; Beaver, D. M.; Nouls, J. C.; Kaushik, S. S.; Firszt, R.; Willis, C.; Kelly, K. T.; Wolber, J.; Kraft, M.; McAdams, H. P. *Radiology* **2012**, *262*, 279−289.

(14) Muradyan, I.; Butler, J. P.; Dabaghyan, M.; Hrovat, M.; Dregely, I.; Ruset, I.; Topulos, G. P.; Frederick, E.; Hatabu, H.; Hersman, W. F.; Patz, S. *J. Magn. Reson. Imaging* **2013**, *37* (2), 457−470.

(15) Walkup, L. L.; Woods, J. C. *NMR Biomed.* **2014**, *27* (12), 1429−1438.

(16) Mazzanti, M. L.; Walvick, R. P.; Zhou, X.; Sun, Y. P.; Shah, N.; Mansour, J.; Gereige, J.; Albert, M. S. *PLoS One* **2011**, *6* (7), 7.
(17) Mugler, J. P.; Altes, T. A. *J. Magn. Reson. Imaging* **2013**, *37* (2), 313−331.
(18) Goodson, B. M. *J. Magn. Reson.* **2002**, *155* (2), 157−216.
(19) Branca, R. T.; Cleveland, Z. I.; Fubara, B.; Kumar, C. S. S. R.; Maronpot, R. R.; Leuschner, C.; Warren, W. S.; Driehuys, B. *Proc. Natl. Acad. Sci. U. S. A.* **2010**, *107* (8), 3693−3697.
(20) Branca, R. T.; He, T.; Zhang, L.; Floyd, C. S.; Freeman, M.; White, C.; Burant, A. *Proc. Natl. Acad. Sci. U. S. A.* **2014**, *111* (50), 18001−18006.
(21) Schroder, L. *Phys. Medica* **2013**, *29* (1), 3−16.
(22) Witte, C.; Schroder, L. *NMR Biomed.* **2013**, *26* (7), 788−802.
(23) Barskiy, D. A.; Coffey, A. M.; Nikolaou, P.; Mikhaylov, D. M.; Goodson, B. M.; Branca, R. T.; Lu, G. J.; Shapiro, M. G.; Telkki, V.-V.; Zhivonitko, V. V.; Koptyug, I. V.; Salnikov, O. G.; Kovtunov, K. V.; Bukhtiyarov, V. I.; Rosen, M. S.; Barlow, M. J.; Safavi, S.; Hall, I. P.; Schröder, L.; Chekmenev, E. Y. *Chem. - Eur. J.* **2017**, *23* (4), 725−751.
(24) Antonacci, M. A.; McHugh, C.; Kelley, M.; McCallister, A.; Degan, S.; Branca, R. T. *Sci. Rep.* **2019**, *9* (1), 14865.
(25) Patz, S.; Hersman, F. W.; Muradian, I.; Hrovat, M. I.; Ruset, I. C.; Ketel, S.; Jacobson, F.; Topulos, G. P.; Hatabu, H.; Butler, J. P. *Eur. J. Radiol.* **2007**, *64* (3), 335−344.
(26) Nikolaou, P.; Goodson, B. M.; Chekmenev, E. Y. *Chem. - Eur. J.* **2015**, *21* (8), 3156−3166.
(27) Goodson, B. M.; Whiting, N.; Coffey, A. M.; Nikolaou, P.; Shi, F.; Gust, B.; Gemeinhardt, M. E.; Shchepin, R. V.; Skinner, J. G.; Birchall, J. R.; Barlow, M. J.; Chekmenev, E. Y., Hyperpolarization Methods for MRS. In *eMagRes: Handbook of in vivo Magnetic Resonance Spectroscopy*; Griffiths, J.; Bottomley, P.; Wasylishen, R. E., Eds.; John Wiley & Sons, Ltd: West Sussex, UK, 2015; Vol. *4*, pp 797−810.
(28) Nikolaou, P.; Coffey, A. M.; Walkup, L. L.; Gust, B. M.; Whiting, N.; Newton, H.; Barcus, S.; Muradyan, I.; Dabaghyan, M.; Moroz, G. D.; Rosen, M.; Patz, S.; Barlow, M. J.; Chekmenev, E. Y.; Goodson, B. M. *Proc. Natl. Acad. Sci. U. S. A.* **2013**, *110*, 14150−14155.
(29) Walker, T. G.; Happer, W. *Rev. Mod. Phys.* **1997**, *69* (2), 629−642.
(30) Walker, T. G. *J. Phys. Conf. Ser.* **2011**, *294*, 012001.
(31) Bhaskar, N. D.; Happer, W.; McClelland, T. *Phys. Rev. Lett.* **1982**, *49* (1), 25−28.
(32) Driehuys, B.; Cates, G. D.; Miron, E.; Sauer, K.; Walter, D. K.; Happer, W. *Appl. Phys. Lett.* **1996**, *69* (12), 1668−1670.
(33) Zook, A. L.; Adhyaru, B. B.; Bowers, C. R. *J. Magn. Reson.* **2002**, *159* (2), 175−182.
(34) Ruset, I. C.; Ketel, S.; Hersman, F. W. *Phys. Rev. Lett.* **2006**, *96* (5), 053002.
(35) Schrank, G.; Ma, Z.; Schoeck, A.; Saam, B. *Phys. Rev. A: At., Mol., Opt. Phys.* **2009**, *80* (6), 063424.
(36) Hersman, F. W.; Ruset, I. C.; Ketel, S.; Muradian, I.; Covrig, S. D.; Distelbrink, J.; Porter, W.; Watt, D.; Ketel, J.; Brackett, J.; Hope, A.; Patz, S. *Acad. Radiol.* **2008**, *15* (6), 10.
(37) Norquay, G.; Collier, G. J.; Rao, M.; Stewart, N. J.; Wild, J. M. *Phys. Rev. Lett.* **2018**, *121* (15), 153201.
(38) Rosen, M. S.; Chupp, T. E.; Coulter, K. P.; Welsh, R. C.; Swanson, S. D. *Rev. Sci. Instrum.* **1999**, *70* (2), 1546−1552.
(39) Saha, I.; Nikolaou, P.; Whiting, N.; Goodson, B. M. *Chem. Phys. Lett.* **2006**, *428* (4−6), 268−276.
(40) Baranga, A. B.-A.; Appelt, S.; Erickson, C. J.; Young, A. R.; Happer, W. *Phys. Rev. A: At., Mol., Opt. Phys.* **1998**, *58*, 2282.
(41) Fink, A.; Brunner, E. *Appl. Phys. B: Lasers Opt.* **2007**, *89* (1), 7.
(42) Ottinger, C.; Scheps, R.; York, G. W.; Gallagher, A. *Phys. Rev. A: At., Mol., Opt. Phys.* **1975**, *11* (6), 14.
(43) Romalis, M. V.; Miron, E.; Cates, G. D. *Phys. Rev. A: At., Mol., Opt. Phys.* **1997**, *56* (6), 4569−4578.
(44) Couture, A. H.; Clegg, T. B.; Driehuys, B. *J. Appl. Phys.* **2008**, *104* (9), 6.
(45) Nikolaou, P.; Whiting, N.; Eschmann, N. A.; Chaffee, K. E.; Goodson, B. M. *J. Magn. Reson.* **2009**, *197* (2), 249−254.
(46) Chann, B.; Nelson, I.; Walker, T. G. *Opt. Lett.* **2000**, *25* (18), 1352−1354.
(47) Zhu, H.; Ruset, I. C.; Hersman, F. W. *Opt. Lett.* **2005**, *30* (11), 1342−1344.
(48) Babcock, E.; Chann, B.; Nelson, I. A.; Walker, T. G. *Appl. Opt.* **2005**, *44*, 3098−3104.
(49) Zerger, J. N.; Lim, M. J.; Coulter, K. P.; Chupp, T. E. *Appl. Phys. Lett.* **2000**, *76* (14), 1798−1800.
(50) Witte, C.; Kunth, M.; Rossella, F.; Schröder, L. *J. Chem. Phys.* **2014**, *140* (8), 084203.
(51) Freeman, M. S.; Emami, K.; Driehuys, B. *Phys. Rev. A: At., Mol., Opt. Phys.* **2014**, *90* (2), 023406.
(52) Antonacci, M. A.; Burant, A.; Wagner, W.; Branca, R. T. *J. Magn. Reson.* **2017**, *279*, 8.
(53) Nikolaou, P.; Coffey, A. M.; Ranta, K.; Walkup, L. L.; Gust, B.; Barlow, M. J.; Rosen, M. S.; Goodson, B. M.; Chekmenev, E. Y. *J. Phys. Chem. B* **2014**, *118* (18), 4809−4816.
(54) Nikolaou, P.; Coffey, A. M.; Barlow, M. J.; Rosen, M.; Goodson, B. M.; Chekmenev, E. Y. *Anal. Chem.* **2014**, *86* (16), 8206−8212.
(55) Cates, G. D.; Benton, D. R.; Gatzke, M.; Happer, W.; Hasson, K. C.; Newbury, N. R. *Phys. Rev. Lett.* **1990**, *65*, 2591−2594.
(56) Gatzke, M.; Cates, G. D.; Driehuys, B.; Fox, D.; Happer, W.; Saam, B. *Phys. Rev. Lett.* **1993**, *70* (5), 690−693.
(57) Six, J. S.; Hughes-Riley, T.; Stupic, K. F.; Pavlovskaya, G. E.; Meersmann, T. *PLoS One* **2012**, *7* (11), 16.
(58) Nikolaou, P.; Coffey, A. M.; Walkup, L. L.; Gust, B.; LaPierre, C.; Koehnemann, E.; Barlow, M. J.; Rosen, M. S.; Goodson, B. M.; Chekmenev, E. Y. *J. Am. Chem. Soc.* **2014**, *136* (4), 1636−1642.
(59) Nikolaou, P.; Coffey, A. M.; Walkup, L. L.; Gust, B. M.; Whiting, N. R.; Newton, H.; Muradyan, I.; Dabaghyan, M.; Ranta, K.; Moroz, G.; Patz, S.; Rosen, M. S.; Barlow, M. J.; Chekmenev, E. Y.; Goodson, B. M. *Magn. Reson. Imaging* **2014**, *32* (5), 541−550.
(60) Skinner, J. G.; Ranta, K.; Whiting, N.; Coffey, A. M.; Nikolaou, P.; Rosen, M. S.; Chekmenev, E. Y.; Morris, P. G.; Barlow, M. J.; Goodson, B. M. *J. Magn. Reson.* **2020**, *312*, 106686.
(61) Mortuza, M. G.; Anala, S.; Pavlovskaya, G. E.; Dieken, T. J.; Meersmann, T. *J. Chem. Phys.* **2003**, *181*, 1581.
(62) Whiting, N.; Nikolaou, P.; Eschmann, N. A.; Barlow, M. J.; Goodson, B. M. *J. Magn. Reson.* **2011**, *208* (2), 298−304.
(63) Bouchiat, M. A.; Brossel, J.; Pottier, L. C. *J. Chem. Phys.* **1972**, *56*, 3703−3714.
(64) Nelson, I. A.; Walker, T. G. *Phys. Rev. A: At., Mol., Opt. Phys.* **2001**, *65*, 012712.
(65) He, M.; Robertson, S. H.; Kaushik, S. S.; Freeman, M. S.; Virgincar, R. S.; Davies, J.; Stiles, J.; Foster, W. M.; McAdams, H. P.; Driehuys, B. *Magn. Reson. Imaging* **2015**, *33* (7), 877−885.

https://dx.doi.org/10.1021/acs.analchem.9b05051
Anal. Chem. 2020, 92, 4309−4316

Zitierweise: *Angew. Chem. Int. Ed.* **2020**, *132*, 8654–8660
Internationale Ausgabe: doi.org/10.1002/anie.201916597
Deutsche Ausgabe: doi.org/10.1002/ange.201916597

Hyperpolarization

Parahydrogen-Induced Radio Amplification by Stimulated Emission of Radiation

*Baptiste Joalland, Nuwandi M. Ariyasingha, Sören Lehmkuhl, Thomas Theis, Stephan Appelt und Eduard Y. Chekmenev**

Abstract: *Radio amplification by stimulated emission of radiation (RASER) was recently discovered in a low-field NMR spectrometer incorporating a highly specialized radio-frequency resonator, where a high degree of proton-spin polarization was achieved by reversible parahydrogen exchange. RASER activity, which results from the coherent coupling between the nuclear spins and the inductive detector, can overcome the limits of frequency resolution in NMR. Here we show that this phenomenon is not limited to low magnetic fields or the use of resonators with high-quality factors. We use a commercial bench-top 1.4 T NMR spectrometer in conjunction with pairwise parahydrogen addition producing proton-hyperpolarized molecules in the Earth's magnetic field (ALTADENA condition) or in a high magnetic field (PASADENA condition) to induce RASER without any radio-frequency excitation pulses. The results demonstrate that RASER activity can be observed on virtually any NMR spectrometer and measures most of the important NMR parameters with high precision.*

Introduction

Suefke and co-workers reported recently (in 2017) on the first experimental observation of radio amplification by stimulated emission of radiation (RASER) of protons.[1,2] Unlike lasers and masers, which employ self-organizing systems emitting coherent optical light and microwaves, RASER is induced by continuous coherent oscillation of radio waves at much lower frequencies through the coupling between nuclear-spin magnetization and an LC resonance circuit.[1] Because the required magnetization, that is, the product of the concentration of nuclear spins and their nuclear-spin polarization (P) or the degree of the spin alignment with the static magnetic field of the NMR magnet, is very high, RASER-based NMR spectroscopy is difficult to achieve using thermal nuclear-spin polarization. Hyperpolarization techniques allow for enhancing the nuclear-spin polarization by several orders of magnitude[3–7] up to unity.[8,9] Suefke and co-workers thus employed the technique of signal amplification by reversible exchange (SABRE) to provide a highly magnetized sample in their pioneering RASER demonstration.[10] SABRE relies on the simultaneous exchange between parahydrogen (p-H_2, the source of hyperpolarization) and a substrate on a metal complex.[11] With SABRE, the spontaneous polarization of proton spins is efficient in the magnetic-field range of 1 to 10 mT.[12] Therefore, Suefke and co-workers employed NMR detection at magnetic fields of several mT with corresponding resonance frequencies in the range of 41–512 kHz.[1,2] These authors also employed SABRE because it allows for continuously regenerating the proton polarization via the sustained delivery of p-H_2 gas to the sample placed inside the NMR detector.[1] RASER activity is initiated when the radiation damping rate $1/\tau_{RD}$ satisfies the following condition:

$$1/\tau_{RD} > 1/T_2^* \quad (1)$$

where $1/T_2^*$ defines the modified spin–spin relaxation rate and $1/\tau_{RD}$ the radiation-damping rate, which is given by

$$1/\tau_{RD} = -(\mu_0/2)\eta\, Q\, \gamma\, M_0 = -(\mu_0/4)\eta\, Q\, \gamma^2\, \hbar\, n_S\, P \quad (2)$$

where μ_0, η, Q, γ, $\hbar$, and n_S are defined as the vacuum permeability, the filling factor of the resonator, the quality factor of the resonator, the gyromagnetic ratio, Planck's constant, and the spin-number density, respectively. The initial magnetization is given as $M_0 = (1/2)\hbar\gamma n_S P$, where P is the degree of spin polarization.[1] Note that if $P > 0$, the rate $1/\tau_{RD}$ is negative and the associated line is additionally broadened by radiation damping with a total damping rate $\kappa_{tot} = (1/T_2^* - 1/\tau_{RD}) > 1/T_2^*$. If $P < 0$, which corresponds to a population inversion, $1/\tau_{RD}$ is positive and the line is narrowed due to the decreased total damping rate $\kappa_{tot} < 1/T_2^*$. RASER activity starts if $\kappa_{tot} < 0$, as described by Equation (1). To fulfill this condition for proton spins at low frequencies,

[*] Dr. B. Joalland, N. M. Ariyasingha, Prof. E. Y. Chekmenev
Department of Chemistry, Integrative Biosciences (Ibio)
Karmanos Cancer Institute (KCI), Wayne State University
Detroit, MI 48202 (USA)
E-Mail: Chekmenev@wayne.edu
Dr. S. Lehmkuhl, Prof. T. Theis
Department of Chemistry, North Carolina State University
Raleigh, NC 27695-8204 (USA)
Prof. S. Appelt
Institut für Technische und Makromolekulare Chemie (ITMC)
RWTH Aachen University
52056 Aachen (Germany),
and
Central Institute for Engineering, Electronics and Analytics—Electronic Systems (ZEA 2), Forschungszentrum Jülich GmbH
52425 Jülich (Germany)
Prof. E. Y. Chekmenev
Russian Academy of Sciences
Leninskiy Prospekt 14, Moscow, 119991 (Russia)
Supporting information and the ORCID identification number(s) for the author(s) of this article can be found under: https://doi.org/10.1002/anie.201916597.

 © 2020 Wiley-VCH Verlag GmbH & Co. KGaA, Weinheim

Suefke and co-workers employed high-quality ($Q \approx 300$) resonators,[13] which reduce the RASER-threshold requirements for polarization and concentration significantly.[1] Hence, the experimental conditions used for this first demonstration RASER, that is, low magnetic field, high-Q resonator, and continuous regeneration of hyperpolarization, seem very peculiar. As a matter of fact, RASER activity is a much more common phenomenon than one could expect, as we will show below.

Results and Discussion

We provide evidence that a commercial high-field NMR system with standard inductive detection (that is, without specialized high-Q resonators) can readily detect RASER when combined with the parahydrogen-induced polarization (PHIP) technique.[14] Specifically, we employ a 1.4 T (61.7 MHz) bench-top NMR spectrometer (SpinSolve Carbon 60, Magritek, New Zealand) with $Q = 68$ to induce RASER of protons in hyperpolarized (HP) ethyl acetate (EA) and 2-hydroxyethyl propionate (HEP). These HP compounds are formed through the pairwise addition of p-H_2 to the unsaturated C=C bonds of the substrates vinyl acetate (VA) and 2-hydroxyethyl acrylate (HEA), respectively (Figure 1 a,b). The symmetry breaking of the nascent p-H_2-derived protons allows for the hyperpolarization to become observable.[7,15] The solutions were prepared with ≈ 0.4 M of substrates and 4 mM of catalyst (bicyclo-[2.2.1]hepta-2,5-diene)[1,4-bis(diphenylphosphino)butane]-rhodium(I) tetrafluoroborate] (Sigma–Aldrich, P/N 341126-100MG) in CD_3OD. Nearly 100 % p-H_2 was employed using a home-built cryogenic generator.[16] At 75 °C and 100 psi, the substrates were fully converted into their respective HP products via bubbling p-H_2 for 15 s with a 150 sccm flow rate controlled by a mass-flow controller, as described previously (Figure 1 c).[17] The chemical conversion was monitored by comparing the ^{1}H NMR spectra of thermally polarized samples taken before and after the PHIP reactions (Figures S1 and S2 in the Supporting Information). The polarization of H_A and H_B was estimated to be between 10 % and 20 % based on a previous study,[18] and their T_1 relaxation times were measured to be $\approx$ 16–25 s (Figure S3).

Two main experimental protocols were followed. The first protocol corresponds to the ALTADENA condition.[19] In this case, the samples were hydrogenated in the Earth's magnetic field (≈ 50 μT). The p-H_2 flow was then interrupted, the sample depressurized, the catheter removed, the pulse-and-acquire sequence initiated, and the sample inserted into the NMR spectrometer (Figure 1 d). To make sure that the sample does not experience any radiofrequency (RF) excitation, the sample was inserted several seconds after a RF pulse with a flip angle lower than 0.01° (for inconvenient technical reasons, we were not able to open the detection channel without executing a pulse). The detector channel was opened for up to 32 s. The second protocol corresponds to the PASADENA condition[20] in which the hydrogenation reaction was performed at 1.4 T, that is, inside the spectrometer. During the hydrogenation reaction, the sample was positioned 4–5 cm above the RF coil so the catheter could be removed without interfering with the signal detection, which was initiated before the hydrogenation reaction was completed. Once the reaction was completed and the catheter removed, the sample was pushed inside the RF coil (Figure 1 e).

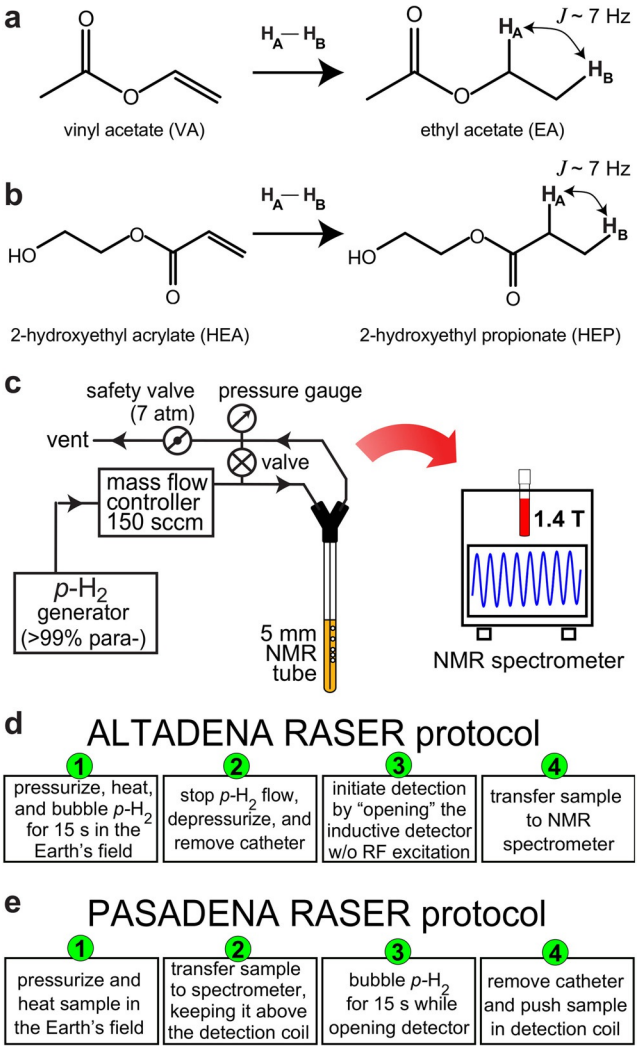


Figure 1. a), b) Reaction schemes for the pairwise p-H_2 addition to vinyl acetate (VA) yielding ethyl acetate (EA) and to 2-hydroxyethyl acrylate (HEA) yielding 2-hydroxyethyl propionate (HEP). c) Experimental setup. d), e) ALTADENA and PASADENA protocols used to evidence parahydrogen-induced RASER activity.

The main results obtained for EA and HEP are illustrated in Figures 2 and 3, respectively. For both ALTADENA and PASADENA experiments, the NMR signal exhibits the characteristic features of RASER activity: Signal persistence for significantly longer periods of time than T_2^* of ≈ 0.6 s.[1,13] The Fourier-transformed spectra of selected regions with a defined duration of the RASER-active signals, for example, Figure 2 b,c for ALTADENA and Figure 2 i–l for PASADENA, clearly show evidence for the enhanced spectral resolution due to RASER activity with sharp peaks with FWHM < 0.2 Hz, whereas the resolution of the spectrometer is ≈ 0.5 Hz after full shimming and ≈ 2 Hz in case of

 © 2020 Wiley-VCH Verlag GmbH & Co. KGaA, Weinheim

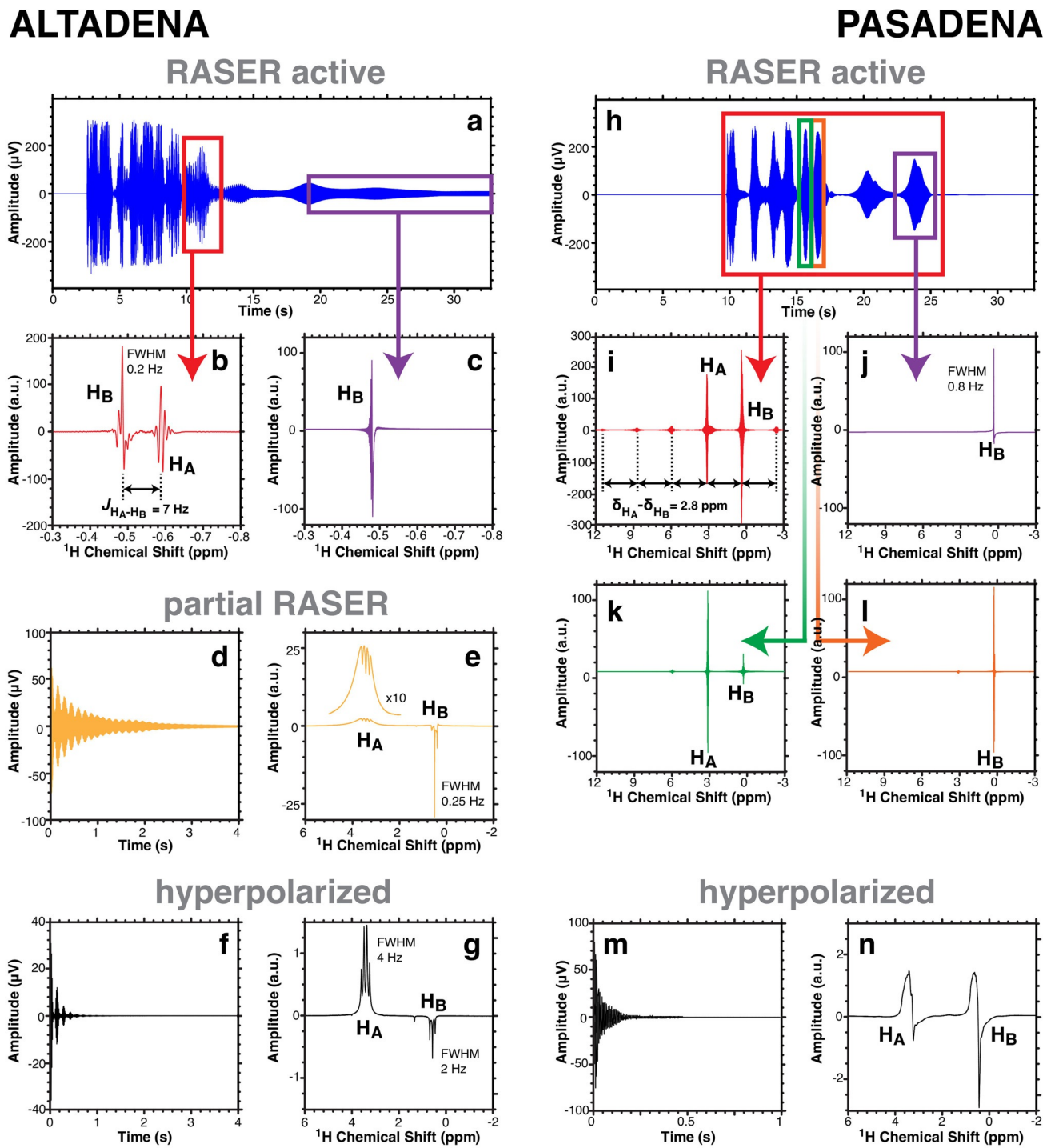


Figure 2. ^{1}H NMR spectroscopy of solution-phase PHIP of 0.4 M HP ethyl acetate (EA) probed at 1.4 T. a) ALTADENA RASER signal recorded without a RF pulse after hydrogenation in the Earth's magnetic field. b), c) Fourier spectra of the regions outlined by red and purple boxes, respectively, in panel (a). d), e) Partial ALTADENA RASER signal and Fourier spectrum obtained with a ≈3° RF pulse. f), g) Canonical ALTADENA (non-RASER) FID and Fourier spectrum recorded after further polarization decay. h) PASADENA RASER signal recorded without a RF pulse after hydrogenation at 1.4 T. i)–l) Fourier spectra of the regions outlined by red, purple, green, and orange boxes, respectively, in panel (h). m), n) Canonical PASADENA (non-RASER) FID and Fourier spectrum acquired with a ≈3° RF pulse after further polarization decay (≈30 s).

conventional HP experiments. Immediately after these RASER-active signals were recorded, additional NMR spectra were acquired using a ≈3.3° excitation RF pulse. The first of those spectra shows partially RASER-active NMR lines (see Figure 2e for ALTADENA and Figure 3l for PASADENA), while the subsequent acquisitions correspond to normal, hyperpolarized ALTADENA (Figures 2g and 3g) and PASADENA (Figures 2n and 3n) spectra.

With ALTADENA, the Fourier spectra of the time slices of the RASER-active signals (displayed in Figures 2a and 3a)

© 2020 Wiley-VCH Verlag GmbH & Co. KGaA, Weinheim

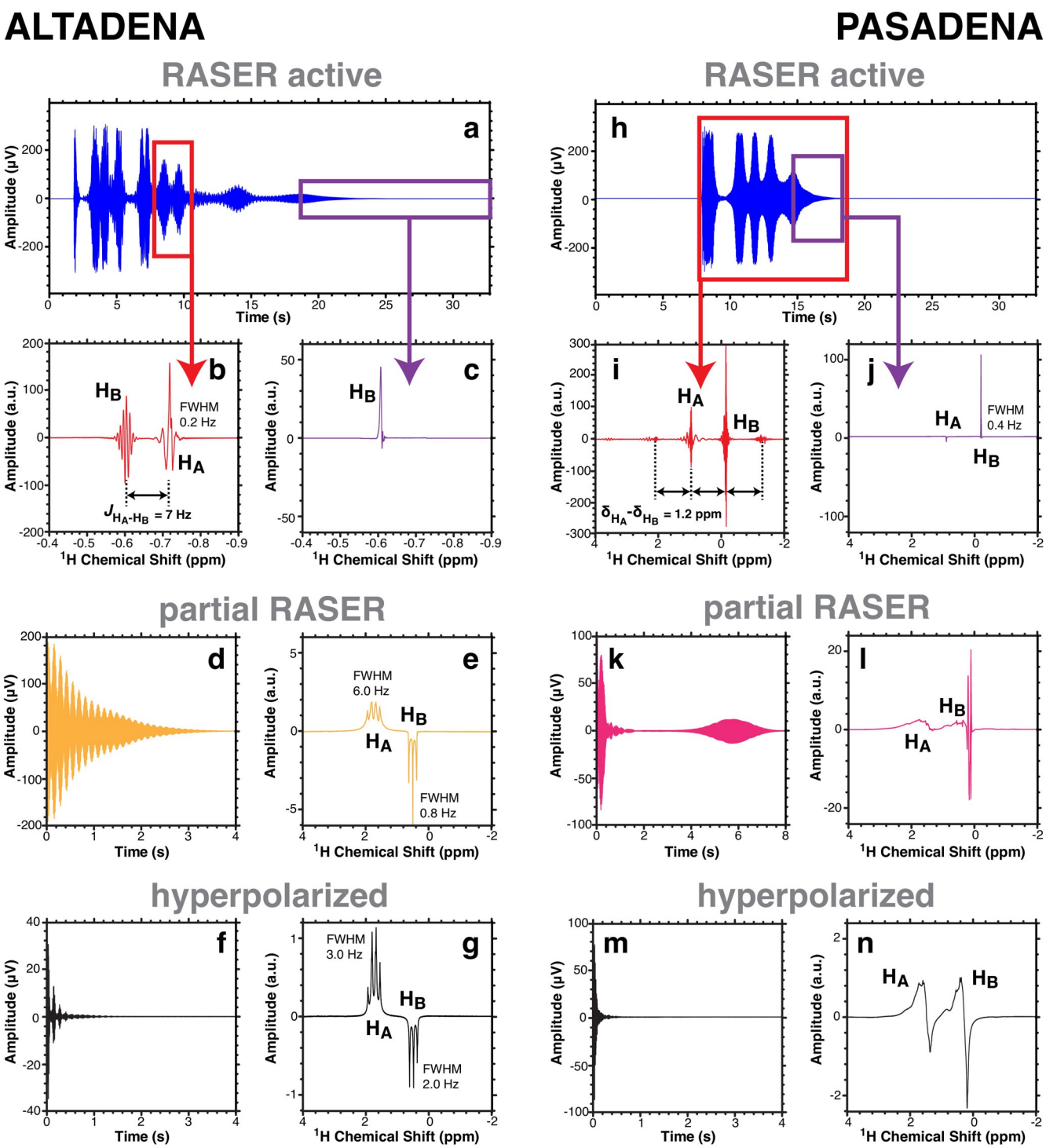


Figure 3. ^{1}H NMR spectroscopy of solution-phase PHIP of 0.4 M HP 2-hydroxyethyl propionate (HEP) probed at 1.4 T. a) ALTADENA RASER signal recorded without a RF pulse after hydrogenation in the Earth's magnetic field. b), c) Fourier spectra of the regions outlined by red and purple lines, respectively, in panel (b). d), e) Partial ALTADENA RASER signal and Fourier spectrum acquired using a ≈3° RF pulse. f), g) Canonical ALTADENA (non-RASER) FID and Fourier spectrum recorded after further polarization decay (≈30 s). h) PASADENA RASER signal recorded without a RF pulse after hydrogenation at 1.4 T. i), j) Fourier spectra of the regions outlined by red and purple lines, respectively, in panel (h). k), l) Partial PASADENA RASER signal and Fourier spectrum acquired using a ≈3° RF pulse. m), n) Canonical PASADENA (non-RASER) FID and Fourier spectrum acquired with a ≈3° RF pulse after further polarization decay (≈30 s).

show a doublet (Figures 2b and 3b). These two RASER resonances can be attributed to lines in the PHIP spectra depicted in Figures 2g and 3g, respectively. In particular, each of the three triplet lines corresponding to proton H_B are population-inverted (have negative sign) and its two most intense lines are RASER-active. The doublet is separated by

© 2020 Wiley-VCH Verlag GmbH & Co. KGaA, Weinheim

a splitting corresponding to the spin–spin coupling $J_{H_A-H_B}$ of 7.0 Hz between proton H_A and H_B in EA and HEP (Figures 2b and 3b, respectively).[21] While the HP state decays, the number of RASER-active lines changes, for example from two RASER-active lines in Figures 2b and 3b to one single line in Figures 2c and 3c. This can be explained by different transverse relaxation rates and multiplicities of each RASER line. For instance, at low polarization, only one line with the highest amplitude in the NMR spectrum and with the smallest linewidth overcomes the RASER threshold and is RASER-active.

All ALTADENA-hyperpolarized RASER spectra in Figures 2 and 3 differ significantly from the corresponding PHIP spectra in Figures 2g and 3g. The latter feature the HP resonances of H_A and H_B with the quartet and triplet lines of opposite signs. These are separated by $\approx$2.8 ppm ($\approx$174 Hz) for EA and $\approx$1.2 ppm ($\approx$74 Hz) for HEP. Specifically, the linewidth of the quartet FWHM of $\approx$4 Hz in Figure 2g is significantly broader compared to the linewidth of each of the triplet lines with a FWHM of $\approx$2 Hz. This is more pronounced in Figure 2e, where the difference in linewidth is more than one order of magnitude. The same trend is observed in Figure 3e,g. The reason for this is the sign and the magnitude of the HP state, which introduce a broadening with $\kappa_{tot} > 1/T_2^*$ of the quartet lines and a narrowing with $\kappa_{tot} < 1/T_2^*$ of the triplet lines. For the RASER lines in Figure 2b and 3b, κ_{tot} is negative and the linewidth, in principal, is only limited by the finite measurement time and ultimately by the Cramér–Rao condition.[22] We conclude that the RASER spectra of VA and HEP hyperpolarized by ALTADENA allow the *J*-coupling constant $J_{H_A-H_B}$ to be determined with enhanced precision but the chemical-shift difference between H_A and H_B is not measurable in this RASER experiment.

The analysis of the RASER-active signals in the PASADENA case (Figures 2h and 3h) renders other interesting observations in addition to the anticipated line-narrowing. In particular, the Fourier spectra of the RASER-active signals (Figures 2i and 3i) exhibit two large central RASER lines separated by the chemical-shift difference $\delta_{H_A}-\delta_{H_B}$ between the H_A and H_B protons, that is, $\delta_{H_A}-\delta_{H_B}=2.8$ ppm ($\approx$174 Hz) for EA and 1.2 ppm ($\approx$74 Hz) for HEP. The two central lines are accompanied by evenly spaced small sidebands, and the distance between two consecutive lines is exactly $\delta_{H_A}-\delta_{H_B}$. This can be explained by the non-linear interaction between different RASER-active modes (here: two) leading to a frequency-comb-like spectrum.[2] We also even found frequency-comb-like spectra in the case of the ALTADENA-pumped RASER, where the two central modes and all sidebands are spaced by $J_{H_A-H_B}$. Moreover, the resonance frequencies of the RASER-active protons (Figures 2b,c and 3b,c) are sometimes shifted by about 1 ppm when compared with the partial RASER and hyperpolarized ones. We speculate that this is due to the magnetic-field fluctuations induced by RASER. A detailed evaluation of these and other non-linear phenomena will be published elsewhere.

A series of additional experiments were performed, demonstrating further that the experimental conditions necessary for observing RASER through PHIP reactions are not stringent at all. RASER bursts can indeed be observed with more dilute samples, as illustrated by the NMR signal shown in Figure S4 and obtained with a 40 mM VA solution. This indicates that PHIP RASER occurs at relatively low concentrations of the HP substrate; in particular, lower concentrations than those reported previously for the spontaneous emission of NMR signals with the dissolution dynamic nuclear polarization (d-DNP) technique.[23] ALTADENA RASER activity was also observed while leaving the catheter (1/16″ outer diameter, 1/32″ inner diameter) inside the NMR tube, thus creating more stringent conditions for its occurrence because the presence of the catheter leads to a significant susceptibility-induced B_0 gradient and effectively shorter T_2^* (see Figures S5,S6). Note that in additional PASADENA experiments, the hydrogenation reactions were performed within the RF coil, and RASER was detected immediately after the cessation of *p*-H_2 bubbling because the bubbles induce a significant degradation of T_2^* (likely below 1 ms) that prevents RASER activity at this magnetic field.

These findings are crucial in the context of PHIP studies and biomedical applications. The HP substrates used here can indeed be employed as in-vivo contrast agents. For example, HP HEP has been extensively studied as a potential contrast agent in angiography studies.[24–26] Because some of the PHIP techniques rely on the application of RF pulses, especially in the case of polarization transfer from protons to ^{13}C nuclei,[27–35] the RF coils may interact with the highly proton-hyperpolarized compounds, resulting in complicated non-linear effects and depletion of hyperpolarization via RASER activity. Therefore, RASER effects may be considered as an obstacle in this context. The use of untuned RF coils[36,37] may help mitigate the occurrence of RASER, so that the hyperpolarized proton pool is not depleted prior to its utilization during contrast-agent preparation. Moreover, the recent advent of PHIP via side-arm hydrogenation (SAH) significantly expanded the range of biomolecules (including ethyl acetate) that can be hyperpolarized via PHIP.[17,38] With this technique, a wide range of carboxylic acids have been hyperpolarized and employed in vivo for metabolism tracking.[21,27,38–42]

Amid the peer-review evaluation of the present work, another interesting study regarding PHIP-RASER by Pravdivtsev and co-workers was reported.[43] In contrast with the common and somewhat ordinary conditions we have presented here, Pravdivtsev et al. designed a specific experiment dedicated to observe parahydrogen-induced RASER activity under PASADENA conditions at a magnetic field of 14 T (600 MHz) and with a cryogenically cooled coil ($Q \approx 500$).[43] The catalyst activity was tuned for building up polarization throughout an extended period of time (about 10 min) with a continuous delivery of *p*-H_2. The pairwise *p*-H_2 addition was performed with two substrates incorporating C≡C triple bonds. Without RF-pulse excitation, RASER activity was detected only after bubbling *p*-H_2 for about 90 s. Only chemical shifts but no *J*-couplings could be determined in these very-high-field experiments and the reported linewidths (in the order of 1 Hz) of the RASER-active lines do not differ significantly from the linewidth obtained by a corresponding standard NMR spectrum (a few ppb at 600 MHz). The work presented in this article differs in many regards. First and

 © 2020 Wiley-VCH Verlag GmbH & Co. KGaA, Weinheim

foremost, the equipment employed here is a commercially available NMR spectrometer with an unaltered room-temperature RF coil with $Q \approx 68$—such instrumentation is widely available, making our observations possible and easy to replicate by others interested in using the PHIP RASER effect. Second, we demonstrated PHIP RASER under both PASADENA and ALTADENA conditions and showed intriguing *J*-coupling and chemical-shift-controlled dynamics of RASER-signal evolution. No RF stimulation was required to induce the RASER effect. Third, we employed two molecular moieties (acetate[44,45] and propionate[25] via pairwise *p*-H_2 addition to the C=C double bond) that have been previously employed in in-vivo bio-imaging studies of perfusion and metabolism. Importantly, we employed the process of batch hyperpolarization,[34,35] when a bolus of material is hyperpolarized over a short period of time (circa 10 s), and such bolus could be employed for in-vivo imaging applications, paving the way to a potential future use of RASER in bio-imaging applications, which have the potential to revolutionize MRI and medical imaging.

Conclusion

To summarize, RASER activity of two PHIP-hyperpolarized compounds is reported here using standard NMR hardware at concentrations as low as 40 mM and at estimated proton-polarization values of over 10% at the time of the detection.[17] RASER activity is observed with and without applications of RF-excitation pulses and under both ALTADENA and PASADENA conditions. *J*-coupling constants as well as chemical-shift differences could be measured with increased precision. As the field of PHIP continues to grow, researchers using standard, commercial NMR spectrometers are therefore expected to experience RASER activity and radiation-damping or line-narrowing phenomena routinely. Appropriate considerations must be made when performing NMR experiments with such highly polarized compounds. Our observations are especially important for PHIP studies that aim at providing highly polarized contrast agents for imaging of metabolism, that is, where high levels of polarization at high substrate concentrations are desired.[46] Despite its complications, the parahydrogen-induced RASER phenomenon described here could enable new applications in magnetic resonance, quantum computing, data encryption, and other things.[1,2,13,47] Further studies are underway in our laboratories to provide additional theoretical and experimental insights about this intriguing phenomenon and its applications.

Acknowledgements

This work was supported by NSF under Grant CHE-1904780, National Cancer Institute under 1R21CA220137, and by DOD CDMRP under BRP W81XWH-12-1-0159/BC112431 and under W81XWH-15-1-0271. Research reported in this publication was also supported by the National Institute of Biomedical Imaging and Bioengineering of the NIH under R21EB025313. T.T. and S.L. acknowledge funding from the North Carolina Biotechnology Center as well as the Mallinckrodt Foundation.

Conflict of interest

The authors declare no conflict of interest.

Stichwörter: Hyperpolarisation · NMR-Spektroskopie · Parawasserstoff · PHIP · RASER

[1] M. Suefke, S. Lehmkuhl, A. Liebisch, B. Blumich, S. Appelt, *Nat. Phys.* **2017**, *13*, 568 – 572.
[2] S. Appelt, A. Kentner, S. Lehmkuhl, B. Blümich, *Prog. Nucl. Magn. Reson. Spectrosc.* **2019**, *114 – 115*, 1 – 32.
[3] P. Nikolaou, B. M. Goodson, E. Y. Chekmenev, *Chem. Eur. J.* **2015**, *21*, 3156 – 3166.
[4] J. H. Ardenkjaer-Larsen, B. Fridlund, A. Gram, G. Hansson, L. Hansson, M. H. Lerche, R. Servin, M. Thaning, K. Golman, *Proc. Natl. Acad. Sci. USA* **2003**, *100*, 10158 – 10163.
[5] J.-H. Ardenkjaer-Larsen, G. S. Boebinger, A. Comment, S. Duckett, A. S. Edison, F. Engelke, C. Griesinger, R. G. Griffin, C. Hilty, H. Maeda, G. Parigi, T. Prisner, E. Ravera, J. van Bentum, S. Vega, A. Webb, C. Luchinat, H. Schwalbe, L. Frydman, *Angew. Chem. Int. Ed.* **2015**, *54*, 9162 – 9185; *Angew. Chem.* **2015**, *127*, 9292 – 9317.
[6] G. Navon, Y. Q. Song, T. Room, S. Appelt, R. E. Taylor, A. Pines, *Science* **1996**, *271*, 1848 – 1851.
[7] K. V. Kovtunov, E. V. Pokochueva, O. G. Salnikov, S. Cousin, D. Kurzbach, B. Vuichoud, S. Jannin, E. Y. Chekmenev, B. M. Goodson, D. A. Barskiy, I. V. Koptyug, *Chem. Asian J.* **2018**, *13*, 1857 – 1871.
[8] P. Nikolaou, A. M. Coffey, L. L. Walkup, B. M. Gust, N. Whiting, H. Newton, S. Barcus, I. Muradyan, M. Dabaghyan, G. D. Moroz, M. Rosen, S. Patz, M. J. Barlow, E. Y. Chekmenev, B. M. Goodson, *Proc. Natl. Acad. Sci. USA* **2013**, *110*, 14150 – 14155.
[9] P. J. Rayner, M. J. Burns, A. M. Olaru, P. Norcott, M. Fekete, G. G. R. Green, L. A. R. Highton, R. E. Mewis, S. B. Duckett, *Proc. Natl. Acad. Sci. USA* **2017**, *114*, E3188 – E3194.
[10] R. W. Adams, J. A. Aguilar, K. D. Atkinson, M. J. Cowley, P. I. P. Elliott, S. B. Duckett, G. G. R. Green, I. G. Khazal, J. Lopez-Serrano, D. C. Williamson, *Science* **2009**, *323*, 1708 – 1711.
[11] R. W. Adams, S. B. Duckett, R. A. Green, D. C. Williamson, G. G. R. Green, *J. Chem. Phys.* **2009**, *131*, 194505.
[12] M. J. Cowley, R. W. Adams, K. D. Atkinson, M. C. R. Cockett, S. B. Duckett, G. G. R. Green, J. A. B. Lohman, R. Kerssebaum, D. Kilgour, R. E. Mewis, *J. Am. Chem. Soc.* **2011**, *133*, 6134 – 6137.
[13] M. Suefke, A. Liebisch, B. Blumich, S. Appelt, *Nat. Phys.* **2015**, *11*, 767 – 771.
[14] T. C. Eisenschmid, R. U. Kirss, P. P. Deutsch, S. I. Hommeltoft, R. Eisenberg, J. Bargon, R. G. Lawler, A. L. Balch, *J. Am. Chem. Soc.* **1987**, *109*, 8089 – 8091.
[15] C. R. Bowers, D. P. Weitekamp, *Phys. Rev. Lett.* **1986**, *57*, 2645 – 2648.
[16] B. Feng, A. M. Coffey, R. D. Colon, E. Y. Chekmenev, K. W. Waddell, *J. Magn. Reson.* **2012**, *214*, 258 – 262.
[17] O. G. Salnikov, N. V. Chukanov, R. V. Shchepin, I. V. Manzanera Esteve, K. V. Kovtunov, I. V. Koptyug, E. Y. Chekmenev, *J. Phys. Chem. C* **2019**, *123*, 12827 – 12840.
[18] B. Joalland, A. Schmidt, M. S. H. Kabir, N. V. Chukanov, K. V. Kovtunov, I. V. Koptyug, J. Hennig, J.-B. Hövener, E. Y. Chekmenev, *Anal. Chem.* **2020**, *92*, 1340 – 1345.

 © 2020 Wiley-VCH Verlag GmbH & Co. KGaA, Weinheim

[19] M. G. Pravica, D. P. Weitekamp, *Chem. Phys. Lett.* **1988**, *145*, 255 – 258.
[20] C. R. Bowers, D. P. Weitekamp, *J. Am. Chem. Soc.* **1987**, *109*, 5541 – 5542.
[21] E. Cavallari, C. Carrera, T. Boi, S. Aime, F. Reineri, *J. Phys. Chem. B* **2015**, *119*, 10035 – 10041.
[22] W. Heil, C. Gemmel, S. Karpuk, Y. Sobolev, K. Tullney, F. Allmendinger, U. Schmidt, M. Burghoff, W. Kilian, S. Knappe-Grüneberg, A. Schnabel, F. Seifert, L. Trahms, *Ann. Phys.* **2013**, *525*, 539 – 549.
[23] H.-Y. Chen, Y. Lee, S. Bowen, C. Hilty, *J. Magn. Reson.* **2011**, *208*, 204 – 209.
[24] P. Bhattacharya, K. Harris, A. P. Lin, M. Mansson, V. A. Norton, W. H. Perman, D. P. Weitekamp, B. D. Ross, *Magn. Reson. Mater. Phys. Biol. Med.* **2005**, *18*, 245 – 256.
[25] K. Golman, O. Axelsson, H. Johannesson, S. Mansson, C. Olofsson, J. S. Petersson, *Magn. Reson. Med.* **2001**, *46*, 1 – 5.
[26] M. Goldman, H. Johannesson, O. Axelsson, M. Karlsson, *Magn. Reson. Imaging* **2005**, *23*, 153 – 157.
[27] S. Korchak, S. Mamone, S. Glöggler, *ChemistryOpen* **2018**, *7*, 672 – 676.
[28] S. Korchak, S. Yang, S. Mamone, S. Glöggler, *ChemistryOpen* **2018**, *7*, 344 – 348.
[29] K. W. Waddell, A. M. Coffey, E. Y. Chekmenev, *J. Am. Chem. Soc.* **2011**, *133*, 97 – 101.
[30] C. Cai, A. M. Coffey, R. V. Shchepin, E. Y. Chekmenev, K. W. Waddell, *J. Phys. Chem. B* **2013**, *117*, 1219 – 1224.
[31] M. Goldman, H. Johannesson, *C. R. Phys.* **2005**, *6*, 575 – 581.
[32] M. Goldman, H. Johannesson, O. Axelsson, M. Karlsson, *C. R. Chim.* **2006**, *9*, 357 – 363.
[33] A. B. Schmidt, S. Berner, W. Schimpf, C. Müller, T. Lickert, N. Schwaderlapp, S. Knecht, J. G. Skinner, A. Dost, P. Rovedo, J. Hennig, D. von Elverfeldt, J. B. Hövener, *Nat. Commun.* **2017**, *8*, 14535.
[34] A. M. Coffey, R. V. Shchepin, M. L. Truong, K. Wilkens, W. Pham, E. Y. Chekmenev, *Anal. Chem.* **2016**, *88*, 8279 – 8288.
[35] A. M. Coffey, R. V. Shchepin, B. Feng, R. D. Colon, K. Wilkens, K. W. Waddell, E. Y. Chekmenev, *J. Magn. Reson.* **2017**, *284*, 115 – 124.
[36] J.-B. Hövener, E. Y. Chekmenev, K. C. Harris, W. Perman, L. Robertson, B. D. Ross, P. Bhattacharya, *Magn. Reson. Mater. Phys.* **2009**, *22*, 111 – 121.
[37] J.-B. Hövener, E. Y. Chekmenev, K. C. Harris, W. Perman, T. Tran, B. D. Ross, P. Bhattacharya, *Magn. Reson. Mater. Phys.* **2009**, *22*, 123 – 134.
[38] F. Reineri, T. Boi, S. Aime, *Nat. Commun.* **2015**, *6*, 5858.
[39] E. Cavallari, C. Carrera, M. Sorge, G. Bonne, A. Muchir, S. Aime, F. Reineri, *Sci. Rep.* **2018**, *8*, 8366.
[40] E. Cavallari, C. Carrera, S. Aime, F. Reineri, *Chem. Eur. J.* **2017**, *23*, 1200 – 1204.
[41] E. Cavallari, C. Carrera, S. Aime, F. Reineri, *J. Magn. Reson.* **2018**, *289*, 12 – 17.
[42] R. V. Shchepin, D. A. Barskiy, A. M. Coffey, I. V. Manzanera Esteve, E. Y. Chekmenev, *Angew. Chem. Int. Ed.* **2016**, *55*, 6071 – 6074; *Angew. Chem.* **2016**, *128*, 6175 – 6178.
[43] A. N. Pravdivtsev, F. D. Sönnichsen, J.-B. Hövener, *ChemPhysChem* **2020**, https://doi.org/10.1002/cphc.201901056.
[44] J. A. M. Bastiaansen, T. Cheng, M. Mishkovsky, J. M. N. Duarte, A. Comment, R. Gruetter, *Biochim. Biophys. Acta Gen. Subj.* **2013**, *1830*, 4171 – 4178.
[45] E. F. R. Mikkelsen, C. Ø. Mariager, T. Nørlinger, H. Qi, R. F. Schulte, S. Jakobsen, J. Frøkiær, M. Pedersen, H. Stødkilde-Jørgensen, C. Laustsen, *Sci. Rep.* **2017**, *7*, 16002.
[46] J.-B. Hövener, A. N. Pravdivtsev, B. Kidd, C. R. Bowers, S. Glöggler, K. V. Kovtunov, M. Plaumann, R. Katz-Brull, K. Buckenmaier, A. Jerschow, F. Reineri, T. Theis, R. V. Shchepin, S. Wagner, P. Bhattacharya, N. M. Zacharias, E. Y. Chekmenev, *Angew. Chem. Int. Ed.* **2018**, *57*, 11140 – 11162; *Angew. Chem.* **2018**, *130*, 11310 – 11333.
[47] E. Y. Chekmenev, *ACS Earth Space Chem.* **2020**, https://dx.doi.org/10.1021/acsearthspacechem.9b00326.

Manuskript erhalten: 26. Dezember 2019
Endgültige Fassung online: 24. März 2020

 © 2020 Wiley-VCH Verlag GmbH & Co. KGaA, Weinheim

A Journal of the Gesellschaft Deutscher Chemiker

Angewandte International Edition Chemie

GDCh

www.angewandte.org

Accepted Article

Title: Parahydrogen-induced Hyperpolarization of Gases

Authors: Kirill V. Kovtunov, Igor V. Koptyug, Marianna Fekete, Simon B. Duckett, Thomas Theis, Baptiste Joalland, and Eduard Y Chekmenev

This manuscript has been accepted after peer review and appears as an Accepted Article online prior to editing, proofing, and formal publication of the final Version of Record (VoR). This work is currently citable by using the Digital Object Identifier (DOI) given below. The VoR will be published online in Early View as soon as possible and may be different to this Accepted Article as a result of editing. Readers should obtain the VoR from the journal website shown below when it is published to ensure accuracy of information. The authors are responsible for the content of this Accepted Article.

To be cited as: *Angew. Chem. Int. Ed.* 10.1002/anie.201915306
Angew. Chem. 10.1002/ange.201915306

Link to VoR: http://dx.doi.org/10.1002/anie.201915306
http://dx.doi.org/10.1002/ange.201915306

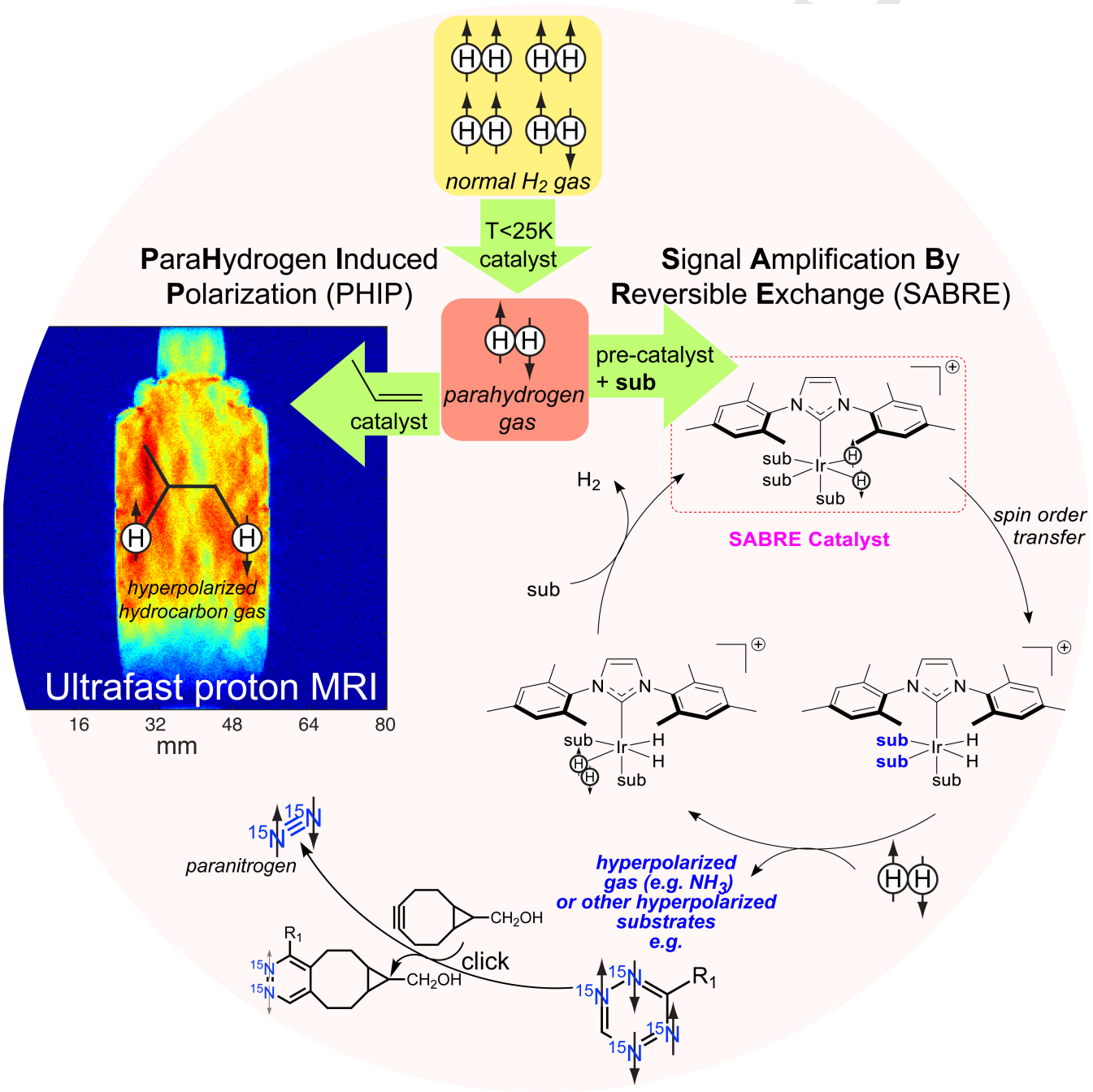
WILEY-VCH

10.1002/anie.201915306

WILEY-VCH

Parahydrogen-induced Hyperpolarization of Gases

Kirill V. Kovtunov,*[a,b] Igor V. Koptyug,*[a,b] Marianna Fekete,[c] Simon B. Duckett,[c] Thomas Theis,[d] Baptiste Joalland,[e] and Eduard Y. Chekmenev*[e,f]



Accepted Manuscript

This article is protected by copyright. All rights reserved.

Abstract: Imaging of gases is a major challenge for any modality including MRI. NMR and MRI signals are directly proportional to the nuclear spin density and the degree of alignment of nuclear spins with applied static magnetic field, which is called nuclear spin polarization. The level of nuclear spin polarization is typically very low, *i.e.*, one hundred thousandth of the potential maximum at 1.5 T and a physiologically relevant temperature. As a result, MRI typically focusses on imaging highly concentrated tissue water. Hyperpolarization methods transiently increases nuclear spin polarizations up to unity, yielding corresponding gains in MRI signal level of several orders of magnitude that enable the 3D imaging of dilute biomolecules including gases. Parahydrogen-induced polarization is a fast, highly scalable, and low-cost hyperpolarization technique. The focus of this Minireview is to highlight selected advances in the field of parahydrogen-induced polarization for the production of hyperpolarized compounds, which can be potentially employed as inhalable contrast agents.

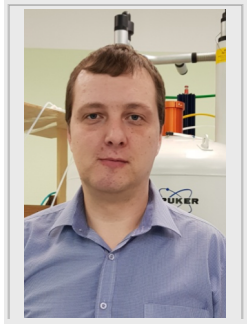
1. Introduction

MRI is an imaging technique based on NMR detection of nuclear spin magnetization. Magnetization is the product of spin density and the degree of alignment (*i.e.*, polarization) of nuclear spin dipoles along the quantization axis determined by the static magnetic field of the MRI scanner. The NMR signal in conventional MRI arises from the very small thermal (Boltzmann) nuclear spin polarization, typically on the order of 10^{-5} at clinical scanner field strengths of 1.5–3T. This low spin polarization limits the ability of MRI to detect molecules at low concentrations. *Hyper*polarization techniques can be used to increase nuclear spin polarization by several orders of magnitude – up to the order of unity – with corresponding gains in detection sensitivity.[1] MRI of hyperpolarized (HP) contrast agents is a revolutionary imaging technique that leverages the 4-6 orders of magnitude of gain in sensitivity for the MRI detection of metabolic and functional exogenous contrast agents at millimolar concentrations.[2, 3] Several HP contrast agents have emerged (most notably ^{13}C-pyruvate [4]) for the visualization of metabolism and organ function *in vivo*.

HP noble gases have been successfully employed for regional imaging of lung function: ventilation, perfusion and gas exchange, as well as for a wide range of sensing applications.[5, 6] Although ^{3}He was initially the leading HP inhalable contrast agent, its limited supply has acted to significantly decrease the access of ^{3}He HP MRI to the biomedical community.[7] As a result, the bulk of research activities with HP noble gases employ ^{129}Xe, which is hyperpolarized via spin exchange optical pumping (SEOP).[8, 9] Despite the major successes of HP ^{129}Xe in clinical research and basic science studies,[7] the clinical translation of HP ^{129}Xe is hindered by two primary obstacles. First and foremost, the instrumentation employed for ^{129}Xe hyperpolarization is highly complex, very costly, and typically requires highly skilled professional operators to enable the production of only 1-2 clinical doses per hour. Second, MRI of HP ^{129}Xe requires specialized MRI scanners, because ^{129}Xe nucleus resonates at a frequency vastly different from that of protons which are used routinely.[7]

Parahydrogen-induced polarization (PHIP) is a chemical-based hyperpolarization technique relying on parahydrogen (p-H_2) as the source of hyperpolarization.[10, 11] PHIP is a highly scalable and relatively low cost method.[12] Recent advances in this field have demonstrated the feasibility of producing HP gases, which may be ultimately suitable for clinical applications, and may mitigate the limitations of HP ^{129}Xe gas. In this Minireview, we focus on selected p-H_2-based hyperpolarization approaches that show the potential to produce HP gases, covering the fundamental principles and applications as well as key advances reported in the literature up to September 2019.

[a] Dr. K. V. Kovtunov. Prof. I. V. Koptyug
International Tomography Center, SB RAS,
630090 Novosibirsk, Russia
E-mail: koptyug@tomo.nsc.ru
E-mail: kovtunov@tomo.nsc.ru
[b] Dr. K. V. Kovtunov. Prof. I. V. Koptyug
Department of Natural Sciences
Novosibirsk State University
Pirogova St. 2, 630090 Novosibirsk, Russia
[c] Dr. M. Fekete, Prof. S. B. Duckett
Center for Hyperpolarization in Magnetic Resonance (CHyM),
University of York, Heslington, York, YO10 5NY, United Kingdom
[d] Prof. Thomas Theis
Department of Chemistry,
North Carolina State University,
Raleigh, North Carolina 27695-8204, United States
[e] Dr. B. Joalland, Prof. E. Y. Chekmenev
Department of Chemistry,
Integrative Biosciences (Ibio),
Karmanos Cancer Institute (KCI),
Wayne State University,
Detroit, Michigan 48202, United States
E-mail: chekmenev@wayne.edu
[f] Prof. E. Y. Chekmenev
Russian Academy of Sciences (RAS)
Leninskiy Prospekt 14, Moscow, 119991, Russia



Dr. Kirill V. Kovtunov studied chemistry at the Novosibirsk State University, Russia. He completed a PhD in physical-chemistry in 2008 at the International Tomography Center under the supervision of Prof. Igor Koptyug. His research interests include heterogeneous catalysis and utilization of PHIP techniques for NMR/MRI and mechanistic studies of heterogeneous reactions involving hydrogen. Currently he is the leading researcher in the group of Prof. Igor Koptyug.

Accepted Manuscript

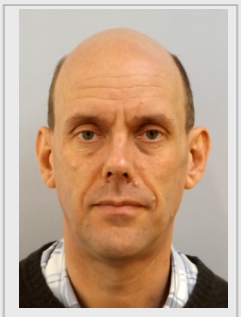
This article is protected by copyright. All rights reserved.



Prof. Igor V. Koptyug received his Ph.D. degree in 1991; in 1992–1995 he was a postdoctoral researcher in the photochemistry group of Professor N. J. Turro (Columbia University, New York). He earned his Dr. Sci. (Habilitation) degree in catalysis in 2003 and a title of Professor in 2006; currently, he is the deputy director of International Tomography Center, Siberian Branch of the Russian Academy of Sciences, Novosibirsk. His research interests include signal enhancement in NMR and applications of NMR and MRI in catalysis.



Dr. Marianna Fekete graduated from Faculty of Physical Chemistry, University of Belgrade, Serbia in 2003. She obtained her PhD in chemistry in 2008 on the use of reaction kinetics to study catalysis by transitional metal N-heterocyclic carbene complexes at the University of Debrecen, Hungary. Afterwards she undertook postdoctoral work with Prof. M. Botta at the Università del Piemonte Orientale, Italy, studying relaxometric properties of paramagnetic complexes in low field. In 2011, she joined the group of Prof. S. Duckett where she is currently undertaking research on the optimisation, kinetics and catalysis of polarisation transfer reaction.



Prof. Simon Duckett is Director of the Centre for Hyperpolarization in Magnetic Resonance in York. His research involves the development of hyperpolarization techniques and the study of inorganic reactions. He gained a D.Phil. from the University of York in 1990 and then undertook postdoctoral work with Prof. W. D. Jones and Prof. R. Eisenberg at the University of Rochester. He has authored over 130 publications on the *para*hydrogen effect.

2. Production of parahydrogen

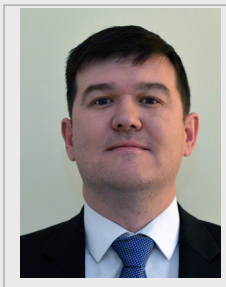
Molecular hydrogen exists as two nuclear spin isomers, which are referred to as *ortho*- and *para*hydrogen.[13] *Ortho*hydrogen (*o*-H_2) is the triplet, while parahydrogen is the singlet. These two spin isomers, which respectively account for 75% and 25% of H_2 at standard temperature and pressure, exhibit different magnetic properties. They also differ in energy as a result of the Pauli exclusion principle, which restricts them to antisymmetric and symmetric rotational states, respectively. Because interconversion between isomers requires a change of two physical properties, the process is forbidden. However, their 120 cm^{-1} separation in energy means that one can produce nearly 100% *para*hydrogen at 20 K according to Boltzmann statistics. Fortunately, the rule that prevents interconversion between the two forms at higher temperatures can be broken by passing normal H_2 gas over a suitable spin conversion catalyst. The catalyst can be charcoal or iron^{III} oxide (or another ferromagnetic



Prof. Thomas Theis is Assistant Professor at North Carolina State University. His research is focused on hyperpolarization technology and unconventional NMR and MRI detection schemes. Dr. Theis completed his masters at the Georg-August University of Goettingen and gained his PhD from UC Berkeley in 2012 working with Prof. A. Pines on "zero-field NMR". He conducted postdoctoral research at Duke University (USA) with Prof. Warren Warren focused on "singlet states for hyperpolarization storage", where he was promoted to Research Professor in 2015. Since 2018, Dr. Theis leads the North Carolina State Hyperpolarization Laboratory.



Dr. Baptiste Joalland is a molecular physicist holding a Master degree from the University of Paris XI (2007) and a Ph.D. degree from the University of Toulouse (2011). His primary research interest in fundamental research is geared towards providing a better understanding of the driving forces at play in chemical reactions. Through numerous adventures between France and the USA, he has developed an original set of skills at the boundaries of experimental physical chemistry (with B. R. Rowe, A. G. Suits, and I. R. Sims), quantum chemistry (with C. J. Marsden and S. J. Klippenstein), molecular dynamics simulations (with A. Simon, F. Spiegelman, and T. J. Martínez), and laboratory astrophysics (with C. Joblin and L. Biennier). In 2019, he joined the group of E. Y. Chekmenev as a Senior Postdoctoral Fellow with one overarching goal: turn parahydrogen-induced polarization methods into a clinical reality.



Prof. Eduard Y. Chekmenev, PhD in Physical Chemistry (supervisor Prof. Richard J. Wittebort) 2003, University of Louisville, KY, USA. Postdoctoral Fellow at NHMFL in Tallahassee, FL (Prof. Timothy Cross), Caltech (Prof. Daniel P. Weitekamp) and HMRI (Dr. Brian D. Ross). In 2009, Dr. Chekmenev started his hyperpolarization program at Vanderbilt University, and he was tenured in 2015. He serves as an Associate Professor of Chemistry at Wayne State University since 2018. Research interests include development of methods of hyperpolarization and their Biomedical and industrial use.

Accepted Manuscript

This article is protected by copyright. All rights reserved.

material) and this process can be rapid but once the gas has moved away from the catalyst its initial stability to spin isomer interchange returns. Cooling hydrogen gas to -196 °C (77 K), using liquid nitrogen is easily achieved and creates a mixture wherein the proportion of *para*hydrogen is around 50%. Further cooling to -250 °C (20 K) results in >99% *para*hydrogen. However, 20 K is the boiling point of H_2 and cooling H_2 gas below this point produces liquid *p*-H_2. Several methods and equipment designs have been suggested for the production of *p*-H_2 for various applications [14-16] including hyperpolarization.[17, 18] A *p*-H_2 converter, suitable for clinical use has been suggested.[19] This apparatus produces a continuous flow at 98% purity (cooling to 25 K) with a maximum output pressure of 50 bar. The half-life of pH_2 is 13.7 ± 0.5 hours in a glass vial and 129 ± 36 days in an aluminum storage cylinder.[20] Commercially available *para*hydrogen generators such as those marketed by Bruker are available, which provide for a large scale use such as that needed for flow studies.[20]

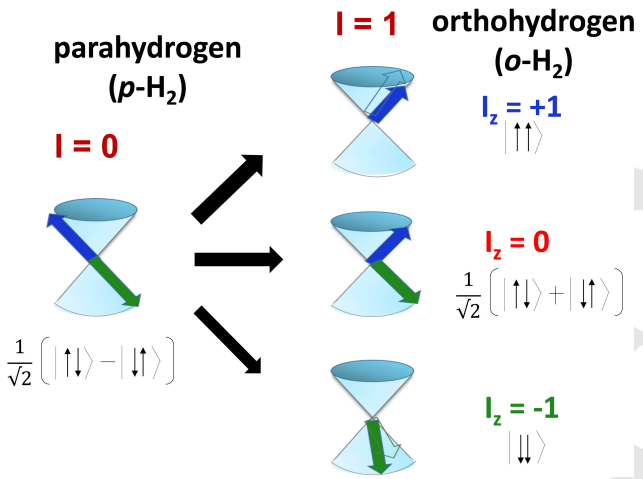


Figure 1. Singlet and triplet spin states of molecular hydrogen.

3. Parahydrogen Induced Polarization (PHIP)

3.1. Breaking the symmetry of parahydrogen via pairwise parahydrogen addition

It is well known that *p*-H_2 does not give an observable NMR signal since it has a total zero spin moment. Thus, the observable NMR signal of hydrogen is obtained from *o*-H_2 only. Despite this, it is possible to use the *p*-H_2 singlet spin state to significantly enhance NMR signals by transferring the H atoms of a *p*-H_2 molecule to magnetically nonequivalent environments as, for example, through a hydrogenation reaction involving pairwise H_2 addition to an unsymmetrical substrate.[21]

The effects of parahydrogen-induced polarization (PHIP) were first discovered by studying the interaction of transition metal complexes with hydrogen by NMR.[22, 23] These effects were represented by the antiphase (absorption-emission) shape of some NMR signals in the ^{1}H NMR spectra and were initially described via chemically induced dynamic nuclear polarization (CIDNP) theory. In 1985, Weitekamp suggested the possibility of using the singlet spin state of *p*-H_2 to significantly enhance the NMR signals of hydrogenation reaction products.[24] This effect – PASADENA (Parahydrogen And Synthesis Allows Dramatically Enhanced Nuclear Alignment[25]) is observed for the product of the hydrogenation with *p*-H_2 in a strong magnetic field and accounted for the earlier results attributed to CIDNP. It is assumed that only the energy spin levels in the reaction product that have a singlet spin symmetry corresponding to the symmetry of parahydrogen molecule will be populated.[10] In 1987, two research groups, working independently, confirmed experimentally the occurrence of the PASADENA effects.[11, 25]

When the hydrogenation reaction with *p*-H_2 is carried out in a low magnetic field (*e.g.*, the Earth's field of about 50 μT) and followed by an adiabatic transfer of the sample to the NMR spectrometer, the NMR signals of the reaction products are enhanced; however, the shape of the polarized peaks differs significantly from the PASADENA experiment. This effect was called ALTADENA (Adiabatic Longitudinal Transport After Dissociation Engenders Nuclear Alignment).[26]

It is important to note that in order to observe PHIP in an NMR spectrum, three main conditions should be realized: the rate of the hydrogenation reaction and the time of NMR spectrum acquisition should not significantly exceed the nuclear spin relaxation time of the hyperpolarized (HP) products; the addition of *p*-H_2 to the unsaturated substrate should proceed in a pairwise manner, *i.e.*, with the two H atoms of a *p*-H_2 molecule ending up in the same reaction product, so that the nuclear spin correlation between them is preserved; the H atoms of *p*-H_2 molecule should become magnetically nonequivalent in the product molecule.[27] Therefore, for PHIP effects to be observed, the pairwise hydrogen addition route should be realized during hydrogenation and it turns out despite these constraints, this is quite a common phenomenon.

3.2. Homogeneous catalysis and migration of HP fluids from the liquid to gaseous phase

Homogeneous catalysts can be used successfully for producing HP gases in biphasic catalytic processes. These gas-liquid systems were shown to be useful for the HP gases formation, where transition metal complex (homogeneous catalyst) was present in the liquid phase, while the reactants and products were in the gas phase.[28] The novelty of this approach is that the products of the hydrogenation reaction with *p*-H_2, which are formed in the liquid phase, can return to the gas phase with preservation of spin polarization. This process allows for the rapid separation of reaction products from the homogeneous catalyst, which makes possible to hyperpolarize a broad class of molecules in the gas phase, including vapors of various liquids.

Homogeneous hydrogenation of gaseous C3-hydrocarbons containing double and triple bonds, with the acquisition of ^{1}H NMR spectra of gaseous products, has provided the first evidence of the usefulness of this biphasic approach to prepare

Accepted Manuscript

This article is protected by copyright. All rights reserved.

HP gaseous molecules. To this end, hydrogenation of propyne or propene was carried out over the following homogeneous catalysts: $[Rh(PPh_3)_3Cl]$, $[Ir(COD)(PCy)_3(Py)]PF_6$, $[Rh(NBD)(PPh_3)_2]BF_4$,[29] $[Rh(P(C_6H_4SO_3Na)_3)_3Cl]*xH_2O$, and $[Rh(PPh_2(CH_2)_4PPh_2)(COD)]BF_4$. The mixture of the gaseous substrate and p-H_2 was bubbled through the catalyst solution and then passed through a Teflon capillary to the NMR tube for recording ^{1}H NMR spectra. It was shown that PHIP effects can be successfully detected. At the same time, due to the relatively short relaxation times of ^{1}H nuclei in the formed gaseous products[30] the NMR signal enhancements did not exceed a factor of 20–50, which is an order of magnitude lower than the typical signal enhancement values observed during homogeneous hydrogenation with p-H_2.[31]

3.3. Heterogeneous PHIP of gases over solid catalysts

By combining the use of p-H_2 with heterogeneous hydrogenation processes, it is possible to develop new fundamental and practical applications for the production of HP gases.[12, 32] In heterogeneous processes, supported metals are often used as catalysts. It was successfully shown that when the p-H_2 based hydrogenation of unsaturated gaseous hydrocarbons is catalyzed by highly dispersed supported metal catalysts, nuclear spin polarized reaction products can be created thus confirming that the pairwise addition of molecular hydrogen can be achieved by a supported metal catalysts.[33] The nature of the catalyst proved to be important with the smallest particle sizes maximizing the signal enhancing PHIP effect.[34]

Once the observation of PHIP effects was successfully demonstrated in heterogeneous hydrogenation reactions, the production of HP gases became an important area of research.[7] Continuous production of HP gases using heterogeneous hydrogenation opens up the way to potential practical applications for void space MR imaging. The first experiments addressing MR imaging with HP propane gas helped visualize various phantoms,[35] and in later studies propane hyperpolarized via PHIP allowed the collection of MR images with ultra-high resolution despite its relatively short relaxation time.[30] One potential solution to increase the magnetic lifetime of HP propane is to create long-lived spin states by using PHIP and a low magnetic field. The spin-locked induced crossing (SLIC) pulse sequence, developed by Rosen et al.[36] has been used to convert this long-lived polarization, created in the Earth's magnetic field, into observable magnetization at 47.5 mT and hence to use HP gas for MR imaging in the low magnetic fields.[37, 38] In addition to obtaining low field MR images from protonated propane, when the fully deuterated precursor propene was used, there was no need to apply special symmetry breaking pulse sequences at 47.5 mT. Consequently, the deuterated variant can be used to obtain low field MR images.[39]

Recently it was shown that the nature of the substrate is also critical, and heterogeneous hydrogenation of cyclopropane was realized as an alternative route to HP propane. Interestingly, one could expect that ring opening cyclopropane would place the protons obtained from p-H_2 into magnetically equivalent positions, *i.e.*, one hydrogen per methyl group. Furthermore, due to the chemical and magnetic equivalence of these two methyl groups, the resulting hyperpolarization should not be detectable directly by NMR; this is similar to the correlated ethylene spin isomers obtained by pairwise addition of p-H_2 to acetylene.[40] However, hydrogenation of cyclopropane with p-H_2 under the conditions of PASADENA experiment led to the clear-cut observation of PASADENA signals of HP propane, similar to the NMR signals of propane itself observed during hydrogenation of propene.[41] Moreover, it was found that the use of cyclopropane as a precursor to HP propane is promising as it yields surprisingly high polarization levels (*ca.* >2%).[41]

Because the potential applications will require relatively large amounts of HP gas, the conditions necessary to hydrogenate propene over a Rh/TiO_2 catalyst were optimized and the clinical-scale production of HP propane gas using the PHIP technique demonstrated. Hence, more than 0.3 liters of HP propane gas was produced in 2 s which, along with significant NMR signal enhancement, allowed the MRI visualization of a 56 mL phantom in less than 2 seconds at 4.7 T (Figure 2).[42]

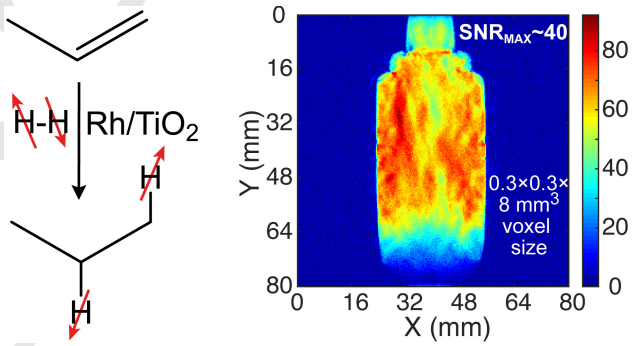


Figure 2. Scheme of heterogeneous hydrogenation of propene with parahydrogen over Rh/TiO_2 catalyst, and 2D MRI of 0.2 standard liters of HP propane gas in an ~56 mL collection container after production of an 0.3-standard-liter batch of HP propane in ~2 s using an ~1:2 mixture of propene with parahydrogen. Adapted with permission from Ref. # [42]. Copyright (2019) American Chemical Society.

4. Signal Amplification by Reversible Exchange (SABRE)

4.1. The SABRE phenomenon

In 2009, an extension to the PHIP technique termed Signal Amplification by Reversible Exchange (SABRE) was reported.[43] This approach, which is multinuclear in nature, harnesses p-H_2 through its reversible binding to a metal catalyst in association with further reversible binding of a substrate and is therefore not associated with changing the chemical identity of the substrate. SABRE then achieves spin order transfer within the resulting scalar coupling network[43, 44] of the catalyst and harnesses substrate dissociation to catalytically build-up hyperpolarized molecules of it in solution according to Figure 3. One consequence of the interconnected chemical and physical

Accepted Manuscript

This article is protected by copyright. All rights reserved.

aspects of SABRE is that its efficiency can be rigorously controlled. In one version, low magnetic fields are used to create a propagating spin-topology that enables spontaneous spin order transfer,[43-47] though other approaches employing more traditional radio frequency excitation are also possible. Density matrix theory[43] and level anti-crossing analysis have been used to rationalize this behavior.[45, 48, 49]

Chemically, both of these approaches require the SABRE catalyst to remain intact for a time period which is set by the size of the propagating spin-spin couplings between the *p*-H_2 derived hydride ligands of the catalyst and the NMR active nuclei of the recipient substrate. Tessari et al. have quantified some of those couplings involved in ^{1}H-transfer at ~1.2 Hz[50] which are small yet sufficient to enable highly efficient transfer if the complex lifetime is around 0.2 s[46] when the sample experiences an ~5-8 mT field.[51, 52] For transfer to heteronuclei such as ^{15}N that occur through the corresponding couplings that can exceed 20 Hz and involve shorter complex lifetimes, the optimum magnetic fields lie in the 0.2-0.4 μT range and thus necessitate the use of μ-metal magnetic shields.[53] This SABRE variation has been termed “SABRE-SHEATH” (Signal Amplification by Reversible Exchange in SHield Enables Alignment Transfer to Heteronuclei).

Successful magnetization transfer at high field through radio frequency excitation was also exemplified in 2009 for an iridium-phosphine catalyst with pyridine-^{15}N hyperpolarization as the outcome.[54] This approach has then been improved through low-power methods such as LIGHT-SABRE[55, 56] and more recently by matching the reaction dynamics.[57-60] One additional consequence of SABRE happening during the finite lifetime of what is commonly a bulky catalyst is that controlling nuclear spin order relaxation within the catalyst framework reflect a route to improve SABRE efficiency. This can be achieved by ^{2}H labeling, and once the catalyst lifetime, its relaxation properties and polarization transfer field are optimized, ^{1}H hyperpolarization levels have reached 20%.[61] Studies on ^{15}N transfer are also well developed with the resulting high polarization levels allowing the ready detection of MR signals without the need for isotope enrichment.[62] Other studies have demonstrated that ^{13}C, ^{31}P and ^{19}F[43] NMR signals can be substantially amplified in what has become a rapidly expanding range of molecules that are functionalized by nitrogen, oxygen, phosphorus[63, 64] and sulfur[65] based catalyst ligation sites. These studies confirm the multinuclear capabilities of SABRE.

One relaxation-related topic deals with the creation of long lived singlet states, as detailed by Levitt.[66, 67] The SABRE technique readily yields them in a HP form, as exemplified by the strongly coupled ^{1}H-pair in 2-aminothiazole[68] whose singlet state has been accessed with 90% efficiency by rf-methods.[66] This approach has been applied to derivatives of nicotinamide and pyrazinamide that have isolated spin-pairs through selective deuteration.[69] For a pyridazine based ^{1}H-spin pair the SABRE HP signal remained visible for 15 minutes after polarization transfer.[70] When this method has been used in conjunction with $^{15}N_2$-diazirines[71, 72] similar singlet states can be populated with decay constants that exceed 23 min in an optimum storage field.

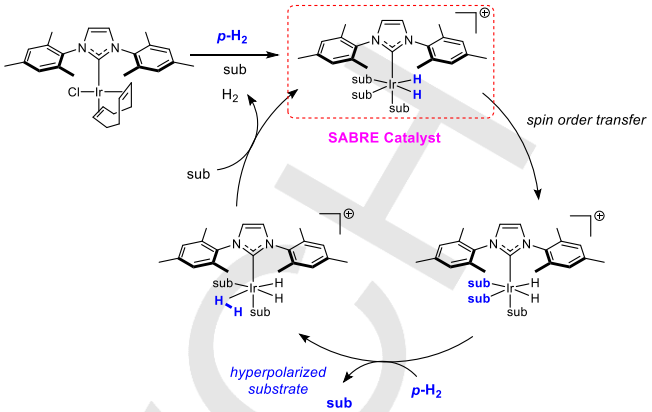


Figure 3. Mechanism of the SABRE process which uses a metal catalyst to harvest the latent magnetism of *p*-H_2 to hyperpolarize materials (sub) without changing their chemical identity.

4.2. RELAYED-SABRE and hyperpolarization of ammonia and beyond

Ammonia represents a common inorganic ligand that binds to SABRE catalysts. This results in the hyperpolarization of its nitrogen and proton sites in a process that can be readily observed in aprotic solvents. Ammonia is a base that undergoes facile proton exchange with acidic protons like those of alcohols, carboxylic acids and water itself. Consequently, the SABRE hyperpolarization of an amine offers a simple route to place a HP proton into a different molecule through chemical exchange.[73] When this process takes place at low field, spin order transfers through low-field thermal mixing result in the hyperpolarization of coupled spins. When this SABRE-RELAY method (Figure 4) was applied to the study of the straight chain alcohols methanol through octanol, signal gains of up to 650-fold and 600-fold per proton and carbon respectively were achieved through the use of [IrCl(COD)(IMes)] (5 mM), the alcohol (1 μL), NH_3 (6-8 eq.) in d_2-dichlormethane (0.6 mL). Examples have established that ^{1}H, ^{13}C, ^{19}F, ^{31}P and ^{15}N signals of compounds can be readily enhanced through this approach, meaning that *p*-H_2 can hyperpolarize a much broader range of biologically relevant substrates without the need for their direct interaction with either *p*-H_2 or a SABRE catalyst. It is not surprising that the rate of relaxation of the NH protons responsible for SABRE-RELAY is an important parameter that can be controlled through ^{2}H labeling and the extension to amines such as d_7-benzylamine.[74]

While SABRE-RELAY works with sodium hydrogen carbonate and therefore offers a route to HP carbon dioxide, its use with pyruvic acid is limited by competing Schiff base condensation.[75] The use of dimethylsulfoxide as a weakly binding co-ligand in conjunction with the original SABRE method overcomes this problem, leading to a simple route to HP pyruvate.[76] It should therefore be clear that SABRE offers a truly versatile route to hyperpolarize many classes of chemical compounds in a simple and low-cost manner including HP gases in the liquid phase.

Accepted Manuscript

This article is protected by copyright. All rights reserved.

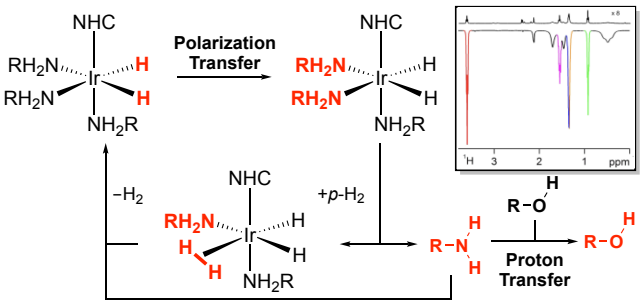


Figure 4. SABRE-RELAY enables substrate hyperpolarization via *p*-H_2 and an amine through proton transfer.

4.3. Production of paranitrogen via SABRE hyperpolarization of ^{15}N-containing heterocycles

Two compelling SABRE approaches have been described for the production of HP $^{15}N_2$ gas, in particular the para spin isomer which we refer to as $^{15}N_2$-paranitrogen (p-$^{15}N_2$). The two published approaches are summarized in Figure 6.

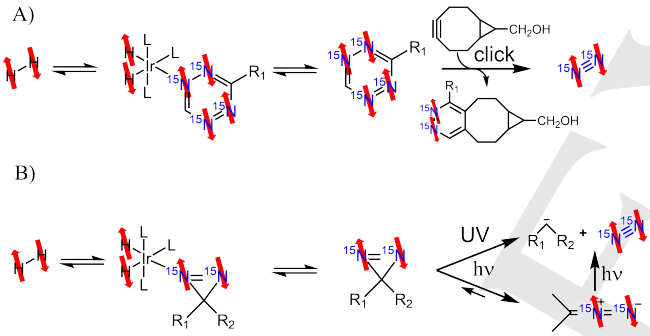


Figure 5. Two routes for the production of $^{15}N_2$-paranitrogen. A) A $^{15}N_4$ labeled tetrazine is hyperpolarized by SABRE, which releases HP $^{15}N_2$, when reacting with a strained alkyne. B) A $^{15}N_2$-diazirine is hyperpolarized by SABRE, which releases HP $^{15}N_2$ when irradiated by UV light.

Both methods can also be used to hyperpolarize $^{15}N_2$-orthonitrogen (o-$^{15}N_2$), the ortho spin isomer of $^{15}N_2$, however, p-$^{15}N_2$ is more intriguing because of its potential to be extremely long lived, in analogy with p-H_2 which can be stored for weeks.[19] The first method, depicted in Figure 5a, involves the hyperpolarization of a tetrazine, which is reacted with a strained alkyne in a click reaction to release HP $^{15}N_2$. Whether p-$^{15}N_2$ or o-$^{15}N_2$ is produced can be controlled by the magnetic field used for SABRE. On one hand, to produce HP o-$^{15}N_2$, magnetization (*i.e.*, spin alignment) has to be created on the $^{15}N_4$-tetrazine first. This is best accomplished at fields of 5 to 10 mG under SABRE-SHEATH conditions. The subsequent click reaction releases HP o-$^{15}N_2$. On the other hand, to produce p-$^{15}N_2$, SABRE should be conducted at fields above the SABRE-SHEATH[53] condition, yet sufficiently low, as not to induce significant chemical shifts between the two ^{15}N nuclei in the tetrazine (bound or free). Specifically, static magnetic fields between 0.1 to 50 G work well. At these fields singlet states are hyperpolarized on the tetrazine and the subsequent click reaction releases p-$^{15}N_2$.[77]

The second method, depicted in Figure 5b, involves the hyperpolarization of a diazirine and subsequent irradiation with UV light to release HP $^{15}N_2$ gas. Just as in the tetrazine case, para- vs. ortho- is controlled by the magnetic field during SABRE. HP o-$^{15}N_2$ is produced when using μT fields, *i.e.*, SABRE-SHEATH conditions, whereas enriched p-$^{15}N_2$ is produced with slightly higher fields for SABRE. Singlet states in $^{15}N_2$-diazirines are also enriched well at fields between 0.5 and 50 G. Subsequent UV irradiation releases the p-$^{15}N_2$. Note that, in Figure 5b, UV irradiation of the diazirine can lead to the carbene and nitrogen directly, or indirectly through formation of an intermediate diazo compound.[78]

5. Nuclear spin relaxation considerations in preparation of HP gases

The very long spin-lattice (T_1) relaxation times of HP heteronuclei, *e.g.* ^{13}C, ^{15}N, etc. can be on the order of up to tens of minutes[72, 79, 80] in solution which makes them highly suitable for HP state storage in the context of biomedical applications: *i.e.* injectable contrast agents.[2] However, the gas-phase T_1 of heteronuclei is typically very short, and although ^{13}C T_1 increases with pressure, it is only ~0.2 s at 10 atm of CO_2.[81] Moreover, ^{19}F fluorocarbons have T_1 values on the time scale of less than 0.1 second at clinically relevant conditions in the context of pulmonary imaging applications.[82, 83] On the other hand, *proton*-hyperpolarized propane has T_1 of ~1 s[84] and T_S of ~3 s[38] at 1 atm (and up to more than 13 s at higher pressures[85]) and other clinically relevant conditions in the gas phase. These decay constants of HP state are significantly longer than those of many heteronuclei, and sufficiently long for potential administration as inhalable contrast agents.

5. Summary and Outlook

To summarize, a wide range of HP gases can be produced via PHIP and SABRE hyperpolarization techniques. These HP gases can be potentially employed for many applications including most importantly bioimaging applications. Clinical-scale production of HP propane has been demonstrated, and it can be potentially extended to many others—ongoing active work in our laboratories, which we hope to report in the near future. *In vivo* bioimaging applications are envisioned for HP gases produced using p-H_2. Efforts are now in progress to study the feasibility and effectiveness of lung ventilation imaging in sheep model of acute lung injury using HP propane gas employing 0.35 T clinical MRI scanner. HP propane gas is expected to have T_S of ~3 s at physiologically relevant conditions,[38] and therefore, hyperpolarization process is integrated in the inhalation apparatus to minimize otherwise significant relaxation-associate polarization losses. Future

Accepted Manuscript

This article is protected by copyright. All rights reserved.

studies will also need to address the potential issues of hydrocarbon flammability, which can be possibly mitigated via administration of HP gas below lower explosive limit (LEL). We envision that paranitrogen may potentially be employed as an inhalable contrast agent—future efforts will be required to perform extraction of paranitrogen from the liquid phase for this application. The key advantages of *proton*-hyperpolarized HP contrast agents produced using p-H_2 include: (i) possibility of detection using clinical MRI scanner, (ii) low-cost and high production speed. The low cost of PHIP and SABRE instrumentation is highly synergistic with the low cost of reagents required for the hyperpolarization process and bode well for future biomedical translation.

Acknowledgements

We thank the following award for funding support: NSF CHE-1904780 (EYC), NIH 1R21CA220137 (EYC), R21EB025313 (TT), and 1U01CA202229 (EYC), DOD CDMRP PRMRP W81XWH-15-1-0271 (EYC). KVK and IVK thank RSF (grant # 19-13-00047) for the support of MRI studies and RFBR (grant # 19-29-10003 and 17-54-33037) for the support of catalysts synthesis, and Russian Ministry of Science and Higher Education (AAAA-A16-116121510087-5) for the access to NMR/MRI equipment. SBD thanks financial support from the Wellcome Trust (Grants 092506 and 098335), the MRC (MR/M008991/1). TT also acknowledges support from the Oak Ridge Associated Universities, Ralph E. Powe Junior Faculty Enhancement Award, the North Carolina Biotechnology Center Translational Research Grant as well as support from the Mallinckrodt foundation.

Keywords: *para*hydrogen • NMR • MRI • hyperpolarization • spectroscopy

[1] P. Nikolaou, B. M. Goodson, E. Y. Chekmenev, *Chem. Eur. J.* **2015**, *21*, 3156-3166.
[2] J. Kurhanewicz, D. B. Vigneron, K. Brindle, E. Y. Chekmenev, A. Comment, C. H. Cunningham, R. J. DeBerardinis, G. G. Green, M. O. Leach, S. S. Rajan, R. R. Rizi, B. D. Ross, W. S. Warren, C. R. Malloy, *Neoplasia* **2011**, *13*, 81–97.
[3] K. Golman, R. in't Zandt, M. Thaning, *Proc. Natl. Acad. Sci. U. S. A.* **2006**, *103*, 11270-11275.
[4] S. J. Nelson, J. Kurhanewicz, D. B. Vigneron, P. E. Z. Larson, A. L. Harzstark, M. Ferrone, M. van Criekinge, J. W. Chang, R. Bok, I. Park, G. Reed, L. Carvajal, E. J. Small, P. Munster, V. K. Weinberg, J. H. Ardenkjaer-Larsen, A. P. Chen, R. E. Hurd, L. I. Odegardstuen, F. J. Robb, J. Tropp, J. A. Murray, *Sci. Transl. Med.* **2013**, *5*, 198ra108.
[5] L. Schroder, *Phys. Medica* **2013**, *29*, 3-16.
[6] J. P. Mugler, T. A. Altes, *J. Magn. Reson. Imaging* **2013**, *37*, 313-331.
[7] D. A. Barskiy, A. M. Coffey, P. Nikolaou, D. M. Mikhaylov, B. M. Goodson, R. T. Branca, G. J. Lu, M. G. Shapiro, V.-V. Telkki, V. V. Zhivonitko, I. V. Koptyug, O. G. Salnikov, K. V. Kovtunov, V. I. Bukhtiyarov, M. S. Rosen, M. J. Barlow, S. Safavi, I. P. Hall, L. Schröder, E. Y. Chekmenev, *Chem. Eur. J.* **2017**, *23*, 725–751.
[8] B. M. Goodson, *J. Magn. Reson.* **2002**, *155*, 157-216.
[9] T. G. Walker, W. Happer, *Rev. Mod. Phys.* **1997**, *69*, 629-642.
[10] C. R. Bowers, D. P. Weitekamp, *Phys. Rev. Lett.* **1986**, *57*, 2645-2648.
[11] T. C. Eisenschmid, R. U. Kirss, P. P. Deutsch, S. I. Hommeltoft, R. Eisenberg, J. Bargon, R. G. Lawler, A. L. Balch, *J. Am. Chem. Soc.* **1987**, *109*, 8089-8091.
[12] J.-B. Hövener, A. N. Pravdivtsev, B. Kidd, C. R. Bowers, S. Glöggler, K. V. Kovtunov, M. Plaumann, R. Katz-Brull, K. Buckenmaier, A. Jerschow, F. Reineri, T. Theis, R. V. Shchepin, S. Wagner, P. Bhattacharya, N. M. Zacharias, E. Y. Chekmenev, *Angew. Chem. Int. Ed.* **2018**, *57*, 11140-11162.
[13] A. Farkas, *Orthohydrogen, Parahydrogen, and Heavy Hydrogen*, Cambridge University Press, Cambridge, **1935**.
[14] S. Tam, M. E. Fajardo, *Rev. Sci. Instrum.* **1999**, *70*, 1926-1932.
[15] J.-B. Hövener, E. Y. Chekmenev, K. C. Harris, W. Perman, L. Robertson, B. D. Ross, P. Bhattacharya, *Magn. Reson. Mater. Phy.* **2009**, *22*, 111-121.
[16] B. A. Tom, S. Bhasker, Y. Miyamoto, T. Momose, B. J. McCall, *Rev. Sci. Instrum.* **2009**, *80*, 3.
[17] B. Feng, A. M. Coffey, R. D. Colon, E. Y. Chekmenev, K. W. Waddell, *J. Magn. Reson.* **2012**, *214*, 258-262.
[18] A. Gamliel, H. Allouche-Arnon, R. Nalbandian, C. M. Barzilay, J. M. Gomori, R. Katz-Brull, *Appl. Magn. Reson.* **2010**, *39*, 329-345.
[19] J.-B. Hövener, S. Baer, J. Leupold, K. Jenne, D. Leibfritz, J. Hennig, S. B. Duckett, D. von Elverfeldt, *NMR Biomed.* **2013**, *26*, 124-131.
[20] M. Fekete, P. J. Rayner, G. G. R. Green, S. B. Duckett, *Magn. Reson. Chem.* **2017**, *55*, 944-957.
[21] S. B. Duckett, C. Sleigh, *J. Prog. Nucl. Magn. Reson. Spectrosc.* **1999**, *34*, 71.
[22] P. F. Seidler, H. E. Bryndza, J. E. Frommer, L. S. Stuhl, R. G. Bergman, *Organometallics* **1983**, *2*, 1701-1705.
[23] S. I. Hommeltoft, D. H. Berry, R. Eisenberg, *J. Am. Chem. Soc.* **1986**, *108*, 5345-5347.
[24] D. P. Weitekamp, in *eMagRes* (Eds.: R. K. Harris, R. L. Wasylishen), **2007**, p. https://doi.org/10.1002/9780470034590.emrhp9780470030195.
[25] C. R. Bowers, D. P. Weitekamp, *J. Am. Chem. Soc.* **1987**, *109*, 5541-5542.
[26] M. G. Pravica, D. P. Weitekamp, *Chem. Phys. Lett.* **1988**, *145*, 255-258.
[27] J. Natterer, J. Bargon, *Prog. Nucl. Mag. Res. Spectrosc.* **1997**, *31*, 293-315.
[28] K. V. Kovtunov, V. V. Zhivonitko, I. V. Skovpin, D. A. Barskiy, O. G. Salnikov, I. V. Koptyug, *J. Phys. Chem. C* **2013**, *117*, 22887–22893.
[29] O. G. Salnikov, D. A. Barskiy, A. M. Coffey, K. V. Kovtunov, I. V. Koptyug, E. Y. Chekmenev, *ChemPhysChem* **2016**, *17*, 3395–3398.
[30] K. V. Kovtunov, D. A. Barskiy, A. M. Coffey, M. L. Truong, O. G. Salnikov, A. K. Khudorozhkov, E. A. Inozemtseva, I. P. Prosvirin, V. I. Bukhtiyarov, K. W. Waddell, E. Y. Chekmenev, I. V. Koptyug, *Chem. Eur. J.* **2014**, *20*, 11636 – 11639.
[31] S. B. Duckett, R. E. Mewis, *Acc. Chem. Res.* **2012**, *45*, 1247-1257.
[32] K. V. Kovtunov, E. V. Pokochueva, O. G. Salnikov, S. Cousin, D. Kurzbach, B. Vuichoud, S. Jannin, E. Y. Chekmenev, B. M. Goodson, D. A. Barskiy, I. V. Koptyug, *Chem. Asian J.* **2018**, *13*, 1857-1871.
[33] D. B. Burueva, L. M. Kovtunova, V. I. Bukhtiyarov, K. V. Kovtunov, I. V. Koptyug, *Chem. Eur. J.* **2019**, *25*, 1420-1431.
[34] D. B. Burueva, K. V. Kovtunov, A. V. Bukhtiyarov, D. A. Barskiy, I. P. Prosvirin, I. S. Mashkovsky, G. N. Baeva, V. I. Bukhtiyarov, A. Y. Stakheev, I. V. Koptyug, *Chem. Eur. J.* **2018**, *24*, 2547-2553.
[35] L. S. Bouchard, K. V. Kovtunov, S. R. Burt, M. S. Anwar, I. V. Koptyug, R. Z. Sagdeev, A. Pines, *Angew. Chem. Int. Ed.* **2007**, *46*, 4064-4068.
[36] S. J. DeVience, R. L. Walsworth, M. S. Rosen, *Phys. Rev. Lett.* **2013**, *111*, 173002-173001-173005.
[37] K. V. Kovtunov, M. L. Truong, D. A. Barskiy, I. V. Koptyug, A. M. Coffey, K. W. Waddell, E. Y. Chekmenev, *Chem. Eur. J.* **2014**, *20*, 14629–14632.
[38] N. M. Ariyasingha, O. G. Salnikov, K. V. Kovtunov, L. M. Kovtunova, V. I. Bukhtiyarov, B. M. Goodson, M. S. Rosen, I. V. Koptyug, J. G. Gelovani, E. Y. Chekmenev, *J. Phys. Chem. C* **2019**, *18*, 11734–11744.
[39] K. V. Kovtunov, M. L. Truong, D. A. Barskiy, O. G. Salnikov, V. I. Bukhtiyarov, A. M. Coffey, K. W. Waddell, I. V. Koptyug, E. Y. Chekmenev, *J. Phys. Chem. C* **2014**, *118*, 28234–28243.
[40] V. Zhivonitko, K. Kovtunov, P. Chapovsky, I. Koptyug, *Angew. Chem. Int. Ed.* **2013**, *52*, 13251-13255.
[41] O. G. Salnikov, K. V. Kovtunov, P. Nikolaou, L. M. Kovtunova, V. I. Bukhtiyarov, I. V. Koptyug, E. Y. Chekmenev, *ChemPhysChem* **2018**, *19*, 2621-2626.
[42] O. G. Salnikov, P. Nikolaou, N. M. Ariyasingha, K. V. Kovtunov, I. V. Koptyug, E. Y. Chekmenev *Anal. Chem.* **2019**, *91*, 4741–4746.

Accepted Manuscript

This article is protected by copyright. All rights reserved.

[43] R. W. Adams, J. A. Aguilar, K. D. Atkinson, M. J. Cowley, P. I. P. Elliott, S. B. Duckett, G. G. R. Green, I. G. Khazal, J. Lopez-Serrano, D. C. Williamson, *Science* **2009**, *323*, 1708-1711.

[44] R. A. Green, R. W. Adams, S. B. Duckett, R. E. Mewis, D. C. Williamson, G. G. R. Green, *Prog. Nucl. Mag. Res. Spectrosc.* **2012**, *67*, 1-48.

[45] A. N. Pravdivtsev, A. V. Yurkovskaya, H.-M. Vieth, K. L. Ivanov, R. Kaptein, *ChemPhysChem* **2013**, *14*, 3327-3331.

[46] D. A. Barskiy, A. N. Pravdivtsev, K. L. Ivanov, K. V. Kovtunov, I. V. Koptyug, *Phys. Chem. Chem. Phys.* **2016**, *18*, 89-93.

[47] K. L. Ivanov, A. N. Pravdivtsev, A. V. Yurkovskaya, H.-M. Vieth, R. Kaptein, *Prog. Nucl. Mag. Res. Spectrosc.* **2014**, *81*, 1-36.

[48] S. Knecht, K. L. Ivanov, *J. Chem. Phys.* **2019**, *150*, 124106.

[49] A. S. Kiryutin, A. V. Yurkovskaya, H. Zimmermann, H.-M. Vieth, K. L. Ivanov, *Magn. Reson. Chem.* **2018**, *56*, 651-662.

[50] N. Eshuis, R. L. E. G. Aspers, B. J. A. van Weerdenburg, M. C. Feiters, F. P. J. T. Rutjes, S. S. Wijmenga, M. Tessari, *J. Magn. Reson.* **2016**, *265*, 59-66.

[51] E. B. Ducker, L. T. Kuhn, K. Munnemann, C. Griesinger, *J. Magn. Reson.* **2012**, *214*, 159-165.

[52] M. J. Cowley, R. W. Adams, K. D. Atkinson, M. C. R. Cockett, S. B. Duckett, G. G. R. Green, J. A. B. Lohman, R. Kerssebaum, D. Kilgour, R. E. Mewis, *J. Am. Chem. Soc.* **2011**, *133*, 6134-6137.

[53] T. Theis, M. L. Truong, A. M. Coffey, R. V. Shchepin, K. W. Waddell, F. Shi, B. M. Goodson, W. S. Warren, E. Y. Chekmenev, *J. Am. Chem. Soc.* **2015**, *137*, 1404-1407.

[54] K. D. Atkinson, M. J. Cowley, S. B. Duckett, P. I. P. Elliott, G. G. R. Green, J. López-Serrano, I. G. Khazal, A. C. Whitwood, *Inorg. Chem.* **2009**, *48*, 663-670.

[55] T. Theis, M. Truong, A. M. Coffey, E. Y. Chekmenev, W. S. Warren, *J. Magn. Reson.* **2014**, *248*, 23-26.

[56] A. Svyatova, I. V. Skovpin, N. V. Chukanov, K. V. Kovtunov, E. Y. Chekmenev, A. N. Pravdivtsev, J.-B. Hoevener, I. V. Koptyug, *Chem. Eur. J.* **2019**, *25*, 8465-8470.

[57] J. R. Lindale, S. L. Eriksson, C. P. N. Tanner, Z. Zhou, J. F. P. Colell, G. Zhang, J. Bae, E. Y. Chekmenev, T. Theis, W. S. Warren, *Nat. Commun.* **2019**, *10*, 395.

[58] T. Theis, N. M. Ariyasingha, R. V. Shchepin, J. R. Lindale, W. S. Warren, E. Y. Chekmenev, *J. Phys. Chem. Lett.* **2018**, *9*, 6136-6142.

[59] C. P. N. Tanner, J. R. Lindale, S. L. Eriksson, Z. Zhou, J. F. P. Colell, T. Theis, W. S. Warren, *J. Chem. Phys.* **2019**, *151*, 044201.

[60] A. N. Pravdivtsev, I. V. Skovpin, A. I. Svyatova, N. V. Chukanov, L. M. Kovtunova, V. I. Bukhtiyarov, E. Y. Chekmenev, K. V. Kovtunov, I. V. Koptyug, J.-B. Hövener, *J. Phys. Chem. A* **2018**, *122*, 9107-9114.

[61] P. J. Rayner, P. Norcott, K. M. Appleby, W. Iali, R. O. John, S. J. Hart, A. C. Whitwood, S. B. Duckett, *Nat. Commun.* **2018**, *9*, 4251.

[62] R. V. Shchepin, J. R. Birchall, N. V. Chukanov, K. V. Kovtunov, I. V. Koptyug, T. Theis, W. S. Warren, J. G. Gelovani, B. M. Goodson, S. Shokouhi, M. S. Rosen, Y.-F. Yen, W. Pham, E. Y. Chekmenev, *Chem. Eur. J.* **2019**, *25*, 8829-8836.

[63] V. V. Zhivonitko, I. V. Skovpin, I. V. Koptyug, *Chem. Comm.* **2015**, *51*, 2506-2509.

[64] M. J. Burns, P. J. Rayner, G. G. R. Green, L. A. R. Highton, R. E. Mewis, S. B. Duckett, *J. Phys. Chem. B* **2015**, *119*, 5020-5027.

[65] R. V. Shchepin, D. A. Barskiy, A. M. Coffey, B. M. Goodson, E. Y. Chekmenev, *ChemistrySelect* **2016**, *1*, 2552-2555.

[66] M. Carravetta, M. H. Levitt, *J. Am. Chem. Soc.* **2004**, *126*, 6228-6229.

[67] J.-N. Dumez, *Mol. Phys.* **2019**, 1-11.

[68] A. M. Olaru, S. S. Roy, L. S. Lloyd, S. Coombes, G. G. R. Green, S. B. Duckett, *Chem. Comm.* **2016**, *52*, 7842-7845.

[69] S. S. Roy, P. Rayner, P. Norcott, G. G. R. Green, S. B. Duckett, *Phys. Chem. Chem. Phys.* **2016**, *18*, 24905-24911.

[70] S. S. Roy, P. Norcott, P. J. Rayner, G. G. R. Green, S. B. Duckett, *Angew. Chem. Int. Ed.* **2016**, *55*, 15642-15645.

[71] K. Shen, A. W. J. Logan, J. F. P. Colell, J. Bae, G. X. Ortiz Jr., T. Theis, W. S. Warren, S. J. Malcolmson, Q. Wang, *Angew. Chem. Int. Ed.* **2017**, *56*, 12112-12116.

[72] T. Theis, G. X. Ortiz , A. W. J. Logan, K. E. Claytor, Y. Feng, W. P. Huhn, V. Blum, S. J. Malcolmson, E. Y. Chekmenev, Q. Wang, W. S. Warren, *Sci. Adv.* **2016**, *2*, e1501438.

[73] W. Iali, P. J. Rayner, S. B. Duckett, *Sci. Adv.* **2018**, *4*.

[74] W. Iali, P. J. Rayner, A. Alshehri, A. J. Holmes, A. J. Ruddlesden, S. B. Duckett, *Chem. Sci.* **2018**, *9*, 3677-3684.

[75] B. J. Tickner, W. Iali, S. S. Roy, A. C. Whitwood, S. B. Duckett, *ChemPhysChem* **2019**, *20*, 241-245.

[76] W. Iali, S. S. Roy, B. J. Tickner, F. Ahwal, A. J. Kennerley, S. B. Duckett, *Angew. Chem. Int. Ed.* **2019**, *58*, 10271-10275.

[77] J. Bae, Z. Zhou, T. Theis, W. S. Warren, Q. Wang, *Sci. Adv.* **2018**, *4*, eaar2978.

[78] B. Procacci, S. S. Roy, P. Norcott, N. Turner, S. B. Duckett, *J. Am. Chem. Soc.* **2018**, *140*, 16855-16864.

[79] H. Nonaka, M. Hirano, Y. Imakura, Y. Takakusagi, K. Ichikawa, S. Sando, *Sci. Rep.* **2017**, *7*, 40104.

[80] J. Kurhanewicz, D. B. Vigneron, J. H. Ardenkjaer-Larsen, J. A. Bankson, K. Brindle, C. H. Cunningham, F. A. Gallagher, K. R. Keshari, A. Kjaer, C. Laustsen, D. A. Mankoff, M. E. Merritt, S. J. Nelson, J. M. Pauly, P. Lee, S. Ronen, D. J. Tyler, S. S. Rajan, D. M. Spielman, L. Wald, X. Zhang, C. R. Malloy, R. Rizi, *Neoplasia* **2019**, *21*, 1-16.

[81] J. A. Surface, Washington University in St. Louis **2013**.

[82] D. O. Kuethe, A. Caprihan, H. M. Gach, I. J. Lowe, E. Fukushima, *J. Appl. Physiol.* **2000**, *88*, 2279-2286.

[83] D. O. Kuethe, A. Caprihan, E. Fukushima, R. A. Waggoner, *Magn. Reson. Med.* **1998**, *39*, 85-88.

[84] D. A. Barskiy, K. V. Kovtunov, E. Y. Gerasimov, M. A. Phipps, O. G. Salnikov, A. M. Coffey, L. M. Kovtunova, I. P. Prosvirin, V. I. Bukhtiyarov, I. V. Koptyug, E. Y. Chekmenev, *J. Phys. Chem. C* **2017**, *121*, 10038–10046.

[85] D. A. Barskiy, O. G. Salnikov, A. S. Romanov, M. A. Feldman, A. M. Coffey, K. V. Kovtunov, I. V. Koptyug, E. Y. Chekmenev, *J. Magn. Reson.* **2017**, *276*, 78-85.

Accepted Manuscript

This article is protected by copyright. All rights reserved.

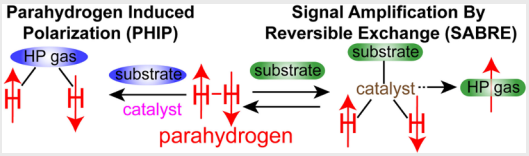
10.1002/anie.201915306

WILEY-VCH

Entry for the Table of Contents

Layout 2:

MINIREVIEW



Kirill V. Kovtunov,[a,b] Igor V. Koptyug,*[a,b] Marianna Fekete,[c] Simon B. Duckett,[c] Thomas Theis,[d] Baptiste Joalland,[e] and Eduard Y. Chekmenev*[e,f]*

Parahydrogen-induced Hyperpolarization of Gases

This minireview reports on selective overview of two hyperpolarization techniques: *Para*Hydrogen Induced Polarization (PHIP) and Signal Amplification By Reversible Exchange (SABRE) in the context of production of hyperpolarized gases for potential applications in bioimaging and beyond.

WILEY-VCH

Accepted Manuscript

This article is protected by copyright. All rights reserved.

Nuclear Inst. and Methods in Physics Research, A 969 (2020) 163961

Contents lists available at ScienceDirect

Nuclear Inst. and Methods in Physics Research, A

journal homepage: www.elsevier.com/locate/nima

A modular apparatus for use in high-precision measurements of parity violation in polarized eV neutron transmission

D.C. Schaper [a,b,*], C. Auton [c], L. Barrón-Palos [d], M. Borrego [a], A. Chavez [a], L. Cole [b], C.B. Crawford [b], J. Curole [c], H. Dhahri [b], K.A. Dickerson [c], J. Doskow [c], W. Fox [c], M.H. Gervais [b], B.M. Goodson [e], K. Knickerbocker [a], C. Jiang [f], P.M. King [g], H. Lu [c], M. Mocko [a], D. Olivera-Velarde [h], J.G. Otero Munoz [c], S.I. Penttilä [f], A. Pérez-Martín [d], B. Short [i], W.M. Snow [c], K. Steffen [c], J. Vanderwerp [c], G. Visser [c]

[a] Los Alamos National Laboratory, Los Alamos, NM, 87545, USA
[b] University of Kentucky, Lexington, KY, 40506, USA
[c] Indiana University, Bloomington, IN, 47405, USA
[d] Instituto de Física, Universidad Nacional Autónoma de México, Apartado Postal 20-364, 01000, Mexico
[e] Southern Illinois University, Carbondale, IL 62901, USA
[f] Oak Ridge National Laboratory, Oak Ridge, TN, 37830, USA
[g] Ohio University, Athens, OH, 45701, USA
[h] Berea College, Berea, KY, 40404, USA
[i] University of Minnesota Twin Cities, Minneapolis, MN, 55455, USA

ARTICLE INFO

Keywords:
Parity violation
Scintillator detector
Neutron resonance
Fundamental symmetry
Time reversal violation

ABSTRACT

We describe a modular apparatus for use in parity-violation measurements in epithermal neutron–nucleus resonances with high instantaneous neutron fluxes at the Manuel Lujan Jr. Neutron Scattering Center at Los Alamos National Laboratory. This apparatus is designed to conduct high-precision measurements of the parity-odd transmission asymmetry of longitudinally polarized neutrons through targets containing nuclei with p-wave neutron–nucleus resonances in the 0.1–10 eV energy regime and to accommodate a future search for time reversal violation in polarized neutron transmission through polarized nuclear targets. The apparatus consists of an adjustable neutron and gamma collimation system, a ^{3}He-^{4}He ion chamber neutron flux monitor, two identical cryostats for target cooling, an adiabatic eV-neutron spin flipper, a near-unit efficiency ^{6}Li-^{7}Li scintillation detector operated in current mode, a flexible CAEN data acquisition system, and a neutron spin filter based on spin-exchange optical pumping of^{3}He gas. We describe the features of the apparatus design devoted to the suppression of systematic errors in parity-odd asymmetry measurements. We describe the configuration of the apparatus used to conduct a precision measurement of parity violation at the 0.7 eV p-wave resonance in^{139}La which employs two identical^{139}La targets, one to polarize the beam on the p-wave resonance using the weak interaction and one to analyze the polarization.

1. Introduction

Compound neutron–nucleus resonance reactions have proven to be an excellent laboratory in which to study parity violation [1,2]. The complex, many-body nature of this nuclear system with its very high level density was predicted theoretically [3,4] and confirmed by experiment [5,6] to provide a natural amplification mechanism for Parity Violating (PV) neutron–nucleus interactions. Statistical spectroscopy has been used to successfully analyze the widths of the distributions of observed parity-odd asymmetries in several heavy nuclei in the isolated resonance regime corresponding to eV–keV neutron energies [7]. The present theory involving the mixing of nearby s-wave and p-wave resonances that accounts for this amplification of parity-odd amplitudes also predicts a similar amplification of Time Reversal Invariance Violating (TRIV) amplitudes [8]. Parity- (P) and Time- (T) odd effects in forward transmission provide null tests for time reversal invariance [9]. Compound nuclear systems are therefore attractive candidates for T-violation searches. With the advent of high-flux MW-class short-pulsed spallation neutron sources, sensitive tests of TRIV in neutron-nucleon interactions can be realized.

* Corresponding author at: University of Kentucky, Lexington, KY, 40506, USA.
E-mail address: schaper@lanl.gov (D.C. Schaper).

https://doi.org/10.1016/j.nima.2020.163961
Received 8 January 2020; Received in revised form 30 March 2020; Accepted 13 April 2020
Available online 20 April 2020
0168-9002/© 2020 Elsevier B.V. All rights reserved.

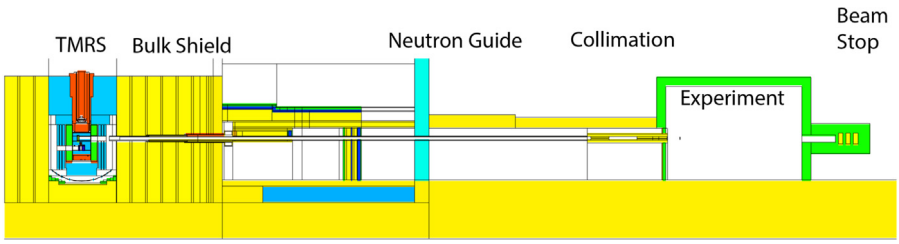


Fig. 1. Elevation view of the FP12 geometry as implemented in the MCNPX model.

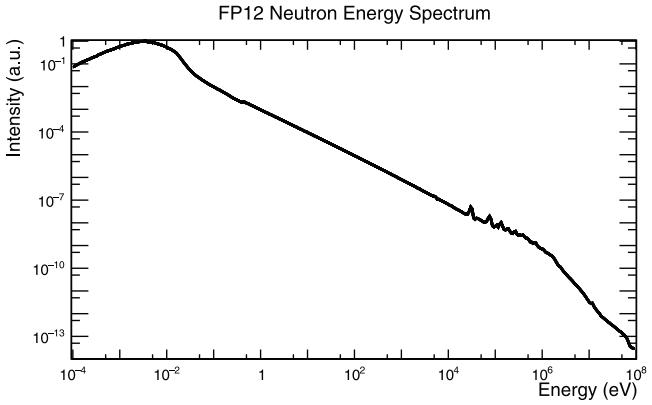


Fig. 2. An MCNPX calculation of the neutron energy spectrum for FP12, normalized to the peak flux intensity. This was generated using MCNPX simulations with the most recent FP12 geometry.

Due to the proportionality between potential TRIV amplitudes and PV amplitudes, these future TRIV tests will need more complete and precise information on the properties of the resonances which exhibit large parity violation effects. In addition to new measurements of (n, γ) angular distributions [10] which can be used to determine the details of the quantum numbers of these $\ell = 1$ (p-wave) resonances, it is also important to repeat previous measurements of P-odd neutron transmission asymmetries [5,11–14] with higher precision. By measuring the transmission asymmetry of longitudinally polarized neutrons through an unpolarized target, one can determine the parity-odd helicity dependence of the total cross section. The transmission asymmetry is defined as

$$A = \frac{Y^+ - Y^-}{Y^+ + Y^-} = \tanh(f_n n t \sigma_p P) \tag{1}$$

where $Y^{\pm}$ is the neutron transmission yield for the two neutron helicities, f_n is the polarization of the neutron beam, σ_p is the p-wave cross section for unpolarized neutrons, n is the number density of the target nuclei, t is the target thickness, and P is the parity-odd longitudinal analyzing power, defined by its relationship to the helicity-dependent cross section, $\sigma^{\pm}$:

$$\sigma^{\pm} = \sigma_p(1 \pm f_n P) \tag{2}$$

The two most effective and well-known methods to polarize neutron beams [15] in the eV energy range are spin-dependent scattering from a polarized proton target [16] and spin-dependent absorption in a polarized ^{3}He target [17]. There also exists a third, lesser-known polarization method which is at present practical only for the ^{139}La nucleus. The ^{139}La nucleus possesses a p-wave resonance near 0.7 eV, whose interference with nearby s-wave resonances results in a 10% parity-odd asymmetry. This is larger than expected on dimensional grounds alone by about a factor of 10^6. As demonstrated by C.D. Bowman et al. [18] and later Yuan et al. [19] this parity violating asymmetry is large enough that one can use it to polarize the beam using the (intrinsically parity-odd) weak interaction. By transmitting such a weakly-polarized beam through a second ^{139}La target, one can realize a measurement of the P-odd asymmetry in which the ^{139}La targets act as both a polarizer and as a polarization analyzer, resulting in the aptly-named 'Double Lanthanum' measurement method. Although the beam polarization produced on the parity-odd 0.7 eV resonance in ^{139}La is small [18,19], its use in this configuration eliminates certain systematic errors associated with measuring P, especially the absolute knowledge of the neutron beam polarization f_n. In this paper we describe how our apparatus may be modified to accommodate setups for both the 'Double Lanthanum' P measurement method as well as a traditional P measurement using a ^{3}He neutron spin filter.

In addition to its relevance for future time reversal violation experiments, a precise determination of P for ^{139}La is of potential use as a standard analyzer in eV neutron scattering and transmission experiments by allowing one to measure the absolute polarization of epithermal neutron beams containing $\ell = 1$, 0.7 eV neutrons. ^{139}La was already used for this purpose in the measurements of P-odd asymmetries in heavy nuclei conducted by the TRIPLE collaboration [2]. It was also used in some pioneering measurements of the depolarization of polarized eV neutrons in transmission through magnetic fields in polarized and aligned nuclear targets to extract information on the internal magnetic domain structure [20–22]. The large P-odd asymmetry on the 0.88 eV $\ell = 1$ resonance in ^{81}Br could also be used for this purpose. The possibility of constructing a compact eV neutron polarization analyzer at these two energies based on neutron absorption in $LaBr_3$ scintillating crystals is under analysis.

In this paper we describe the apparatus and experimental setup we have realized to perform precision measurements of the parity violation, P, present in the eV neutron energy range as configured for the Double Lanthanum experiment. The Los Alamos Neutron Science Center (LANSCE) beam facility is described in Section 2. The mechanical apparatus used for the parity violation measurement, including the collimation, cryostats, mechanical rotation stage, and detector shieldhouse, are all described in Section 3. The custom spin flipper constructed for this experiment and optimized for 0.7 eV neutrons is described in Section 4. Details of the electronics design for the spin flipper are described in Section 5. The fast-response current mode ^{6}Li-^{7}Li glass scintillator detector designed for this experiment is discussed in Section 6. Section 7 describes the data acquisition system, including all measured parameters and their experimental relevance. Section 8 describes the design of the polarized ^{3}He neutron spin filter for eV neutrons to be installed for future parity violation measurements. A brief summary and description of possible future measurements which can be conducted with this instrument is given in Section 9.

2. The FP12 neutron beam facility at LANSCE

The apparatus described in this paper was located in an experimental hutch on Flight Path 12 (FP12) at LANSCE. Neutrons which are delivered to FP12 are produced by the 1L Lujan Target-Moderator-Reflector-Shield (TMRS) Mark-III assembly and are moderated by a partially-coupled cold hydrogen moderator. The flight path is equipped with an $m = 3$, 10 cm×10 cm supermirror neutron guide designed to transport a large fraction of cold neutrons to the experimental hutch [23]. The neutron flux and spectrum in the slow neutron regime

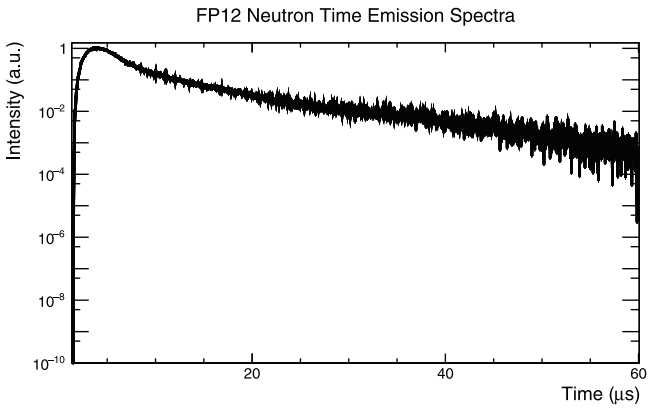


Fig. 3. A calculation of the time emission spectra for neutrons of energy 0.7 eV, normalized to the peak intensity.

between 1–80 meV was already measured in the past and described in the literature [24]. MCNPX simulations of FP12 were performed to extract the energy spectrum and emission time distributions of 0.7 eV neutrons. The detailed 3D geometry as implemented in the MCNPX model is shown in Fig. 1. The model included a detailed implementation of the TMRS Mark-III surrounded by the Bulk Shielding. The neutron guide is surrounded with concrete/steel/polyethylene shielding and the experimental hutch is shielded with borated polyethylene clad in 3/8" thick steel. The neutron beam terminates in a beam stop made of steel and borated polyethylene.

The calculations of the time-emission spectra followed the methodology outlined in [25]. The TMRS model used in these simulations was based on the as-built engineering design. The thermal neutron scattering kernels that were used are for hydrogen and deuterium in water, ortho- and para-hydrogen in liquid hydrogen, aluminum in alloys, and iron in steel. All calculations utilized the next-event-estimator (point detector) variance reduction technique [26] to ensure efficient convergence of all extracted observables. The relatively sharp proton pulse (270 ns pulse width) incident on the spallation target at a short-pulsed spallation neutron source like LANSCE is a very valuable feature for precision measurements of parity violation and time reversal violation on neutron–nucleus resonances as it greatly improves the time resolution of the neutron time-of-flight measurements necessary to accurately determine the neutron energy (see Figs. 2 and 3).

The FP12 hutch is a steel enclosure shaped like a trapezoid, as seen in Fig. 4. It is approximately 4.73 m long in the beam direction, 2.74 m tall, and 4.61 to 6.22 meters in the transverse direction. The beam pipe is centered 1.37 meters above the floor. The most upstream components are collimators that scrape the neutron beam to a 10 cm diameter and a ^{3}He-^{4}He ion chamber to measure the neutron flux. Next downstream is the first cryogenically cooled ^{139}La target, an adiabatic spin flipper, and a second ^{139}La target. The furthest downstream component is a shielded ^{6}Li-rich scintillator neutron detector buried in shielding designed to attenuate both neutrons and gamma rays to reduce background noise. Fig. 5 shows a detailed view of these components and their placement.

3. Mechanical apparatus components

Previous experiments have measured P on the 0.7 eV resonance in ^{139}La to $\sim 4\%$ accuracy [19]. In order to achieve a measurement with 1% accuracy as needed for the future time reversal and neutron polarimetry physics, we decided to use cryogenic targets to minimize the Doppler broadening of the transmitted resonance profile. To prepare for the future NOPTREX time reversal search experiment described in [9], we mounted these cryostats on a rotating turntable and chose a ^{3}He neutron spin filter polarized by spin-exchange optical pumping (SEOP) methods which can later be placed in the position of the upstream cryostat. These decisions strongly influenced the apparatus design, which otherwise possesses several components very similar to an earlier instrument built by the TRIPLE Collaboration [27]. The apparatus also possesses some common features with the POLYANA instrument at the IBR-30 pulsed reactor neutron source at Dubna [28].

The apparatus can be divided into three major beamline components; the collimator stand; the main apparatus stand (mounted on the rotation stage); and the detector stand/shieldhouse. One key feature of almost all components is the use of non-magnetic materials. Due to the oscillating magnetic fields produced by the neutron spin-flip coils, any magnetic material could be magnetized, leading to stray fields that could affect the neutron spin-flip efficiency as well as cause magnetic-field dependent gain shifts in our detector electronics. Therefore much of the apparatus is constructed from aluminum, brass, and plastic.

3.1. Collimators and stand

The collimator stand, located furthest upstream at the exit of the beam pipe, supports interchangeable collimators and the ^{3}He-^{4}He beam monitor. The stand is made from aluminum held together with brass screws and bolts. A 96 cm long rectangular aluminum channel provides a reliable way to interchange up to 16 collimators and ensures that all collimators are coaxial with the beam. Adjustable feet allow for precision alignment of the collimators to the beam axis using a theodolite. The beam monitor rests at the downstream end of the stand and is electrically isolated from the rest of the stand via a polycarbonate plastic base. The collimators define the neutron beam and minimize the contribution of fast neutrons and gamma rays to the radiation backgrounds in the hutch. 5.01 cm thick borated polyethylene collimators attenuate fast neutrons outside of the desired beam profile. The borated polyethylene collimator located the furthest upstream has an additional 1 mm layer of ^{6}Li-loaded fluorinated plastic which collimates slow neutrons and produces a very small number of gamma rays per absorbed neutron. After the borated polyethylene collimators, 3.65 cm thick brass collimators attenuate gamma rays produced both by the ‘gamma flash’ characteristic of spallation targets as well as any gamma rays produced by neutrons absorbing in the borated polyethylene collimators. The collimator collection is also draped with ^{6}Li fluorinated plastic to absorb high energy neutrons scattered by the hydrogen but not absorbed by the boron in the fast neutron collimators before they can create additional neutron and gamma ray backgrounds signals in the detector. Collimators made of ^{10}B-loaded plastic are also placed outside the upstream ends of the cryostat vacuum flanges to sharply define the beam that passes through the targets. The stand is stable enough to also support a calibration resonance target wheel and a local neutron chopper if needed.

We measure the neutron time-of-flight spectrum on a pulse-by-pulse basis using a beam monitor, which is a low efficiency ion chamber with ^{3}He and ^{4}He gas chambers located back-to-back along the neutron beam and operated in current mode. Since the neutron absorption cross section in ^{3}He is very large (of order kilobarns) and well known [29], the neutron absorption cross section in ^{4}He is extremely small, and the gamma interactions of these two isotopes are essentially identical, the difference signal from these two chambers is directly proportional to the instantaneous neutron flux. We do not elaborate any more on the details of the design for this device as it is identical to the one used by the TRIPLE collaboration as it is already described in great detail in the scientific literature [30].

3.2. Main apparatus and rotation stage

The main apparatus frame is constructed from extruded aluminum profiles (manufactured by 80/20 Inc, hereafter referred to as “8020") mounted to a large rotation stage with adjustable feet. The base of the main apparatus is a large aluminum table with large 8020 support legs. On top of this table sits a Franke TSD-830M rotation stage, labeled in

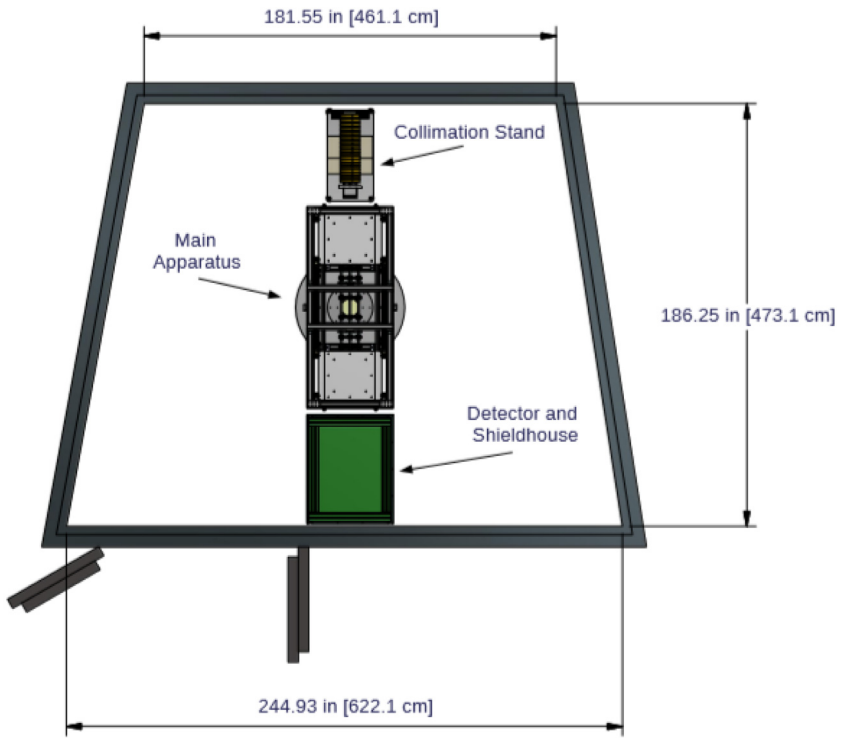


Fig. 4. Top-down view of the FP12 hutch at LANSCE showing the hutch dimensions and general position of the experimental setup.

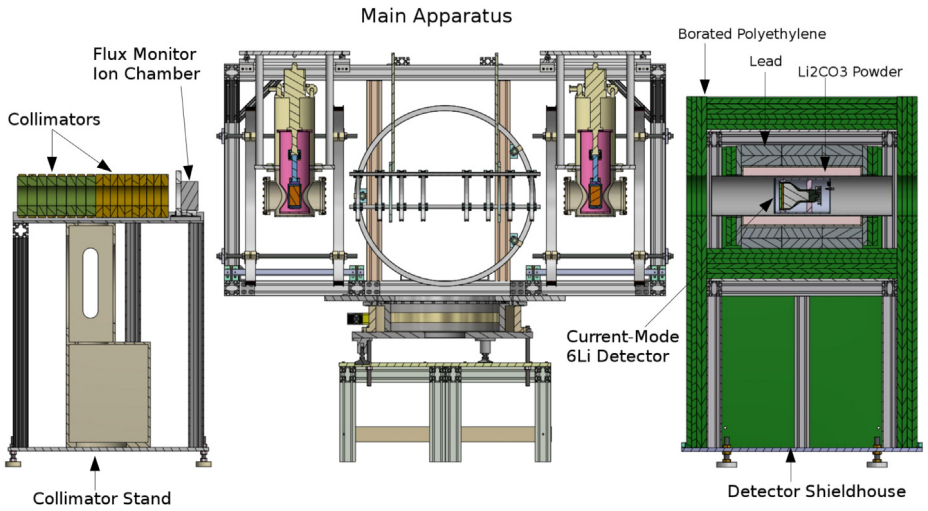


Fig. 5. A cross-section view of the experimental setup in FP12 at LANSCE as viewed from the side. The three components are the collimator stand, the main apparatus containing the cryostats and the spin flipper coil assembly, and the detector/shieldhouse assembly.

Fig. 6. The rotation stage has a 57,000 N load rating and allows for 360 degree rotation of the main apparatus. The rotation stage is mounted to adjustable feet which allow for fine-tuned adjustments to center the targets on the beam axis. A large (1.22 m diameter and 2.54 cm thick) circular aluminum plate rests on the rotation stage and supports the main rectangular frame constructed from 8020. The frame supports the cryostat/cryogenic target assemblies, adiabatic spin-flipper coils, and can be modified to include additional equipment such as a ^{3}He polarizer (described in further detail in Section 8). The spin-flipper coils are affixed directly to the 8020 aluminum frame using specially-designed plastic clamps.

The aluminum housing for the cryostats are supported from the top of the 8020 frame on sliding rails, allowing for easy adjustment of the target location along the neutron beam. The maximum distance between the two targets is 152 cm. The cryogenic housing is mounted to the sliding rails by three V-groove-and-ball kinematic mounts. This allows for reproducible, precision placement of the targets when moving or replacing the cryogenic housing during a target change. In this modular design other components such as a large ^{3}He polarizer can also couple to the sliding rails or the 8020 frame. One nice feature of using 8020 for the frame is the ease with which components can be precisely and repeatably aligned using mechanically-defined reference points. The aluminum table was aligned to the beam using a theodolite. All other components used mechanically-defined reference points to define alignment.

3.3. Target environment

Cryo-Torr 8 cryopumps were stripped of their internal cryopumping surfaces and used as mechanical refrigerators to cool the targets to

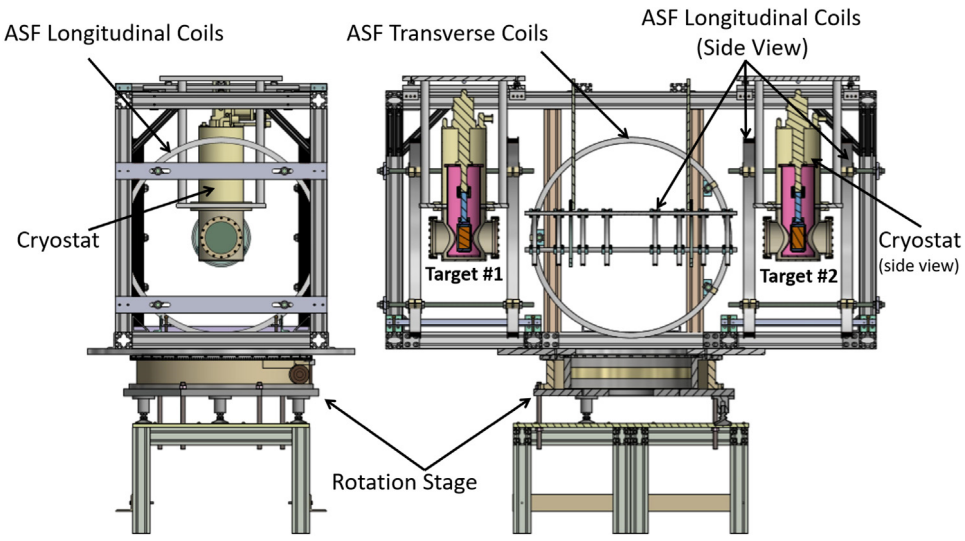


Fig. 6. The main apparatus in the Double Lanthanum experimental setup as configured with two cryogenic ^{139}La targets installed. The lefthand diagram shows a downstream view of the apparatus (i.e. looking down the axis of the neutron trajectory) whereas the righthand shows a sidelong, cross-section view.

~15 K. The cryopumps couple to the aluminum housing and then to an aluminum vacuum chamber below. The neutron beam passes through 1.27 mm thick aluminum vacuum windows centered on the beam. Inside the cryostat vacuum chamber, the target cell is thermally coupled to the 15 K stage of the cold head, while a surrounding radiation shield is coupled to the 80 K stage of the cold head. The target cells are contained in 12.03 cm diameter aluminum cans, filled in an inert argon atmosphere in a glovebox and sealed with indium o-rings. This prevents potential oxidation of sensitive or reactive target materials such as lanthanum to preserve the integrity of the target and to promote the safe handling of activated targets. To monitor the temperatures inside of the cryostats, four silicon diode temperature sensors were placed at different stages of the cryostat; one on the radiation shield, one on the coldhead, one at the top of the cell clamp, and one at the bottom of the cell clamp. The temperatures measured by diode thermometers were read using a Lakeshore 218 temperature monitor. The temperature distribution in the cryogenic system under steady state operation was stable at the level of 0.2 K.

3.4. Detector and shieldhouse

Located furthest downstream from the beam pipe entrance to the hutch is the detector stand and shielding assembly, known as the shieldhouse. The purpose of this shieldhouse is to protect the ^{6}Li neutron detector from any neutrons and gamma rays originating from outside the defined neutron beam (e.g. multiply-scattered neutrons from the hutch or gamma rays produced in neutron capture reactions on materials in the hutch). The support structure frame is made of 8020 and sheets of borated polyethylene. The outermost layer of shielding consists of 15 cm of borated polyethylene, followed by 10 cm of lead bricks and 5 cm of lithium carbonate powder as seen in Fig. 5. The detector sits in an aluminum tube and was aligned to the neutron beam axis using a theodolite and crosshairs of fishing line anchored to the aluminum tube using offset set screws.

3.5. Field mapper

In order to successfully make a precision measurement of the parity violation in the target nuclei, it is critical to understand the dynamics of the neutron spin motion in the fields and determine the spin-flip efficiency. To do so, detailed maps of the magnetic fields produced by the spin flipper array (discussed in more detail in Section 4) were needed.

One of the challenges presented with the design of the spin flipper coils was a difficulty in mapping the magnetic field. Mounting a magnetic probe to a motorized mapper system was very difficult due to spatial constraints enforced by the coils, their supports, and lead wires. A simple mapping system was constructed by mounting a Lakeshore 460 triple axis probe to a three-dimensional, manually translatable apparatus. Continuous translational range of motion was possible in the xy plane perpendicular to the direction of the neutron beam. In the longitudinal z direction, pairs of threaded holes were machined into a long, metal plank; pairs of screws were then placed in each set of holes and by laying the y-directional translation stage such that an edge was laid flush to both screws, unique points along the z axis were defined. Cross-sectional x, y slices of the magnetic field were then mapped for each of the points defined along the z-axis. 12 planar maps were taken for each configuration of the spin flip field. This data, shown in Fig. 10, was then reconstructed and interpolated using COMSOL and used in calculating the neutron spin flip efficiency as discussed further in Section 4 (see Fig. 7).

4. Adiabatic spin flipper for ev neutrons

Following the design of Roberson et al. [27], we simulated and built a neutron Adiabatic Spin Flipper (ASF) based on adiabatic spin motion in static magnetic fields. This spin flipper is mounted and aligned to the 8020 frame, ensuring that the ASF longitudinal coils shown in Fig. 6 are coaxial with both the lanthanum targets and the neutron beam. The coil geometry and currents were optimized for neutron energies near 1 eV as needed for the Double Lanthanum experiment, though the adiabatic condition can be met for a broad range of neutron energies. As in the TRIPLE apparatus, the neutron spin flipper consists of longitudinal and transverse coils that produce static gradient magnetic fields. The combination of these fields produces a total field with approximately constant amplitude B_0 that turns the neutron spin over the distance L on the z-axis over which the spin rotation occurs. The spin flipper operates in two field configurations, which we shall call the *no-flip* and *flip* configurations. For the *no-flip* configuration, only the longitudinal B_z coils are turned on. If the direction of the neutron beam is along the z-axis and $x = y = z = 0$ is taken to be the center of the spin flipper as shown in Fig. 8, then the magnetic field produced by the longitudinal coils in the *no-flip* state can be approximated as

$$B_z = \begin{cases} B_0 & \text{if } z < -L/2 \\ -B_0 \sin(\pi z/L) & \text{if } -L/2 \le z \le L/2 \\ -B_0 & \text{if } z > L/2 \end{cases} \quad (3)$$

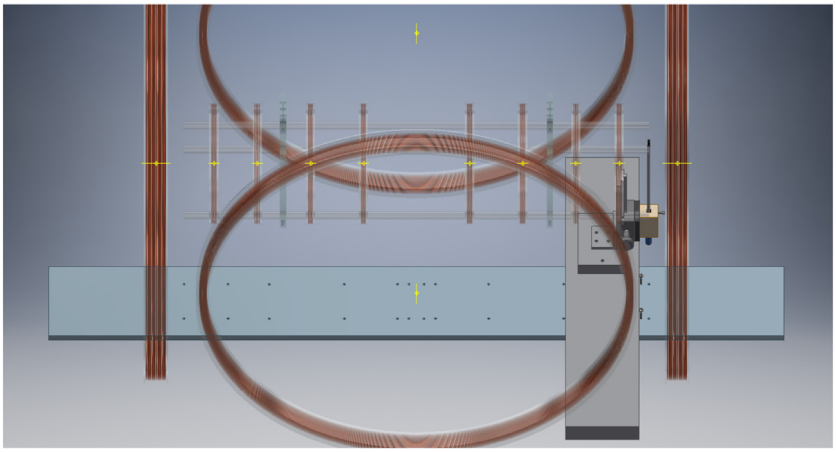


Fig. 7. CAD drawing of the mapper used to map the B-field. Note the pairs of holes machined into the longitudinal plank; these were used to uniquely define points along the z-axis for maps to be taken.

Recall that the magnetic torque $\vec{\tau}$ experienced by a particle with a magnetic moment $\vec{\mu}$ in an external magnetic field $\vec{B}$ is

$$\vec{\tau} = \vec{\mu} \times \vec{B} \tag{4}$$

For the *flip* configuration, the transverse B_y coils are turned on (in addition to the B_z coils). The component produced by the transverse coils is given by

$$B_y = \begin{cases} \pm B_0 \cos(\pi z/L) & \text{if } -L/2 \le z \le L/2 \\ 0 & \text{otherwise} \end{cases} \tag{5}$$

The $\pm$ sign indicates that the B_y component can be either parallel or anti-parallel to the y-axis, depending on the direction of the current in the transverse coils. The superposition of the B_z and B_y fields produces a field $\vec{B}_{\text{total}}$ that is constant in magnitude but rotates by 180° in the zy plane over the length L. A positive B_y component will produce a counter-clockwise rotation of the total field in the zy plane, while a negative B_y component produces a clockwise rotation.

As the neutron magnetic moment $\vec{\mu}_n$ is related to the neutron spin $\vec{\sigma}$ by the gyromagnetic ratio γ_n, one can construct the Hamiltonian of the magnetic interaction with an external magnetic field $\vec{B}$. Substituting this Hamiltonian into the Schrödinger equation for a time dependent $\vec{B}$ field, the Larmor equation for the spin can be obtained [31]:

$$\frac{d}{dt}\vec{\sigma}(t) = \gamma_n \vec{\sigma}(t) \times \vec{B}(t) \tag{6}$$

The change in the neutron spin direction is normal to both $\vec{B}$ and $\vec{\sigma}$ at any given time. For the *no-flip* state there should not be a change in the neutron spin as the spin and the magnetic field are parallel. If the field as seen in the rest frame of the neutron varies slowly enough (i.e. adiabatically), the neutron spin will precess about the field direction with the Larmor frequency $\omega_L = \gamma_n B$ and will "follow" the direction of the external field from its initial direction $+z$ to the opposite direction $-z$ at the end of the flipper. The rotation frequency ω_B of the magnetic field as seen in the rest frame of the neutron is given by

$$\omega_B = \frac{\pi}{t} = \frac{\pi}{L/v} \tag{7}$$

where t is the time the neutron spends in the spin flipper and is given by L/v, where v is the neutron speed and L is the length of the spin flip region. The ratio of the field rotation frequency ω_B and the Larmor frequency ω_L, is defined as the adiabaticity parameter for this system:

$$\gamma = \frac{\omega_B}{\omega_L} = \frac{\pi v}{\gamma_n L B} \tag{8}$$

If $\gamma \ll 1$ the spin direction will undergo several rotations around the $\vec{B}$ direction for every small variation of the field, keeping its precession axis approximately aligned with $\vec{B}$ at any given time. In other words, as long as the neutron speed v is below a certain limit, the transport of the spin will be adiabatic.

Fig. 8 shows the magnetic field configuration for the *flip* and *no-flip* states of the spin flipper, as well as the total magnetic field and neutron spin projection along the field direction as neutrons propagate across the spin flipper length.

This simplified description assumes that all of the neutrons travel directly down the longitudinal axis of the coils. Realistic spin flipper efficiency calculations must account for the finite radius of the beam as well as deviations away from the on-axis magnetic field. Bowman, Penttilä, and Tippens [32] investigated these effects for neutrons whose trajectories deviate slightly from the axis of symmetry. One must consider not only the efficiency of the spin flipper in the *flip* configuration but the efficiency in the *no-flip* configuration. The total efficiency of the spin flipper is the average of the efficiencies for the *flip* state and the *no-flip* state:

$$\epsilon_{\text{flip}} = 1 - \frac{1}{\sqrt{1+\gamma^{-2}}}\left[1 - \cos\left(\pi\sqrt{\gamma^{-2}+1}\right)\right], \tag{9}$$

and the spin-preserving efficiency in the *no-flip* state is

$$\epsilon_{\text{no-flip}} = 1 - \frac{\pi^3 r^2}{8\gamma L^2}, \tag{10}$$

with r the distance of the neutron trajectory from the spin flipper axis. It can be seen that $\epsilon_{\text{flip}} \to 1$ when $\gamma \to 0$; the smaller the adiabaticity parameter, the higher the spin-flip efficiency. Also, $\epsilon_{\text{no-flip}} = 1$ when $r = 0$; if all neutrons travel over the beam axis every spin remains unchanged in the *no-flip* state.

It now makes sense to define a 'total' efficiency, ϵ_{tot}, as a figure of merit for the design which describes both how well the *flip* configuration flips the spin and how well the *no-flip* configuration preserves the spin. We therefore define

$$\epsilon_{\text{total}} = \frac{\epsilon_{\text{flip}} + \epsilon_{\text{no-flip}}}{2} \tag{11}$$

For an ideal spin flipper that flips all neutron spins in the *flip* configuration and leaves all neutron spins unchanged in the *no-flip* configuration, we see $\epsilon_{tot} = 1$.

To define the optimum parameters for our spin flipper, we calculated the *flip*, *no-flip* and total efficiency for different values of magnetic field amplitude B_0 and spin flipper length L using Eqs. (9)–(11). We assumed a 10 cm diameter neutron beam and used the square root of the average value of r^2, $\sqrt{\langle r^2 \rangle}$=3.54 cm to calculate the spin-preserving efficiency. Fig. 9 shows these calculations. Considering the constraints in length for the Double Lanthanum experiment at FP12, we chose L = 120 cm for the flipping length, the maximum allowed in the apparatus. From $z = -60$ cm to $z = 60$ cm the field $\vec{B}$ has the described form for

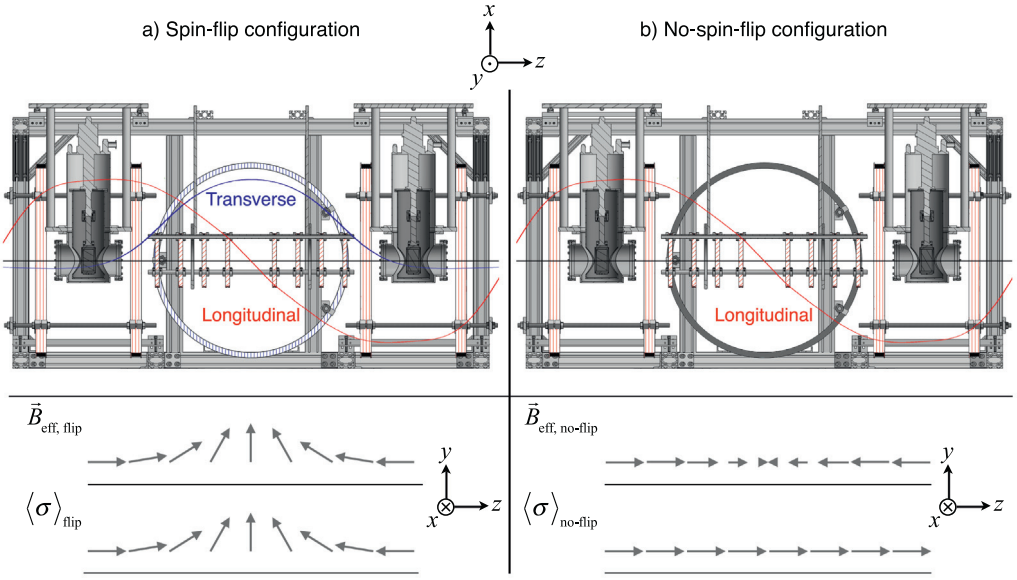


Fig. 8. Components of the magnetic field in the (a) spin-flip and (b) no-spin-flip configurations. The elements of the apparatus producing each component of the magnetic field (longitudinal -red- coils and transverse -blue- coils) are highlighted. Also the total magnetic field $\vec{B}_{\text{total}}$ and the projection of the neutron spin $\langle\vec{\sigma}\rangle$ along its axis of precession are shown in the zy plane for each case.

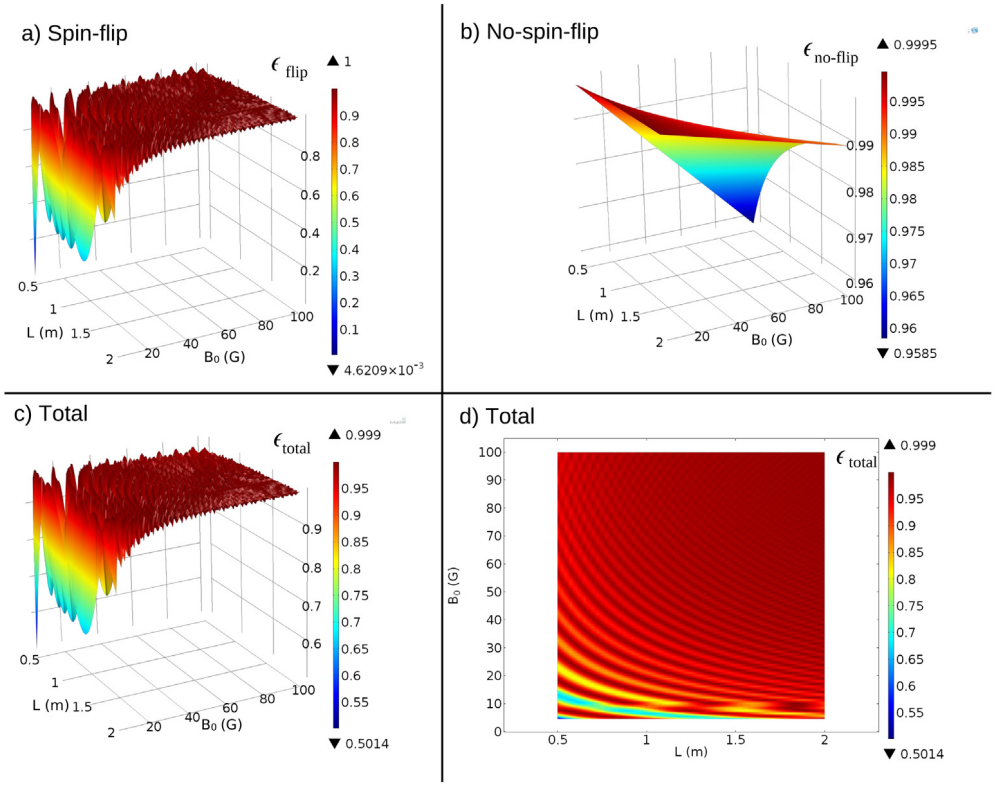


Fig. 9. Calculations of the (a) spin flipper efficiency and (b) spin preserving efficiency as functions of the parameters B_0 and L for 1 eV neutrons at $r = 3.54$ cm, the value of $\sqrt{\langle r^2\rangle}$ over a 10 cm diameter beam. The total efficiency is shown in (c) and (d).

the *flip* and *no-flip* states (Eqs. (3) and (5)). For 60 cm < |z| < 75 cm we aimed to produce a longitudinal constant field of amplitude $\pm B_0$, providing a uniform field in the region of the La targets (see Fig. 10). The choice of B_0 values were constrained by practical experimental and safety reasons: it has to be generated by reasonably attainable electric currents and voltages, yet also has to be large enough to assure a good efficiency. We found that for $L = 120$ cm, a magnetic field amplitude of B_0=16-17 G can produce a total efficiency between 92%–98%, as seen in Fig. 9.

To establish the position along z and the parameter NI (number of turns of a particular coil multiplied by the current) for each of the coils comprising the longitudinal field array (see Fig. 10), we considered the current I to be fixed, and in an iterative process of varying the position and obtaining the number of turns by the Single Value Decomposition (SVD) method, we obtained the optimum coil configuration. With I =

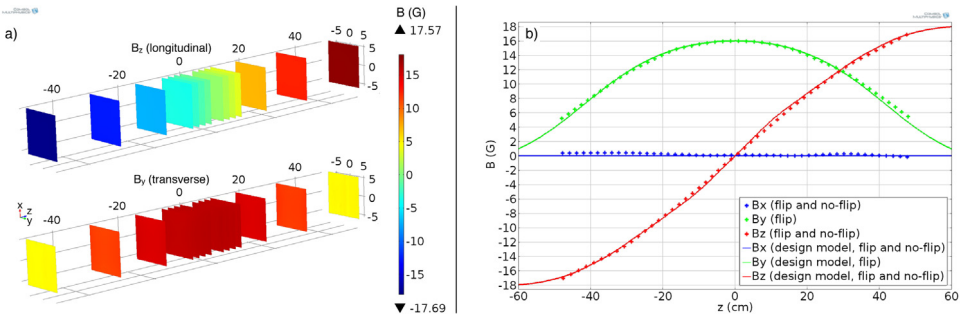


Fig. 10. (a) Field maps for the longitudinal and transverse components of the spin flipper; 14 xy planes were scanned at positions between −50 to 50 cm along the z-axis. (b) Measured magnetic field components along the z-axis and their comparison with the design model fields..

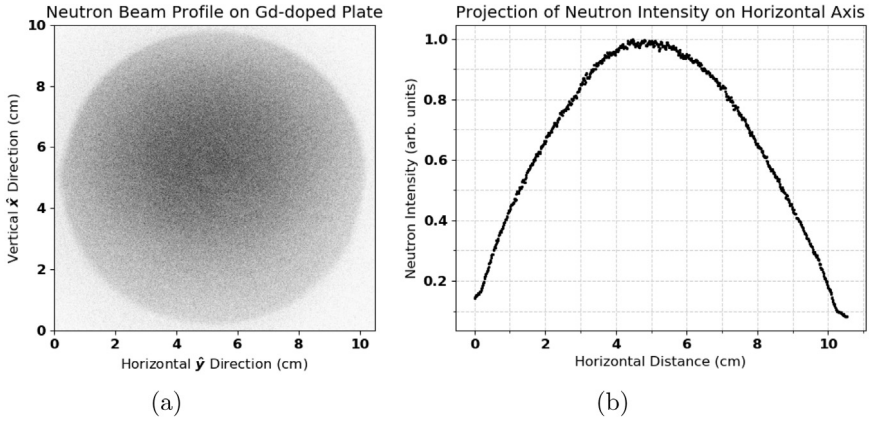


Fig. 11. The image on the left shows the neutron beam spot as imaged on a Gd-doped image plate. The neutron beam intensity distribution was extracted using ImageJ software.

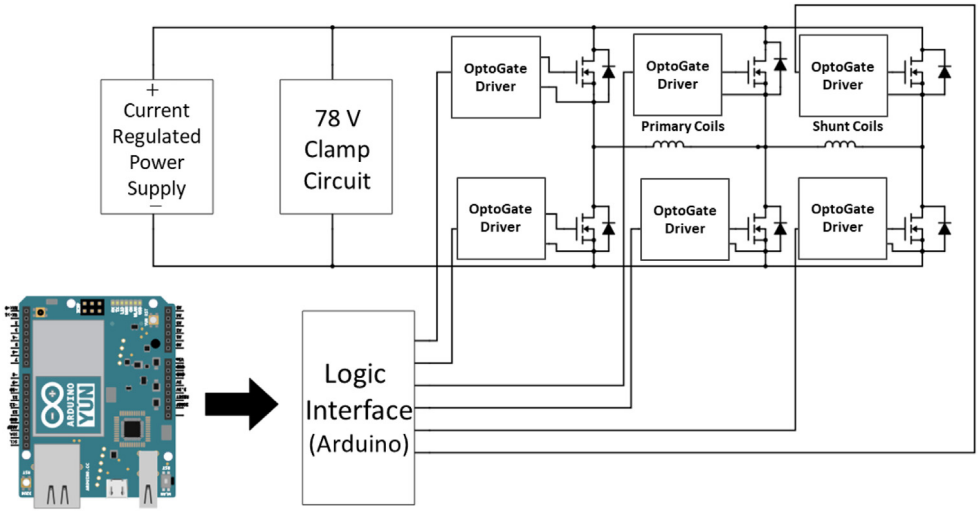


Fig. 12. A simplified schematic of the spin flipper circuit including the primary transverse coils and the shunt transverse coils. The circuit was controlled by an Arduino Mega 2560 board.

15 A and a maximum number of turns that vary from 1–2 turns for the small coils to ∼80 for the large coils, the voltage requirement using 10 AWG copper wire is close to 40 V, which is achievable with the system described in Section 3.

The field maps of the actual spin flipper that was constructed on FP12 were obtained using the mapper described in Section 3.5. A total of 14 xy planes of 11 cm × 11 cm of cross section around the SF axis were scanned in steps of 5 mm. The field maps span the region between −50 to 50 cm in the z-axis, as shown in Fig. 10a. A comparison of the measured magnetic fields and the initially calculated magnetic fields along the spin flipper axis is shown in Fig. 10b; a good agreement is observed in general, however it is important to point out that the longitudinal magnetic field (pictured in red), has a higher amplitude than the transverse magnetic field, producing a total magnetic field that, although performing the desired rotation by 180° in the yz plane, does not maintain a constant amplitude. The field map was obtained in the middle of the experimental run; therefore the spin flipper was operated with the magnetic fields configuration shown in Fig. 10.

These field maps, in combination with the images of the neutron beam profile and data from a Monte Carlo neutron spin transport simulation, can be used to estimate the actual spin flipper efficiency 0.7 eV neutrons.

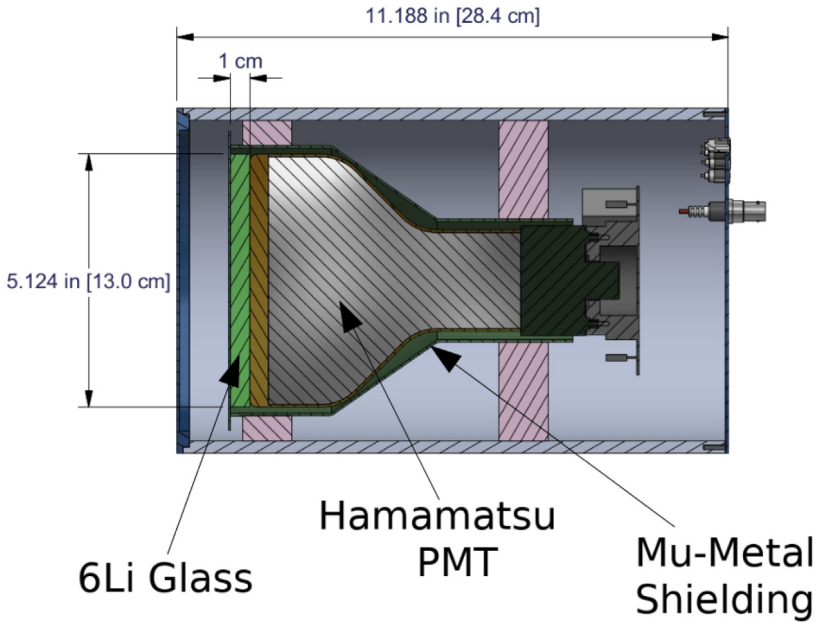


Fig. 13. Side view of the detector design. From left to right: an aluminum window 18 cm in diameter, the ^{6}Li glass scintillator, the Hamamatsu R1513 PMT with its μ-metal magnetic shield, the PCB, and the exit window with electrical feedthroughs. Not shown in this cutaway is the LED installed to produce pulsed light used for calibration purposes.

4.1. Neutron beam intensity maps

The radial dependence of the neutron beam intensity must be mapped to sufficient accuracy that it can be included with the magnetic field map to calculate the neutron spin flipper efficiency. We determined that an intensity map with a few mm spatial resolution over the 10 cm diameter beam would suffice to determine the spin flip efficiency with an accuracy more than one order of magnitude better than our statistical accuracy goal. This measurement was performed with a commercial imaging plate using a neutron-sensitive Gd-doped film. Its spatial resolution is one order of magnitude better than required for our purposes. Fig. 11 shows an example of such a map. The neutron imaging plate technology used to produce these intensity maps has been demonstrated to possess a linear response over a dynamic range of about 4 orders of magnitude as determined in the course of careful studies conducted at NIST for a Penning-trap-based neutron lifetime experiment [33].

5. Mechanical design of the adiabatic spin flipper and controls

The spin flipper consists of twelve axially concentric longitudinal coils of different radii and winding numbers connected in series to produce the sinusoidally varying longitudinal field along the z-axis (Eq. (3)) and one pair of axially concentric Helmholtz coils that produce the cosinusoidally varying transverse field along the y-axis (Eq. (5)). The coils were designed using COMSOL to determine the coil parameters (coil dimensions, number of turns, positions, and necessary currents) needed to produce the desired fields. In addition, one pair of 'shunt' coils was constructed, consisting of two coils identical in construction to the transverse field coils. Because of the relatively large ($\sim$ 15 A) currents needed to produce these fields and the relatively short timescales ($\sim$100 ms) needed for the transverse field on/off transitions, the shunt coils were introduced to the circuit so that instead of turning the current in the transverse coils on and off and potentially producing electronic crosstalk, the current was instead diverted to the shunt coils via a switch box module. The longitudinal and transverse coils were mounted to the frame of the apparatus and the shunt coils were placed in a corner of the experimental hutch as far away as possible from the spin-flip region of interest, approximately 3 meters from the center of the spin flipper. The field produced by the shunt coils at the center of the spin flipper was measured and determined to be negligible.

5.1. Switch box design

To control the neutron spin flip coils, we designed a switch box containing an array of FET switches with opto-isolated gate drivers controlled by TTL signals sent from an Arduino Mega 2560 board. The switch box was designed to be able to handle a maximum current of 20 A and to react quickly enough during a change of state that viable neutron pulses were not lost due to a slow slew time for the switch box. The limiting factor for the switching rate was found to be the intrinsic 120 ms settling time that it took for the currents to achieve a steady state in the coils. This characteristic time was due to the large inductance of the coils and the settling time of the eddy currents in the aluminum coil frames.

The switch box allowed complete control over the state of the spin flipper. By sending the appropriate logic signal from the Arduino board to the switch box, current to the coils could be turned on/off, reversed in polarity, or diverted to/from the shunt coils. The Arduino board was connected to the external Lujan Center t_0 signal as a trigger source, and its output 5 V logic signals were sent through a simple conditioning circuit before entering the switch box. Three LEDs were included in the conditioning circuit to visually confirm that the state of the Arduino and that the states were changing as expected (see Figs. 12 and 13).

5.2. Neutron spin flip sequencing

The choice of neutron spin flip sequencing is a critical factor in avoiding systematic errors that would create a false asymmetry and compromise the validity of this experiment. For example, the gain of the detector may drift linearly in time due to effects such as temperature-dependence of the detector electronics. Even more dangerous are gain effects that correlate directly to the absolute spin state of the neutron; stray magnetic fields produced by the spin flipper may influence the gain of the PMT dynode chain and cause the detector to have a different gain for each neutron spin state. An important feature of the spin flipper is that it works equally well for both configurations ($\pm$) of the field produced by the transverse coils. Therefore, a careful choice of the pattern with which the neutron spins are flipped can cancel systematic effects. Following the prescription by Roberson et al. [27], the base spin sequence pattern F N N F N F F N was chosen, where N and F denote the *no-flip* and *flip* states, respectively.

A discussion of how the spin state was determined during the data analysis process is discussed in Section 7.2.

Because the neutron spin flip behavior is identical for the cases where the transverse field is aligned (+) or anti-aligned (−) with the y-axis and recalling that the transverse field off (0) is the *no-flip* state, we can additionally alternate the polarity of the field used to produce the *flip* states, making our spin flip sequence + 0 0 - 0 - + 0. One can write the change in the neutron yield as a function of the stray field produced by the spin flipper, B_s, as

$$Y(B_s) = Y(B_0) + \frac{\partial Y}{\partial B} B_s + \frac{1}{2}\frac{\partial^2 Y}{\partial B^2} B_s^2 + \cdots \tag{12}$$

then the difference in the neutron yields for the *flip* and *no-flip* states, ΔY, is found to be [32]:

$$\Delta Y = \overline{Y(F)} - \overline{Y(N)} = \frac{1}{2}\frac{\partial^2 Y}{\partial B^2} B_s^2 + \cdots \tag{13}$$

We can see here that the dependence on a term linear in $\vec{B}_s$ vanishes, leaving us to only have to measure the change in the gain of the magnetic field at the detector location to estimate the quadratic term.

6. Fast-response current mode ^{6}Li glass scintillator detector

The current mode detector used in our apparatus was designed to be identical to one used by the TRIPLE Collaboration [34]. The reasons for this design choice were the similarities in neutron flux and the sensitivities achieved in the TRIPLE Collaboration's previous experiments [18,19]. The main goal of the design is to convert the neutron flux in a neutron-absorbing scintillator detector into an output current as a function of neutron time-of-flight. When the neutron rate is low, the detector can also resolve individual pulses in pulse counting mode.

6.1. Scintillator characteristics

The neutron detector shown in Fig. 1 contains a 13.3 cm diameter × 1 cm thick cylinder of Scintacor GS20 ^{6}Li loaded glass optically coupled to a photomultiplier tube (PMT). The GS20 ^{6}Li loaded glass has a density of 2.5 g/cm^3. The reaction n + ^{6}Li → ^{7}Li* → ^{4}He + ^{3}H + 4.8 MeV is used to detect neutrons. The GS20 glass is 6.6% lithium by weight, enriched to 95% ^{6}Li. The 1 cm thickness of lithium glass gives a neutron absorption efficiency of 90% for 1 eV neutrons. Due to the $1/v_n$ dependence of the n + ^{6}Li → ^{4}He + ^{3}H reaction cross section, the efficiency is lower at higher energies. The cross section of this reaction at 1 eV neutron energy is approximately 147 b [35]. The scintillation light from neutron capture in GS20 glass has a fast 18 ns component, a slower 57 ns component, and a 98 ns rise time for the signal to rise from 10% to 90% of its full value. The scintillation light produced by the energy deposited by the ^{4}He and ^{3}H ions is detected in the PMT.

An otherwise identical detector/PMT combination was constructed which uses glass depleted in ^{6}Li so that it is very insensitive to neutrons but has an almost identical response to gammas. The attenuation of gammas in the materials used in the scintillator/PMT is low enough that one can place the ^{7}Li-rich detector directly behind the ^{6}Li-rich detector to measure and subtract out the signal from the gammas in the beam if needed. Based on the high signal/background ratio of our signal at neutron time of flights corresponding to the 1 eV region, we decided not to install the ^{7}Li-rich backing detector for the double lanthanum measurements.

6.2. PMT And analog electronics

We chose a Hamamatsu R1513 PMT with a S-20 photocathode for its low photocathode resistivity and corresponding superior performance in current mode [34]. The maximum gain for this PMT is around 3.3 ×10^5. A single photoelectron pulse at the anode of the PMT has a rise-time of around 7 ns. The PMT base circuitry is shown in Fig. 14. The photocathode current was specified to output 2 μA with a full scale of 2 mA. The full scale current requires a gain of 1000 within the dynode chain. This gain was achieved with a 1050 V input. The 2 μA current enables the detector to handle an instantaneous rate of 10^{11} neutrons/s striking the detector given that there are typically 100 photoelectrons produced in the PMT when a single neutron is captured. The cathode within the PMT was grounded to ensure stable, low-noise operation of the PMT. The baseline level was designed to be 0.0 V which corresponded to 0 μA. A 2 μA current in the PMT produced an output voltage of −2.0 V. The PMT uses an active voltage divider so that the divider ratio is unaffected by load currents from the PMT. A light emitting diode was also included in the design of the PMT assembly so that testing could be performed with a internal LED. In addition to the high voltage supply needed to run the PMT, a +8V/-8V supply powers a buffering stage operational amplifier. All output signal cables are LEMO connections.

7. Data acquisition

This setup was designed to measure the total neutron transmission through matched disks of ^{139}La. Because of the high instantaneous flux rates needed for such a transmission measurement, it is not feasible to count individual neutron pulses; instead, the total integrated current output of the detector is measured. Our data acquisition system, like our detector, must be designed to handle the output signal in real time.

We used a CAEN V1724 8-channel, 14-bit digitizer with a maximum sampling rate of 100 MS/s to record the signals from the ^{3}He ion chamber, current-mode neutron detector, and 3 Faraday pickup loops (5 signals in total). The facility t_0 signal from the 20 Hz Lujan Center accelerator proton current pickup coil was used to simultaneously trigger the spin-flipper controller and the data acquisition. Upon receiving a t_0 trigger, 75000 2-byte samples were recorded for each of the 5 input voltage signals and stored in the onboard memory buffers where it was read out via an optical link to the data acquisition computer. In order to reduce the data file size, the respective waveforms were then decimated in software before being written to long-term storage. All further data manipulation and analysis was handled offline.

7.1. Signal processing

Higher-resolution spectroscopy of the 0.7 eV resonance was desired in order to increase the precision with which we could measure the Doppler-narrowed 0.7 eV resonance peak. To do so, each of the 5 signals were sampled every 10 ns by the V1724 digitizer and then decimated on-board by a factor of $2^6 = 64$. After being read out by the CAEN board to the data acquisition desktop computer, the data underwent further decimation where it was structured into 'windows,' i.e. different regions of the waveform were decimated by different factors in order to keep the data files at a reasonable size. The total data set for the Double Lanthanum experiment was ∼ 4 TB. If such a decimation scheme had not been implemented, the data set was expected to be well over 400 TB, which is unwieldy in terms of data storage and manipulation during the analysis process.

7.2. Determination of spin state

Extreme caution must be exercised when deciding how to record the spin state of the flipper in the datastream. If one chooses to measure a signal that correlates directly with the absolute spin state of the flipper (e.g. using a magnetic field probe to monitor the actual value of the $\vec{B}$ field in real time), then it is possible that nonzero false asymmetries may creep into the data via insidious means such as electronic cross-talk between channels on the data acquisition modules. Although data acquisition modules are designed to minimize cross-talk, we did not want to risk such an occurrence in a high-statistics, precision experiment. Systematic uncertainties that effectively mimic a physics asymmetry completely compromise the validity of such an experiment.

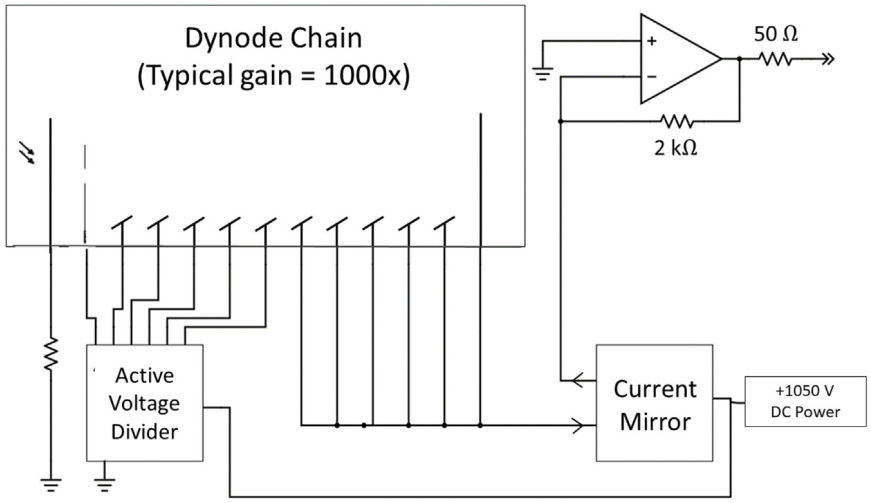


Fig. 14. A simplified schematic of the PMT assembly.

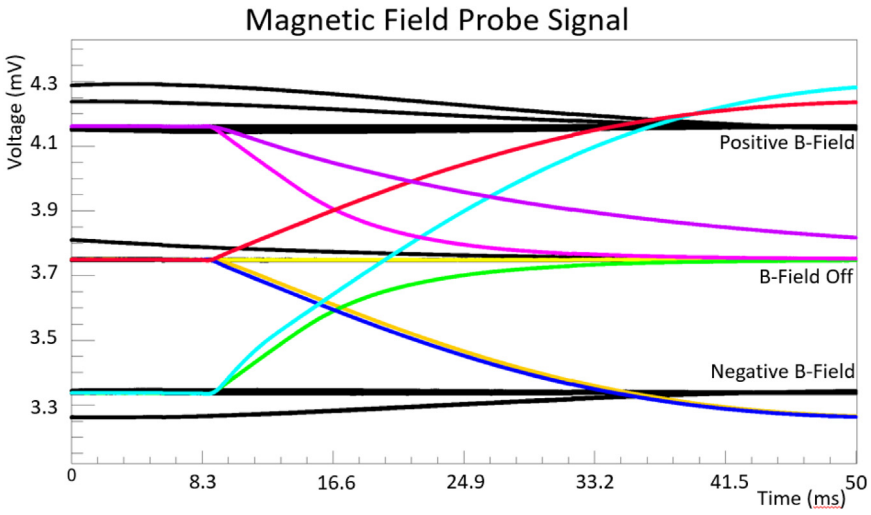


Fig. 15. This figure shows the pulses that were identified using the cuts made on the histograms of integrated voltage signals. Note all eight transitions are present, including the 'no change in state' transition, shown in yellow. (For interpretation of the references to color in this figure legend, the reader is referred to the web version of this article.)

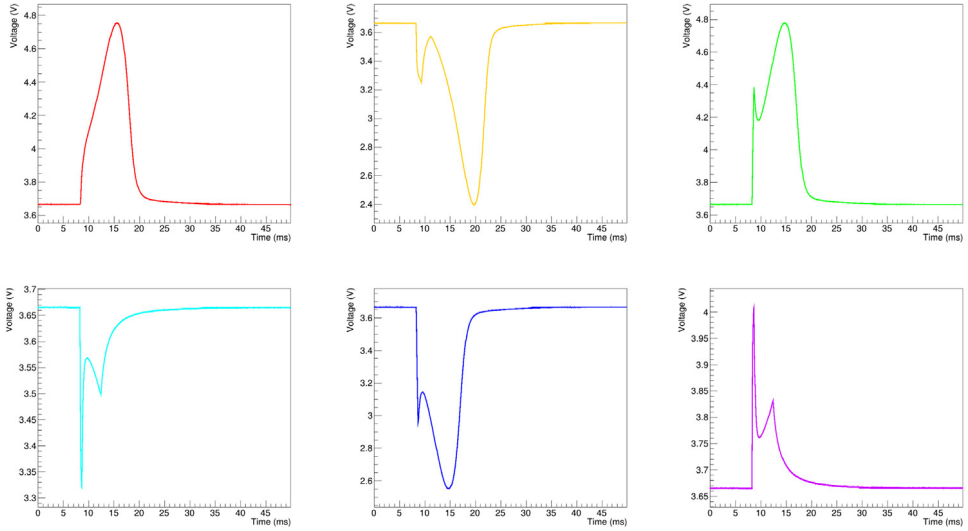


Fig. 16. Voltage signals were produced in the pickup coils by changing the currents flowing through the spin flipper coils. Here we see examples of 6 different spin state transitions.

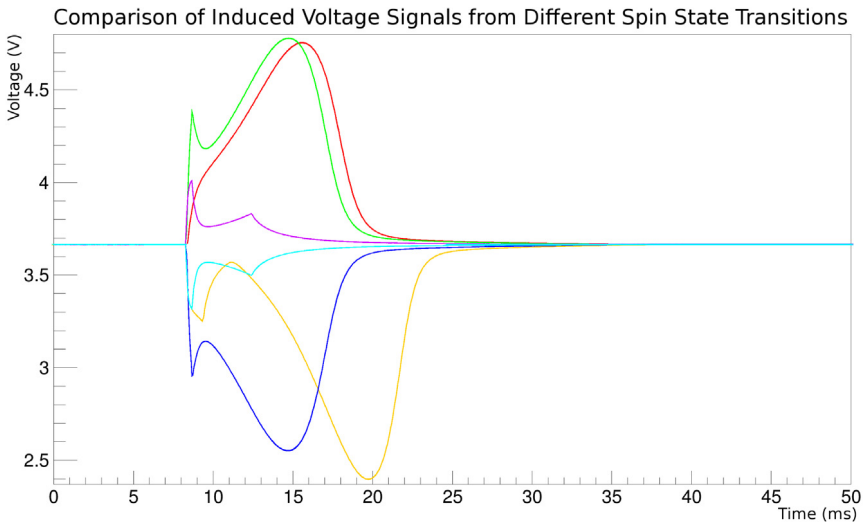


Fig. 17. Induced voltage signals for all 6 spin state transitions, superimposed to allow for comparison.

To monitor the spin flipping process, each of the three coil sets (longitudinal, transverse, and shunt) had a respective lead wire threaded through its own pickup coil. Each pickup coil consisted of a toroidal solenoid wrapped around an iron core. The ferromagnetic core ensured that maximal magnetic flux was captured. Because the state of the flipper is determined by the direction of the current through the coils, any change in current will induce a voltage in the pickup coil. We measured these induced voltages to determine spin state transitions, from which the preceding and succeeding spin states could be determined.

Because the longitudinal spin transport field is always on, our spin flipper state can be defined by the state of the transverse field coil, of which there are three: off, no transverse field (0); on, positive transverse field (+); on, negative transverse field (-). For some early test runs, a Lakeshore 460 triple axis magnetic field probe was placed at the center of the spin flipper to record the absolute state of the transverse field to be used to test our sorting algorithm (this probe was later removed so that there was no chance of interference with our dataset). Fig. 15 shows the overlaid field probe readings of a few thousand pulses. We can see that there are three stable magnetic field states, indicated by the three distinct levels in Fig. 15, as well as the transitions happening between them. We have developed a method to sort the spins by identifying the pickup coil voltage signature for each transition and used this information to tag each pulse as either *flip* or *no-flip*, described below.

Given our spin flip pattern of $(+00-0-+0)$, we can see that we should have six unique transitions between states: $(+\rightarrow 0), (0\rightarrow 0), (0\rightarrow -), (-\rightarrow 0)$, $(-\rightarrow +)$, and $(0\rightarrow +)$. Fig. 16 shows a few examples of these voltage signatures that were produced when the spin flipper transitioned states, and Fig. 17 shows these same traces superimposed on one another to show relative lineshapes and amplitudes. However, we have found that all eight transitions (the six unique transitions and the two degenerate $(0\rightarrow -)$ and $(+\rightarrow)$ transitions)

between states can be uniquely identified by the pickup loop signature–this is due to the small differences in the placement of the pickup coils in relation to the spin flipper, allowing each to capture dissimilar enough magnetic flux changes to produce distinct voltage signatures.

To sort the data pulses by spin state, each voltage signal for a given pickup coil was integrated over the 50 ms pulse to return a single value for each pulse. These values were then histogrammed and clear peaks emerged for each spin state transition. By defining the upper and lower bounds for each peak on the histogram, we were able to determine and sort each spin state by understanding which transition was happening for each pulse and tagging the preceding spin states appropriately. Fig. 18 shows a sample of some of the peaks, though it is worth noting that there were more than 8 peaks due to the summation of the pulses immediately preceding the initial transitional pulses causing small peaks very near the 'no spin state change' peak.

8. ^{3}He Spin filter apparatus and design

A polarized ^{3}He gas neutron spin-filter works by utilizing the spin dependent neutron absorption cross section of polarized ^{3}He. Neutrons with their spins parallel to that of the ^{3}He gas will be transmitted while neutrons with anti-parallel spins will be absorbed. A polarized ^{3}He neutron spin filter of sufficient thickness and ^{3}He polarization can polarize the neutron energies of interest between 0.1–10 eV with neutron polarization and transmission high enough to conduct several interesting experiments. The efficient removal of the antiparallel spins by absorption rather than scattering as in a neutron spin filter based on polarized proton scattering, combined with the spatial uniformity of the ^{3}He gas polarization in the cell, makes the polarized neutron beam phase space highly uniform, This is an advantageous property for an eventual time reversal violation experiment as it suppresses possible sources of systematic error associated with neutron small angle scattering in the polarized target. The energy-dependent neutron transmission measurements possible at a pulsed spallation neutron source like LANSCE allow the neutron beam polarization produced by such a neutron spin filter to be determined to high accuracy by comparing the relative neutron transmission intensity for the ^{3}He in the spin filter polarized versus unpolarized [36]. Polarized ^{3}He gas is produced using spin-exchange optical pumping (SEOP) [37]. SEOP refers to the process of using optical pumping to polarize rubidium vapor and allowing the spin polarization of the Rb electrons to be transferred to ^{3}He nuclei via spin exchange during gas-phase collisions. This spin-exchange is mediated by the hyperfine interaction between the Rb valence electron and the ^{3}He nucleus. Below we include a brief description of the physics behind this process and our design of the system. Extensive references to previous work on polarized ^{3}He neutron spin filters can be found in a recent review [38].

8.1. Spin exchange optical pumping (SEOP) theory

8.1.1. Rubidium optical pumping

Optical pumping describes the process by which photons are used to redistribute the occupied states of some collection of atoms. Resonant absorption of light stimulates these states out of thermodynamic equilibrium toward a single desired state. Rubidium, as an alkali metal, is

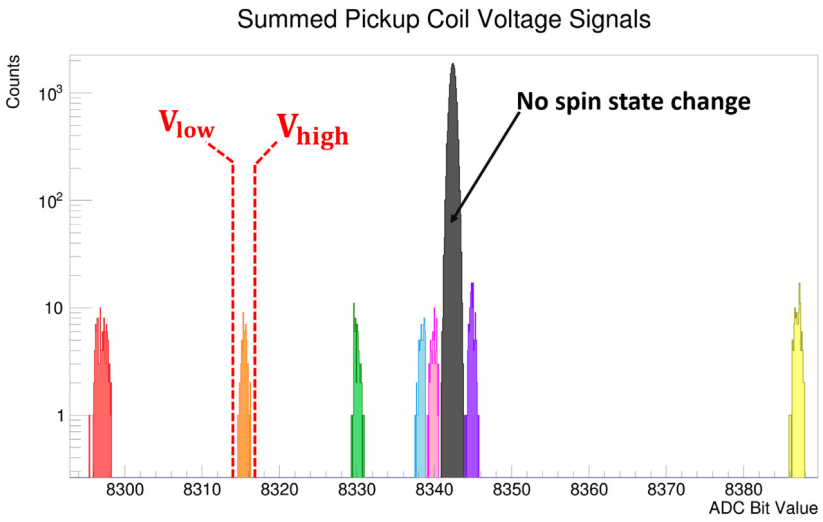


Fig. 18. A histogram showing the summation of each voltage signal produced by a spin state transition shows unique values for each of the states. These values were then used to sort pulses into their appropriate spin states.

hydrogen-like because its outermost electron is shielded by complete inner shells. The Hamiltonian for the ground state of Rb in a static magnetic field $B_0\hat{z}$ is:

$$\mathcal{H} = A_g \vec{I}\cdot\vec{S} + g_s\mu_B S_z B_0 \; - \frac{\mu_I}{I} I_z B_0 \tag{14}$$

where $\vec{I}$ is the Rb nuclear spin, $\vec{S}$ is the electron spin, A_g is the isotropic magnetic dipole coupling coefficient, g_s is the electron g-factor, μ_B is the Bohr magneton, and μ_I is the nuclear magnetic moment. The first term in the Hamiltonian is the hyperfine interaction between the nucleus and electron, while the second and third terms are the Zeeman interactions of the electron and nucleus with the external magnetic field. In the weak-field limit, the hyperfine interaction is larger than the Zeeman interaction, producing hyperfine splitting on the order of GHz and Zeeman splitting on the order of MHz. The total angular momentum of the atom is then $\vec{F} = \vec{I} + \vec{J}$ with its projection m_F onto the z-axis.

For rubidium, the ground state $^2S_{1/2}$ and excited state $^2P_{1/2}$ have an energy separation corresponding to a light wavelength of $\lambda = 794.8$ nm. These states are separated further into two F states due to hyperfine splitting. Increasing the B-field further separates the F-states into $2F+1$ subdivisions. In the ^{3}He gas cell there are two isotopes of Rubidium: ^{85}Rb with nuclear spin $I = 5/2$ and hyperfine levels $F = 3, 2$ and ^{87}Rb with nuclear spin $I = 3/2$ and hyperfine levels $F = 2, 1$. An unpolarized 794.8 nm photon will cause a $^2S_{1/2} \rightarrow {}^2P_{1/2}$ transition according to the selection rules: $\Delta F = 0, \pm 1$ and $\Delta m_F = 0, \pm 1$. However, if said photon is circularly polarized with angular momentum pointing in the direction of the static magnetic field, this further restricts the allowed transition. The new selection rules are then: $\Delta F = 0, \pm 1$ and $\Delta m_F = \pm 1$. The excited state will then spontaneously decay back into the ground state by emission of a photon with arbitrary polarization and $\Delta m_F = 0, \pm 1$ selection rules. Given sufficient time, nearly all the Rb atoms will migrate to the highest m_F value possible because there is no transition out of this state. This m_F value corresponds to a situation where the electron and nuclear magnetic moments point in the same direction as the static magnetic field. The Rb atoms are therefore polarized and in the ground state.

To improve the efficiency of this process a small amount of N_2 gas is added to the cell. When an excited Rb atom spontaneously decays the emitted photon has a random polarization and can re-excite another Rb atom. Because the photon is not circularly polarized, this allows for $\Delta m_F = 0, \pm 1$ transitions. This in turn will slow down the polarization of the Rb atoms. The N_2 in the cell circumvents this bottleneck by allowing the Rb atoms to de-excite before they spontaneously decay. This relaxation is achieved by transferring the energy to the rotational and vibrational states of the N_2 molecules. This is made possible by the large quenching cross section of 5.8×10^{-15} cm^{-2} for N_2 gas [39]. The relaxation takes place ~10 times faster than the spontaneous decay.

8.1.2. Spin-exchange

The next stage in polarization of ^{3}He is the spin-exchange between the Rb valence electron and the ^{3}He nucleus. From the perspective of the spins, the collision is dominated by two interactions:

$$V = \gamma \vec{N}\cdot\vec{S} + \alpha \vec{K}\cdot\vec{S} \tag{15}$$

The first interaction is between the Rb valence electron spin $\vec{S}$ and the rotational angular momentum $\vec{N}$ of the Rb and ^{3}He pair. The second interaction is the hyperfine coupling between the Rb valence electron spin $\vec{S}$ and the nuclear spin $\vec{K}$ of the ^{3}He atom. The constants γ and α are functions of the separation distance R and determine the interaction strength. Spin relaxation of the Rb electron is from the spin-rotation interaction while the spin-exchange is caused by the hyperfine interaction. During a collision, the spin angular momentum of the Rb electron is transferred to the ^{3}He nucleus. Because this spin exchange is a slow processes, acquiring maximally polarized ^{3}He gas takes on the order of 10 h.

8.1.3. Cell and oven

The ^{3}He gas cell, shown in Fig. 19, is 12.1 cm in diameter and 10.8 cm thick in the longitudinal direction. The cell contains ^{3}He gas at 2 bar pressure, 0.09 bar of N_2 gas, and solid Rb inside. To turn the solid Rb into a vapor, the cell needs to be heated to an ambient temperature of about 200 °C. The cell is held in place with a Teflon holder and high temperature polyimide tape. Teflon is used because of its high heat-resistant properties and flexibility. Additionally, the Teflon holder supports two coils used for free induction decay (FID) NMR. The purpose of FID NMR is to measure the ^{3}He polarization in a non-destructive way.

The oven used to heat the cell is a $26.7 \times 26.7 \times 63.5$ cm^3 rectangular box with 3 layers. The first layer is made of 1.27 cm Garolite "G7" and supports the gas cell and adiabatic fast passage (AFP) NMR coil. The AFP NMR coil is used to flip the ^{3}He polarization direction. The second layer is made of aluminum and holds six 7.6 cm electrical heating cartridges (Omega: CSH 103220). The third layer is also made of 1.9 cm G7, supports the first two layers and provides insulation. The end caps, also made of 1.27 cm G7, hold sapphire glass windows. G7 is a glass-silicon laminate, has a density of 4.57 g/cm^3, tensile strength of 20,000 PSI, and a maximum continuous operating temperature of



Fig. 19. ^{3}He gas cell in its Teflon holder.

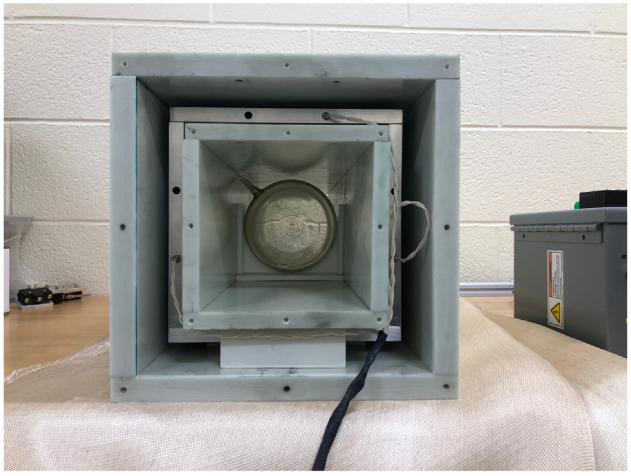


Fig. 20. Picture of oven with ^{3}He gas cell and cartridges heaters installed.

221 °C. These properties make it especially appropriate as a support and as an insulator for an oven with a target temperature of 200 °C. The purpose of the aluminum layer is to better distribute the heat created by the cartridge heaters. The outermost layer is supported by an adjustable support to better align the ^{3}He gas cell to the neutron beam. Almost all oven components are made with non-magnetic material such as aluminum and brass. Fig. 20 shows the ^{3}He cell situated inside of the oven.

8.1.4. Laser optics

To excite the Rb atoms, a 50 W fiber-coupled 795 nm laser is used. Circularly polarized light is created by passing linearly polarized light through a quarter wave plate at a 45° angle. First, the laser fiber is coupled to a beam collimator (ThorLabs: F220SMA-780) that focuses and reduces the spread of the beam. The laser is then incident on a polarizing cube beam-splitter (Edmund Optics: 49-872) that linearly polarizes and splits the beam 90° into two paths. Both paths are then incident on a 2.54 cm diameter, 795 nm quarter wave plate (QWP). Each QWP is mounted on a precision motorized rotation device (ThorLabs: K10CR1). These devices allow for remote flipping of the direction of circular polarization by rotating the QWPs by 90°. One path is then reflected by 90° using a 50 mm diameter dielectric mirror (Edmund Optics: 33-189). Finally, both paths are reflected in the oven with large 8 inch diameter dielectric coated silicon mirrors. The mirrors reflect the laser light, but are nearly transparent to neutrons. The laser light then passes through the sapphire glass windows and into the ^{3}He gas cell. Fig. 21 shows a schematic of the optical layout. All optical components and oven are mounted on to a 48.2 × 119.3 × 1.27 cm (19 × 47 × 0.5 inch) optical breadboard. Additionally, the breadboard and optics are enclosed in a black-anodized light tight box, shown in Fig. 22. All optical components are made as non-magnetic as possible by using brass and aluminum parts.

8.1.5. μ-Metal solenoid and support

A μ-metal shielded solenoid provides the uniform magnetic field required for the SEOP process. The μ-metal shielded solenoid is approximately 61 cm × 61 cm × 122 cm in size. The internal structure of the μ-metal shield is made of an 8020 frame of 2.5 cm ×2.5 cm profiles. The light tight box (with the optical components and oven mounted to the optical bread board) slides into the μ-metal shield on a Teflon sheet. Fig. 23 shows the shieldhouse that surrounds the solenoid, light tight box, and oven assembly. The μ-metal shield is critical due to the ^{3}He spin-filter's close proximity to the adiabatic spin-flipper. Because a very small magnetic field gradient is needed over the length of the ^{3}He gas cell, it is crucial to shield it from external magnetic fields; μ-metal works well as a magnetic shield due to its high magnetic permeability. Stray, slowly-varying magnetic fields are distributed around the shielding and away from the center where the ^{3}He cell is located. The solenoid enclosed in the μ-metal shield produces a magnetic field along the neutron beam direction that holds the polarization of ^{3}He atoms. In the central 7 cm × 16 cm region where the ^{3}He cell is located, the magnetic field has an average gradient $\langle \frac{\nabla B_x}{B_i} \rangle = 5.55\times10^{-4}\pm2.66\times10^{-4}$ cm^{-1} along the longitudinal polarization direction, and an average gradient $\langle \frac{\nabla B_y}{B_i} \rangle = 6.03 \times 10^{-4} \pm 1.68 \times 10^{-4}$ cm^{-1} in the transverse direction. Based on these measurements, the expected relaxation time of the ^{3}He is $100 - 200$ hours. The solenoid has a resistance of $R = 25.8\ \Omega$, and is driven at 1.00 A with a current stability of 0.1%. At this current, the solenoid produces a holding field of 9.26 gauss at its center which, along with an 30 kHz NMR pickup coil, is tuned to the 3.24 kHz/gauss gyromagnetic ratio of ^{3} He [40]. The NMR signal is then used to determine the polarization of the ^{3}He gas.

Due to the modular nature of the apparatus, this polarized ^{3}He neutron spin filter can be installed at the location of the first cryostat (upon removal of the cryostat from the apparatus). It can then be operated continuously on-line during measurements, as was successfully done several years ago using a similar apparatus [41] for the first phase of the NPDGamma neutron–proton weak interaction experiment [42].

9. Summary and outlook

We have described a flexible, rotatable cryogenic apparatus for the measurement of parity violation in the transmission of longitudinally polarized neutrons in neutron–nucleus resonances in the 0.1–10 eV energy range at a short-pulsed spallation neutron source. The apparatus employs beam monitors and transmission detectors combining both (n, γ) discrimination and current mode operation, a broadband neutron spin flipper with a flipping mode and sequence designed to suppress systematic errors, and a neutron polarizer based on spin-exchange optical pumping of ^{3}He. The apparatus design employs several features used in previous neutron parity violation experiments at LANSCE, especially from work performed by the TRIPLE and NPDGamma collaborations and referred to in the text.

The apparatus that we have described also possesses sufficient flexibility to accommodate several modifications that can greatly extend the range of possible experiments beyond the Double Lanthanum experiment that we concentrated on as an example in this paper. The first major addition to the apparatus we envision for the measurement of P-odd transmission asymmetries in other nuclei beyond ^{139}La is the addition of the polarized ^{3}He neutron spin filter based on spin-exchange optical pumping (described in Section 8) and which was first

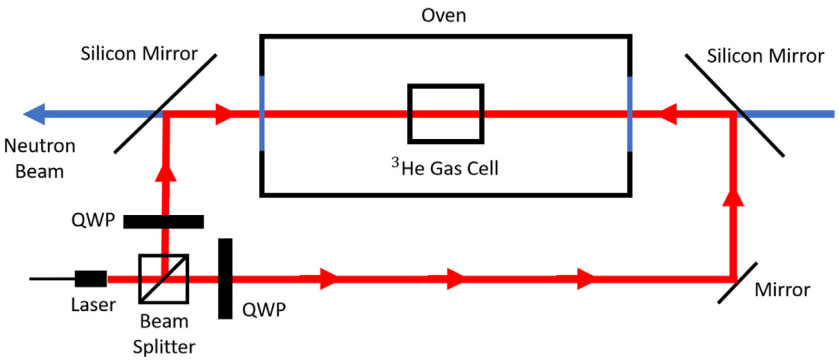


Fig. 21. Diagram showing the optics layout for creating circularly polarized light.

demonstrated at LANSCE [17]. The experimental hutch on the FP12 beamline possesses an access path through the ceiling near the present location of the downstream refrigerator that we plan to use for the operation of cryostats, which require safe venting of cryogenic liquids into a storage volume on top of the hutch, as done in the past for liquid parahydrogen targets operated on FP12 [43,44]. In particular, this implementation would allow us to conduct a new measurement of the parity-odd asymmetry in the 3.2 eV p-wave resonance in ^{131}Xe, which is one of the leading candidates for a sensitive time reversal test, using a solid xenon target. Liquid helium supply and venting for the dilution refrigerator required for the polarized nuclear targets to be used in the time reversal test can also be provided through this path.

Much care was taken in designing this apparatus to minimize any systematic effects that would affect the uncertainty associated with the P-violation measurements. Because this apparatus was designed to be modified to accommodate several nuclear species, each measurement will have its own associated systematic effects. The most dominant systematic effect associated with the design of the apparatus itself lies in how well one can determine the neutron spin flip efficiency. In this paper, we present a method to calculate this efficiency using flux monitor measurements of the beam intensity convoluted with the image plate beam profiles and measurements of the B-field combined with a Monte Carlo calculation of the neutron intensity-weighted spin flip efficiency integrated over the beam cross sectional area. In this case, the dominant uncertainty will lie in how well one can reconstruct the B-field produced by the spin flipper coils, i.e. the spatial resolution of the B-field maps, which is on the order of a few parts in 10^3. If this accuracy does not suffice one can install a ^{3}He polarizer/ analyzer pair and measure the neutron spin flip efficiency directly using the method described by Musgrave et al. in [36].

The beamline components can be translated upstream far enough to accept gamma detector arrays downstream of the target to conduct parity violation measurements using (n, γ) reactions [45] as well as in neutron transmission measurements. The addition of a gamma detector array to this apparatus would enable one to efficiently search for large P-odd asymmetries between 0.1–10 eV in the several isotopes of heavy nuclei which have never been measured. The TRIPLE collaboration concentrated its choice of nuclei for measurement near the peaks of the 3p and 4p p-wave strength functions in an attempt to maximize the number of p-wave resonance per unit energy interval in the isolated resonance eV-keV regime for their statistical analysis of parity violation in heavy nuclei. Since that work was conducted, improved data on the p-wave strength function [46] has resolved an additional small peak near A=160, which is split off from the 4p giant resonance due to nuclear deformation effects as predicted long ago [47], whereas the spherical optical model by contrast predicts a minimum at A=160. It therefore may be worthwhile to search in this A range to see if one can discover more p-wave resonances that amplify parity violation. One could also search for large parity-odd effects in the (n, γ) channel for nuclei that undergo neutron-induced fission and try to confirm

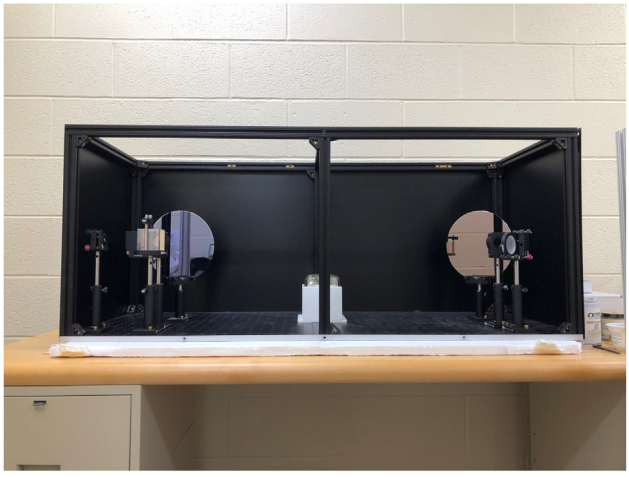


Fig. 22. Picture of optics setup in black-anodized light tight box.

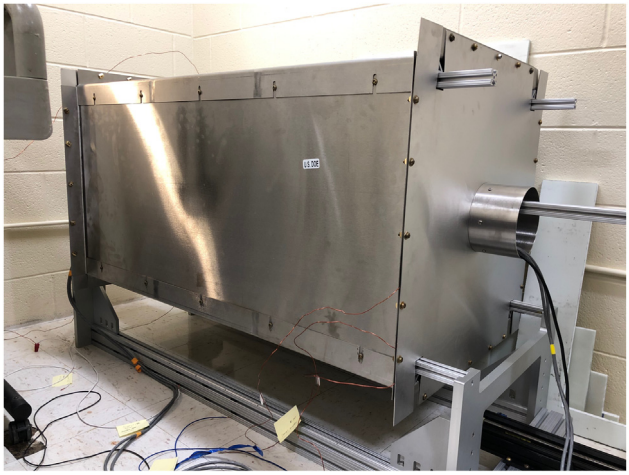


Fig. 23. Picture of μ-metal shielded solenoid.

and extend the many large P-odd asymmetries already measured in the fission channel [4,48–58]. In particular one could measure the P-odd asymmetries in the (n, γ) channel in very low energy resonances in ^{235}U [59,60], which is a nucleus that can be safely handled and supplied at the LANSCE facility. There is an already-proven method for nuclear polarization of ^{235}U using the very large hyperfine fields produced at the nucleus in the low-temperature ferromagnetic phase of uranium sulfide. This phenomenon was exploited in the past to determine the spin assignments in ^{235}U using spin-dependent polarized

neutron transmission through polarized ^{235}U [61]. The nonmagnetic composition of the apparatus also lends itself to the use of polarized xenon targets produced by a spin-exchange optical pumping process very similar to that described above for ^{3}He. The 10 cm x 10 cm cross section, m=3 supermirror neutron guide presently installed upstream of the LANSCE FP12 hutch [24] could be replaced in the future with other types of neutron guides that can increase the fraction of neutrons transmitted to the apparatus near 1 eV. The dimensions of the FP12 hutch transverse to the neutron beam direction are wide enough to allow for the complete rotation of the relevant components of the apparatus by 180 degrees as envisioned in one of the modes of realization for a precision test of time reversal invariance [9]. According to the results of MCNP simulations of the new configuration of the LANSCE target/moderator/reflector system scheduled to be installed in early 2020 [62] we do not expect the projected changes, including the removal of the liquid hydrogen slow neutron moderator, to significantly influence the beam characteristics in our energy range of interest between 1–10 eV and therefore the performance of the components of the apparatus presented above should remain essentially unchanged after this upgrade.

Declaration of competing interest

The authors declare that they have no known competing financial interests or personal relationships that could have appeared to influence the work reported in this paper.

CRediT authorship contribution statement

D.C. Schaper: Methodology, Software, Formal analysis, Investigation, Data curation, Writing - original draft, Writing - review & editing, Visualization, Supervision, Project administration, Funding acquisition. **C. Auton:** Methodology, Investigation, Writing - original draft, Visualization. **L. Barrón-Palos:** Conceptualization, Methodology, Software, Formal analysis, Writing - original draft, Visualization, Supervision, Project administration, Funding acquisition. **M. Borrego:** Resources. **A. Chavez:** Resources. **L. Cole:** Investigation. **C.B. Crawford:** Conceptualization, Methodology, Software, Formal analysis, Investigation, Writing - review & editing, Supervision, Funding acquisition. **J. Curole:** Software, Investigation. **H. Dhahri:** Investigation. **K.A. Dickerson:** Investigation. **J. Doskow:** Resources, Visualization. **W. Fox:** Resources, Visualization. **M.H. Gervais:** Investigation. **B.M. Goodson:** Conceptualization, Investigation, Writing - review & editing, Funding acquisition. **K. Knickerbocker:** Resources. **C. Jiang:** Resources, Methodology, Conceptualization. **P.M. King:** Conceptualization, Investigation, Writing - review & editing. **H. Lu:** Investigation. **M. Mocko:** Formal analysis, Resources, Writing - original draft. **D. Olivera-Velarde:** Investigation, Writing - review & editing, Formal analysis. **J.G. Otero Munoz:** Investigation. **S.I. Penttilä:** Conceptualization, Methodology, Investigation, Writing - review & editing. **A. Pérez-Martín:** Software, Formal analysis. **B. Short:** Software, Formal analysis, Investigation. **W.M. Snow:** Conceptualization, Methodology, Formal analysis, Investigation, Resources, Writing - original draft, Writing - review & editing, Supervision, Project administration, Funding acquisition. **K. Steffen:** Software, Investigation. **J. Vanderwerp:** Conceptualization, Methodology, Investigation. **G. Visser:** Conceptualization, Methodology, Software, Formal analysis, Investigation, Resources, Writing - review & editing.

Acknowledgments

This material is based upon work supported by the U.S. Department of Energy, Office of Science, Office of Nuclear Physics, under Award Number DE-SC-0014622. D. Schaper would also like to acknowledge support by the National Science Foundation Graduate Research Fellowship Program, USA under Grant Number 1247392. The work of C. Auton, J. Curole, J. Doskow, W. Fox, H. Lu, W. M. Snow. K. Steffen, J Vanderwerp, B. Short, and G. Visser was supported by NSF, USA PHY-1614545, NSF, USA PHY-1913789, and the Indiana University Center for Spacetime Symmetries. J. Curole also acknowledges support from the GAANN fellowship program of the US Department of Education and the Department of Energy SCGSR program, USA. L. Cole and D. Olivera would like to acknowledge funding from the KY-NSF EPSCoR Research Scholar Program. B.M. Goodson acknowledges funding from NSF, USA (CHE-1905341), DoD, USA (W81XWH-15-1-0272), and a Cottrell SEED Award from the Research Corporation for Science Advancement. We gratefully acknowledge the local support of the LANSCE neutron facility at Los Alamos National Lab where this measurement was performed. Test measurements for the current mode detector electronics used for this work were conducted in part on the NOBORU instrument at the JPARC MLF through proposal 2016B0021, Characterization of High Counting Rate Epithermal Neutron Detectors

References

[1] G.E. Mitchell, J.D. Bowman, H.A. Weidenmuller, Rev. Modern Phys. 71 (1999) 445.
[2] G.E. Mitchell, J.D. Bowman, S.I. Penttilä, E.I. Sharapov, Phys. Rep. 354 (2001) 157.
[3] O.P. Sushkov, V.V. Flambaum, JETP Lett. 32 (1980) 352.
[4] O.P. Sushkov, V.V. Flambaum, Sov. Phys. Usp. 25 (1982) 1.
[5] V.P. Alfimenkov, S.B. Borzakov, V. Van Tkhuan, Yu.D. Mareev, L.B. Pikelner, A.S. Khrykin, E.I. Sharapov, Nuclear Phys. A 398 (1983) 93.
[6] V.P. Alfimenkov, S.B. Borzakov, V. Van Tkhuan, Yu.D. Mareev, L.B. Pikel'ner, I.M. Frank, A.S. Khrykin, E.I. Sharapov, JETP Lett. 39 (1984) 416.
[7] S. Tomsovic, M.B. Johnson, A. Hayes, J.D. Bowman, Phys. Rev. C 62 (2000) 054607.
[8] P. Fadeev, V.V. Flambaum, Phys. Rev. C 100 (2019) 015504.
[9] J.D. Bowman, V. Gudkov, Phys. Rev. C 90 (2014) 065503.
[10] T. Okudaira, S. Takada, K. Hirota, A. Kimura, M. Kitaguchi, J. Koga, K. Nagamoto, T. Nakao, A. Okada, K. Sakai, H.M. Shimizu, T. Yamamoto, T. Yoshioka, Phys. Rev. C 97 (2018) 034622.
[11] H.M. Shimizu, T. Adachi, L. Ishimoto, A. Masaike, Y. Masuda, K. Morimoto, Nuclear Phys. A 552 (1993) 293.
[12] C.M. Frankle, et al., Phys. Rev. C 46 (1992) 1542.
[13] J.J. Szymanski, W.M. Snow, J.D. Bowman, B. Cain, B.E. Crawford, P.P.J. Delheij, R.D. Hartman, T. Haseyama, C.D. Keith, J.N. Knudson, A. Komives, M. Leuschner, L.Y. Lowie, A. Masaike, Y. Matsuda, G.E. Mitchell, S.I. Penttilä, H. Postma, D. Rich, N.R. Roberson, S.J. Seestrom, E.I. Sharapov, S.L. Stephenson, Y.F. Yen, V.W. Yuan, Phys. Rev. C 53 (1996) R2576.
[14] V.R. Skoy, et al., Phys. Rev. C 53 (1996) R2573.
[15] W.G. Williams, Polarized Neutrons, Clarendon Press, Oxford, 1988.
[16] V.I. Lushchikov, Yu.V. Taran, F.L. Shapiro, Sov. J. Nucl. Phys. 10 (1970) 669.
[17] K.P. Coulter, et al., Nucl. Instrum. Methods A 288 (1990) 463.
[18] C.D. Bowman, J.D. Bowman, V.W. Yuan, Phys. Rev. C 39 (1989) 1721.
[19] V.W. Yuan, et al., Phys. Rev. C 44 (1991) 5.
[20] V.P. Alfimenkov, A.N. Chernikov, L. Lason, Yu.D. Mareev, V.V. Novitsky, L.B. Pikelner, V.R. Skoy, M.I. Tsulaya, C.R. Gould, D.G. Haase, N.R. Roberson, in: J.L. Duggan, I.L. Morgan (Eds.), Application of Accelerators in Research and Industry, vol. 345, AIP Proceedings, 1997.
[21] V.P. Alfimenkov, A.N. Chernikov, L. Lason, Yu.D. Mareev, V.V. Novitsky, L.B. Pikelner, V.R. Skoy, M.I. Tsulaya, C.R. Gould, D.G. Haase, N.R. Roberson, J. Appl. Phys. 81 (1997) 1358.
[22] V.P. Alfimenkov, Yu.D. Mareev, V.V. Novitsky, L.B. Pikelner, V.R. Skoy, C.R. Gould, D.G. Haase, N.R. Roberson, X, Nucl. Instrum. Methods A 352 (1995) 592.
[23] P.E. Koehler, 1L Mark-IV Target Design Review, Los Alamos National Laboratory Technical Report, 2017, http://dx.doi.org/10.2172/1409747.
[24] P.-N. Seo, J.D. Bowman, M. Gericke, G. Greene, J. Long, G.S. Mitchell, S.I. Penttilä, W.S. Wilburn, Nucl. Instrum. Methods A 517 (2004) 285.
[25] M. Mocko, G. Muhrer, T. Ino, M. Ooi, L.L. Daemen, Y. Kiyanagi, Nucl. Instrum. Methods A 594 (2008) 373.
[26] D.B. Pelowitz (Ed.), MCNPX User's Manual, la-CP-07-1473.
[27] N.R. Roberson, et al., Nucl. Instrum. Methods A 326 (1993) 549.
[28] V.P. Álfimenkov, Yu.D. Mareev, L.B. Pikelner, V.R. Skoy, V.N. Shvetsov, Sov. J. Nucl. Phys. 54 (1991) 9071.
[29] C.D. Keith, Z. Chowdhuri, D.R. Rich, W.M. Snow, J.D. Bowman, S.I. Penttilä, E.I. Sharapov, D.A. Smith, M.B. Leuschner, V.R. Pomeroy, G.L. Jones, Phys. Rev. C 69 (2004) 034005.
[30] J.J. Szymanski, et al., Nucl. Instrum. Methods A 340 (1994) 564.
[31] W.H. Kraan, Instrumentation to Handle Thermal Polarized Neutron Beams (Ph.D thesis), Delft University, Deutschland, 2004.

[32] J.D. Bowman, S.I. Penttilä, W.B. Tippens, Nucl. Instrum. Methods A 369 (1995) 195.
[33] J.S. Nico, M.S. Dewey, D.M. Gilliam, F.E. Wietfeldt, X. Fei, W.M. Snow, G.L. Greene, J. Pauwels, R. Eykens, A. Lamberty, J. Van Gestel, R.D. Scott, Phys. Rev. C 71 (2005) 055502.
[34] J.D. Bowman, J.J. Szymanski, V.W. Yuan, C.D. Bowman, A. Silverman, C. Zhu, et al., Nucl. Instrum. Methods A 297 (1990) 183.
[35] J.A. Harvey, N.W. Hill, Nucl. Instrum. Methods 162 (1979) 507.
[36] M.M. Musgrave, et al., Nucl. Instrum. Methods A 895 (2018) 19.
[37] T.G. Walker, W. Happer, Rev. Modern Phys. 69 (1997) 629.
[38] T.R. Gentile, P.J. Nacher, B. Saam, T.G. Walker, Rev. Modern Phys. 89 (2017) 045004.
[39] E.S. Hrycyshyn, L. Krause, Can. J. Phys. 48 (1970) 2761.
[40] J.L. Flowers, et al., Metrologia 30 (1993) 75.
[41] T.E. Chupp, K.P. Coulter, M. Kandes, M. Sarma, T.B. Smith, G.L. Jones, W.C. Chen, T.R. Gentile, D.R. Rich, B. Lauss, M.T. Gericke, R.C. Gillis, S.A. Page, J.D. Bowman, S.I. Penttilä, W.S. Wilburn, M. Dabaghyan, R.W. Hersman, M. Mason, Nucl. Instrum. Methods A 574 (2007) 500.
[42] M.T. Gericke, R. Alarcon, S. Balascuta, L. Barron-Palos, C. Blessinger, J.D. Bowman, R.D. Carlini, W. Chen, T.E. Chupp, C. Crawford, S. Covrig, M. Dabaghyan, N. Fomin, S.J. Freedman, T.R. Gentile, R.C. Gillis, G.L. Greene, F.W. Hersman, T. Ino, G.L. Jones, B. Lauss, M. Leuschner, W.R. Lozowski, R. Mahurin, Y. Masuda, J. Mei, G.S. Mitchell, S. Muto, H. Nann, S.A. Page, S.I. Penttilä, W.D. Ramsay, A. Salas-Bacci, S. Santra, M. Sharma, P.-N. Seo, E.I. Sharapov, T.B. Smith, W.M. Snow, W.S. Wilburn, V. Yuan, Phys. Rev. C 83 (2011) 015505.
[43] S. Santra, L. Barron-Palos, J.D. Bowman, R.D. Carlini, T.E. Chupp, K.P. Coulter, C. Crawford, M. Dabaghyan, M. Dawkins, S.J. Freedman, T. Gentile, M.T. Gericke, R.C. Gillis, G.L. Greene, F.W. Hersman, G.L. Jones, M. Kandes, B. Lauss, M.B. Leuschner, R. Mahurin, M. Mason, J. Mei, G.S. Mitchell, H. Nann, S.A. Page, S.I. Penttilä, W.D. Ramsay, A. Salas Bacci, P.-N. Seo, E. Sharapov, M. Sharma, T.B. Smith, W.M. Snow, W.S. Wilburn, H. Zhu, Nucl. Instrum. Methods A 620 (2010) 421.
[44] L. Barron-Palos, R. Alarcon, S. Balascuta, C. Blessinger, J.D. Bowman, T.E. Chupp, S. Covrig, C. Crawford, M. Dabaghyan, M. Dawkins, W. Fox, M.T. Gericke, R.C. Gillis, B. Lauss, M.B. Leuschner, B. Lozowski, R. Mahurin, M. Mason, J. Mei, H. Nann, S.I. Penttilä, W.D. Ramsay, A. Salas Bacci, P.-N. Seo, M. Sharma, W.M. Snow, W.S. Wilburn, V. Yuan, Nucl. Instrum. Methods A 659 (2011) 579.
[45] S.J. Seestrom, C.M. Frankle, J.D. Bowman, B.C. Crawford, T. Haseyama, A. Masaike, A. Matsuda, S.I. Penttilä, R.N. Roberson, E.I. Sharapov, S.L. Stephenson, Nucl. Instrum. Methods A 433 (1999) 603.
[46] S.F. Mughabghab, Atlas of Neutron Resonances: Resonance Properties and Thermal Cross Sections Z=1-60, vol. 1, sixth ed., Elsevier, Amsterdam, 2018.
[47] B. Buck, F. Perey, Phys. Rev. Lett. 8 (1962) 444.
[48] A.K. Petukhov, et al., JETP Lett. 30 (1979) 4951.
[49] N.V. Borovikova, et al., JETP Lett. 30 (1979) 495.
[50] N.V. Borovikova, et al., JETP Lett 31 (1980) 6631.
[51] A.K. Petukhov, et al., JETP Lett. 32 (1980) 41.
[52] G.V. Danilian, Sov. Phys. Usp. 23 (1980) 3231.
[53] V.E. Bunakov, V.P. Gudkov, Nuclear Phys. A 401 (1983) 93.
[54] A.Ya. Alexandrovich, et al., Sov. J. Nuct. Phys. 39 (1984) 5091.
[55] A.Ya. Alexandrovich, et al., J. Phys. Colloq. C 3 45 (1984) 84.
[56] A.Ya. Alexandrovich, et al., Sov. J. Nucl. Phys. 45 (1987) 772.
[57] G.A. Petrov, G.V. Valskii, A. K.Petukhov, A.Y. Alexandrovich, Y.S. Pleva, V.E. Sokolov, A.B. Laptev, O.A. Scherbakov, Nuclear Phys. A 502 (1989) 297.
[58] A.Y. Alexandrovich, A.M. Gagarski, I.A. Krasnoschekova, G.A. Petrov, V.I. Petrova, A.K. Petukhov, Yu. S. Pleva, P. Geltenbort, J. Last, K. Schreckenbach, Nuclear Phys. A 567 (1994) 541.
[59] V.P. Alfimenkov, et al., Nuclear Phys. A 645 (1999) 31.
[60] V.P. Alfimenkov, et al., Phys. At. Nucl. 63 (2000) 539.
[61] M.S. Moore, J.D. Moses, G.A. Keyworth, J.W.T. Dabbs, N.W. Hill, Phys. Rev. C 18 (1978) 1328.
[62] L. Zavorka, M. Mocko, P.E. Koehler, Nucl. Instrum. Methods A 901 (2018) 189.

Check for updates

View Article Online
View Journal

ChemComm
Chemical Communications

Accepted Manuscript

This article can be cited before page numbers have been issued, to do this please use: J. Colell, A. W. J. Logan, Z. Zhou, J. R. Lindale, R. Laasner, R. Shchepin, E. Chekmenev, V. Blum, W. S. Warren, S. J. Malcolmson and T. Theis, *Chem. Commun.*, 2020, DOI: 10.1039/D0CC01330G.



This is an Accepted Manuscript, which has been through the Royal Society of Chemistry peer review process and has been accepted for publication.

Accepted Manuscripts are published online shortly after acceptance, before technical editing, formatting and proof reading. Using this free service, authors can make their results available to the community, in citable form, before we publish the edited article. We will replace this Accepted Manuscript with the edited and formatted Advance Article as soon as it is available.

You can find more information about Accepted Manuscripts in the Information for Authors.

Please note that technical editing may introduce minor changes to the text and/or graphics, which may alter content. The journal's standard Terms & Conditions and the Ethical guidelines still apply. In no event shall the Royal Society of Chemistry be held responsible for any errors or omissions in this Accepted Manuscript or any consequences arising from the use of any information it contains.

ROYAL SOCIETY OF CHEMISTRY

rsc.li/chemcomm

Please do not adjust margins

ROYAL SOCIETY OF CHEMISTRY View Article Online
DOI: 10.1039/D0CC01330G

Journal Name

ARTICLE

Rational ligand choice extends the SABRE substrate scope

Johannes F. P. Colell[a‡], Angus W. J. Logan[a‡], Zijian Zhou[a], Jacob R. Lindale[a], Raul Laasner[b], Roman V. Shchepin[c], Eduard Y. Chekmenev[d,e], Volker Blum[a,b], Warren S. Warren[a,f]*, Steven J. Malcolmson[a]* and Thomas Theis[a,g,h]*

Received 00th January 20xx,
Accepted 00th January 20xx

DOI: 10.1039/x0xx00000x

www.rsc.org/

Signal Amplification By Reversible Exchange (SABRE) is a particularly simple hyperpolarisation approach. However, compared to other hyperpolarisation methods, SABRE is more limited in substrate scope. Therefore, it is critical to understand and overcome the factors limiting generalization. Past developments in SABRE catalyst optimization have emphasized large enhancements in the canonical SABRE substrate: pyridine and structurally closely related motifs. However, the pyridine-optimized catalysts are not efficient at hyperpolarising more sterically demanding substrates, including 2-substituted pyridine derivatives. Here we report that modifications of the catalyst ligand sphere, using a chelating ligand in particular, can increase the volume fraction available for substrate coordination to the iridium catalyst, thus permitting significant signal enhancements on otherwise sterically hindered substrates. The system yields ^{1}H enhancements on the order of 100-fold over 8.5 T thermal measurements for 2-substituted pyridine derivatives, and smaller, yet significant ^{1}H enhancement for provitamin B_6 and caffeine. For the 2-substituted pyridine derivatives we further show ^{15}N enhancements on the order of 1000-fold and ^{19}F enhancements of 30-fold over 8.5 T thermal polarisations.

Introduction

Signal Amplification By Reversible Exchange (SABRE) is a relatively recent discovery among hyperpolarisation methods (2009).[1-5] Hyperpolarisation is transferred from *para*-hydrogen (*p*-H_2) to nuclei in a substrate molecule through *J*-coupling interactions mediated by the metal centre of a polarisation transfer catalyst. Both parahydrogen and substrate are in reversible exchange on the catalyst and polarisation flows from parahydrogen derived hydrides[6] to ligated substrates during the lifetime of the complex. [1, 7]

SABRE is an attractive hyperpolarisation technique because it allows for efficient polarisation of ^{1}H and ^{15}N spins within about one minute.[8-10] The technique uses simple and low-cost hardware and has been expanded to a wide range of other spin-1/2 nuclei including ^{13}C, ^{19}F, ^{31}P, and others[5, 11-16] Moreover, heterogeneous SABRE and SABRE in aqueous medium have been demonstrated.[17-27] All-in-all, this technique has made large advances for preparation of hyperpolarised substances, and has demonstrated the potential to generate injectable hyperpolarised contrast agents for *in vivo* magnetic resonance spectroscopic imaging.[28-32,33]

In this paper, we capitalize on the simple insight that steric considerations are of essence and can make a drastic difference in SABRE efficiency. Particularly, substrate size and binding pocket must be well matched. Guided by this insight, we introduce a hyperpolarisation catalyst able to hyperpolarise larger, sterically hindered substrates, primarily 2-substituted pyridines, that are not efficiently hyperpolarised with current widely used catalysts.[10, 34] Moreover, we demonstrate hyperpolarisation of provitamin B_6 and caffeine, which bear substituents in the ortho position to the N-heteroatom as well.

Historically, SABRE was discovered with Crabtree's catalyst [Ir(PR_3)(pyr)(COD)]PF_6 (**1**) (R = cyclohexyl, pyr = pyridine, COD = 1,5-cyclooctadiene) (**see Figure 1**)[1]. Initially, ^{1}H signal amplifications over thermal signals (enhancements) were found to scale favourably with electron density and steric bulk of the phosphine ligand[2], but phosphine ligands were quickly replaced by N-heterocyclic carbenes (NHCs), most importantly, IMes[35] **(2)** and **(2a) (Figs. 1 and 2,** IMes = 1,3-bis(2,4,6-trimethylphenyl)imidazole-2-ylidene)**),** giving rise to a drastic increase of enhancements.[35-37]

[a] Department of Chemistry, Duke University, Durham, NC 27708, USA.
[b] Department of Mechanical Engineering and Materials Science, Duke University, Durham, NC 27708, USA.
[c] Department of Chemistry, Biology, and Health Sciences, South Dakota School of Mines and Technology, Rapid City, South Dakota 57701, USA
[d] Russian Academy of Sciences, Leninskiy Prospekt 14, 119991 Moscow, Russia.
[e] Department of Chemistry, Integrative Biosciences (IBio), Karmanos Cancer Institute (KCI), Wayne State University, Detroit, MI 48202, USA.
[f] Departments of Physics, Radiology and Biomedical Engineering, Duke University, Durham, NC 27707, USA.
[g] Department of Chemistry, North Carolina State University, Raleigh, NC 27695
[h] Joint Department of Biomedical Engineering University of North Carolina at Chapel Hill and North Carolina State University, Chapel Hill, NC, USA
‡ These authors contributed equally.
Corresponding Authors
Steven J. Malcolmson, steven.malcolmson@duke.edu
Warren Warren, warren.warren@duke.edu
Thomas Theis, ttheis@ncsu.edu
Electronic Supplementary Information (ESI) available: Synthesis of the catalyst, detailed DFT calculations, spectral data, magnetic evolution field dependence, and description of experimental details. See DOI: 10.1039/x0xx00000x

Published on 13 April 2020. Downloaded by North Carolina State University on 4/13/2020 9:37:46 PM.

ChemComm Accepted Manuscript

Please do not adjust margins

Published on 13 April 2020. Downloaded by North Carolina State University on 4/13/2020 9:37:46 PM.

Most optimization efforts using the NHC motif were geared towards pyridine and structurally similar compounds.[38, 39] Large improvements for ^{1}H SABRE were recently afforded with perdeuterated[8] or chlorinated [40] variant of the [IrCl(IMes)(COD)] (**2**) system with record polarisations on the order of 50%. However, these improvements do not extend to other substrates with higher steric demands. In efforts to target a broader substrate scope, auxiliary compounds (co-ligands) have been utilized to increase the number of viable polarisation transfer targets and to focus transferred polarisation.[16, 41-44] Also, chelating ligands have been explored, but polarisation levels remained low. [45, 46] While a variety of smaller pyrazole derivatives were studied in Ref.[47], polarisation on 2-substituted pyridines was not reported.

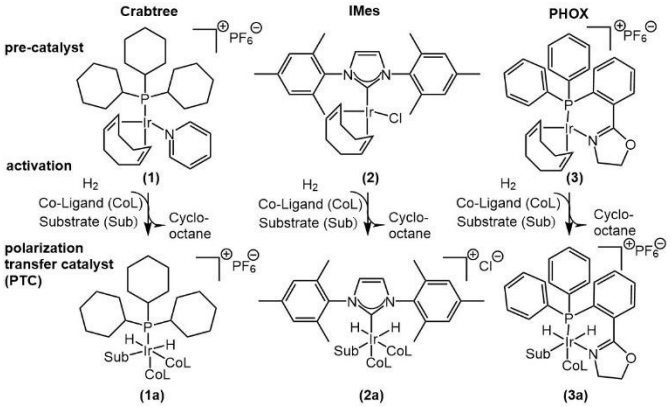


Figure 1: Three generations of catalysts for SABRE. The canonical Crabtree's catalyst (**1**), the IMes catalyst (**2**) yielding maximal enhancements on pyridine, and the Phox catalyst (**3**) applicable to sterically demanding substrates, as shown here. Coligands (CoL) are constituted by solvent, substrate or an auxiliary compound.

Here we demonstrate that [Ir(COD)(Phox)]PF_6 (**3**) (Phox = 2-(2-(diphenylphosphanyl)phenyl)-4,5-dihydrooxazole) (Figure 1), a catalyst for asymmetric hydrogenation of olefins[48], can serve as a polarisation transfer catalyst for more sterically demanding substrates.[49, 50] We target ^{1}H, ^{15}N and ^{19}F hyperpolarisation in ortho-substituted pyridine derivatives, including provitamin B_6 and caffeine. It is noteworthy, that although **(3)** performs *worse* as a polarisation transfer catalyst for pyridine, compared to **(2)**, it is superior for sterically congested substrates, which are not hyperpolarised with the IMes catalyst **(2)** at all.

As illustrated in Figure 1, in SABRE experiments, precatalysts are transformed into their catalytically active species under a H_2 atmosphere in presence of polarisation transfer targets. For precatalyst (**2**) and the substrate pyridine, one obtains $[Ir(H)_2(IMes)(pyr)_3]^+$ (**2a**). This dihydride derived from *p*-H_2 constitutes the catalytically active complex in polarisation transfer reactions.[35, 51] One important consequence of monodentate ligands (e.g. an NHC or Phosphines) and the octahedral iridium dihydride complexes is that three sites remain for coordination (pyridine in **(2a)**). By using a bidentate ligand, such as [Ir(COD)(Phox)]PF_6 **(3)** the binding pocket size is significantly increased over that of complexes with monodentate ligands.

When pre-catalyst **(3)** is activated under a hydrogen atmosphere in the presence of substrates, **(3a)** is formed (see Fig. 1 and 2A). Evidence for (3a) is provided by NMR data (Fig. 2B and see below) and accompanying density-functional theory (DFT) calculations.[52-56] The DFT code used (FHI-aims[52, 57, 58]) is a high-precision, all-electron implementation that has been benchmarked extensively in past work,[59, 60] including a history of successful use for molecular structure prediction (e.g., Refs.[61-64]). Detailed analysis of the DFT calculations, including extensive benchmark and validation data for the methods used, is presented in the Supporting Information. The DFT calculations find **(3a)** to be the lowest energy dihydride complex. Consistent with this structure, we find different chemical shifts for the two hydride species attached to Ir, as displayed in Fig. 2. Specifically, if *para*-hydrogen is bubbled through the solution at high field (8.45 T) the anti-phase spectrum of Figure 2B is obtained. [65, 66] We observe chemical shifts of -19.0 and -22.5 ppm for the hydride resonances, pointing to trans-to nitrogen coordination for both hydrides, where the chemical shift at -22.5 ppm is identical with the *trans*-to-pyridine hydride in **(2a)**.

The observed hydride to hydride *J*-coupling in **(3a)** is $J_{HH'} \approx -7$ Hz and the hydride to ^{31}P *J*-couplings are $J_{HP} = J_{H'P} \approx 20$ Hz. The *J*-couplings, chemical shifts, and magnetic field dependence of hyperpolarisation (see supplement) are very similar to those of

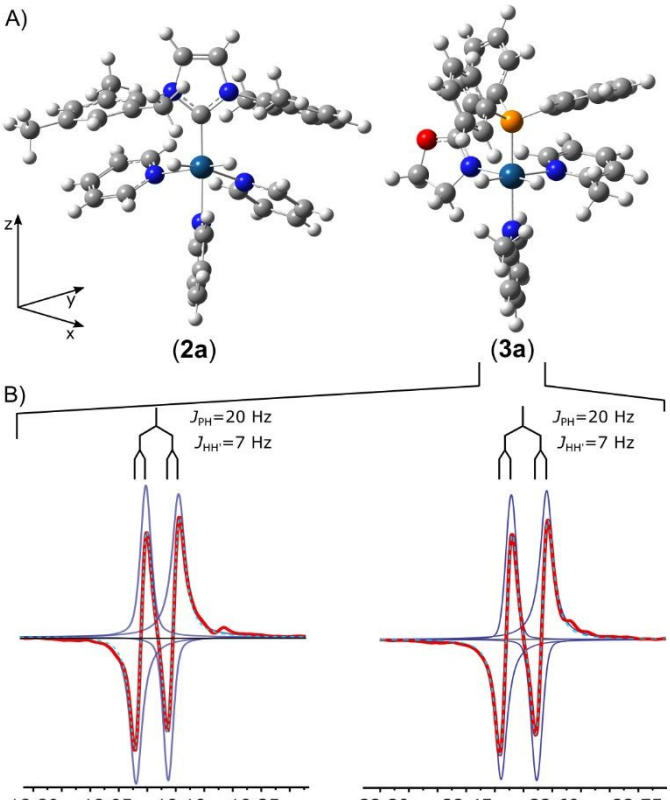


Figure 2: A) Comparison of the structure of $[Ir(H)_2(IMes)(pyr)_3]^+$ (**2a**) and the structure predicted for $[Ir(H)_2(Phox)(MP)_2]^+$ (**3a**) (MP = 2-methylpyridine). B) Experimental Spectrum (red) and fit (dashed line, cyan) of the hydride resonances of (**3a**). For the experiment, constant *para*-H_2 flow was supplied at 8.45 T and the excitation pulse is 45°. The fit is the sum of individual resonances (blue curves). The maxima of the blue curves can be used to extract δ = -19.03 and -22.55 ppm, using $J_{HH'} \approx -7$ Hz, $J_{HP} = J_{H'P} \approx 20$ Hz as shown in the small insets directly above the spectra. With a chemical shift difference of approximately 3.5 ppm, a PASADENA-like spectrum is obtained.

View Article Online DOI: 10.1039/D0CC01330C

ChemComm Accepted Manuscript

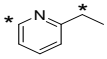
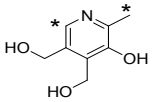
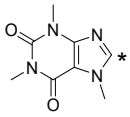
This journal is © The Royal Society of Chemistry 20xx

View Article Online
DOI: 10.1039/D0CC01773C

Crabtree's catalyst, serving as further evidence for structure **(3a)**. While a full conformational study of **(3a)** at relatively low concentrations remains beyond the scope of this work, the proposed structure **(3a)** provides a consistent mechanistic explanation for the main observation of this paper, which is the ability of **(3)** and its activated state to successfully hyperpolarize substrates that are much more difficult to access with other commonly used catalysts.

We found that **(3)** allows ^{1}H polarisation in a range of 2-substituted pyridines, where the conventional IMes catalyst **(2)** is not applicable. Table 1 contrasts ^{1}H enhancements obtained with the first-generation Crabtree's catalyst **(1)**, the IMes catalyst **(2)** optimized for pyridine, and the bidentate Phox catalyst **(3)**. As in studies using **(1)**, maximum enhancements on substrate ^{1}H nuclei with **(3)** are obtained at 140 G irrespective of substrate identity (see SI). This is consistent with the study of Pravdivtsev *et al.*, where presence of ^{31}P in the first coordination sphere of Ir changes the matching conditions to a higher magnetic field when compared to **(2)**.[67] It is noteworthy that catalyst **(3)** yields enhancements of aromatic protons in α-picoline and 2-fluoropyridine (Table 1, entries 2 and 3), comparable to those originally reported for SABRE with Crabtree's catalyst **(1)** and pyridine (Table 1, entry 1).[1, 2] Interestingly, Crabtree's catalyst yields a small but non-negligible hyperpolarisation effect on 2-fluoropyridine in that the sign of the polarisation changed compared to simple thermal polarisation. This shows that the activity of Crabtree's catalysts is not strictly zero for this substrate but still drastically lower than that of the Phox catalyst **(3)**. Similar small but non-zero activity is possible for the other cases labeled "-" in Table 1, however, remained below the detection limits of our experiments.

Table 1: Comparison of average ^{1}H enhancements ε at RT (over thermal signals at 8.5 T). Asterisks in the molecular sketches denote the enhanced ^{1}H moieties. No enhancements are observed for substrate 6.

Entry	substrate name	structure	^{1}H ε with Crabtree **(1)**	^{1}H ε with IMes **(2)**	^{1}H ε with Phox **(3)** aromatic/ aliphatic
1	pyridine		100	130 0	2
2	α-picoline		–	–	132/11
3	2-fluoro-pyridine		1[a]	–[b]	140
4	2-ethyl-pyridine		–	–	25/5
5	provitamin B_6		–[c]	–[c]	7/2[c]
6	2,6-lutidine		–	–	–
7	caffeine		–	–	4[d]

a) Non-thermal signal (negative sign relative to thermal reference) but identical integral observed. b) HD exchange of 2-fluoropyridine with solvent observed, see Fig. S16 in SI. c) From pyridoxine*HCl (neutralized with NaOD 40 wt% in D_2O).
d) Saturated in MeOH-d_4 (23 mM); only aromatic H enhanced.

The enhancements for aliphatic proton are relatively poor for all entries (~10-fold). Comparing entries 2 and 4, increasing the chain length of the aliphatic substituent reduces aromatic proton enhancements by 80%. Potentially the most interesting structure, from an application viewpoint, is provitamin B_6 (entry 5). In our experiments, enhancements of aromatic and aliphatic protons of 7 and 2 respectively were achieved. The enhancements were limited since the provitamin B6 was commercially available only as a hydrochloride salt, which necessitated addition of a base (triethylamine or NaOD) for neutralization. This procedure also resulted in addition of a small amount of water, which reduces SABRE efficiency somewhat. Regarding the limitations by sterical congestion, we note that hyperpolarisation of 2,6-dimethylpyridine (entry 6) remained unsuccessful. To rationalize this finding, we show in the supplement (Figure S5, Table S9, as well as an analysis of strain effects in Supplemental section 2d and Tables S10-S13) that DFT modelling of the substitution of 2-methylpyridine (entry 2) in **(3a)** by 2,6-dimethylpyridine results in an approximate energy increase of +0.5 eV (48 kJ/mol), much larger than $N_a k_B T$. Adding additional co-ligands (CH_3CN, H_2O, Pyridine), an approach that was successful in prior instances with sterically hindered substrates,[10, 16, 41, 43, 68] also failed to effect hyperpolarisation of 2,6-dimethylpyridine in the present work. Entries 1 (pyridine) and 7 (caffeine) show small but non-zero enhancements. For caffeine (entry 7), small enhancements are expected as caffeine is the largest substrate we examined and may require a catalyst optimized for even larger motifs.

Next, we used the Phox catalyst **(3)** for polarising ^{15}N at μT magnetic fields with SABRE-SHEATH.[7, 10, 17, 69-71] The simple substrate CH_3CN has previously been found to show 190-fold ^{1}H polarisation enhancements when used as a coligand with the IMes catalyst.[72] We investigated ^{15}N polarisation with $CH_3C^{15}N$ (50 mM) and 2.6 mM solutions of **(3)** as a function of temperature at microTesla fields as displayed in Fig. 3. We found that ^{15}N polarisation levels of 1.5 % are readily obtained, identical to polarisation levels achieved with **(2)** at these moderately high concentrations.[10] As indicated in Fig. 3, the optimal temperature is elevated when using the Phox catalyst **(3)**. Here the maximum is found between 60 °C and 70 °C, whereas IMes works best at room temperature for ^{15}N-acetonitrile **(2)**.[10] Next, as shown in the bottom of Fig. 3, the Phox catalyst **(3)** hyperpolarises ^{15}N at natural abundance in substrates 1-4 using 2.6 mM catalyst and 50 mM substrate (see Fig. 3, bottom). Notice that the nitrogen enhancements ε are larger for ^{15}N than for ^{1}H. However, the absolute polarisation levels are similar because the enhancement refers to thermal polarisation of ^{15}N, which is ten times lower than for ^{1}H. We also note that similar temperature dependent measurements were not possible for ^{1}H with our present

Published on 13 April 2020. Downloaded by North Carolina State University on 4/13/2020 9:37:46 PM.

ChemComm Accepted Manuscript

View Article Online
DOI: 10.1039/D0CC01730C

setup since ^{1}H relaxation times are shorter, leading to larger uncertainties as a result of having to transfer samples manually between a temperature controlled mT field environment and the spectrometer.

Finally, we also tested the previously challenging[12] ^{19}F polarisation of 2-fluoropyridine (i.e., ^{19}F in the ortho position) and achieved a 30-fold enhancement over thermal polarisation at 9.4 T, at an optimised polarisation transfer field of 5.4 mT (Figure S15 in the supplement). In Ref.[12], it was shown that ^{19}F in the ortho position was difficult to hyperpolarize with the IMes catalyst (attributed to steric hindrance) whereas here we achieve hyperpolarisation with the Phox catalyst.

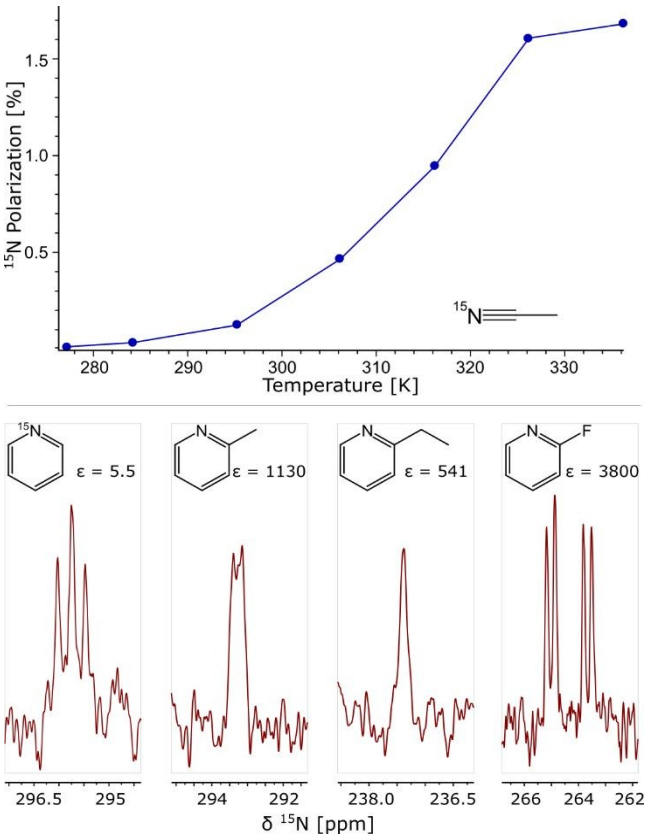


Figure 3: (Top) ^{15}N Polarisation with PHOX **(3)** as a function of the sample temperature during polarisation build-up on ^{15}N labelled CH_3CN in the magnetic shield. Evolution field is 0.66 μT, build-up time 60 s. (Bottom) ^{15}N spectra of naturally abundant 2-substituted pyridine derivatives and ^{15}N labelled pyridine hyperpolarised by SABRE-SHEATH at room temperature. 2.6 mM catalyst (3) and 50 mM substrate were used in all samples.

In conclusion, the introduced PHOX multidentate ligand for SABRE catalysts allows for polarisation of bulkier substrates, including biologically relevant molecules such as provitamin B_6 or caffeine. Interestingly, hyperpolarisation is worse for pyridine than for 2-substituted pyridine derivatives. This shows that testing potential SABRE catalysts on a small set of substrates is insufficient and opportunities for expanding the SABRE substrate scope may be missed. Indeed, the Phox catalyst performs better than the highly optimised (for pyridine) IMes catalyst when considering bulkier substrates. Moreover, attractive features of chelating ligands, such as reliable immobilization and simplification of kinetics to supress non-hyperpolarising exchange pathways, give a promising handle towards the rational design of SABRE catalysts. Altogether, these finding provide a path towards a broader scope of SABRE hyperpolarisation with numerous applications in biomedicine and beyond.[42, 73]

Acknowledgements

There are no conflicts of interests to declare. The authors gratefully acknowledge the support by the National Institute of Biomedical Imaging and Bioengineering of the NIH (R21EB025313). We also gratefully acknowledge funding by the NSF (CHE-1665090) and by Duke University. EYC is grateful for funding support from NSF CHE-1904780, NIH 1R21EB020323 and 1R21CA220137; and DOD CDMRP W81XWH-12-1-0159/BC112431 and W81XWH-15-1-0271. Furthermore, support from the Donors of the American Chemical Society Petroleum Research Fund is gratefully acknowledged.

Author Contributions

J. F. P. C and A. W. J. L. contributed equally, conducted most experimental work, wrote and edited the paper. Z.Z and J. R. L. helped with experimental work and edited the paper. R. L. conducted all ab-initio calculations. R V. S. and E.Y.C. conducted the fluorine hyperpolarisation experiments and edited the paper. V. B. advised the ab-initio calculations and edited/revised the paper, W. S. W. advised the team. S. J. M. advised on chemical design and edited the paper. T. T. advised on data acquisition, wrote, edited and revised the paper.

References

1. R. W. Adams, J. A. Aguilar, K. D. Atkinson, M. J. Cowley, P. I. P. Elliott, S. B. Duckett, G. G. R. Green, I. G. Khazal, J. Lopez-Serrano and D. C. Williamson, *Science*, 2009, **323**, 1708-1711.
2. K. D. Atkinson, M. J. Cowley, P. I. P. Elliott, S. B. Duckett, G. G. R. Green, J. López-Serrano and A. C. Whitwood, *J. Am. Chem. Soc.*, 2009, **131**, 13362-13368.
3. R. W. Adams, S. B. Duckett, R. A. Green, D. C. Williamson and G. G. R. Green, *J. Chem. Phys.*, 2009, **131**.
4. P. Nikolaou, B. M. Goodson and E. Y. Chekmenev, *Chem. Eur. J.*, 2015, **21**, 3156-3166.
5. J.-B. Hövener, A. N. Pravdivtsev, B. Kidd, C. R. Bowers, S. Glöggler, K. V. Kovtunov, M. Plaumann, R. Katz-Brull, K. Buckenmaier, A. Jerschow, F. Reineri, T. Theis, R. V. Shchepin, S. Wagner, N. M. M. Zacharias, P. Bhattacharya and E. Y. Chekmenev, *Angew. Chem. Int. Ed.* , 2018, DOI: 10.1002/anie.201711842.
6. S. B. Duckett and N. J. Wood, *Coordination Chemistry Reviews*, 2008, **252**, 2278-2291.
7. T. Theis, M. L. Truong, A. M. Coffey, R. V. Shchepin, K. W. Waddell, F. Shi, B. M. Goodson, W. S. Warren and E. Y. Chekmenev, *J. Am. Chem. Soc.*, 2015, **137**, 1404-1407.

Published on 13 April 2020. Downloaded by North Carolina State University on 4/13/2020 9:37:46 PM.

ChemComm Accepted Manuscript

This journal is © The Royal Society of Chemistry 20xx

View Article Online
DOI: 10.1039/D0CC01330G

8. P. J. Rayner, M. J. Burns, A. M. Olaru, P. Norcott, M. Fekete, G. G. R. Green, L. A. R. Highton, R. E. Mewis and S. B. Duckett, *Proc. Natl. Acad. Sci.*, 2017, **114**, E3188-E3194.
9. D. A. Barskiy, R. V. Shchepin, A. M. Coffey, T. Theis, W. S. Warren, B. M. Goodson and E. Y. Chekmenev, *J. Am. Chem. Soc.*, 2016, **138**, 8080-8083.
10. J. F. P. Colell, A. W. J. Logan, Z. Zhou, R. V. Shchepin, D. A. Barskiy, G. X. Ortiz, Q. Wang, S. J. Malcolmson, E. Y. Chekmenev, W. S. Warren and T. Theis, *J. Phys. Chem. C*, 2017, 6626–6634.
11. Z. Zhou, J. Yu, J. F. P. Colell, R. Laasner, A. Logan, D. A. Barskiy, R. V. Shchepin, E. Y. Chekmenev, V. Blum, W. S. Warren and T. Theis, *J. Phys. Chem. Lett.*, 2017, **8**, 3008-3014.
12. A. M. Olaru, T. B. R. Robertson, J. S. Lewis, A. Antony, W. Iali, R. E. Mewis and S. B. Duckett, *ChemistryOpen*, 2018, **7**, 97-105.
13. R. V. Shchepin, B. M. Goodson, T. Theis, W. S. Warren and E. Y. Chekmenev, *Chem. Phys. Chem.*, 2017, **18**, 1961-1965.
14. D. A. Barskiy, R. V. Shchepin, C. P. N. Tanner, J. F. P. Colell, B. M. Goodson, T. Theis, W. S. Warren and E. Y. Chekmenev, *Chem. Phys. Chem.*, 2017, **18**, 1493-1498.
15. V. V. Zhivonitko, I. V. Skovpin and I. V. Koptyug, *Chem. Commun.*, 2015, **51**, 2506-2509.
16. R. E. Mewis, R. A. Green, M. C. R. Cockett, M. J. Cowley, S. B. Duckett, G. G. R. Green, R. O. John, P. J. Rayner and D. C. Williamson, *J. Phys. Chem. B*, 2015, **119**, 1416-1424.
17. J. F. P. Colell, M. Emondts, A. W. J. Logan, K. Shen, J. Bae, R. V. Shchepin, G. X. Ortiz, P. Spannring, Q. Wang, S. J. Malcolmson, E. Y. Chekmenev, M. C. Feiters, F. P. J. T. Rutjes, B. Blümich, T. Theis and W. S. Warren, *J. Am. Chem. Soc.*, 2017, **139**, 7761-7767.
18. S. Lehmkuhl, M. Emondts, L. Schubert, P. Spannring, J. Klankermayer, B. Blümich and P. Schleker, *Chem. Phys. Chem.*, 2017, DOI: 10.1002/cphc.201700750.
19. P. Spannring, I. Reile, M. Emondts, P. P. M. Schleker, N. K. J. Hermkens, N. G. J. van der Zwaluw, B. J. A. van Weerdenburg, P. Tinnemans, M. Tessari, B. Blümich, F. P. J. T. Rutjes and M. C. Feiters, *Chem. Eur. J.*, 2016, **22**, 9277-9282.
20. K. V. Kovtunov, L. M. Kovtunova, M. E. Gemeinhardt, A. V. Bukhtiyarov, J. Gesiorski, V. I. Bukhtiyarov, E. Y. Chekmenev, I. V. Koptyug and B. M. Goodson, *Angew. Chem. Int. Ed.*, 2017, **56**, 10433-10437.
21. F. Shi, P. He, Q. A. Best, K. Groome, M. L. Truong, A. M. Coffey, G. Zimay, R. V. Shchepin, K. W. Waddell, E. Y. Chekmenev and B. M. Goodson, *J. Phys. Chem. C*, 2016, **120**, 12149-12156.
22. M. L. Truong, F. Shi, P. He, B. Yuan, K. N. Plunkett, A. M. Coffey, R. V. Shchepin, D. A. Barskiy, K. V. Kovtunov, I. V. Koptyug, K. W. Waddell, B. M. Goodson and E. Y. Chekmenev, *J. Phys. Chem. B*, 2014, **18** 13882–13889.
23. H. Zeng, J. Xu, M. T. McMahon, J. A. B. Lohman and P. C. M. van Zijl, *J. Magn. Reson.*, 2014, **246**, 119-121.
24. M. Fekete, C. Gibard, G. J. Dear, G. G. R. Green, A. J. J. Hooper, A. D. Roberts, F. Cisnetti and S. B. Duckett, *Dalton Trans.*, 2015, **44**, 7870-7880.
25. J.-B. Hövener, N. Schwaderlapp, R. Borowiak, T. Lickert, S. B. Duckett, R. E. Mewis, R. W. Adams, M. J. Burns, L. A. R. Highton, G. G. R. Green, A. Olaru, J. Hennig and D. von Elverfeldt, *Anal. Chem.*, 2014, **86**, 1767-1774.
26. F. Shi, A. M. Coffey, K. W. Waddell, E. Y. Chekmenev and B. M. Goodson, *J. Phys. Chem. C*, 2015, **119**, 7525–7533.
27. F. Shi, A. M. Coffey, K. W. Waddell, E. Y. Chekmenev and B. M. Goodson, *Angew. Chem. Int. Ed.*, 2014, **53**, 7495–7498.
28. A. M. Olaru, M. J. Burns, G. G. R. Green and S. B. Duckett, *Chem. Sci.*, 2017, **8**, 2257-2266.
29. R. V. Shchepin, D. A. Barskiy, A. M. Coffey, T. Theis, F. Shi, W. S. Warren, B. M. Goodson and E. Y. Chekmenev, *ACS Sensors*, 2016, 640-644.
30. H. Zeng, J. Xu, J. Gillen, M. T. McMahon, D. Artemov, J.-M. Tyburn, J. A. B. Lohman, R. E. Mewis, K. D. Atkinson, G. G. R. Green, S. B. Duckett and P. C. M. van Zijl, *J. Magn. Reson.*, 2013, **237**, 73-78.
31. S. S. Roy, K. M. Appleby, E. J. Fear and S. B. Duckett, *J. Phys. Chem. Lett.*, 2018, **9**, 1112-1117.
32. P. J. Rayner and S. Duckett, *Angew. Chem. Int. Ed.*, 2018, DOI: 10.1002/anie.201710406.
33. K. M. Appleby, R. E. Mewis, A. M. Olaru, G. G. R. Green, I. J. S. Fairlamb and S. B. Duckett, *Chem. Sci.*, 2015, **6**, 3981-3993.
34. R. V. Shchepin, M. L. Truong, T. Theis, A. M. Coffey, F. Shi, K. W. Waddell, W. S. Warren, B. M. Goodson and E. Y. Chekmenev, *J. Phys. Chem. Lett.*, 2015, **6**, 1961-1967.
35. M. J. Cowley, R. W. Adams, K. D. Atkinson, M. C. R. Cockett, S. B. Duckett, G. G. R. Green, J. A. B. Lohman, R. Kerssebaum, D. Kilgour and R. E. Mewis, *J. Am. Chem. Soc.*, 2011, **133**, 6134-6137.
36. X. Bantreil and S. P. Nolan, *Nat. Protoc.*, 2010, **6**, 69-77.
37. L. S. Lloyd, A. Asghar, M. J. Burns, A. Charlton, S. Coombes, M. J. Cowley, G. J. Dear, S. B. Duckett, G. R. Genov, G. G. R. Green, L. A. R. Highton, A. J. J. Hooper, M. Khan, I. G. Khazal, R. J. Lewis, R. E. Mewis, A. D. Roberts and A. J. Ruddlesden, *Catal. Sci. Technol.*, 2014, **4**, 3544-3554.
38. B. J. A. van Weerdenburg, N. Eshuis, M. Tessari, F. P. J. T. Rutjes and M. C. Feiters, *Dalton Trans.*, 2015, 15387-15390.
39. B. J. A. van Weerdenburg, S. Glöggler, N. Eshuis, A. H. J. Engwerda, J. M. M. Smits, R. de Gelder, S. Appelt, S. S. Wymenga, M. Tessari, M. C. Feiters, B. Blümich and F. P. J. T. Rutjes, *Chem. Commun.*, 2013, **49**, 7388.
40. P. J. Rayner, P. Norcott, K. M. Appleby, W. Iali, R. O. John, S. J. Hart, A. C. Whitwood and S. B. Duckett, *Nat. Commun.*, 2018, **9**, 4251.
41. N. Eshuis, R. L. E. G. Aspers, B. J. A. van Weerdenburg, M. C. Feiters, F. P. J. T. Rutjes, S. S. Wijmenga and M. Tessari, *Angew. Chem. Int. Ed.*, 2015, **54**, 14527-14530.
42. N. Eshuis, B. J. A. van Weerdenburg, M. C. Feiters, F. P. J. T. Rutjes, S. S. Wijmenga and M. Tessari, *Angew. Chem. Int. Ed.*, 2015, **54**, 1372-1372.
43. I. Reile, R. L. E. G. Aspers, J.-M. Tyburn, J. G. Kempf, M. C. Feiters, F. P. J. T. Rutjes and M. Tessari, *Angew. Chem. Int. Ed.*, 2017, **56**, 9174-9177.
44. N. Eshuis, N. Hermkens, B. J. A. van Weerdenburg, M. C. Feiters, F. P. J. T. Rutjes, S. S. Wijmenga and M. Tessari, *Journal of the American Chemical Society*, 2014, **136**, 2695-2698.
45. A. J. Holmes, P. J. Rayner, M. J. Cowley, G. G. R. Green, A. C. Whitwood and S. B. Duckett, *Dalton Trans.*, 2015, **44**, 1077-1083.
46. A. J. Ruddlesden, R. E. Mewis, G. G. R. Green, A. C. Whitwood and S. B. Duckett, *Organometallics*, 2015, **34**, 2997-3006.

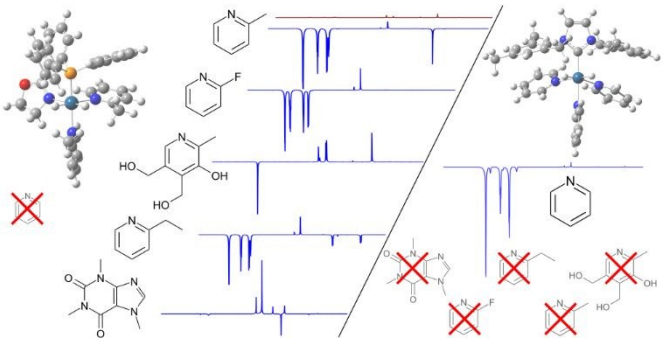
Published on 13 April 2020. Downloaded by North Carolina State University on 4/13/2020 9:37:46 PM.

ChemComm Accepted Manuscript

View Article Online
DOI: 10.1039/D0CC01330G

47. E. B. Ducker, L. T. Kuhn, K. Munnemann and C. Griesinger, *Journal of magnetic resonance*, 2012, **214**, 159-165.
48. C. Mazet, S. P. Smidt, M. Meuwly and A. Pfaltz, *J. Am. Chem. Soc.*, 2004, **126**, 14176-14181.
49. A. Pfaltz, J. Blankenstein, R. Hilgraf, E. Hörmann, S. McIntyre, F. Menges, M. Schönleber, S. P. Smidt, B. Wüstenberg and N. Zimmermann, *Adv. Synth. Catal.*, 2003, **345**, 33-43.
50. B. Wüstenberg and A. Pfaltz, *Adv. Synth. Catal.*, 2008, **350**, 174-178.
51. D. A. Barskiy, A. N. Pravdivtsev, K. L. Ivanov, K. V. Kovtunov and I. V. Koptyug, *Phys. Chem. Chem. Phys.*, 2015, **89**, 89-93.
52. V. Blum, R. Gehrke, F. Hanke, P. Havu, V. Havu, X. Ren, K. Reuter and M. Scheffler, *Comput. Phys. Commun.*, 2009, **180**, 2175-2196.
53. M. Sinstein, C. Scheurer, S. Matera, V. Blum, K. Reuter and H. Oberhofer, *J. Chem. Theory Comput.*, 2017, **13**, 5582-5603.
54. J. P. Perdew, K. Burke and M. Ernzerhof, *Phys. Rev. Lett.*, 1996, **77**, 3865-3868.
55. A. Tkatchenko and M. Scheffler, *Phys. Rev. Lett.*, 2009, **102**.
56. Y. Zhao and D. G. Truhlar, *Theor. Chem. Acc.*, 2007, **120**, 215-241.
57. V. Havu, V. Blum, P. Havu and M. Scheffler, *Journal of Computational Physics*, 2009, **228**, 8367-8379.
58. X. Ren, P. Rinke, V. Blum, J. Wieferink, A. Tkatchenko, A. Sanfilippo, K. Reuter and M. Scheffler, *New Journal of Physics*, 2012, **14**.
59. K. Lejaeghere, G. Bihlmayer, T. Björkman, P. Blaha, S. Blügel, V. Blum, D. Caliste, I. E. Castelli, S. J. Clark, A. Dal Corso, S. de Gironcoli, T. Deutsch, J. K. Dewhurst, I. Di Marco, C. Draxl, M. Dułak, O. Eriksson, J. A. Flores-Livas, K. F. Garrity, L. Genovese, P. Giannozzi, M. Giantomassi, S. Goedecker, X. Gonze, O. Grånäs, E. K. U. Gross, A. Gulans, F. Gygi, D. R. Hamann, P. J. Hasnip, N. A. W. Holzwarth, D. Iuşan, D. B. Jochym, F. Jollet, D. Jones, G. Kresse, K. Koepernik, E. Küçükbenli, Y. O. Kvashnin, I. L. M. Locht, S. Lubeck, M. Marsman, N. Marzari, U. Nitzsche, L. Nordström, T. Ozaki, L. Paulatto, C. J. Pickard, W. Poelmans, M. I. J. Probert, K. Refson, M. Richter, G.-M. Rignanese, S. Saha, M. Scheffler, M. Schlipf, K. Schwarz, S. Sharma, F. Tavazza, P. Thunström, A. Tkatchenko, M. Torrent, D. Vanderbilt, M. J. van Setten, V. Van Speybroeck, J. M. Wills, J. R. Yates, G.-X. Zhang and S. Cottenier, *Science*, 2016, **351**.
60. S. R. Jensen, S. Saha, J. A. Flores-Livas, W. Huhn, V. Blum, S. Goedecker and L. Frediani, *The Journal of Physical Chemistry Letters*, 2017, **8**, 1449-1457.
61. M. Rossi, V. Blum, P. Kupser, G. Von Helden, F. Bierau, K. Pagel, G. Meijer and M. Scheffler, *Journal of Physical Chemistry Letters*, 2010, **1**, 3465-3470.
62. S. Chutia, M. Rossi and V. Blum, *Journal of Physical Chemistry B*, 2012, **116**, 14788-14804.
63. M. Rossi, S. Chutia, M. Scheffler and V. Blum, *The Journal of Physical Chemistry A*, 2014, **118**, 7349-7359.
64. F. Schubert, M. Rossi, C. Baldauf, K. Pagel, S. Warnke, G. von Helden, F. Filsinger, P. Kupser, G. Meijer, M. Salwiczek, B. Koksch, M. Scheffler and V. Blum, *Physical chemistry chemical physics : PCCP*, 2015, **17**, 7373-7385.
65. T. Theis, G. X. Ortiz, A. W. J. Logan, K. E. Claytor, Y. Feng, W. P. Huhn, V. Blum, S. J. Malcolmson, E. Y. Chekmenev, Q. Wang and W. S. Warren, *Sci. Adv.*, 2016, **2**, e1501438-e1501438.
66. C. R. Bowers and D. P. Weitekamp, *J. Am. Chem. Soc.*, 1987, **109**, 5541-5542.
67. A. N. Pravdivtsev, A. V. Yurkovskaya, H.-M. Vieth, K. L. Ivanov and R. Kaptein, *Chem. Phys. Chem*, 2013, **14**, 3327-3331.
68. K. Shen, A. W. J. Logan, J. F. P. Colell, J. Bae, G. X. Ortiz, T. Theis, W. S. Warren, S. J. Malcolmson and Q. Wang, *Angew. Chem. Int. Ed.*, 2017, **56**, 12112-12116.
69. M. L. Truong, T. Theis, A. M. Coffey, R. V. Shchepin, K. W. Waddell, F. Shi, B. M. Goodson, W. S. Warren and E. Y. Chekmenev, *J. Phys. Chem. C*, 2015, **119**, 8786-8797.
70. S. S. Roy, G. Stevanato, P. J. Rayner and S. B. Duckett, *J. Magn. Reson.*, 2017, **285**, 55-60.
71. T. Theis, M. Truong, A. M. Coffey, E. Y. Chekmenev and W. S. Warren, *J. Magn. Reson.*, 2014, **248**, 23-26.
72. M. Fekete, P. J. Rayner, G. G. R. Green and S. B. Duckett, *Magnetic Resonance in Chemistry*, 2017, **55**, 944-957.
73. R. V. Shchepin, D. A. Barskiy, A. M. Coffey, B. M. Goodson and E. Y. Chekmenev, *ChemistrySelect*, 2016, **1**, 2552-2555.

TOC Figure: Phox ligands enable new substrates for SABRE.



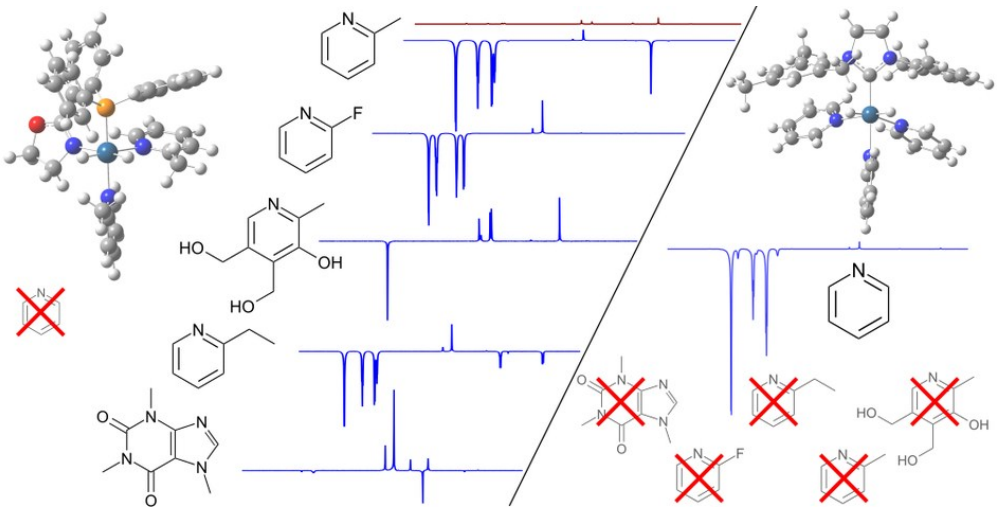
Published on 13 April 2020. Downloaded by North Carolina State University on 4/13/2020 9:37:46 PM.

ChemComm Accepted Manuscript

This journal is © The Royal Society of Chemistry 20xx

View Article Online
DOI: 10.1039/D0CC01330G

Published on 13 April 2020. Downloaded by North Carolina State University on 4/13/2020 9:37:46 PM.



80x40mm (300 x 300 DPI)

ChemComm Accepted Manuscript